MODELING AND ANALYSIS OF THE LATENT HEAT COLD THERMAL ENERGY STORAGE (LTES) SYSTEM USING SALT HYDRATE

by

Mahfuja A. Khuda

A dissertation submitted to the faculty of
The University of North Carolina at Charlotte
in partial fulfillment of the requirements
for the degree of Doctor of Philosophy in
Mechanical Engineering

Charlotte

2024

Approved by:

____
Dr. Nenad Sarunac

____
Dr. Harish Cherukuri

____
Dr. Russell Keanini

____
Dr. Wesley Williams

____
Dr. Shen-En Chen

©2024
Mahfuja A. Khuda
ALL RIGHTS RESERVED

ABSTRACT

MAHFUJA A. KHUDA. Modeling and Analysis of the Latent Heat Cold Thermal Energy Storage (LTES) System Using Salt Hydrate. (Under the direction of Dr. NENAD SARUNAC)

Energy storage plays a crucial role in addressing the growing demand for energy and electricity while simultaneously reducing greenhouse gas emissions. Most of the power infrastructure in the U.S. heavily relies on water-cooling technology, leading to significant freshwater withdrawals. To mitigate high water withdrawal rates and the thermal pollution of water sources, an alternative solution involves implementing dry cooling towers (DCT) or air-cooled condensers (ACC). However, the effectiveness of dry cooling techniques depends on the dry bulb temperature of the ambient cooling air, resulting in a plant performance penalty equivalent to approximately a 2%-point efficiency loss compared to wet cooling.

The current research focuses on designing a cost-effective latent heat cold thermal energy storage (LTES) system to enhance the performance of DCT/ACC during the summer months. This is achieved by storing cold energy during the nighttime in inexpensive materials like phase change materials (PCM), such as $CaCl_2$ hexahydrate or CC6. To guide the LTES design, a numerical analysis of the melting and solidification processes of PCM within the tube array was conducted. Transient two-dimensional Navier-Stokes equations and a Realizable k-ε turbulence model were used to predict fluid flow and heat transfer in LTES heat storage modules. The enthalpy-porosity technique was employed to model PCM melting and solidification.

The numerical results show excellent agreement with experimentally obtained values. The resulting design successfully met the predefined performance criteria, achieving a cooling effect of 4 °C for a four-hour duration while maintaining a pressure drop of less than 100 Pa. The proposed prototype-scale tube array design can efficiently cool the incoming ambient air, and PCM in the LTES can be fully frozen overnight. The energy storage density of the system falls within the range of 22 to 27 kWh/m^3, with the maximum energy efficiency reaching around 96% during the system charging and discharging processes, assuming no heat loss from the system. Apart from its primary focus on coal power plant dry cooling technology, the suggested concept can also be used for industrial, commercial, and residential applications, including concentrated solar power (CSP).

ACKNOWLEDGEMENTS

I wish to express my heartfelt appreciation and gratitude to my advisor, Dr. Nenad Sarunac, for his unwavering assistance and support throughout this challenging research project. Without his invaluable guidance, I would not have reached this stage of accomplishment. I am profoundly grateful for the opportunity to collaborate with him during my doctoral studies at the University of North Carolina at Charlotte.

I extend my sincere thanks to Dr. Harish Cherukuri, Dr. Russell Keanini, Dr. Wesley Williams, and Dr. Shen-En Chen for agreeing to be on my doctoral committee and for generously sharing their expertise. Additionally, I am grateful to the Graduate School at UNC Charlotte for their support through tuition and health insurance (GASP) during my PhD program.

I would like to thank Dr. Carlos Romero and the team from Lehigh University for giving me the opportunity to conduct the tests required for numerical modeling. I am thankful to my friends Dr. Javad Khalesi and Dr. Hossain Nemati for helping me with design and numerical modeling during my PhD studies.

Additionally, I acknowledge that this dissertation is based on work supported by the U.S. Department of Energy, Office of Fossil Energy, FE-1 under Award Number DE-FE0031886.

DEDICATION

To my teachers and mentors for their unwavering support.

TABLE OF CONTENTS

LIST OF FIGURES

LIST OF TABLES

NOMENCLATURE

A	Cross-sectional area, m^2
A_{mush}	Mushy zone parameter
$C_{p_{air}}$	Specific heat of air at constant pressure, J/kg.K
$C_{p_{liquid}}$	Specific heat of liquid PCM at constant pressure, J/kg.K
$C_{p_{solid}}$	Specific heat of solid PCM at constant pressure, J/kg.K
c_{P_s}	Specific heat of the tube wall at constant pressure, J/kg.K
$C_{P_{\text{wall}}}$	Specific heat of the duct wall surrounding the module, J/kg.K
D	Diameter of the tube, m
E_{in}	Energy transferred through the system, kJ
E_{st}	Energy stored/ released from PCM filled tubes, kJ
Ex_{in}	Exergy transferred through the system, kJ
Ex_{st}	Exergy stored/ released from PCM filled tubes, kJ
f	Friction factor
Fo	Fourier number ($\alpha t/D^2$)
g_i	Gravitational force, m^2/s
h	Enthalpy, J/kg
$h_{avg.}$	Average heat transfer coefficient, $W/m^2.K$
k	Thermal conductivity of PCM, W/m.K
k_{air}	Thermal conductivity of air, W/m.K
k_s	Thermal conductivity of the tube wall, W/m.K

L_f	Latent heat of fusion, J/kg
$\dot{m}$	Mass flow rate of inlet air, kg/s
m_{wall}	Mass of the duct wall surrounding the module, kg
N_L	Number of tube rows
Nu_D	Nusselt number
P	Pressure, Pa
Pr	Prandtl number ($\mu c_p/k$)
PVC	Poly Vinyl Chloride
Q_{loss}	Heat loss from the system, kJ
Q_{wall}	Heat loss between the duct wall and the module, kJ
q_w''	Wall heat flux, W/m^2
r_i	Inner wall radius of the tube, m
r_0	Outer wall radius of the tube, m
Re_D	Reynolds number ($\rho uD/\mu$)
RTD	Resistance Temperature Detector
S_L	Lateral (row) tube spacing, m
S_T	Transverse tube spacing, m
T	Temperature of PCM, K
T_{in}	Inlet air temperature, K
T_o	Temperature of air at the environmental condition, K
T_{out}	Outlet air temperature, K
T_w	Temperature of the tube wall, K
$T_{w,i}$	Inner wall temperature of the tube, K

$T_{w,o}$	Outer wall temperature of the tube, K
u	Velocity, m/s
v_∞	Free stream velocity, m/s
x	Axial coordinate, m
y	Transverse coordinate, m

Greek symbols

α	Volume fraction of fluid
α_d	Thermal diffusivity, m^2/s
β	Thermal expansion coefficient, 1/K
γ	PCM liquid fraction
Δ	Difference in the quantity
ε	Turbulent energy dissipation rate, m^2/s^3
η	Energy efficiency
κ	Turbulence kinetic energy, m^2/s^2
μ	Dynamic viscosity of PCM, Pa s
μ_{air}	Dynamic viscosity of air, Pa s
ρ	Density of PCM, kg/m^3
ρ_{air}	Density of air, kg/m^3
ρ_s	Density of the tube wall, kg/m^3
χ	Exergy effectiveness
ϵ	Energy effectiveness
$\boldsymbol{\Xi}$	Exergy efficiency

Subscripts

Air	Heat transfer fluid
Avg.	Average value
DF	Driving force
Exp	Experiment
high	Temperature higher than the phase change temperature
i, j	Direction vector
low	Temperature lower than the phase change temperature
Max	Maximum value
Num	Numerical
PCM	Phase change material
Ph. change	Phase change
wall	Wall
Zu	Zukauskas correlation

CHAPTER 1: INTRODUCTION, BACKGROUND AND PROBLEM STATEMENT

1.1. Overview

This section provides information on different energy systems used to meet the high electricity demand, followed by the novelty and significance of the project. A brief review of previous literature is provided to highlight knowledge gaps that motivate this project work. Finally, the dissertation outline is presented.

1.2. Energy storage

The discrepancy between the limited energy supply and high demand for energy has received greater attention over the last couple of years. Global energy use is estimated to increase by 29% from the year 2015 to 2040, according to the U.S. Energy Information Administration [1]. Additionally, greenhouse gas emissions have increased by approximately 90% since 1970 due to the combustion of fossil fuels and industrial processes used to produce electricity [2]. Energy storage plays an important role in meeting the high demand for electricity supply by reducing emissions. It improves plant and system flexibility and allows for higher penetration of renewable energy sources. Figure 1.1 shows a schematic of an energy storage system illustrating how energy is stored and supplied later to the power plant during times of high electricity demand.

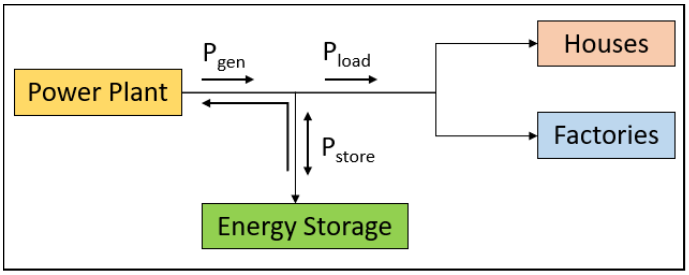

Figure 1. 1 Schematic of Energy Storage Flow Diagram

The design of energy storage is crucial to meet the increasing demand for flexibility. However, there are challenges to implementing energy storage systems, such as high implementation costs.

Regulatory policies and market designs are not up to date. Additionally, seasonal variations in weather make the operation of the system less predictable, for example, with solar and wind energy. Diurnal swings in ambient temperature make power plant systems more challenging to meet power demand.

There are four types of energy storage systems: mechanical, electrochemical, electrical, and thermal. For space heating, cooling, and air-conditioning of residential and commercial buildings, thermal energy storage (TES) systems are a great substitution, offering increased effectiveness and economic viability. There are three different types of TES systems: sensible heat, latent heat, and thermochemical. Sensible heat storage systems utilize heat directly, but their low energy density necessitates more space. Thermochemical storage presents a higher energy density and longer storage duration, but its commercial application is restricted by the high temperatures, sluggish reactions, and associated costs [3]. Conversely, latent heat storage employing phase change materials (PCMs) offers high-density energy storage by capitalizing on the phase transition that occurs at a specific temperature [4]. For this dissertation work, latent heat thermal energy storage (LTES) is selected.

1.3. Latent heat thermal energy storage (LTES)

In the case of LTES systems, energy is stored through heat absorption and released during a phase change of the storage material from one state to another, including solid-solid, solid-liquid, solid-gas, liquid-gas, and vice versa. This method utilizes off-peak power to enhance cooling capacity by extracting heat from a storage medium, such as ice, chilled water, or other phase change materials (PCM). Compared to sensible heat thermal energy storage systems, LTES has become the most common system due to its high thermal energy storage density, which occurs at nearly constant temperature. The liquid-solid phase change (melting/solidification) is typically employed in many storage systems due to its high efficiency and storage capacity. In an LTES system, the amount of stored energy (E_{st}) is determined using the following equation [5]:

$$E_{st} = m\left[\int_{T_{low}}^{T_{melt}} Cp_{solid}(1-\gamma)\, dT + \gamma L_f + \int_{T_{melt}}^{T_{high}} Cp_{liquid}\, \gamma\, dT\right] \tag{1.1}$$

where, m is the mass, Cp_{solid} is the specific heat in solid phase, γ is the fraction melted, L_f is the latent heat per unit mass, Cp_{liquid} is the specific heat in liquid phase, T_{low} is the initial temperature, T_{melt} is PCM melting temperature, T_{high} is the final temperature.

LTES finds extensive application across various engineering domains, including electronic cooling technology, enhancing thermal comfort in buildings, waste heat recovery, textiles, and heating, ventilation, and air conditioning (HVAC) [6]. Materials selected for latent heat storage are determined by their compositions and phase change temperatures. Phase change materials (PCMs) are categorized into three main groups: organic, inorganic, and eutectic formulations. It is important to select appropriate PCMs as a storage medium to achieve the most thermal efficiency from the storage system.

The thermal efficiency of LTES is significantly influenced by factors such as the shape, aspect ratio, and orientation of the PCM container. To ensure sustained thermal effectiveness over the long term, it is imperative that the size and shape of the container correspond to the required cooling capacity of the PCM, specific to the geographical location.

1.4. Significance and novelty of the project

Most of the coal-fired power plants in the US use water-cooled condensers for cooling (heat rejection), which causes high water withdrawals, 75-150 m^3/MWh and thermal pollutions of the water source [7]. Power plants in the US account for approximately 40% of freshwater withdrawals where 90% of it is used in condenser cooling [8]. The alternative option to condenser is wet cooling tower. However, the system is not suitable for the areas subject to drought because of its increased rates of water consumption through evaporation (2.3 m^3/MWh) [9]. Dry cooling technology using air cooled condenser (ACC) is an attractive alternative for the cooling process of coal-fired powerplants. However, the performance of dry cooling technology depends on the ambient conditions which causes 2%-point efficiency loss compared to wet cooling technology. Hence, it is important to improve the dry cooling technique.

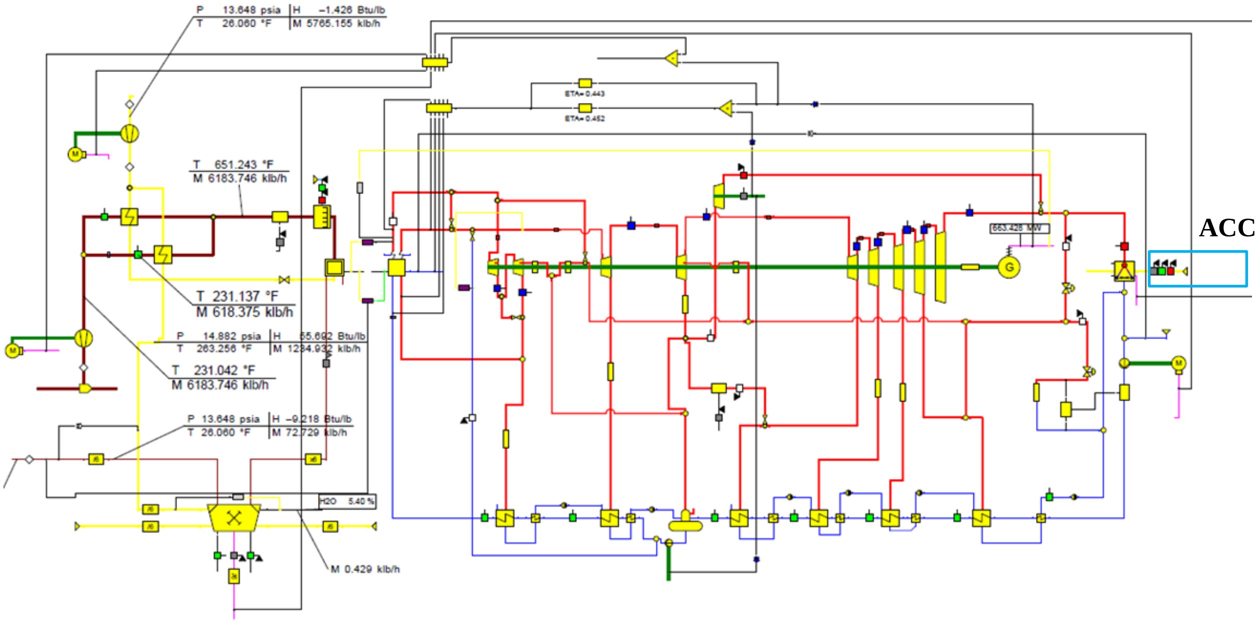

(a)

(b)

Figure 1. 2 (a) Model of a Reference plant with mechanical draft Air Cooled Condenser (ACC), (b) Photo of a multi-bay (cell) ACC [10]

A dry cooling tower (DCT)/ Air-Cooled Condenser (ACC) was employed to a reference steam Rankine cycle coal power plant using EBSILON® Professional (EP) [11] modeling tool, Version 14.00 [11] as shown in Figure 1.2a. The ACC is represented by a triangle-shaped symbol located near the right edge of Figure 1.2a. Physical size of the equipment such as heat exchangers, steam turbine, steam generators, and other components was developed for different design conditions. The model was used to simulate performance of a subcritical nominal 650 MW_{gross} dry cooled power plant. Figure 1.2b shows a photo of a multi-bay ACC located in Turkey, used for the dry cooling systems of a combined cycle power plant [10].

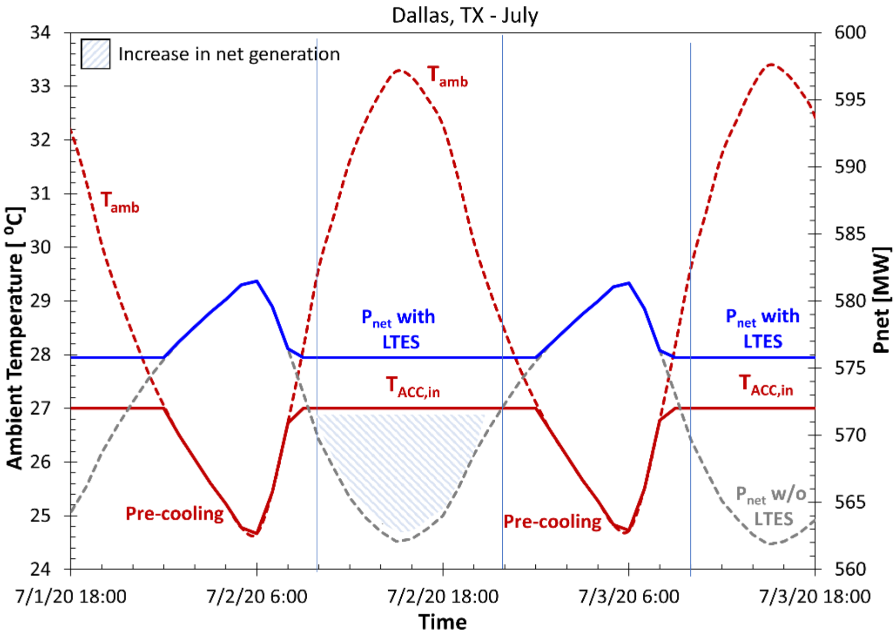

Figure 1. 3 The effect of LTES on air temperature at the ACC inlet and net power output of the reference plant with time for Dallas, TX

Some parameters such as ambient air temperature, humidity, steam condensing pressure, minimum allowed condensing pressure, terminal temperature difference (TTD), and average heat transfer coefficient were considered to design ACC. The variation of ambient temperature throughout the day in Dallas, Texas, during the summertime is presented by the red dotted line in Figure 1.3. The grey dotted line in Figure 1.3 shows how the power output is adversely affected due to the increase in ambient temperature, resulting in a reduction of 20 MW compared to the coldest time of the night for the reference plant. Lowering the inlet temperature using LTES would increase the plant power output by approximately 5% during the hottest period of the day when the power demand is high (see blue solid line in Figure 1.3). The dissertation proposes a concept of improving the plant performance by lowering the inlet temperature to generate more power during the peak demand.

Figure 1.4 details out the cooling technique using latent heat cold thermal energy storage (LTES) system. The latent heat of PCM stored in the cold thermal energy storage during the nighttime is discharged during the hottest period of the day to cool the inlet air to the air-cooled condenser (ACC).

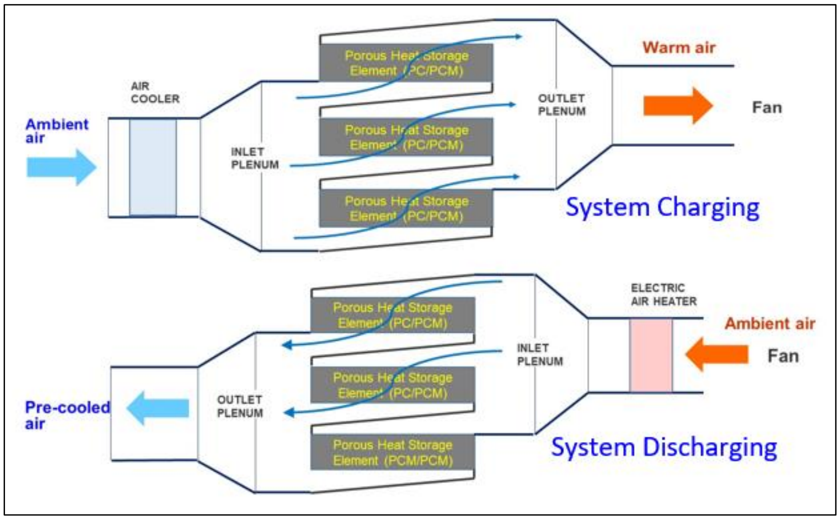

Figure 1. 4 Charging and discharging process of LTES system

The purpose of this dissertation is to propose a solution to the high demand for energy during the hottest periods of the day using LTES systems. The power plant with an integrated energy storage system can be implemented in various geographical locations across the United States.

1.5. Previous studies and knowledge gaps

The approach of storing energy as latent heat utilizing phase change materials (PCMs) represents a promising technology within the realm of thermal energy storage (TES). PCMs offer the advantage of tailoring temperature transitions, storage durations, and cycle consistency, making them a preferred choice for low-temperature energy storage in industrial and commercial buildings [12]. Among various configurations used for latent heat thermal energy storage (LTES), the shell and tube arrangement has gained popularity due to its minimal heat loss and efficient cylindrical geometries [13, 14].

Designing an efficient LTES system tailored for HVAC applications is crucial. Numerous studies have focused on improving heat transfer and enhancing the design of LTES systems [15-18]. For instance, Guo and Zhang [15] conducted a numerical study to evaluate the impact of heat exchanger geometry and thermal boundary conditions on the energy storage performance of a vertical shell-and-tube LTES. Wang et al. [16] investigated how the temperature difference between the Heat Transfer Fluid (HTF) and the PCM's melting point, as well as the inlet mass flow rate, influence the charging performance of a horizontal shell-and-tube LTES. Freeman et al. [19] discussed various thermal energy storage solutions for a residential-scale solar combined heat and power (CHP) system to fulfill both heat and electricity requirements during the night, although they did not consider its heat transfer performance under dynamic inlet parameters.

The choice of PCM significantly impacts latent heat thermal energy storage (TES) systems by increasing storage capacity, thereby enhancing energy supply security [20]. Noteworthy PCMs documented by Zalba et al. [21] include Glauber's salt, calcium chloride hexahydrate/salt hydrate, sodium thiosulfate pentahydrate, sodium carbonate decahydrate, fatty acids, and paraffin waxes. Koca et al. [22] utilized salt hydrate ($CaCl2·6H2O$) as a PCM to conduct an energy and exergy analysis of latent heat thermal energy storage in a flat-plate solar collector. Ghalambaz and Zhang [23] conducted a numerical study to examine how the use of a transient heat load influences the phase change behavior of a PCM in metal foams.

PCM melting is a transient process significantly influenced by factors such as container shape, orientation, heat source position, and mode of heat transfer. Dhaidan and Khodadadi [6] conducted a comprehensive review on PCM melting within containers of diverse shapes, encompassing rectangular, spherical, cylindrical, and annular enclosures. Chen et al. [24] conducted both experimental and numerical analyses on PCM melting and freezing processes within a cylindrical tube, examining various filling rates. The authors extended their numerical analysis to include horizontal ellipses, vertical ellipses, and circular geometries to enhance the efficiency of the cylindrical unit during both charging and discharging phases. Khedher et al. [25] investigated various shapes of PCM container frames, including smooth, arc-shaped, reverse arc-shaped, and zigzag-shaped structures, to assess their impact on the melting performance of a vertical latent heat double-pipe heat exchanger. The findings indicate that the reverse arc-shaped structure enhances thermal energy storage performance the most. Chatterjee et al. [26] performed numerical studies to analyze the influence of angular variation of trapezoidal containers and tube position on the melting behavior of three distinct PCMs. Their findings suggest that modifying the cavity shape and ensuring correct tube placement can significantly impact the melting process, resulting in a notable improvement in the charging rate.

Numerical and experimental analyses were conducted to examine the flow and heat transfer characteristics of a crossflow heat exchanger using various tube shapes [27-31]. Horvat et al. [27] conducted detailed transient numerical simulations of fluid and heat flow, investigating heat exchanger segments with cylindrical, ellipsoidal, and wing-shaped tubes arranged in a staggered configuration. Mangrulkar et al. [28] performed a combined numerical and experimental investigation focusing on heat transfer and friction characteristics of in-line elliptical tubes, exploring different aspect ratios (AR) across a range of Reynolds numbers (Re) to enhance thermal performance. Mohanan et al. [29] carried out numerical investigations of heat transfer and fluid flow in a crossflow heat exchanger with elliptical tubes, studying the impact of varying longitudinal and transverse pitch-to-diameter ratios, different aspect ratios of elliptical tubes, and tube arrangements (inline and staggered) on the overall performance of the crossflow heat exchanger. Jang and Yang [31] conducted experiment and 3D numerical analysis to investigate the hydraulic and thermal performance in elliptic finned-tube heat exchangers for different tube arrangements and compared the results with those of corresponding circular-finned tube heat exchangers.

Swain and Das [32] conducted a numerical investigation to assess the impact of elliptical and flattened tube bundle geometries (both staggered and inline configurations) on convective heat transfer and pressure drop for various pitch-to-diameter ratios across a laminar Reynolds number range, aiming to design a compact and efficient single-phase shell and tube heat exchanger. Jodaei and Zamzamian [33] conducted a 3D numerical investigation to assess the performance of a heat exchanger utilizing cam-shaped tube banks. The study involved comparing this configuration in both aerodynamic and inverse aerodynamic directions in crossflow air with elliptical tube banks for a range of Reynolds numbers and a constant tube surface temperature. The results reveal that elliptical tube banks exhibit superior heat transfer performance compared to cam-shaped tube banks, regardless of the flow direction (inverse aerodynamic or aerodynamic) in both configurations. Numerical investigations were conducted in the literature [34, 35] to examine the thermal and hydraulic performance of heat exchangers utilizing mixed tube bundles, incorporating both circular and elliptical tubes in various orientations, arranged in both staggered and inline configurations. The study found that while transitioning from circular to elliptical tube bundles and maintaining a constant inlet velocity and pitch-to-diameter ratio, the heat transfer coefficient decreases [34].

Ding et al. [36] conducted numerical analyses to study heat transfer and fluid flow in various types of latent heat storage units, including shell-and-tube, rectangular, and cylindrical configurations. These units were filled with the same amount of PCM but packed in differently shaped containers. Their research revealed that the shell-and-tube configuration offers the highest exergy efficiency for the thermal storage-release cycle. Fabrykiewicz et al. [37] conducted numerical and experimental analyses of a latent heat storage unit to compare three organic PCMs in a cylinder and seven tube bundles arranged in a staggered tube configuration inside the cylinder, where the heat transfer fluid (HTF) flows through the tubes, and the cylinder wall maintains a constant temperature. Rana et al. [38] conducted a two-dimensional computational study on the melting process of PCM and the heat transfer properties of a shell-and-tube heat exchanger, where circular, rectangular, and elliptical tubes were used at a constant wall temperature. The findings indicate that the PCM melts the fastest in heat exchangers with rectangular tubes, followed by those with elliptical tubes and circular tubes, respectively.

Most of the previous research has focused on shell and tube heat exchangers with the heat transfer fluid (HTF) outside the tube and condensing steam inside. Gaps exist in understanding Latent Heat Cold Thermal Energy Storage (LTES) systems with phase change material (PCM) inside the tube and HTF outside. Research is needed on the effects of tube shapes, sizes, and inlet boundary conditions in LTES systems that use PCM and employ tube array geometry with a conjugate heat transfer boundary condition approach. The aim of this project is to guide LTES system design through numerical studies.

This work proposes an effective and inexpensive design of latent heat cold thermal energy storage (LTES) system considering different performance parameters, i.e., ambient temperature, air flow velocity, minimum allowed condensing pressure, tube size, and tube material. The dissertation includes energy and exergy efficiency of the system.

1.6. Challenges and design criteria

There are a few challenges associated with the numerical modeling as follows:

- The problem is transient, with solid and liquid phases present in each cell of the computational domain. The fraction of the cell in liquid form is modeled by the liquid fraction (γ), which varies from 0 to 1.

$$\gamma = 0 \; if \; T < T_{solid}$$

$$\gamma = 1 \; if \; T > T_{liquid}$$

$\gamma = \frac{T - T_{solid}}{T_{liquid} - T_{solid}} \; if \; T_{solid} < T < T_{liquid}$ (“mushy” zone – narrow green line in PCM contours)

- Flow within the tube array is turbulent due to the staggered configuration.
- In reality, the tubes are partially filled to accommodate the increased volume of liquid PCM during phase transition (see Figure 1.5).

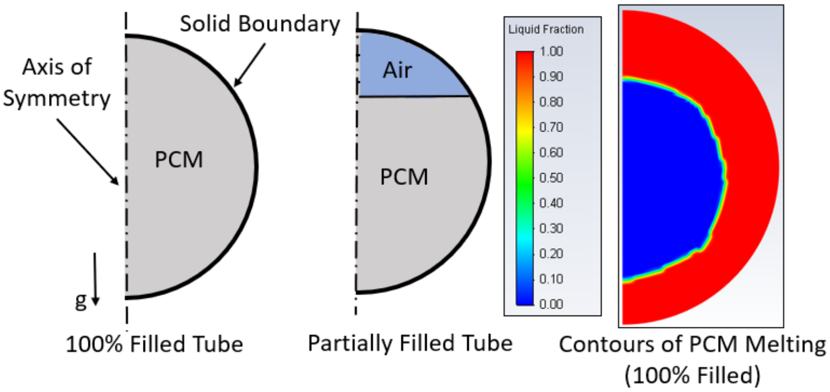

Figure 1. 5 Challenges associated with PCM Melting/ solidification model

The proposed design aims to improve the dry cooling technique of a thermal power plant utilizing Air Cooled Condensers (ACC), tailored for suitability in Dallas, TX, Phoenix, AZ, and Las Vegas, NV. The geographically tailored LTES design criteria are as follows:

- Achieve a cooling effect of 4 °C for a duration of four hours
- Maintain pressure drop, $\Delta P < 100$ Pa
- Cool down the system to freeze PCM overnight

Numerical analysis of PCM melting and solidification within a tube array was conducted using ANSYS Fluent to guide LTES design. Flow conditions within the tube bank, influenced by boundary layer separation effects and wake interactions, significantly impact convection heat transfer within the PCM-filled tubes. A staggered arrangement of tube rows in a horizontal orientation was adopted to enhance heat transfer by promoting a more tortuous flow.

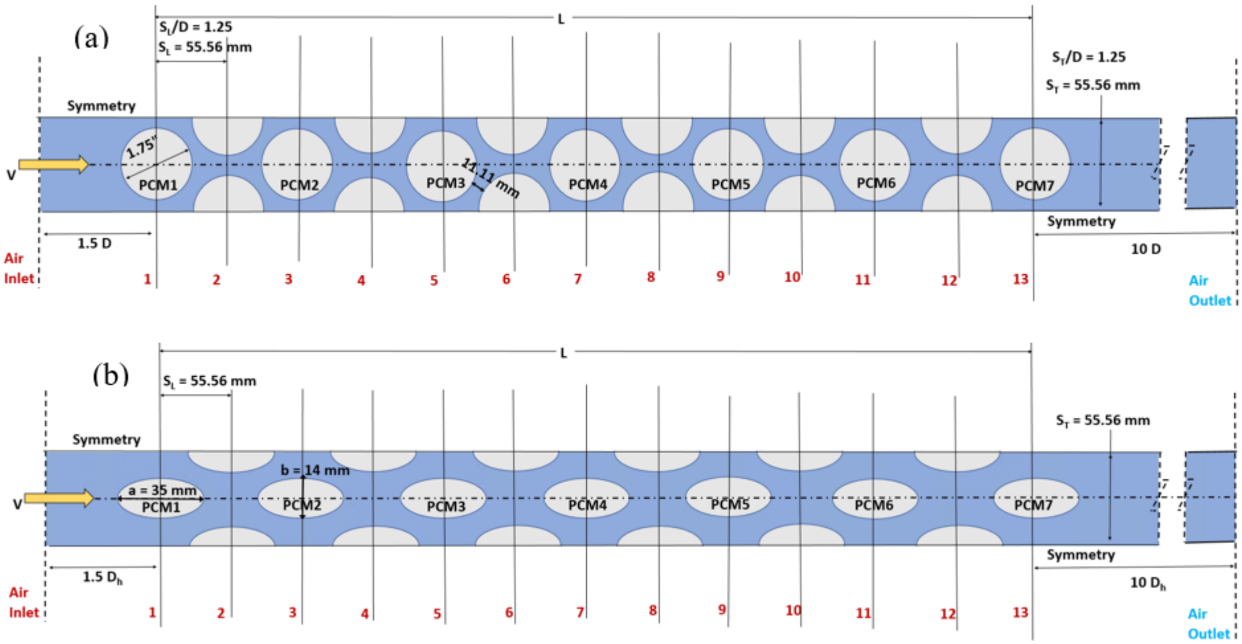

Figure 1. 6 A schematic of 2-D computational domain for the tube bank: (a) circular, (b) elliptical

Transient two-dimensional Navier-Stokes equations and a Realizable k-ε turbulence model were utilized to predict fluid flow and heat transfer in LTES heat storage modules, where $CaCl_2$

hexahydrate was employed as PCM. The enthalpy-porosity method was used to numerically model the melting and solidification of PCM. Following the design obtained from numerical analysis, a smaller-scale module was constructed for experimentation, and the numerical results were then compared against the experimental data. After examining the smaller-scale module, a parametric analysis was performed numerically to design a prototype-scale module using 1.75″ OD circular tubes in a 13-row tube array. A prototype-scale module was built at Lehigh University for testing and comparison with the numerical results. A comparative study was conducted by replacing the circular tubes with elliptical tubes to enhance the hydraulic performance through the aerodynamic shape of the elliptical geometry (see Figure 1.6). Energy and exergy analyses were carried out for the smaller-scale and prototype-scale LTES systems. An uncertainty analysis was performed to identify the reasons for the discrepancy between the experimental and numerical results as documented in the literature [39].

1.7. Outline of the study

This section provides a concise overview of the study. Chapter 1 describes the problem statement, significance, and novelty of the research, as well as the knowledge gaps and challenges associated with it. Additionally, a brief description of the numerical analysis used to design the LTES system is provided.

In Chapter 2, the selection of PCM and an appropriate model for PCM melting and solidification are presented. A detailed analysis of the effects of different boundary conditions is provided for a single circular tube. Furthermore, a comparison of experimental and numerical results of PCM melting and freezing in a single tube is presented in this chapter.

Chapter 3 details a lab-scale module using a 4-row tube array, along with a comparison of experimental and numerical results. Energy and exergy analyses are performed for the lab-scale module. A parametric analysis to design a prototype-scale module is provided in Chapter 4. The final design of the prototype-scale module was built to perform tests and compare the results with the numerical analysis.

Chapter 5 offers a detailed energy and exergy analysis of the prototype-scale module for both numerical and experimental results. In Chapter 6, a comparative study is presented using circular and elliptical tube arrays to enhance the hydraulic performance of the LTES system and reduce the pumping power required to flow the heat transfer fluid through the system.

Chapter 7 provides a comparative study considering different tube materials: Carbon Steel and PVC, to reduce the module weight and eventually the construction cost of the system. Finally, Chapter 8 offers conclusions and findings from this study, along with recommendations for future research.

CHAPTER 2: NUMERICAL ANALYSIS OF PCM MELTING AND SOLIDIFICATION IN A HORIZONTAL SINGLE TUBE

2.1 Overview

This chapter presents a computational analysis of a simple geometry - a single horizontal tube filled with phase change material (PCM). Despite the significant difference between the flow around a single tube (a circular cylinder in crossflow) and the flow in a tube array, we initially analyze a single horizontal tube due to its uncomplicated geometry. The primary objectives are to develop a model for PCM melting and freezing, validate the results for this simple geometry, establish a correlation between the tube size (diameter) and PCM melting/freezing time, and examine the impact of various boundary conditions (isothermal, constant heat flux, constant convection heat transfer coefficient, and conjugate heat transfer). Additionally, a detailed analysis of the selection process for PCM and the numerical model is provided. The chapter concludes by comparing the results obtained from experiments with the numerically predicted outcomes.

2.2. Selection of PCM

When employing latent heat energy storage, it is crucial to take various factors into account. These factors encompass the phase transition temperature ($T_{\text{Ph. change}}$), enthalpy of fusion in liquid/solid state (L_f), thermal conductivity (k), long-term thermal stability of the material during repeated cycling, supercooling, volume change during phase transition, cost, and availability of the PCM, safety and environmental considerations, as well as containment requirements and corrosiveness. As a result of these considerations, inorganic PCMs, specifically hydrated salts, are being explored for this application. If paraffins were utilized instead of hydrated salts, the significantly higher cost would likely make a large-scale thermal energy storage system immediately noncompetitive from a cost perspective.

A list of hydrated salt PCMs that were characterized by Lehigh University is included in Table 2.1. Calcium Chloride Hexahydrate [$CaCl_2 \cdot 6H_2O$] was selected after considering its suitability with the criteria listed in the earlier paragraph, which has a melting (or phase change) temperature between 27 and 30 ºC and a high heat of phase change, between 160 and 200 kJ/kg.

Table 2. 1. Hydrated Salt PCMs Characterized by Lehigh University

PCM	$T_{\text{Ph. change}}$ [°C]	L_f [kJ/kg]
Sodium Hydroxide 3.5 Water [$NaOH \cdot 3.5H_2O$]	15.0 - 15.5	219
Potassium Fluoride Tetrahydrate [$KF \cdot 4H_2O$]	18.0 – 20.0	230 - 246
Calcium Chloride Hexahydrate + Magnesium Chloride Hexahydrate [$CaCl_2 \cdot 6H_2O + MgCl_2 \cdot 6H_2O$ (33 wt%)]	23.0 - 25.0	127
Calcium Chloride Hexahydrate + Magnesium Chloride Hexahydrate [$CaCl_2 \cdot 6H_2O + MgCl_2 \cdot 6H_2O$ (50 wt%)]	25.0	95
Calcium Chloride Hexahydrate [$CaCl_2 \cdot 6H_2O$]	27.0 – 29.9	160 - 201
Sodium Sulfate Decahydrate [$Na_2SO_4 \cdot 10H_2O$] (Glauber's Salt)	31.1 – 32.5	222 - 254

A combination of thermogravimetric analysis (TGA), differential scanning calorimetry (DSC), a drop calorimeter, and a programmable water bath was employed at Lehigh University to characterize the thermal performance of laboratory-grade, high-purity $CaCl_2 \cdot 6H_2O$. Various additives were introduced to act as seed crystals or nuclei, promoting the formation of a crystal structure in the PCM and reducing the extent of supercooling. Specifically, strontium chloride ($SrCl_2 \cdot 6H_2O$) was added at a concentration of 3 wt% to prevent supercooling and alleviate its adverse effects on the melting temperature and heat of fusion of the base compound.

Due to the elevated cost of laboratory-grade (~$30/kg) PCM and considering the future scale-up of its application, the exploration of commercial-grade $CaCl_2 \cdot 6H_2O$ with relatively high purity became a viable option. One of the chosen commercial products was Briners Choice anhydrous calcium chloride from Occidental Chemical Corporation, identified as a cost-effective but with poor-quality control material. Another alternative, OxyChem, is available directly and in bulk from specific vendors for less than $1/kg. The specifications of lab-grade and commercial salts are outlined in Table 2.2. The findings suggest a trade-off between PCM quality and associated costs, which could impact system size and the levelized cost of the technology. The average latent heat of commercial salts, OxyChem and Briner's Choice, is 125.8 kJ/kg and 154.9 kJ/kg, respectively, representing a 29% and 21.73% decrease compared to the lab-grade PCM. However, by hydrating and incorporating additives, similar results can be attained with the commercial PCMs.

Table 2. 2. Thermal performance of lab-grade and commercial made salt hydrates

PCM	$T_{Ph. change}$ [°C]	L_f [kJ/kg]
Lab-Grade [95% $CaCl_2 \cdot 6H_2O$ + 2% KCl + 3% $SrCl_2 \cdot 6H_2O$]	26.4	176.95 (± 2.59)
OxyChem [94.5% $CaCl_2$ + 2.5% KCl + 1.6% NaCl + 0.9% $CaBr_2$ + 0.5% H_2O]	23.8	125.8 (± 0.61)
Briners Choice [94-97% $CaCl_2$ + 2-3% KCl + > 1 - < 2% NaCl + < 1% H_2O + < 1 $CaBr_2$]	24.1	154.90 (± 10)

To assess the cycling performance of the commercial material, an automated thermal cycling unit was conceptualized and constructed at Lehigh University. A total of 1,500 cycles were executed for each PCM. Cycling performance was evaluated using approximately 200 g PCM samples corresponding to the lab-grade, OxyChem, and Briner's Choice PCM materials. The latent heat of these samples was measured utilizing a drop calorimeter, and the outcomes are depicted in Figure 2.1. The standard deviations for lab-grade, OxyChem, and Briner's Choice are 7.86, 4.09, and 3.39 kJ/kg, respectively. These values fall within the performance target of ±5% of the initial latent heat.

With a frequency of two cycles per day, the completion of 1500 cycles equates to 750 days of continuous operation. Considering that the LTES system is designed to function exclusively during the hottest period of the year, typically spanning 3 to 4 months, the PCMs demonstrate the capacity to maintain thermal performance for an estimated duration of approximately 6 to 8 years.

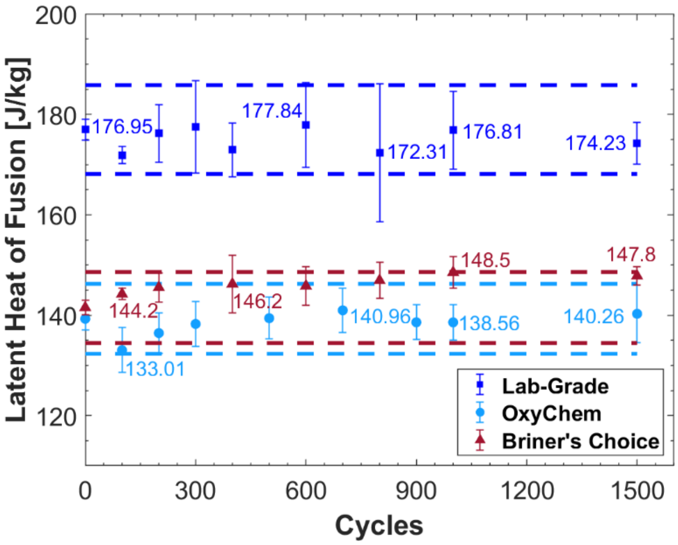

Figure 2. 1 Results of Cycling Performance for Different PCMs

Table 2.3 summarizes the ultimate thermophysical properties of lab-grade and commercial PCM after adding additives that were used for the computational procedure.

Table 2. 3. Thermophysical properties of PCM (CC6)

Physical parameter (unit)	Lab-grade PCM	Commercial PCM
Melting/solidifying point (°C) (average)	26.4	25
Density (solid/liquid) (kg/m^3)	1706/ 1538	1706/ 1538
Specific heat (solid/liquid) (J/kg-K)	2360/ 1560	2540/ 1680
Conductivity (solid/liquid) (W/m-K)	1.09/ 0.546	1.09/ 0.546
Latent heat (kJ/kg)	170	150
Dynamic viscosity (mPa-s)	11.94/ 18.50	11.94/ 18.50
Thermal expansion coefficient (K^{-1})	0.0005	0.0005

2.3. Computational domain

The schematic representation of the computational domain for a single tube geometry is illustrated in Figure 2.2. The tube, composed of stainless steel, is filled with PCM (CC6). A 2D transient model was created to simulate the melting and freezing of PCM in a horizontal circular tube. The 2D computational domain shown in Figure 2.2a was used for isothermal wall, constant wall heat flux, and constant heat transfer coefficient boundary conditions. Conversely, the 2D computational domain presented in Figure 2.2b was used for a real-world scenario involving conjugate heat transfer boundary conditions under the influence of a crossflow of air. The conventional rule for the computational domain, with a length of two times the tube diameter upstream of the tube bank and ten times the tube diameter downstream of the tube bank, was applied to mitigate the effects of entrance effects at the inlet and wake at the outlet.

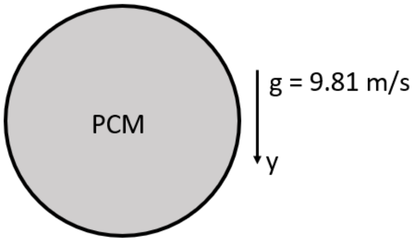

(a) PCM filled tube

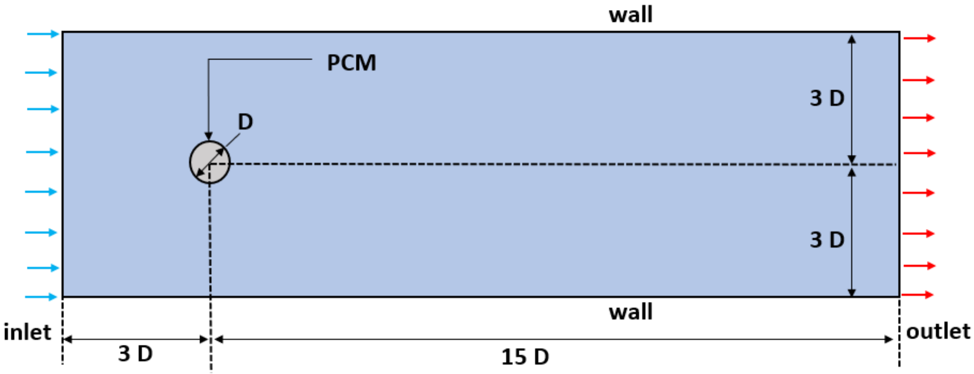

(b) PCM filled tube in the presence of crossflow of air

Figure 2. 2 A 2D computational domain for a single horizontal circular tube

For the numerical analysis of single horizontal circular tube, commercial PCM was used. The thermophysical properties of stainless steel used for the tube wall were taken from the literature [40], density (ρ_s), specific heat (c_{P_s}) and thermal conductivity (k_s) as 8,000 kg/m^3, 500 J/kg-K and 21.5 W/m-K, respectively.

2.4. Selection of numerical model

2.4.1. Governing equations for the PCM domain

The assumptions applied to the PCM domain in this analysis were as follows:

- 2D model
- Solid PCM:
  - Hear transfer by conduction
- Liquid PCM:
  - Incompressible
  - Laminar flow
  - Natural convection
  - Buoyancy force due to density change

This section summarizes different methods used to model melting and solidification processes of PCM.

2.4.1.1. Enthalpy-porosity method

The continuity, momentum, and energy conservation equations for the 2D PCM domain are given by Eqns. (2.1)-(2.3) using the summation convention for repeated indexes:

$$\frac{\partial \rho}{\partial t} + \frac{\partial \rho u_i}{\partial x_i} = 0 \tag{2.1}$$

$$\frac{\partial(\rho u_i)}{\partial t} + \frac{\partial(\rho u_j u_i)}{\partial x_j} = \mu \frac{\partial^2 u_i}{\partial x_j \partial x_j} - \frac{\partial p}{\partial x_i} + \rho g_i + S_i \tag{2.2}$$

$$\frac{\partial(\rho h)}{\partial t} + \frac{\partial(\rho h_{latent})}{\partial t} + \frac{\partial(\rho u_i h)}{\partial x_i} = \frac{\partial}{\partial x_i}\left(k \frac{\partial T}{\partial x_i}\right) \tag{2.3}$$

where, ρ is the density; u is the velocity of the liquid PCM in the transverse direction caused by the density difference; μ is the viscosity; P is the pressure; g is the gravitational acceleration; ρg_i

is the buoyancy force arising due to density difference. Quantity h is the sensible enthalpy in the energy equation, defined as follows:

$$h = h_{ref} + \int_{T_{ref}}^{T} C_p\,(T)dT \tag{2.4}$$

Enthalpy-porosity method is used to calculate the latent portion of PCM:

$$\gamma = \left\{ \begin{array}{c} \frac{h_{latent}}{L_f} = 0 \;\; if\, T < T_{solid} \\ \frac{h_{latent}}{L_f} = 1 \;\; if\, T > T_{liquid} \\ \frac{h_{latent}}{L_f} = \frac{T - T_{solid}}{T_{liquid} - T_{solid}} \;\;\; if\, T_{solid} < T < T_{liquid} \end{array} \right\} \tag{2.5}$$

Source term S_i is used to model the effect of natural convection on phase change as follows:

$$S_i = -A_{mush} \cdot u_i \tag{2.6}$$

$$A_{mush} = \frac{C(1-\gamma)^2}{\gamma^3 + \delta} \tag{2.7}$$

where, $\delta = 0.001$ and C is “mushy” zone constant ($10^5 – 10^7$). “mushy” zone refers to the portion of the domain with a liquid fraction (γ) between 0 and 1. For the present analysis, a value of 10^5 is used as mushy zone constant following the literature [41].

2.4.1.2. Effective specific heat capacity method

The effective heat capacity method considers the increase in sensible heat capacity during phase change. This method was proposed by Poirier and Salcudean [42]. The first term in Eq. (2.3) is replaced by the effective heat capacity (C_{eff}) using a specific heat approximation as follows [43]:

$$\frac{\partial(\rho C_{eff})}{\partial t} + \frac{\partial(\rho h_{latent})}{\partial t} + \frac{\partial(\rho u_i h)}{\partial x_i} = \frac{\partial}{\partial x_i}\left(k \frac{\partial T}{\partial x_i}\right) \tag{2.8}$$

where,

$$C_{eff} = \int_{T_s}^{T_l} C_p\, dT \tag{2.9}$$

and,

$$C_p = \begin{cases} C_{p,solid} & T < T_{solid} \\ (1-\gamma)\, C_{p,solid} + \gamma C_{p,liquid} + \frac{L_f}{T_{liquid} - T_{solid}} & T_{solid} \le T \le T_{liquid} \\ C_{p,liquid} & T > T_{liquid} \end{cases} \tag{2.10}$$

2.4.1.3. Lattice Boltzmann method

A single-relaxation-time (SRT) and a multiple-relaxation-time (MRT) thermal lattice Boltzmann models are used in this method [44]. While the SRT model is well-known for its simplicity, it consistently faces numerical instability issues when the relaxation time approaches 0.5. MRT lattice Boltzmann equation is discussed here. The total enthalpy H distribution function is expressed as [45]:

$$m_g(x, t + \delta_t) = m_g(x, t) - S\,[m_g(x, t) - m_g^{eq}(x, t) \tag{2.11}$$

where, distribution in momentum, m_g is given as:

$$m_g(x, t) = \left[m_{g0}(x, t), m_{g1}(x, t), \ldots..\right]^T \tag{2.12}$$

and, the equilibrium momentum, m_g^{eq} is given as:

$$m_g^{eq} = \Big[H, -4H + 2C_{p,ref}T + 3C_pT\frac{u^2}{c^2}, 4H - 3C_{p,ref}T - 3C_pT\frac{u^2}{c^2}, C_pT\frac{u_x}{c}, -C_pT\frac{u_x}{c}, C_pT\frac{u_y}{c}, -C_pT\frac{u_y}{c}, C_pT\frac{u_x^2 - u_x^2}{c^2}, C_pT\frac{u_xu_y}{c^2}\Big]^T \tag{2.13}$$

where, T represents temperature and specific heat, C_p is determined by interpolation following the given expression:

$$C_p = (1-\gamma)\, C_{p,solid} + \gamma\, C_{p,liquid} \tag{2.14}$$

and the reference specific heat is interpreted by the mean of $C_{p,solid}$ and $C_{p,liquid}$ for the numerical stability as follows:

$$C_{p,ref} = \frac{2C_{p,solid}\, C_{p,liquid}}{C_{p,solid} + C_{p,liquid}} \tag{2.15}$$

2.4.1.4. Monte Carlo method

The Bayesian Markov chain Monte Carlo (MCMC) technique [46] is utilized as an efficient nonlinear regression method for generating appropriate models to predict the melting rate and surface average Nusselt number. The following mathematical expression is used in this method:

$$X^{t+1} \sim P_{trans}(x|X^t = x^t) \tag{2.16}$$

where, X^0, X^1, X^2, … are independent variables and the term in the right-hand side of the expression is a transition function that determines the conditional probability of the next value. For the transient variations melting rate is calculated using the instantaneous mass of PCM (m) as follows:

$$\gamma = \frac{m}{M} \tag{2.17}$$

where, M is the total mass of PCM. Three dimensionless parameters: Stefan (Ste) number, Grashof (Gr) number, and Fourier (Fo) number are used as dependent variables in the model. More details of the model can be found in the literature [47].

A literature review was conducted to show the techniques used for PCM modeling. Table 2.4 lists out all the methods used to model PCM melting/ solidification processes in different literature. Following the literature, the most widely used technique – Enthalpy-porosity method was selected for the further numerical analysis.

Boussinesq model was adopted to calculate density change due to the phase change and natural convection as presented in the following equation:

$$\rho = \rho_o[1 - \beta(T - T_o)] \tag{2.18}$$

Table 2. 4 Summary of method used for PCM melting and solidification in literature

Method	Container shape	Literature	PCM used
Enthalpy-porosity	Sphere, Ellipsoid, Annulus/ shell and tube, Vertical cylinder, Horizontal cylinder, Rectangular/ square, Trapezoid, Hexagon, Channel/ Wavy channel	[48] [49] [50] [51] [52] [53] [54] [55] [56] [57] [24] [58] [59] [60] [61] [62] [63] [64] [65] [66] [67] [68] [69] [70] [71] [72]	Paraffin, water, n-eicosane, NEPCM
Effective specific heat capacity	Ellipsoid, Vertical cylinder	[73] [74] [75]	Paraffin, NEPCM, Sodium nitrate
Lattice Boltzmann	Horizontal cylinder, Rectangular/ square	[76] [77] [44] [45]	Paraffin, NEPCM, Metal foams
Monte Carlo	Sphere	[47]	1-Dodecanol
Moving grid	Sphere, Horizontal cylinder: circular cross section	[78] [79] [80]	Water

2.4.2. Governing equations for the fluid domain

The assumptions applied to the fluid domain in this analysis were as follows:

- One dimensional
- Incompressible
- Transient flow
- No body force
- Laminar flow
- No heat source

Navier-Stokes equations for the fluid and energy equations for the solid and fluid domains are solved simultaneously to determine heat flux between the air flowing around the circular tube and tube wall. Navier-Stokes equations using the summation convention for repeated indexes for the 2D fluid domain (air) are as follows:

$$\frac{\partial \rho_{air}}{\partial t} + \frac{\partial \rho_{air} u_i}{\partial x_i} = 0 \tag{2.19}$$

$$\frac{\partial(\rho_{air} u_i)}{\partial t} + \frac{\partial(\rho_{air} u_j u_i)}{\partial x_j} = -\frac{\partial p}{\partial x_i} + \mu_{air} \frac{\partial^2 u_i}{\partial x_j \partial x_j} \tag{2.20}$$

$$\rho_{air} C_{p_{air}} \left(\frac{\partial T}{\partial t} + u_i \frac{\partial T}{\partial x_i} \right) = -\frac{\partial p}{\partial t} + \frac{\partial}{\partial x_i} \left(k_{air} \frac{\partial T}{\partial x_i} \right) \tag{2.21}$$

where ρ_{air}, $C_{p_{air}}$, μ_{air}, and k_{air} are density, specific heat, viscosity, and the thermal conductivity of the heat transfer fluid (air), respectively.

2.4.3. Governing equations for the tube wall

The energy conservation equation for the solid domain (tube wall) for transient condition is given by the following expression:

$$\rho_s c_{P_s} \frac{\partial T}{\partial t} = k_s \left(\frac{\partial^2 T}{\partial {x_i}^2} + \frac{\partial^2 T}{\partial {x_j}^2} \right) \tag{2.22}$$

where ρ_s, c_{P_s} ,and k_s are density, specific heat, and the thermal conductivity of the tube wall, respectively.

2.5. Numerical setup

The solution of the governing Navier-Stokes equations for mass, momentum, and energy conservation was performed using ANSYS Fluent 20.0 [81]. The computational approach involved the utilization of the SIMPLE algorithm and the Implicit method for coupling pressure and velocity. To enhance accuracy, the second-order upwind discretization scheme was applied to both momentum and energy equations. For the discretization of momentum equations, the PRESTO! (PREssure STaggering Option) scheme was chosen, as it yields more precise results in cases such as natural convection and porous media by mitigating interpolation errors and pressure gradient assumptions on boundaries.

A convergence criterion of 10^{-6} for the RMS residuals was specified for continuity, momentum, and energy equations. Under-relaxation factors of 0.2, 0.7, and 0.7 were set for pressure, momentum, and liquid fraction, respectively, to ensure solution convergence and stability.

A transient model was employed to predict the melting and solidification process of the phase change material (PCM) over time. In this study, a time step size of 0.5 s was chosen. The use of an Implicit time scheme ensures that the numerical results are independent of the time step size. A detailed analysis of the selection of the time step size is presented in a later section.

2.6. Validation of the numerical model

To validate the melting/solidification model, the numerical results of liquid fraction and temperature from the present study were compared with those of Das et al. [59], as illustrated in Figures 2.3c and 2.3d. In the reference [59], a horizontal annulus (Figure 2.3a) filled with n-eicosane as the PCM was used as the geometry. The inner wall of the annulus was maintained at a constant temperature of 333 K (60 °C), while the outer wall was insulated (adiabatic). The observed discrepancy of approximately 7% in the liquid fraction (see Figure 2.3c) is attributed to the impact of density variations in the Boussinesq approximation, underscoring the critical importance of precise knowledge of the operating temperature. However, the existing literature [59] lacks clarification regarding the assumed operating temperature. It is worth noting that a robust agreement was evident in the PCM temperature (Figure 2.3d). Nonetheless, in the vicinity of the phase change temperature, a discrepancy of around 5% was noted between the reference [59] and our current study. As previously highlighted, the literature lacks sufficient information about the assumed operating temperature in the Boussinesq approximation, potentially contributing to the differences observed in both temperature and liquid fraction results. The temperature contours of the PCM at 10800 s exhibit nearly identical contours (Figure 2.3b).

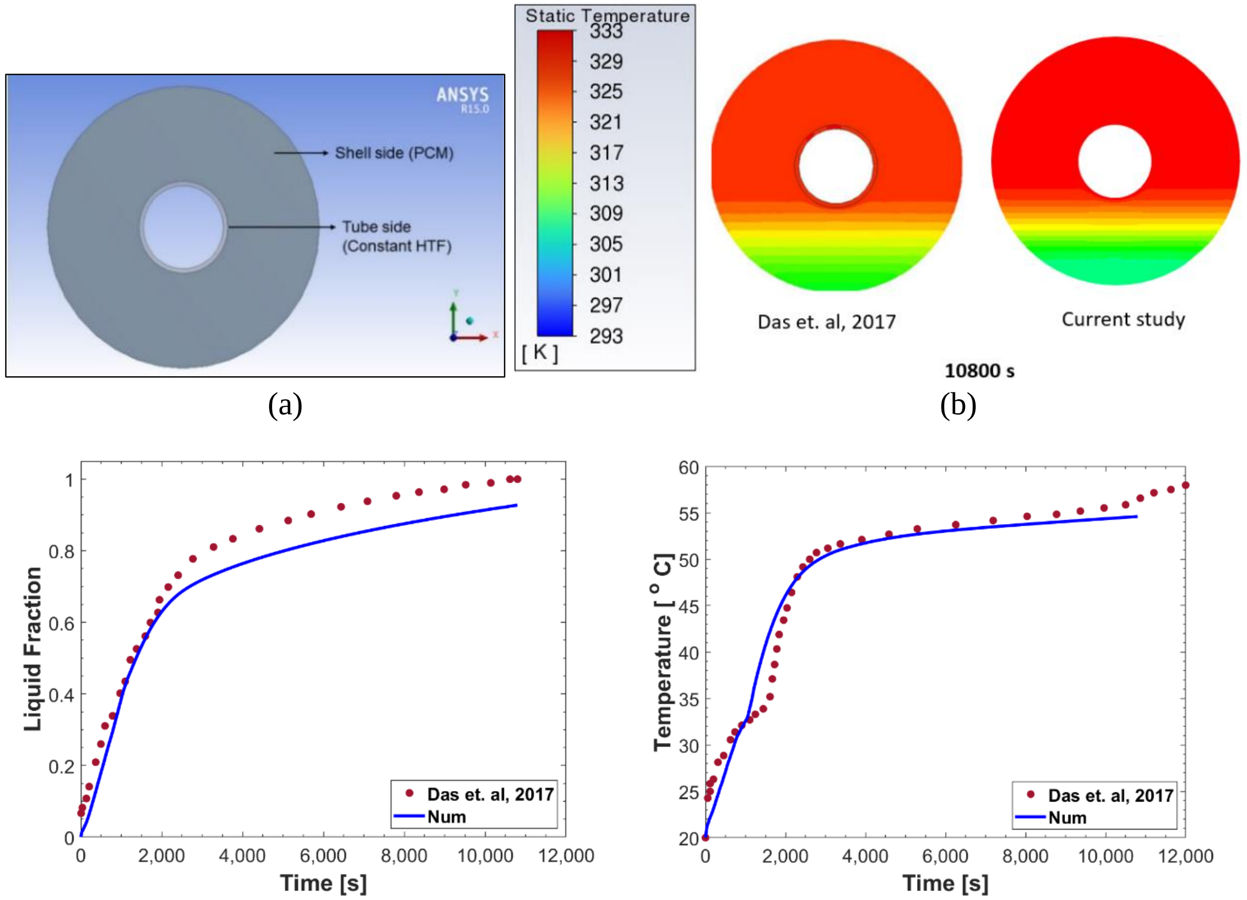

(a) (b)

(c) (d)

Figure 2. 3 (a) Computational domain from the reference [59], (b) comparison of the temperature contours with the reference [59], (c), (d) model verification using the liquid fraction and PCM temperature, respectively

2.7. Grid sensitivity analysis and selection of time step size

The impact of discretization mesh was examined on a 1" outer diameter tube by employing a full structured Quad mesh with 1,840 and 7,360 elements and an Unstructured Quadratic mesh with 4,229 elements. Figure 2.4a shows discretization mesh and their corresponding liquid fraction contours for the flow time of 2400 s.

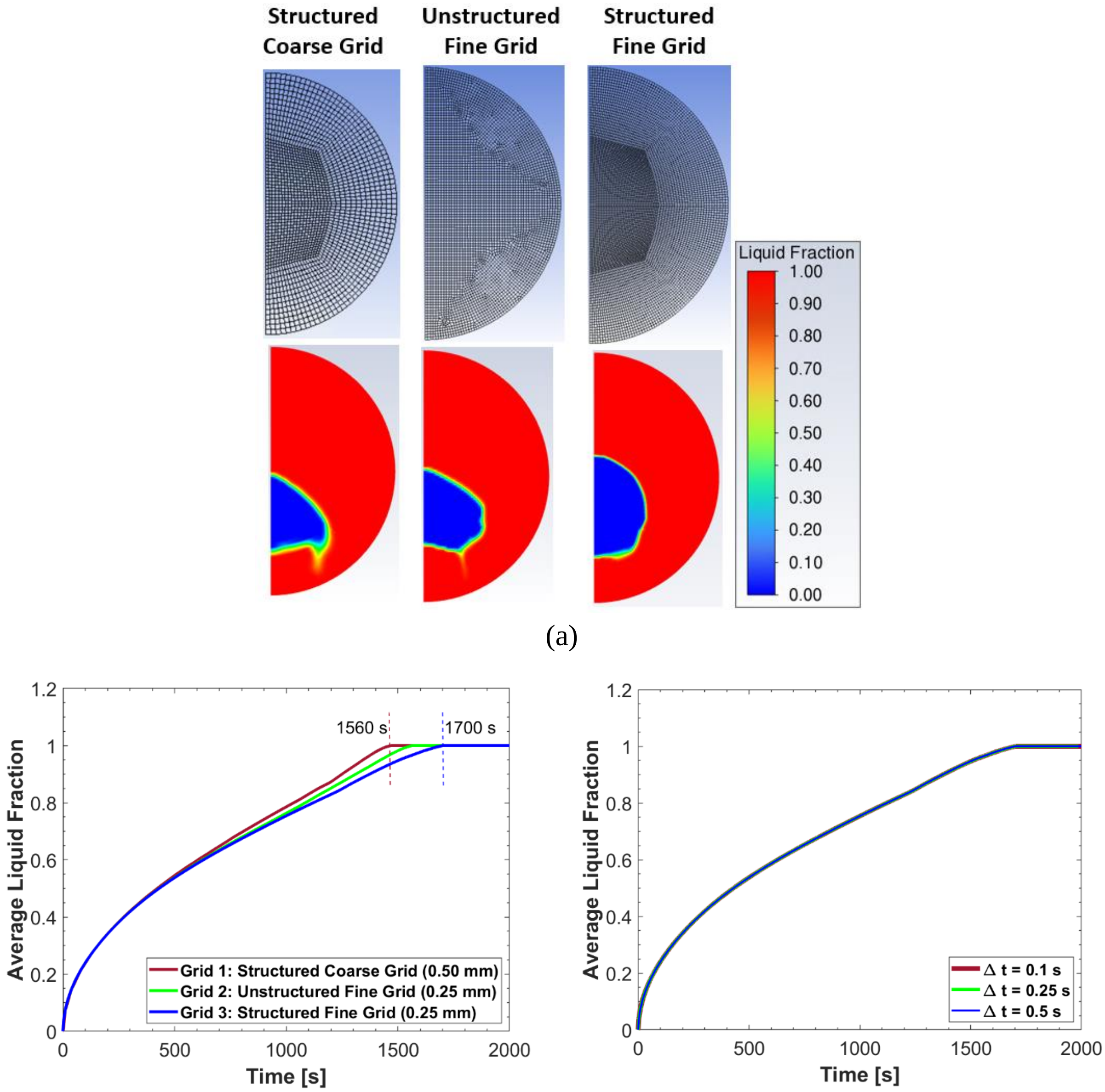

(a)

(b) (c)

Figure 2. 4 (a) Discretization mesh and contours of liquid fraction of different grids at 2400 s , (b) the effect of discretization mesh on the average liquid fraction, (c) the effect of different time step size on the average liquid fraction

Table 2.5 summarizes the computational time required for three different grids. Computational time increases by 20% for the structured fine grid compared to the coarse grid. Figure 2.4b shows the effect of discretization mesh on the average liquid fraction. At the beginning of the results, the liquid fraction is identical for three different grid sizes. A very small difference is observed at the end when the PCM is completely melt and the liquid fraction equals 1. Grid 3, the structured fine grid, is selected for further analysis.

Table 2. 5. Effect of discretization mesh

Grid	Element size [mm]	No of elements	Computational time [hr]
Grid 1: Structured coarse grid	0.50	1,840	10
Grid 2: Unstructured fine grid	0.25	4,229	15
Grid 3: Structured fine grid	0.25	7,360	12

The effect of different time step sizes (0.1 s, 0.25 s, and 0.5 s) was taken into consideration. Figure 2.4c illustrates that the solution is independent of the time step size, as mentioned earlier. No difference is observed in the average liquid fraction due to different time step sizes. However, selecting a time step size of 0.5 s reduces the computational cost by approximately 56% compared to a time step size of 0.1 s (see Table 2.6). The simulation was performed on an HP Precision 5820 workstation equipped with 12 cores, 3.7/4.7 GHz, and 64 GB ECC memory.

Table 2. 6. Effect of time step size

Time Step Size [s]	Computational Time [hours]
0.10	27
0.25	21
0.50	12

2.8. Variation of boundary conditions

A parametric analysis for different tube wall boundary conditions was conducted for the 1" outer diameter tube with thin tube wall thickness. The results are detailed in this section.

2.8.1. Boundary condition of the first kind, Dirichlet – constant wall temperature

The most basic scenario for the boundary condition (B.C.) of the PCM tube wall is to keep the temperature constant. This is frequently used in simulations that model the melting and freezing of phase change material (PCM) in tubes and various geometric configurations. The numerical analyses involved assuming a wall temperature consistently above and below the PCM (CC6) phase change temperature to simulate melting and freezing, respectively.

In this study, the temperature driving force, ΔT_{DF} is characterized as the temperature difference between the outer tube wall ($T_{w,o}$) and the PCM phase change temperature ($T_{ph.change}$) as follows:

$$\Delta T_{DF} = T_{w,o} - T_{ph.change} \tag{2.23}$$

Three different constant wall temperatures: 308 K (35 °C), 303 K (30 °C) and 300.5 K (27.5 °C) were selected for the sensitivity analysis of PCM melting using first kind boundary conditions, which results in a positive driving force of 10, 5 and 2.5 °C (K), respectively. Figure 2.5 presents different melting parameters as a function of time for the first kind boundary condition using constant wall temperature. Figure 2.5a shows the average liquid fraction as a function of flow time. Due to higher temperature driving force , PCM in the tube with constant wall temperature 35 °C melts faster than other two cases.

The graph in Figure 2.5b illustrates the variation of the average temperature of the PCM within the tube over time. The initial, phase change, and tube wall temperatures are also depicted. The findings reveal that the temperature of the solid PCM, initially at 20 °C, rises quickly until reaching the phase change temperature. During the phase change, as heat is transferred through the tube wall and the PCM transitions from solid to liquid (melting), the average PCM temperature increases steadily until all solid PCM has melted. Subsequently, after the PCM has completely melted, the temperature sharply rises to match the tube wall temperature.

Therefore, the process of PCM melting can be categorized into three phases: (1) a rapid increase in temperature of the solid phase, (2) an approximately linear temperature increase during the phase change, where added heat is utilized to overcome the latent heat of fusion, and (3) a rapid temperature increase (superheat) of the melted PCM to align with the tube wall temperature.

Figure 2.5c illustrates the effect of the driving force on the wall heat flux. The findings indicate that following the initial period of PCM heating, when the PCM reaches the phase change temperature and initiates melting, the wall heat flux remains relatively constant. After the PCM melting phase, as its temperature surpasses the fusion temperature, the wall heat flux diminishes due to a reduction in the temperature difference between the tube wall and PCM (refer to Figure 2.5b). As the PCM temperature approaches the wall temperature, the wall heat flux gradually diminishes until it reaches zero.

The wall heat flux q_w through the tube wall can be determined from Fourier's law:

$$q_w = kA\left.\frac{\partial T}{\partial r}\right|_{r=r_0} = \frac{kA}{r_0 - r_i}\left(T_{w,o} - T_{w,i}\right) = \frac{\Delta T_w}{R_{t,cond}} \tag{2.24}$$

where ΔT_w is temperature difference between the outer and inner tube wall surface and $R_{t,cond}$ is thermal resistance for conduction.

For a tube (circular cylinder) thermal resistance can be written as:

$$R_{t,cond} = \frac{ln(r_o/r_i)}{2\pi k(r_o - r_i)} \tag{2.25}$$

For a thin tube wall and high thermal conductivity k, thermal resistance to conduction is very low. For the tube geometry of interest, $R_{t,cond} = 8.73 \times 10^{-5}$ m^2-K/W resulting in high wall heat flux (see Figure 2.5c) and very small temperature difference between the inner and outer tube walls $T_{w,i}$ and $T_{w,o}$, respectively.

As depicted in Figure 2.5d, the melting time and wall heat flux are notably influenced by the driving force. A decrease in the driving force results in an exponential increase in the time needed for PCM melting, accompanied by a sharp decrease in wall heat flux. Extremely small driving forces lead to extended melting times. Hence, there exists a critical minimum value of wall heat flux necessary to accomplish PCM melting within the specified timeframe.

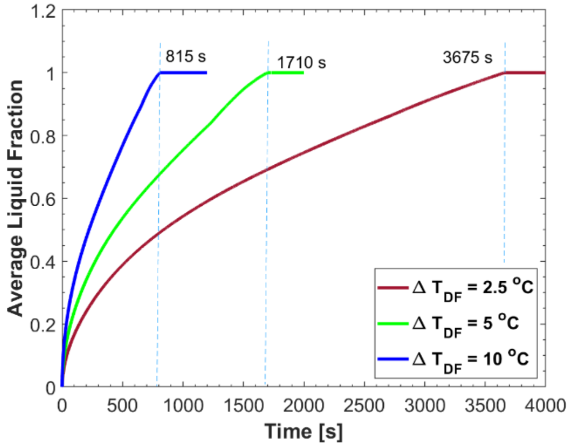
Average Liquid Fraction
Time [s]
815 s
1710 s
3675 s
Δ T_DF = 2.5 °C
Δ T_DF = 5 °C
Δ T_DF = 10 °C
0
0.2
0.4
0.6
0.8
1
1.2
0
500
1000
1500
2000
2500
3000
3500
4000

(a)

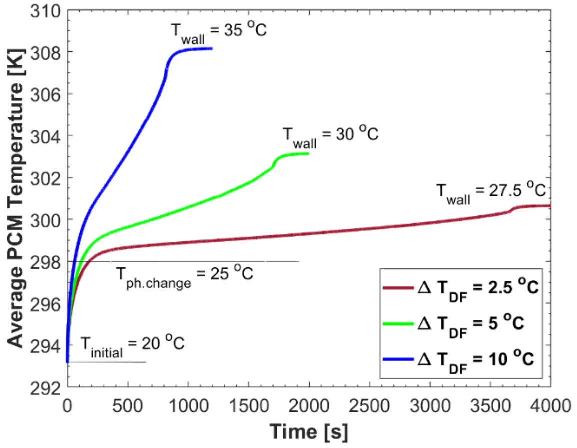
Average PCM Temperature [K]
Time [s]
T_wall = 35 °C
T_wall = 30 °C
T_wall = 27.5 °C
T_ph.change = 25 °C
T_initial = 20 °C
Δ T_DF = 2.5 °C
Δ T_DF = 5 °C
Δ T_DF = 10 °C
292
294
296
298
300
302
304
306
308
310
0
500
1000
1500
2000
2500
3000
3500
4000

(b)

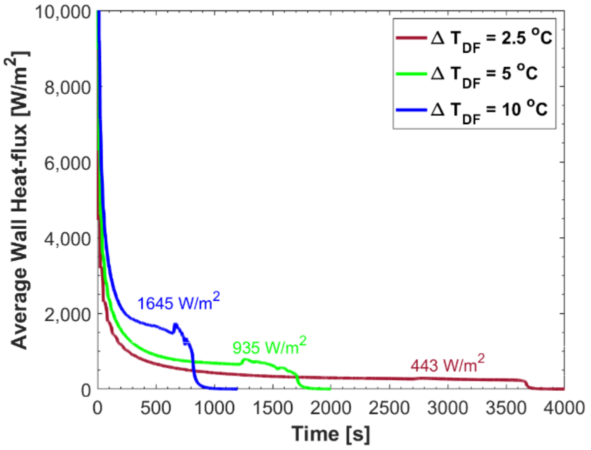
Average Wall Heat-flux [W/m²]
Time [s]
1645 W/m²
935 W/m²
443 W/m²
Δ T_DF = 2.5 °C
Δ T_DF = 5 °C
Δ T_DF = 10 °C
0
2,000
4,000
6,000
8,000
10,000
0
500
1000
1500
2000
2500
3000
3500
4000

(c)

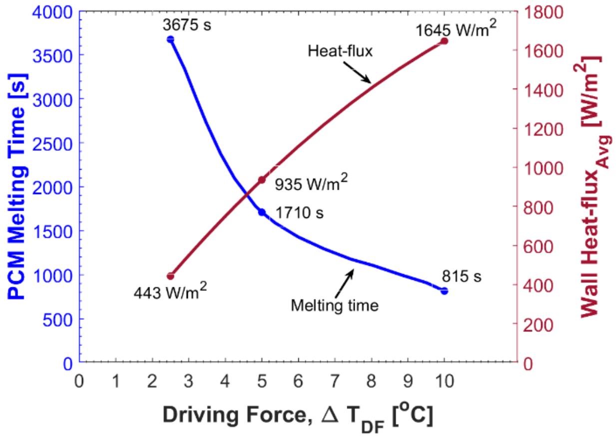
PCM Melting Time [s]
Wall Heat-flux_Avg [W/m²]
Driving Force, Δ T_DF [°C]
3675 s
1710 s
815 s
1645 W/m²
935 W/m²
443 W/m²
Heat-flux
Melting time
0
500
1000
1500
2000
2500
3000
3500
4000
0
200
400
600
800
1000
1200
1400
1600
1800
0
1
2
3
4
5
6
7
8
9
10

(d)

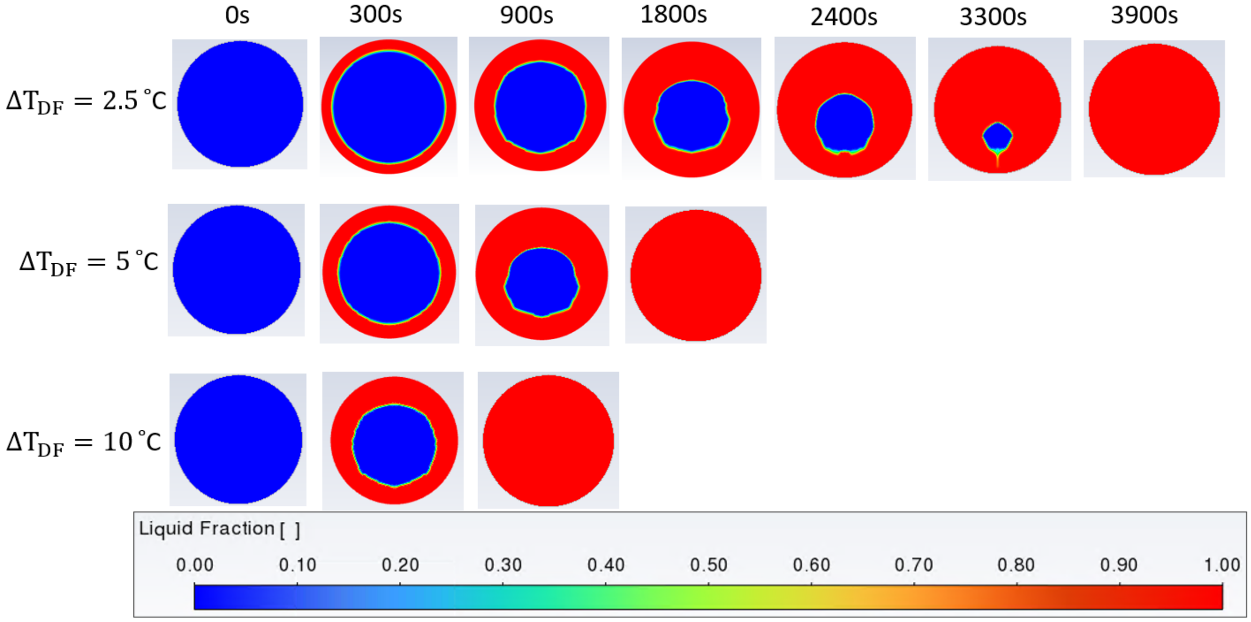
0s
300s
900s
1800s
2400s
3300s
3900s
ΔT_DF = 2.5 °C
ΔT_DF = 5 °C
ΔT_DF = 10 °C
Liquid Fraction [ ]
0.00
0.10
0.20
0.30
0.40
0.50
0.60
0.70
0.80
0.90
1.00

(e)

Figure 2. 5 Melting parameters as a function of time for three different driving forces: (a) Average liquid fraction of PCMs, (b) Average Temperature of PCM, (c) Peripherally averaged wall heat flux (q″), (d) The effect of driving force ΔT_{DF} on PCM melting time and average wall heat flux, (e) Contours of liquid fraction

Figure 2.5e illustrates the propagation of the melting front as a function of time for the variation of temperature driving force. In the liquid fraction legend, the red color signifies a liquid fraction of one, indicating complete melting, while the blue color represents frozen PCM with a liquid fraction of zero. The presence of a thin green-yellow ring around the solid PCM indicates the mushy zone. As the tube wall temperature surpasses the PCM phase change temperature, the melting of PCM initiates near the tube wall. Over time, the melting process advances deeper into the tube. Due to buoyancy effects, the PCM melting is asymmetrical around the horizontal axis of the tube; the upper half of the tube experiences a more rapid PCM melting compared to the lower half. Figure 2.5e illustrates that a small section of PCM in the bottom half of the tube melts last. As mentioned earlier, higher driving force results in higher heat flux, thus faster melting rate. For a melting driving force of 10, 5 and 2.5 °C (K) and an outer tube diameter (OD) of 1", the melting time for CC6 is approximately 800 s, 1,700 s and 3,600 seconds, respectively.

Similar to PCM melting, a sensitivity analysis was performed for PCM freezing in a 1" OD tube using constant wall temperatures of 15 °C, 20 °C, and 23.5 °C. Thus, the temperature driving force varied by 10 °C, 5 °C, and 2.5 °C, respectively, lower than the PCM phase change temperature (25 °C). Figure 2.6 displays various freezing parameters over time for the first-type boundary condition with a constant wall temperature. In Figure 2.6a, the average liquid fraction is depicted as a function of flow time. The tube with a constant wall temperature of 15 °C exhibits faster freezing of PCM compared to the other two cases, attributed to the higher temperature driving force.

The variation of the average PCM temperature within the tube is depicted over time in Figure 2.6b. The initial, phase change, and tube wall temperatures are also presented. According to the results, the temperature of the solid PCM, initially at 30°C, rapidly reaches the phase change temperature in less than 300 seconds. As heat is extracted through the tube wall and the PCM undergoes a phase change from liquid to solid, the average PCM temperature decreases linearly until all liquid PCM solidifies (freezes). Following the freezing of PCM, its temperature quickly drops to match the tube wall temperature.

Similar to the melting process, the PCM freezing can be divided into three phases: (1) a rapid temperature decrease of the liquid phase, (2) an approximately linear temperature decrease during the phase change, where the latent heat of fusion is removed through the tube wall, and (3) a rapid temperature decrease of the frozen PCM (subcooling) to the tube wall temperature.

In Figure 2.6c, the impact of the driving force on the wall heat flux is illustrated. The same analysis and conclusions apply to PCM freezing, with the difference being that the wall heat flux exits the tube, i.e., the heat of fusion needs to be removed to freeze the PCM. The results suggest that after the initial phase of PCM freezing, when the PCM reaches the phase change temperature and begins solidifying, the wall heat flux remains relatively constant. After the PCM solidified, as its temperature exceeds the fusion temperature, the wall heat flux decreases due to a decrease in the temperature difference between the tube wall and PCM (see Figure 2.6b). As the PCM temperature approaches the wall temperature, the wall heat flux gradually diminishes until it reaches zero.

As shown in Figure 2.6d, the freezing time and wall heat flux are significantly influenced by the driving force. A reduction in the driving force leads to an exponential increase in the time required for PCM to freeze, coupled with a sharp decrease in wall heat flux. Extremely small driving forces result in prolonged freezing times. Therefore, a critical minimum value of wall heat flux is necessary to achieve PCM freezing within the specified timeframe. It is important to note that a curve-fitting function was employed to plot the freezing time required curve for the variation of the temperature driving force, resulting in an optimum/minimum point that would not exist if more sets of data were used for the sensitivity analysis.

Figure 2.6e depicts the progression of the freezing front over time in response to variations in the temperature driving force. As the wall temperature is lower than the PCM phase change temperature, the freezing of PCM initiates around the tube periphery. Over time, the freezing process extends deeper into the tube. As illustrated in Figure 2.6e, PCM at the tube center freezes last. The freezing of PCM is symmetrical and uniform around the tube's horizontal axis. The mushy zone, depicted in green, exists between the solid and liquid zones. For a driving force of 10 °C (T_{wall} = 15 °C), PCM completes freezing by 1,400 seconds, while it takes a longer time, approximately 8,900 seconds, for PCM to freeze completely with a driving force of 2.5 °C (T_{wall} = 22.5 °C). The freezing time is prolonged compared to the melting time due to the weaker effect of natural convection during freezing. Additionally, the liquid phase diminishes in size during PCM freezing, reducing the impact of natural convection over time.

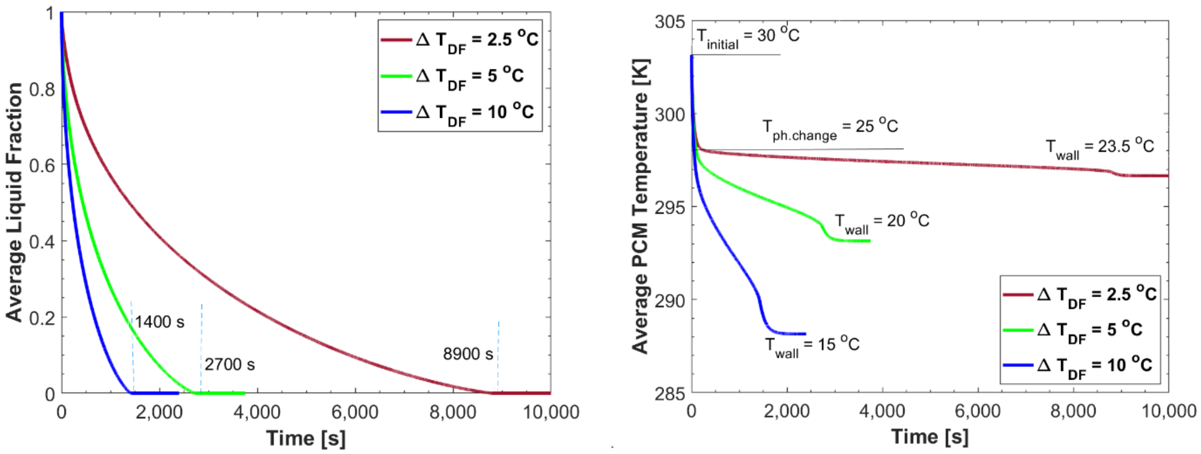

(a)

(b)

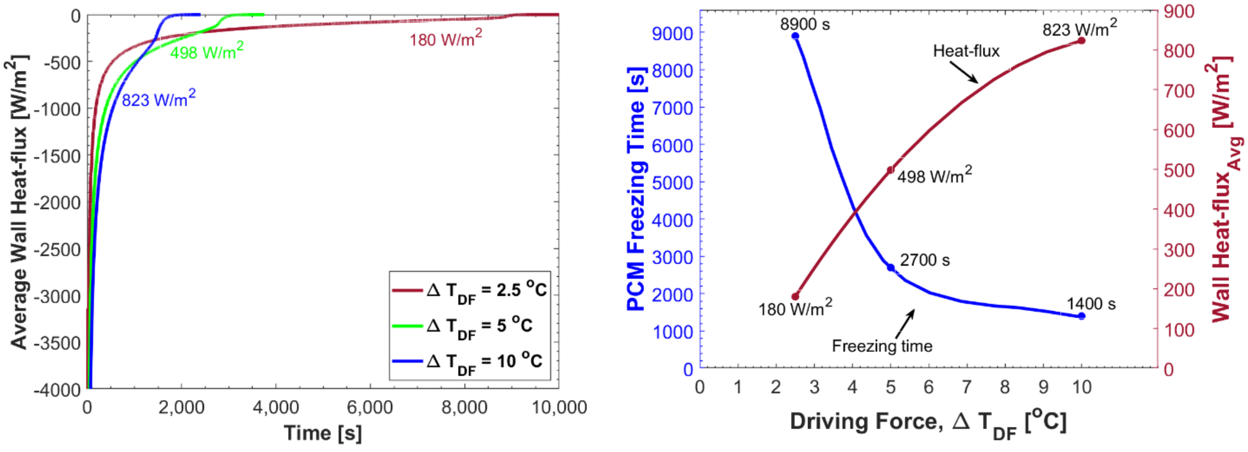

(c) (d)

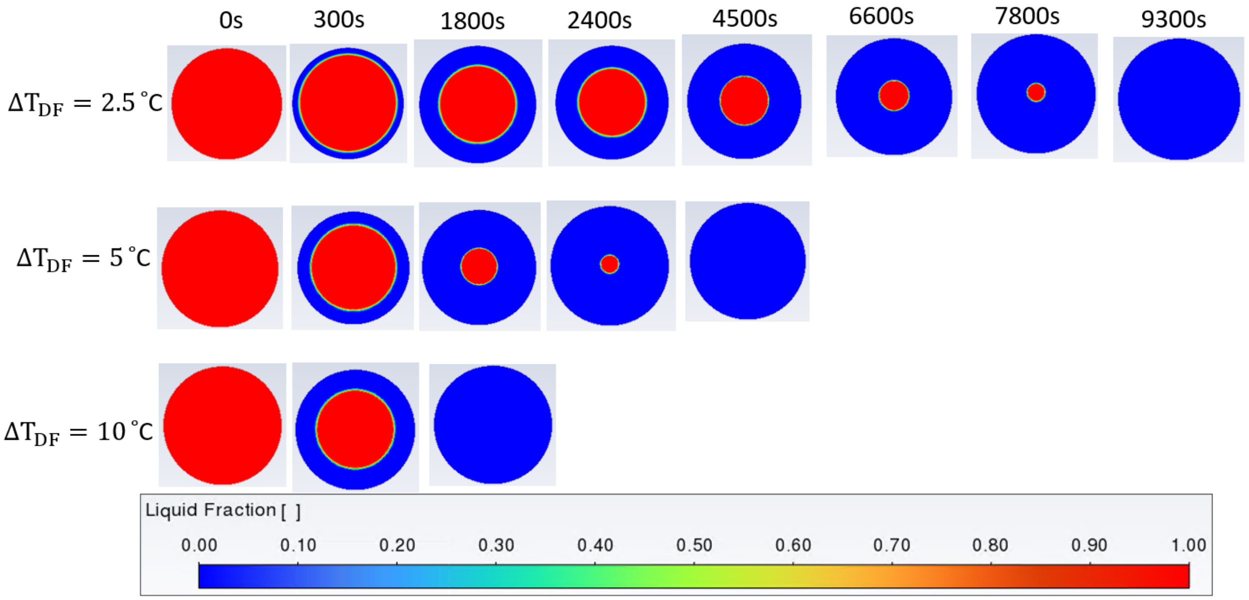

(e)

Figure 2. 6 Freezing parameters as a function of time for three different driving forces: (a) Average liquid fraction of PCMs, (b) Average Temperature of PCM, (c) Peripherally averaged wall heat flux (q″), (d) The effect of driving force ΔT$_{DF}$ on PCM freezing time and average wall heat flux, (e) Contours of liquid fraction

The melting and freezing times are important parameters for the heat storage module and LTES design. After PCM reaches the phase change temperature, the PCM melting/freezing rate can be determined from the energy balance. For PCM melting/ freezing:

$$q_w'' \cdot A \cdot \Delta\tau = \Delta m_{PCM} \cdot L_f \tag{2.26}$$

where $q_w^{"}$ is the wall heat flux into/ out of the tube, A is the tube surface area, $\Delta\tau$ is the heating/ solidifying time, L_f is the latent heat of PCM phase change, and Δm_{PCM} is the mass of melted/ frozen PCM. The melting/ freezing rate R is then

$$R = \frac{\Delta m_{PCM}}{\Delta\tau} = \frac{A}{L_f} \cdot q_w^{"} = \frac{D\pi L}{L_f} \cdot q_w^{"} = K \cdot q_w^{"} \tag{2.27}$$

where D is tube diameter and L is tube length. As the above equation shows, PCM melting/ freezing rate is proportional to the wall heat flux.

Because the driving force is affecting the wall heat flux, it is also affecting the melting and freezing rates, and melting and freezing times. Smaller ΔT_{DF} decreases the wall heat flux and melting/freezing rates, and thus increases the melting and freezing times, while larger driving force increases the wall heat flux and melting/freezing times, and thus decreases the melting and freezing times, as discussed earlier.

2.8.2. Boundary condition of the second kind, von Neumann – constant wall heat flux

The numerical analyses were performed using a constant wall heat flux on a 1" outer diameter tube. For the PCM melting and freezing processes, a constant wall heat flux of 150 W/m² was applied to the tube wall. During the melting process, the heat flow is inward as heat is transferred from the air to the PCM. In contrast, for the freezing process, the heat flow is outward as heat is rejected from the PCM to the air. The initial temperature for the PCM melting process was 20 °C, while it was 30 °C for the PCM solidification process.

Figure 2.7 illustrates different melting parameters as a function of time for the constant wall heat flux boundary condition. Similar to the isothermal boundary condition, the temperature of the PCM rises rapidly from the initial temperature, remains almost constant during the phase transition, and starts to superheat once the PCM is completely melted (see Figure 2.7b). The tube wall temperature is slightly higher than the average PCM temperature and gradually increases during the solid PCM phase transition to liquid, as shown in Figure 2.7b. Figure 2.7a shows the average liquid fraction of the PCM as a function of flow time. Contours of the propagation of PCM melting fraction are presented in Figure 2.7c. Initially, the melting process is symmetrical around the horizontal axis. After around 6,300 s, due to buoyancy, the PCM at the upper portion of the tube melts faster than the PCM at the bottom of the tube, and the solid PCM drops to the bottom of the tube. It takes approximately 12,000 s for the PCMs to melt completely.

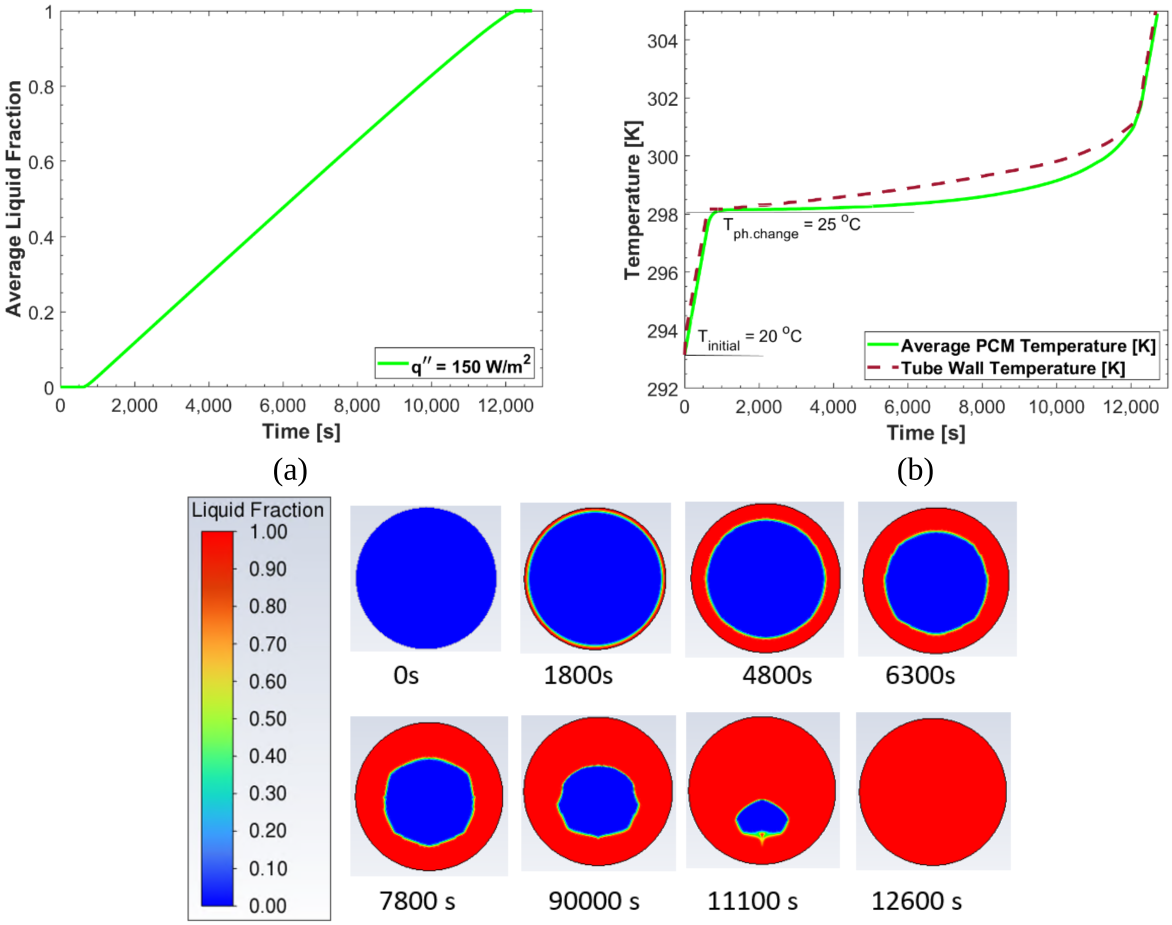

(a) (b)

(c)

Figure 2. 7 Melting parameters as a function of time for constant wall heat flux: (a) Average liquid fraction of PCMs, (b) Average Temperature of PCM and temperature of the tube wall, (c) Contours of liquid fraction

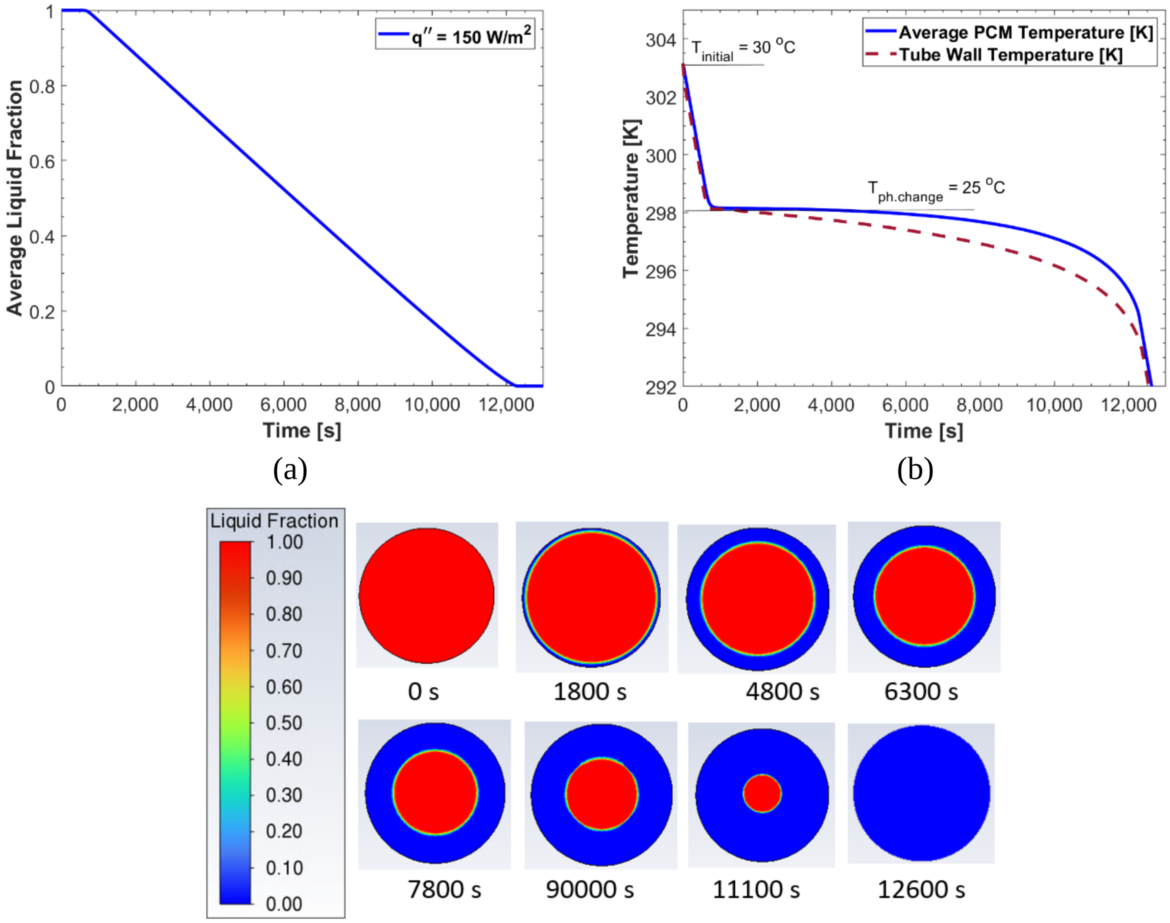

(a) (b)

(c)

Figure 2. 8 Freezing parameters as a function of time for constant wall heat flux: (a) Average liquid fraction of PCMs, (b) Average Temperature of PCM and temperature of the tube wall, (c) Contours of liquid fraction

Similar to PCM melting, Figure 2.8 presents parameters related to the freezing process over time under the constant wall heat flux boundary condition. Like the isothermal boundary condition, the PCM temperature decreases rapidly from its initial state, remains nearly constant during the phase transition, and then begins to supercool once the PCM is entirely frozen (refer to Figure 2.8b). In Figure 2.8b, it is observed that the tube wall temperature is slightly lower than the average PCM temperature and gradually decreases during the transition from liquid PCM to solid. The liquid fraction of the PCM, as shown in Figure 2.8a, varies with flow time. Figure 2.8c illustrates contours depicting the propagation of the PCM freezing front. The solidification process is symmetrical around the horizontal axis. The PCM at the nuclei or center of the tube freezes last. It takes approximately 12,000 s for complete solidification of the PCMs.

For a constant wall heat flux, melting/ freezing rate is constant and melting/ freezing time, τ is proportional to the tube diameter and inversely proportional to wall heat flux.

$$\tau = 0.25D \cdot \frac{L_f \rho_{PCM}}{q_w^{"}} \tag{2.28}$$

For tubes with diameters D_1 and D_2, the ratio of melting/ freezing times can be expressed as:

$$\frac{\tau_1}{\tau_2} = \frac{D_1}{D_2} \cdot \frac{q_{w2}^{"}}{q_{w1}^{"}} \tag{2.29}$$

Thus, for a smaller diameter tube, melting/ freezing time is shorter. Due to time constraints, the sensitivity analysis involving varying values of constant wall heat flux was not conducted.

2.8.3. Boundary condition of the third kind – convection heat transfer

The convection boundary condition becomes applicable when a single tube is positioned in a cross flow of air. Differentiating between specifying a constant convection heat transfer coefficient on the tube surface and specifying the wall temperature is important. This distinction arises because (1) the thermal resistance to convection heat transfer at the tube surface contributes to an increase in the overall thermal resistance to heat transfer, consequently reducing the wall heat flux, and (2) the tube wall temperature is not initially known and must be determined through the energy balance at the tube surface.

Total thermal resistance to heat transfer can be written as a sum of thermal resistances to convection $R_{t,conv}$ on the outside tube surface and conduction $R_{t,cond}$ through the tube wall:

$$R_{t,tot} = R_{t,conv} + R_{t,cond} = \frac{1}{2\pi r_o h} + \frac{ln(r_o/r_i)}{2\pi k(r_o - r_i)} \tag{2.30}$$

As previously mentioned, in the case of a thin tube wall with high thermal conductivity (k), the thermal resistance to heat conduction is remarkably low. For the specific tube geometry in question, the thermal resistance to heat conduction ($R_{t,cond}$) is calculated as 8.73×10^{-5} m^2-K/W. Contrastingly, the thermal resistance to heat convection is contingent upon the convection heat transfer coefficient (h). In the range of 30 to 70 W/m^2-K for h (corresponding to the relevant air velocities), the thermal resistance to convection surpasses the resistance to conduction by a significant margin. For h = 30 W/m^2-K, the thermal resistance to convection ($R_{t,conv}$) is 0.1295 m^2-K/W, approximately 1,500 times higher than the thermal resistance to conduction. Consequently, this results in a markedly lower wall heat flux compared to pure conduction.

For the convection boundary condition, the driving force ΔT_{DF} can be defined as

$$\Delta T_{DF} = \left(T_{\infty} - \Delta T_{R,conv}\right) - T_{ph.change} \tag{2.31}$$

In the context of the convection boundary condition, the driving force is reduced due to the resistance to convection heat transfer and the associated temperature difference $\Delta T_{R,conv}$, which is contingent on the convection heat transfer coefficient (h). With an increase in the convection heat transfer coefficient, there is a reduction in thermal resistance to convection, leading to an increase in wall heat flux. A minimum value of the convection heat transfer coefficient, denoted as h, is crucial for the given tube diameter and free stream temperature. This minimum value is necessary to facilitate the melting and freezing of PCM within the specified time frame, approximately 4 hours for the LTES application.

Therefore, under the same ΔT_{DF} (temperature difference at the freezing/melting interface), the wall heat flux is lower, and the melting/freezing time is prolonged for the convection boundary condition compared to the isothermal boundary condition. The primary aim of the analysis outlined in this section is to establish the relationship between tube diameter, convection heat transfer coefficient, and the duration of melting/freezing.

In this study, the correlations proposed by Zukauskas [82, 83], Churchill and Bernstein [83, 84], and Hilpert [83, 85] were used to determine the convection heat transfer coefficient (h). These correlations were applied to determine the value of h between the air surrounding the tube and the tube surface. It is assumed that this value remains uniform and does not vary with the angular location on the tube surface, typically measured from the forward stagnation point. The assumptions considered in these correlations are described in the following section.

2.8.3.1. Zukauskas (Zu) correlation

According to Zukauskas, the average Nusselt number for a circular tube can be determined from:

$$\overline{Nu}_D = CR_{e_D}^{m} Pr^{n} \left(\frac{Pr}{Pr_s}\right)^{1/4} \quad \text{for} \begin{Bmatrix} 0.7 \le Pr \le 500 \\ 1 \le Re_D \le 10^6 \end{Bmatrix} \tag{2.32}$$

where, $\bar{N}u_D$ is the average Nusselt number based on tube diameter D, Re_D is the Reynolds numbers based on tube diameter D. All properties are evaluated at T_∞ (free stream temperature, fluid temperature far upstream of the tube), except Pr_s which is evaluated at the tube surface temperature T_s. Values of C and m are listed in Table 2.7. The value of n should be chosen as follows:

$$Pr \le 10,\ \text{n} = 0.37$$

$$Pr \ge 10,\ \text{n} = 0.36$$

It should be noted here that the constants C, m, and n were derived from the results obtained by comparing them with the literature under constant wall temperature and constant wall heat flux boundary conditions.

Table 2. 7. Constants in Zukauskas Correlation [83]

Re_D	C	m
1- 40	0.75	0.4
40 -1,000	0.51	0.5
1,000 - 20,000	0.26	0.6
>20,000	0.076	0.7

2.8.3.2. Churchill and Bernstein correlation

Churchill and Bernstein have proposed a single comprehensive equation that covers the entire range of Re_D for which the data is available, as well as a wide range of Pr. The equation is recommended for all $Re_D Pr \geq 0.2$ and has the following form where all properties are evaluated at the film temperature $T_f = 0.5(T_s + T_\infty)$.

$$\overline{Nu}_D = 0.3 + \frac{0.62\, Re_D^{1/2}\, Pr^{1/3}}{\left[1+\left(\frac{0.4}{Pr}\right)^{2/3}\right]^{1/4}} \cdot \left[1+\left(\frac{ReD}{282{,}000}\right)^{5/8}\right]^{4/5} \tag{2.33}$$

2.8.3.3. Hilpert correlation

To account for various Prandtl numbers, the modified correlation of Hilpert is as follows:

$$\overline{Nu}_D = CR_{e_D}^{m} Pr^{1/3} \text{ for Pr} \geq 0.7 \tag{2.34}$$

Values of C and m are listed in Table 2.8.

Table 2. 8. Constants in Hilpert Correlation

Re_D	C	m
0.4 – 4	0.989	0.330
4 – 40	0.911	0.385
40 – 4000	0.683	0.466
4000 – 40,000	0.193	0.618

The graphs in Figure 2.9 illustrate the convection heat transfer coefficient (h), determined through correlations, across a range of free stream velocities and a constant free stream temperature of 30 °C. As depicted in the figure, the convection heat transfer coefficient (h) exhibits an increase with air velocity. Additionally, variations in the predicted values of h from the Zukauskas, Churchill & Bernstein, and Hilpert correlations become more pronounced with higher air velocities. It is important to note that, unless otherwise specified, Zukauskas correlation will be employed for subsequent analyses in this study. This choice is made due to its tendency to predict conservative values of the heat transfer coefficient (*h*).

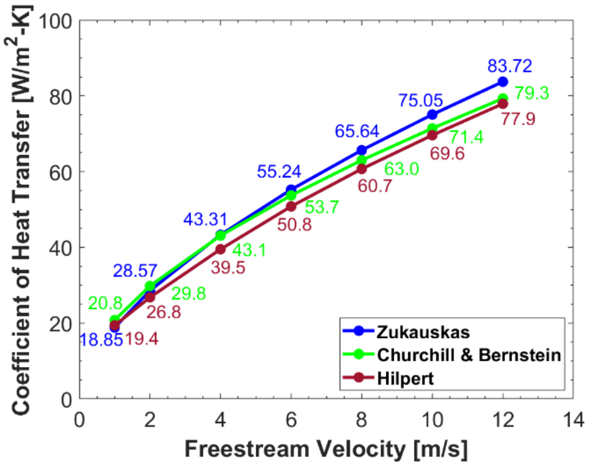

Figure 2. 9 Convection heat transfer coefficient, *h* as a function of air velocity for the free stream temperature of 30 °C

It is important to emphasize that none of the preceding correlations should be regarded as absolute. Each correlation holds validity within a specific range of conditions; however, for most engineering calculations, one should not anticipate accuracy beyond 20%. Upon scrutiny of the Zukauskas correlation, it becomes evident that at low-Reynolds number portion of the correlation tends to overestimate the Nusselt number.

A parametric analysis was conducted for constant convection heat transfer coefficients, *h* =30, 40 and 50 W/m2-K, using two different outer diameters, 0.75" and 1". The results are presented in Figure 2.10. Figures 2.10a and 2.10b illustrate the average liquid fraction and average PCM temperature as functions of time, respectively. As the results indicate, after all PCM melts, the average PCM temperature rapidly increases as the liquid PCM is superheated, approaching the free stream temperature for the boundary condition of the constant convection heat transfer coefficient. For lower values of the convection heat transfer coefficient, the melting time is longer due to lower wall heat flux (see Figure 2.10c).

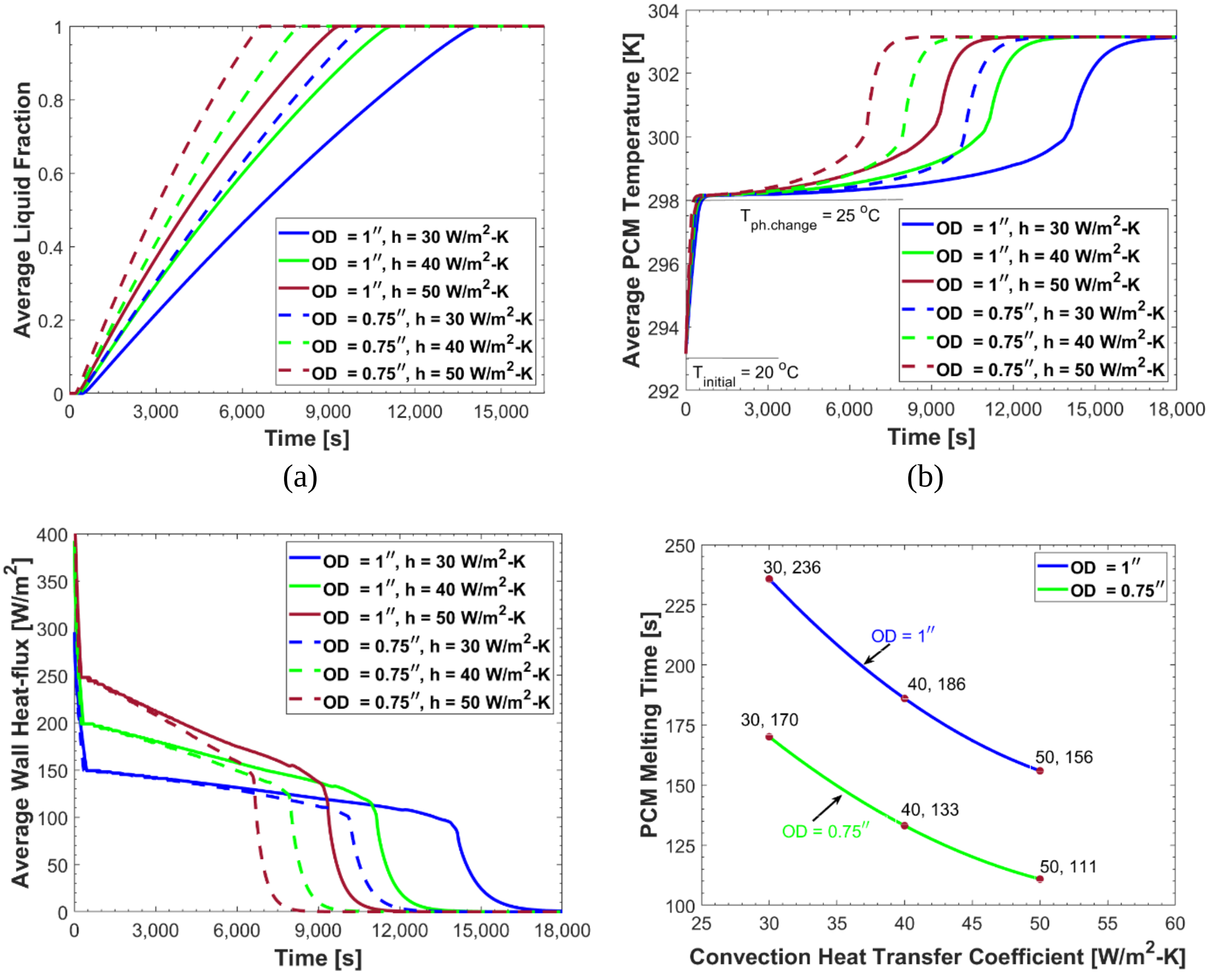

(a) (b)

(c) (d)

Figure 2. 10 PCM melting parameters as a function of time for constant convection heat transfer coefficients: (a) average PCM liquid fraction, (b) average PCM temperature, (c) average wall heat flux and (d) PCM melting time as a function of convection heat transfer coefficients for OD = 0.75" and 1"

As depicted in Figure 2.10c, the wall heat flux for a smaller tube is somewhat lower compared to the larger diameter tube. However, the PCM melting time in a smaller tube is shorter due to a smaller PCM mass and shorter heat diffusion paths for the constant convection heat transfer coefficient (see Figure 2.10d). Under the analyzed conditions, for the same value of the convection heat transfer coefficient, the melting time is approximately 40% higher for a 1" tube compared to the 0.75" tube. For the same value of convection heat transfer coefficient, the change in melting time is approximately proportional to the ratio of tube diameters ($\tau_{melting,D1}/\tau_{melting,D2} = D_1/D_2$).

Similar to the PCM melting process, a parametric analysis was performed for the freezing process, considering constant convection heat transfer coefficients, *h* =30, 40 and 50 W/m2-K, and utilizing two different outer diameters, 0.75" and 1". During PCM freezing, the heat flux is directed outward as heat transfers from the tube wall to the surrounding air. The results are depicted in Figure 2.11. Figures 2.11a and 2.11b illustrate the average liquid fraction and average PCM temperature as functions of time, respectively. As the results indicate, following complete PCM freezing, the average PCM temperature decreases rapidly as the solid PCM is subcooled, approaching the free stream temperature based on the boundary condition of the constant convection heat transfer coefficient. For lower values of the convection heat transfer coefficient, the freezing time is extended due to lower wall heat flux (see Figure 2.10c). As illustrated in Figure 2.10c, the wall heat flux for a smaller tube is somewhat lower compared to the larger diameter tube. The heat flux is higher at the beginning, decreasing linearly during phase change, and eventually dropping to zero when there is no driving force. Similar to PCM melting, under the analyzed conditions, for the same value of the convection heat transfer coefficient, the freezing time is greater for the larger tube compared to the smaller one (see Figure 2.10d). The results indicate that the freezing time is somewhat longer compared to the melting time, with the difference primarily dependent on the convection heat transfer coefficient, *h*.

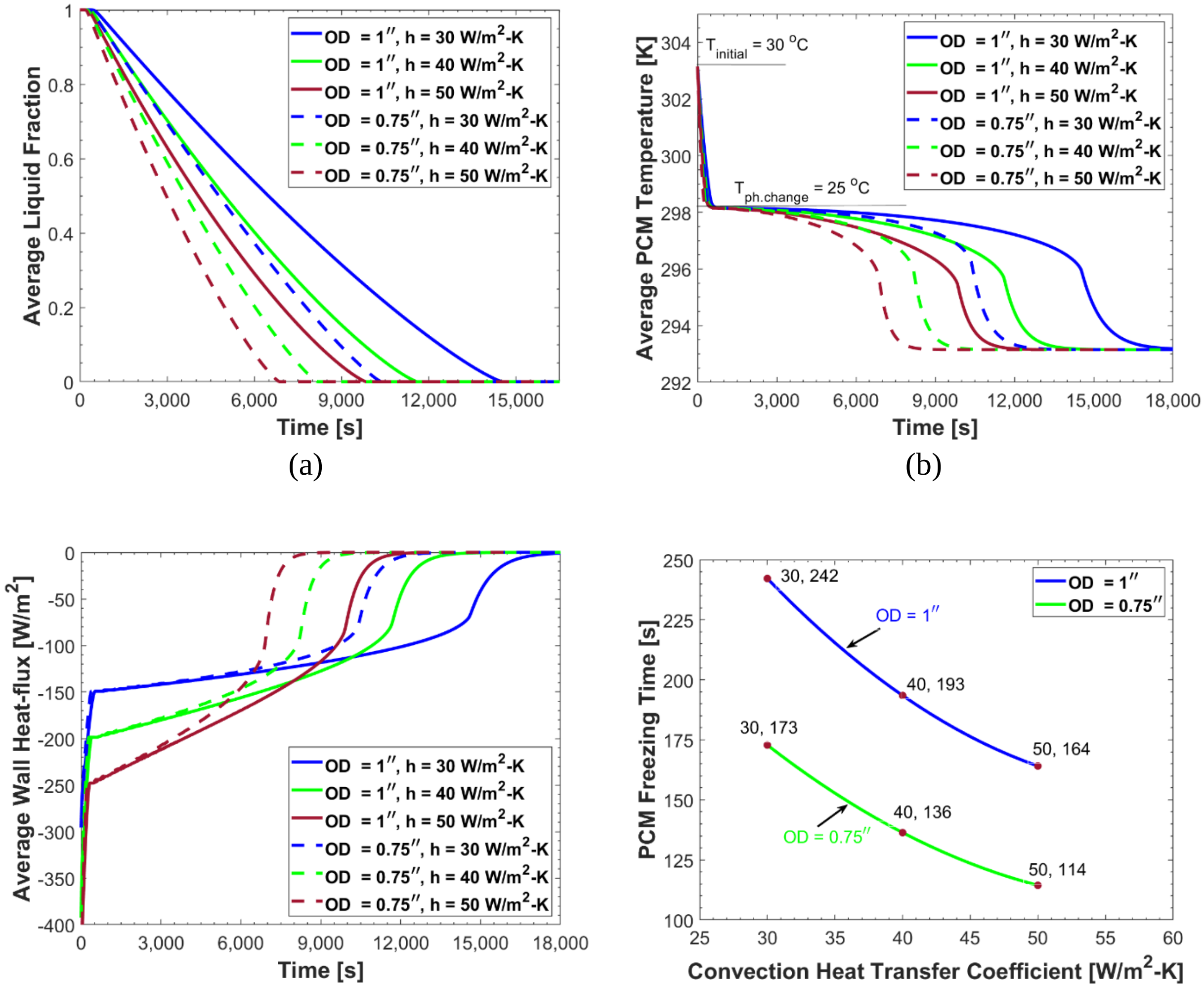

(a) (b)

(c) (d)

Figure 2. 11. PCM freezing parameters as a function of time for constant convection heat transfer coefficients: (a) average PCM liquid fraction, (b) average PCM temperature, (c) average wall heat flux and (d) PCM freezing time as a function of convection heat transfer coefficients for OD = 0.75" and 1"

2.8.4. Conjugate heat transfer

Instead of relying on empirical correlations for the convection heat transfer coefficient, one can opt for a numerical approach through conjugate heat transfer analysis to determine its value. In this method, the Navier-Stokes equations and energy conservation equations for the fluid (refer to Section 2.4.2) and the energy equation for the solid(s) (refer to Section 2.4.3) are simultaneously solved. This simultaneous solution provides the heat flux between the air flowing around the circular cylinder (tube).

The free stream temperature and velocity of the fluid and tube diameter need to be given. The analysis was performed for the free stream velocity of 1.9 m/s and driving force ΔT_{DF} (temperature difference between the free stream and PCM phase change temperature) of 5 °C to predict PCM melting/ freezing time.

Within the conjugate heat transfer approach, the heat flux is computed individually at every grid point on the tube surface. Consequently, local values of the convection heat transfer and the peripheral distribution of convection heat transfer coefficient on the tube surface were established. While this method provides the most realistic results, it is also the most computationally intensive approach for calculating the heat transfer coefficient on the tube surface.

The peripheral heat transfer coefficient, h is determined from the calculated value of the wall heat flux, free-stream temperature and wall temperature as presented in the following expression:

$$h = \frac{q_w''}{T_\infty - T_w} \tag{2.35}$$

The computed peripherally averaged heat transfer coefficient (h_{avg}) of 27 W/m²-K aligns closely with the value of 28.7 W/m²-K obtained from the Zukauskas correlation under the same operating conditions (see Table 2.9). Non-uniform distribution of the heat transfer coefficient around the periphery of a circular tube is illustrated in Figure 2.12 for conjugate heat transfer approach. Positive heat transfer coefficient represents melting where heat transfer is transferred from air to PCM, while negative heat transfer coefficient represents freezing where heat transfer is transferred from PCM to air. Figure 2.13 shows the velocity profile around the single tube after the flow reaches the steady state. At the stagnation point upstream of the tube and at the downstream of the tube, the velocity is lower compared to the free-stream flow.

Table 2. 9 Validation – Conjugate heat transfer

v_∞ (m/s)	h_{avg} (W/m^2-K)		Difference (%)
1.9 (Re = 2,965)	Numerical	Zu Correlation	5.6
	27.0	28.7	

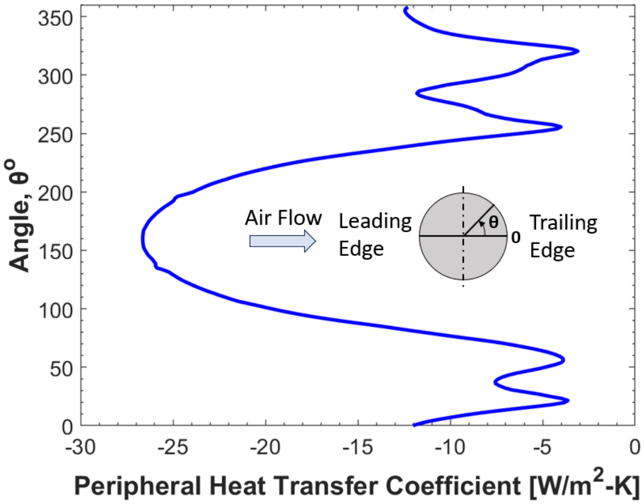

Figure 2. 12. Distribution of peripheral heat transfer coefficient ($h_{peripheral}$)

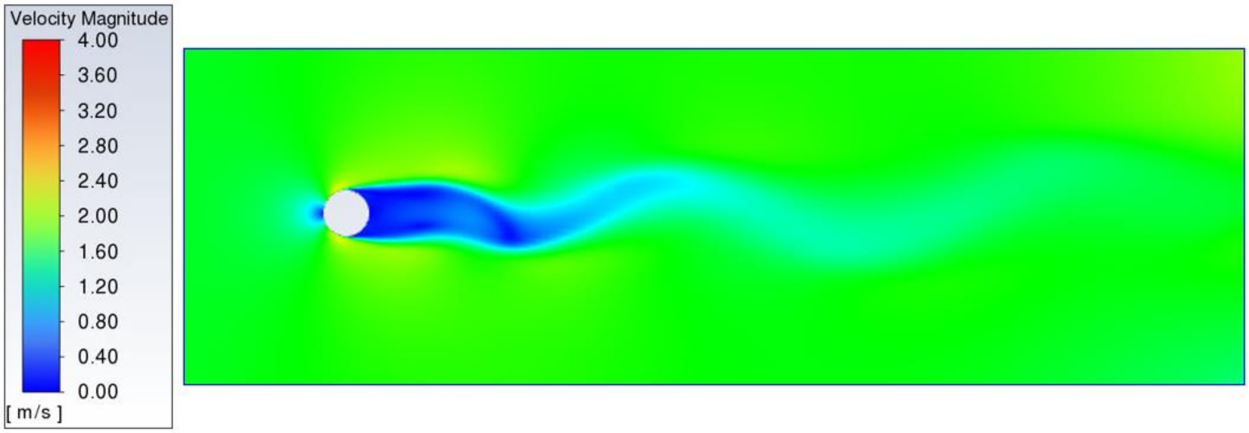

Figure 2. 13. Velocity profile after the flow reaches the steady state

Figure 2.14 compares melting parameters as a function of time for both convection and conjugate heat transfer approaches. Figure 2.14a presents the average liquid fraction, while Figure 2.14b displays the average PCM temperature for both approaches. As discussed earlier, there is a rapid increase in temperature from the initial temperature, followed by a constant temperature plateau, and then a gradual increase in PCM temperature until it reaches the freestream temperature (30 ºC). Under the analyzed operating conditions, the predicted PCM melting time determined from the conjugate heat transfer analysis is approximately the same as that from the pure convection approach.

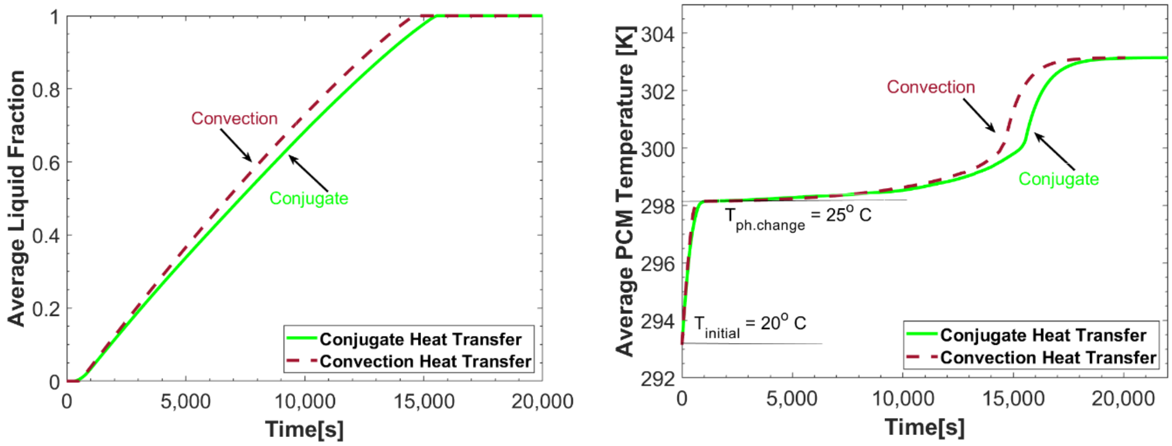

(a) (b)

Figure 2. 14. PCM melting parameters as a function of time for convection and conjugate heat transfer approaches: (a) average PCM liquid fraction, (b) average PCM temperature

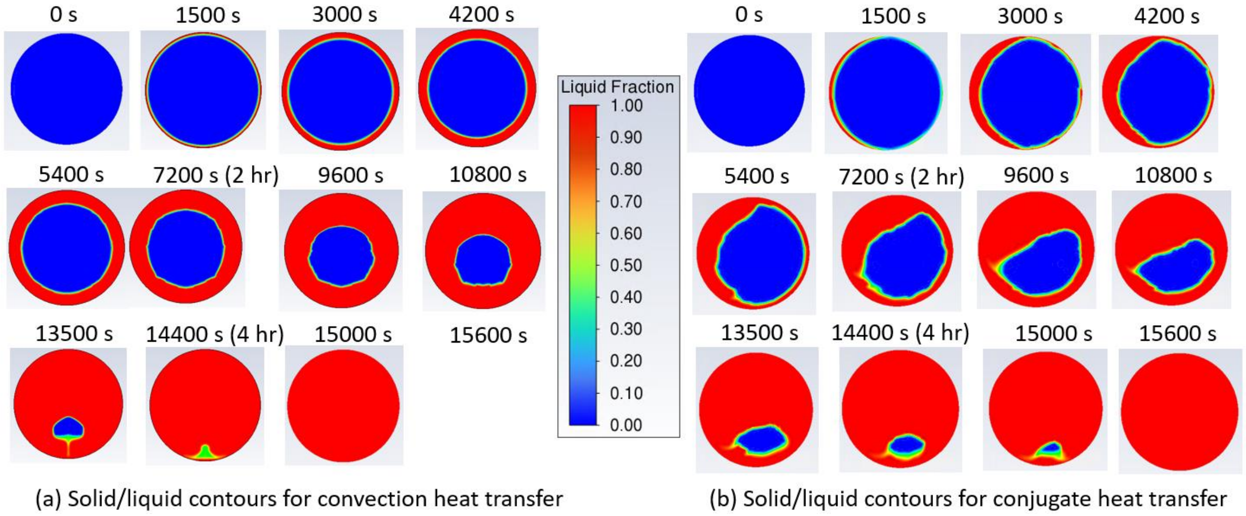

(a) (b)

Figure 2. 15. PCM melting contours for (a) constant convection heat transfer and (b) conjugate heat transfer approach

Since the heat transfer coefficient varies along the tube geometry, PCM melting is not symmetric. The comparison of melting contours, predicted by conjugate heat transfer analysis and by using a uniform value of convection heat transfer coefficient from empirical correlations (Figure 2.15), illustrates the differences between the two approaches at different time intervals.

In the constant convection heat transfer coefficient approach (Figure 2.15a), a uniform and symmetric melting process around the periphery is observed. Due to buoyancy, the solid region starts to sink, resulting in higher heat transfer above it due to natural convection in the liquid PCM.

On the other hand, the conjugate heat transfer approach (Figure 2.15b) reveals a non-symmetric PCM melting process. Heat transfer is higher near the leading edge and above the solid region due to natural convection. The larger heat transfer coefficient at the leading edge (see Figure 2.12) causes the PCM at the leading edge to melt earlier compared to the trailing edge.

Figure 2.16 illustrates a comparison of freezing parameters over time for both convection and conjugate heat transfer approaches. In Figure 2.16a, the average liquid fraction is presented, while Figure 2.16b showcases the average PCM temperature for both approaches. As previously discussed, there is an initial rapid temperature decrease, followed by a consistent temperature plateau, and ultimately, a gradual decline in PCM temperature until it aligns with the freestream temperature (20 °C).

In contrast to PCM melting, under the analyzed operating conditions, the predicted PCM freezing time derived from the conjugate heat transfer analysis is approximately 30 minutes longer compared to pure convection. This disparity is attributed to the non-symmetric and non-uniform freezing process.

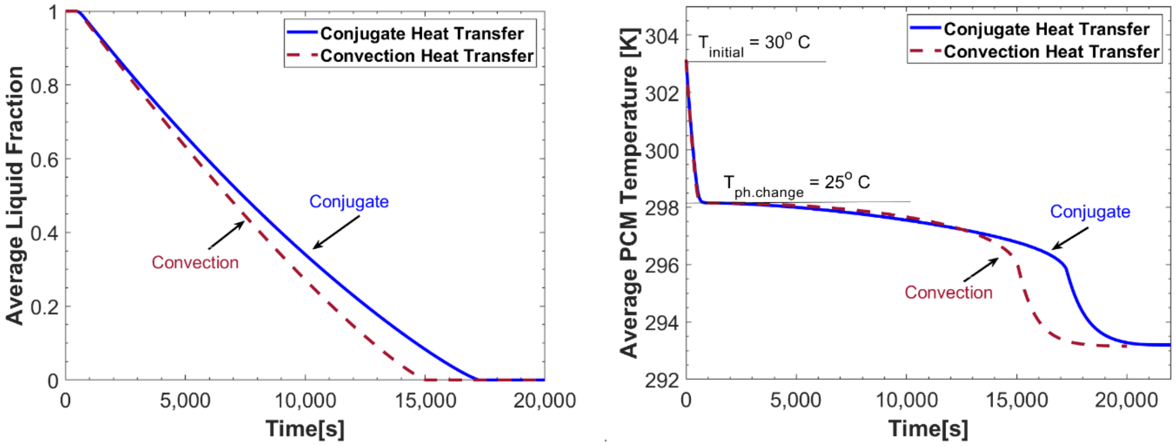

(a) (b)

Figure 2. 16. PCM freezing parameters as a function of time for convection and conjugate heat transfer approaches: (a) average PCM liquid fraction, (b) average PCM temperature

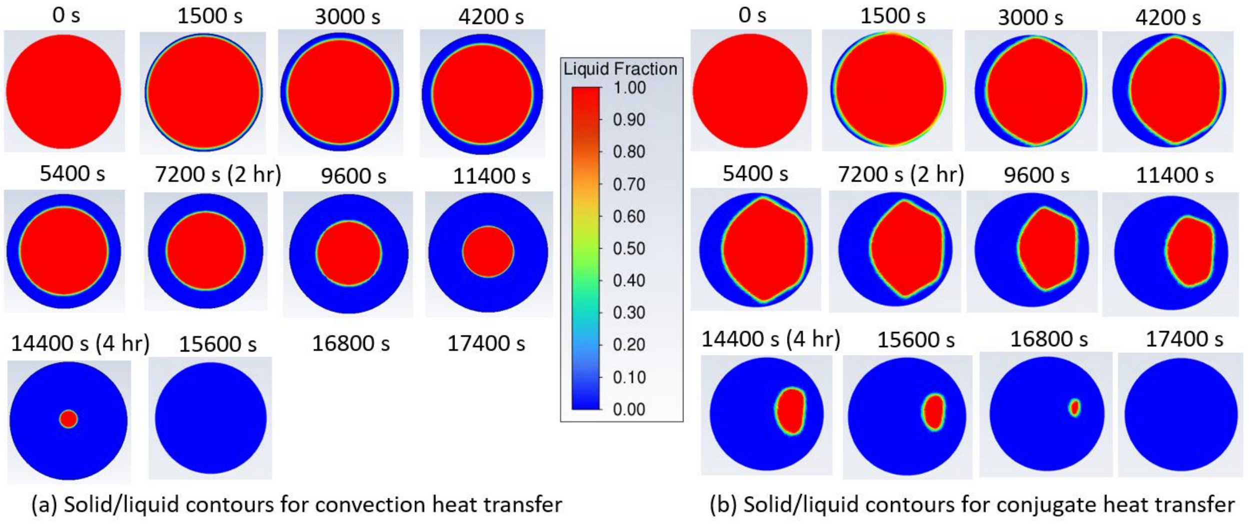

(a) (b)

Figure 2. 17. PCM freezing contours for (a) constant convection heat transfer and (b) conjugate heat transfer approach

Similar to PCM melting, the comparison of freezing contours, as predicted by both conjugate heat transfer analysis and the use of a uniform convection heat transfer coefficient from empirical correlations (Figure 2.17), highlights the distinctions between the two approaches at various time intervals.

Uniform distribution of the heat transfer coefficient around the periphery results in symmetric and uniform freezing process for the pure convection (Figure 2.17a). On the other hand, the conjugate heat transfer approach reveals a non-symmetric PCM freezing process (Figure 2.17b). Since the peripheral heat transfer coefficient is larger at the leading edge (see Figure 2.12), the freezing is faster around the leading edge of the tube compared to the trailing edge.

A parametric analysis was performed considering the variation of Re_D, freestream temperature, and outer diameter of the tube using conjugate heat transfer approach. The results are discussed in the following section.

2.8.4.1. Variation of Reynolds number (Re)

Numerical analysis of PCM melting was performed for different Reynolds numbers: 100, 500, and 1000 using 1″ outer diameter of the tube. Figure 2.18 illustrates PCM melting parameters: average liquid fraction and average PCM temperature as functions of time for the variation in Reynolds number with a temperature driving force (ΔT_{DF}) of 10 K (ºC). Faster melting occurs with the increase in Reynolds number from 100 to 1000 since the average heat transfer coefficient increases with the velocity, thus with Reynolds number (see Figure 2.9). Similar to other boundary conditions mentioned earlier, three phases of PCM melting are observed (Figure 2.18b): starting with the rapid increase in PCM temperature from the initial value (293.15 K), followed by a constant temperature plateau during the phase transition, and ending with the superheating of PCM until its temperature reaches the incoming air temperature at the inlet (309.65 K).

Similar to PCM melting, numerical analysis was performed for different Reynolds numbers: 100, 500, and 1000 for PCM freezing, using 1″ outer diameter of the tube. In Figure 2.19, the parameters related to PCM freezing are illustrated, depicting the average liquid fraction and average PCM temperature over time for different Reynolds numbers with a temperature driving force of ΔT_{DF} = 10 K (ºC). As observed in PCM melting, faster freezing is observed with an increase in Reynolds number from 100 to 1000 due to the corresponding increase in the average heat transfer coefficient with velocity. The freezing process can be divided into three phases, as shown in Figure 2.19b: an initial rapid drop in PCM temperature from its starting value of 303.15 K, followed by a period of constant temperature during the phase transition, and finally, subcooling of the PCM until it reaches the incoming air temperature at the inlet (289 K). The numerical analysis for PCM freezing was terminated upon complete freezing of the PCM in the tube ($\gamma = 0$) due to time constraints.

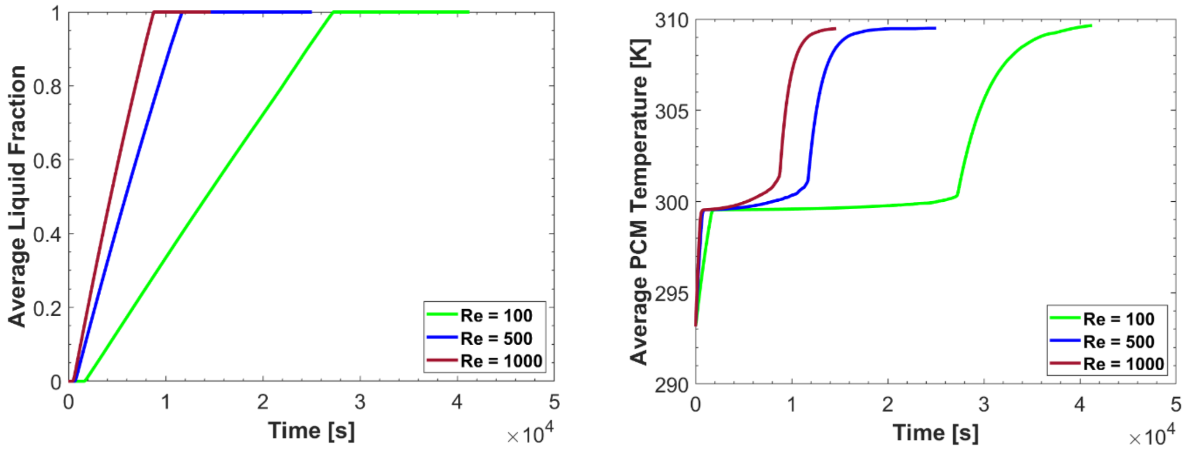

(a) (b)

Figure 2. 18. PCM melting parameters as a function of time for different Re number: (a) average PCM liquid fraction, (b) average PCM temperature

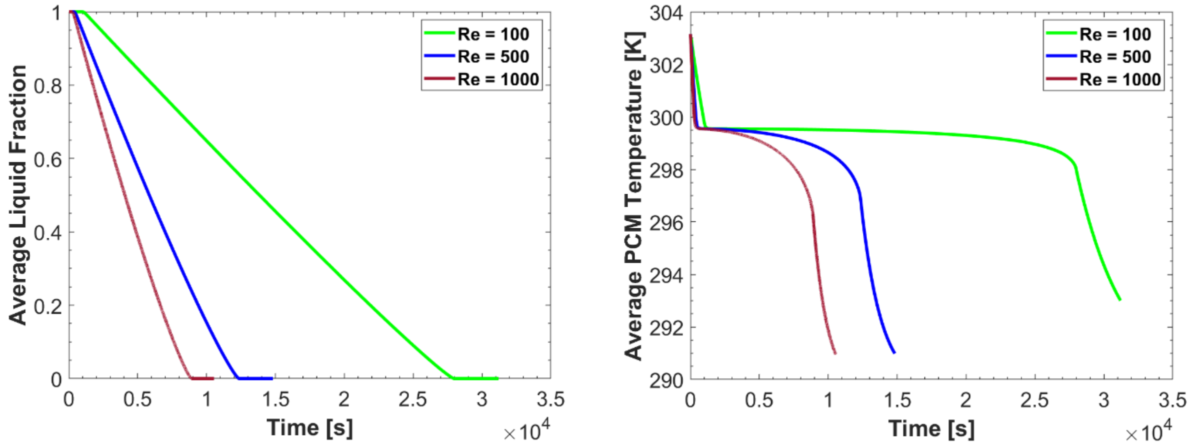

(a) (b)

Figure 2. 19. PCM freezing parameters as a function of time for different Re number: (a) average PCM liquid fraction, (b) average PCM temperature

Figure 2.20 illustrates hydraulic and thermal performance parameters: pressure drop across the tube, average heat transfer coefficient, and melting/freezing time as functions of Reynolds number (Re) for the conjugate heat transfer boundary conditions. The numerical results of pressure drop across the tube and average heat transfer coefficient were compared with those derived from the experimental correlation by Zukauskas [82] and Churchill & Bernstein [84]. It should be mentioned that the uncertainty of these correlations is around 20% and holds validity within a specific range of conditions [83].

The numerical results of the pressure drop are presented in blue, while for the correlation, it is shown in green (see Figure 2.20a). The solid line represents the melting case, and the dotted line represents the freezing case. Figure 2.20a shows that with an increase in Reynolds number, the pressure drop also increases. There is a small difference between the pressure drop during melting and freezing, which is most likely due to the variation in density with the inlet air temperature.

For low Reynolds numbers, the pressure drop from the numerical analysis and the pressure drop from the correlation are almost the same. However, as the Reynolds number increases, the pressure drop calculated from the numerical analysis starts diverging from that of the correlation (see Figure 2.20a). The possible reasons behind the difference in pressure drop determined from the numerical analysis and the correlation are the uncertainty in the correlation, the boundary conditions considered by the author to develop the correlation, and numerical errors.

The variation of the heat transfer coefficient is presented as a function of Reynolds number in Figure 2.20b. Once again, the solid line represents melting, and the dotted line represents freezing. The heat transfer coefficients determined using the Zukauskas and Churchill & Bernstein correlations differ from each other, which is evidence that each correlation has its limitations.

Interestingly, the heat transfer coefficients calculated from these correlations during melting and freezing overlap.

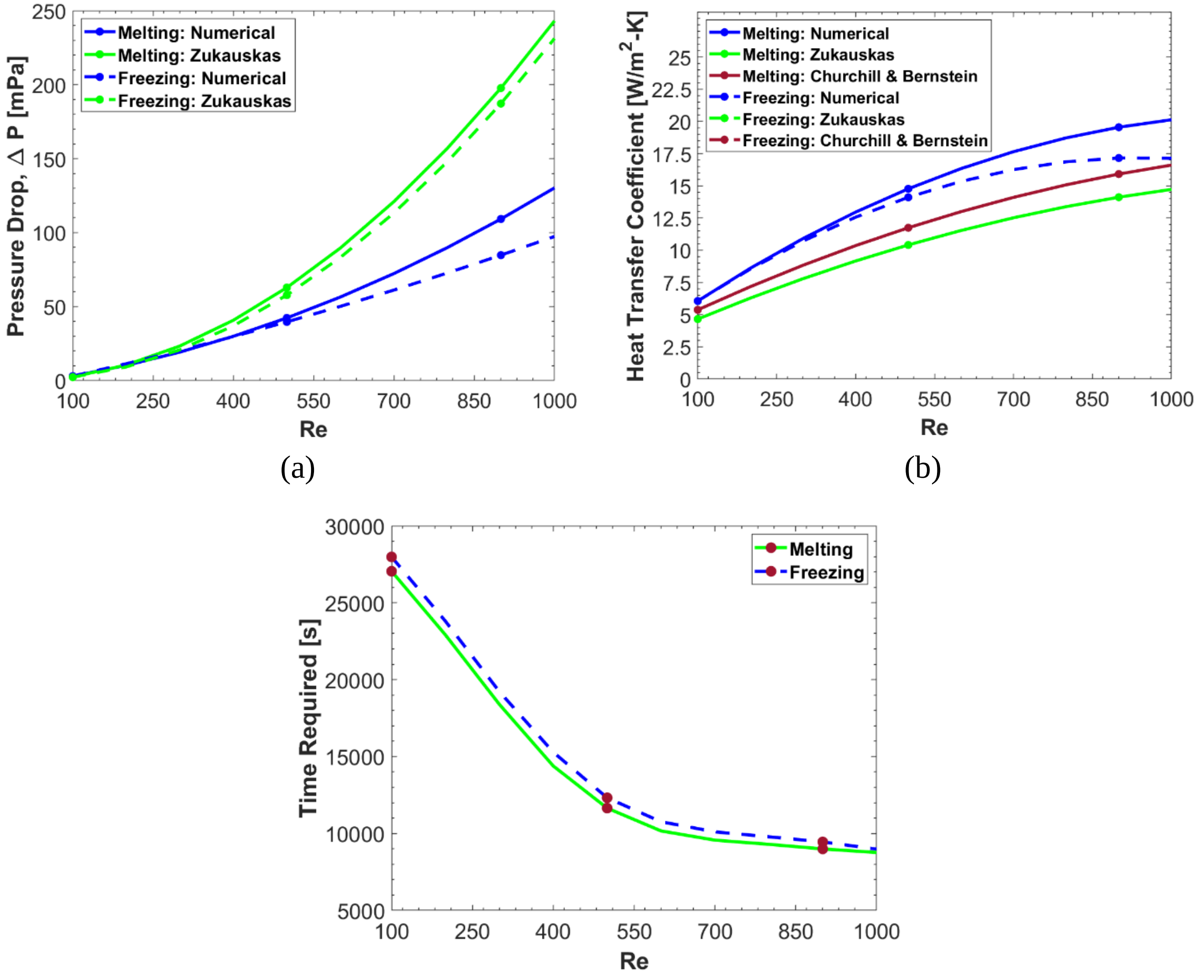

(a) (b)

(c)

Figure 2. 20. Melting and freezing performance parameters as a function of Re number: (a) pressure drop across the tube, (b) average heat transfer coefficient, (c) time required for PCM melting/ freezing

However, the heat transfer coefficient predicted from the numerical analysis of melting and freezing is initially the same for low Reynolds numbers and differs as the Reynolds number increases. Additionally, there is a difference between the numerically predicted heat transfer coefficient and the correlations, which is small for low Reynolds numbers and increases as the Reynolds number increases (see Figure 2.20b).

Figure 2.20c depicts the time required for complete PCM melting and freezing as a function of Reynolds number. The results show that it takes almost the same amount of time for the PCM to melt or freeze completely. As discussed earlier, a faster melting/freezing process occurs with an increase in Reynolds number. It takes around 9000, 12600, and 27000 s for the melting/freezing of PCM for Reynolds numbers 1000, 500, and 100, respectively.

2.8.4.2. Variation of the inlet air temperature

Numerical analysis of PCM melting and freezing processes was performed for different temperature driving forces, ΔT_{DF} (T_{in} - T_{PCM}): 10, 15, and 20 K (^{0}C), with a Reynolds number of 1000, using 1″ outer diameter of the tube. Figure 2.21 illustrates PCM melting parameters: average liquid fraction and average PCM temperature as functions of time for the variation in temperature driving force or inlet air temperature higher than the PCM phase change temperature. With an increase in inlet air temperature, faster melting occurs due to higher heat transfer rates between air and PCM. For example, a PCM-filled tube subjected to an inlet air temperature 20 K (^{0}C) higher than the phase change temperature melts earlier compared to the tube subjected to an inlet air temperature 10 K (^{0}C) higher. As mentioned earlier, there are three distinct phases during the PCM melting process, similar to other boundary conditions, which are not discussed again to avoid redundancy (see Figure 2.21b).

Similarly to the melting process, Figure 2.22 demonstrates PCM freezing parameters: the average liquid fraction and average PCM temperature over time, in response to variations in temperature driving force or inlet air temperature 10, 15, and 20 K (^{0}C) lower than the PCM phase change temperature. As the inlet air temperature decreases, solidification occurs more rapidly due to enhanced heat transfer rates between the air and PCM. For instance, a PCM-filled tube exposed to an inlet air temperature 20 K (^{0}C) lower than the PCM's phase change temperature solidifies sooner compared to one subjected to an inlet air temperature 10 K (^{o}C) lower. As previously mentioned, the PCM freezing process exhibits three distinct phases, akin to other boundary conditions, which are not readdressed to avoid redundancy (refer to Figure 2.22b).

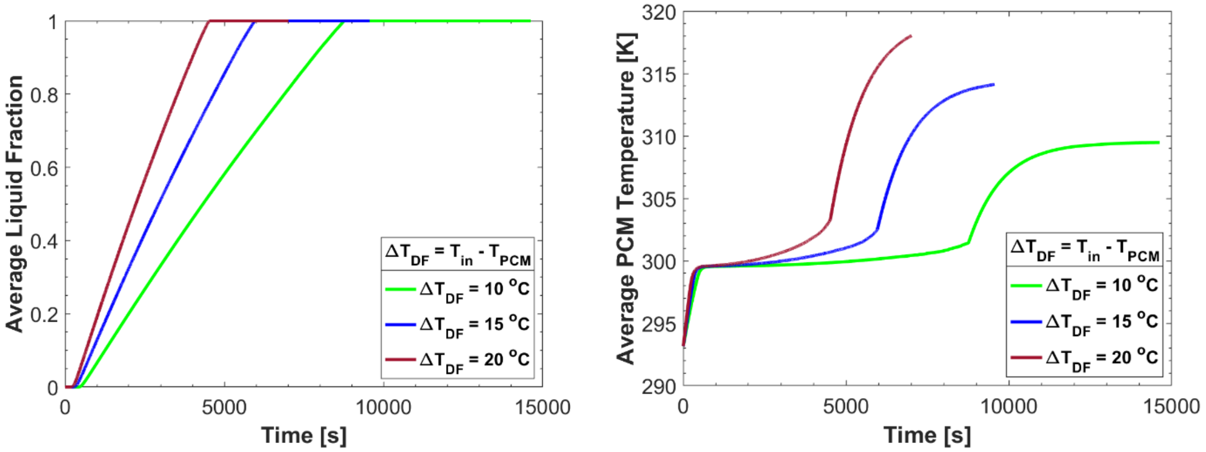

(a) (b)

Figure 2. 21. PCM melting parameters as a function of time for different temperature driving force, ΔT_{DF}: (a) average PCM liquid fraction, (b) average PCM temperature

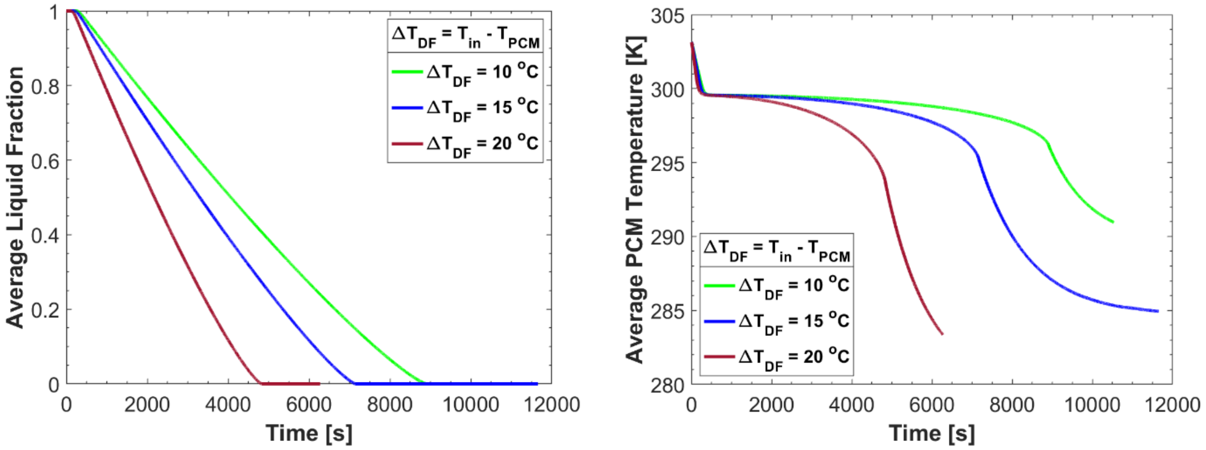

(a) (b)

Figure 2. 22. PCM freezing parameters as a function of time for different temperature driving force, ΔT_{DF}: (a) average PCM liquid fraction, (b) average PCM temperature

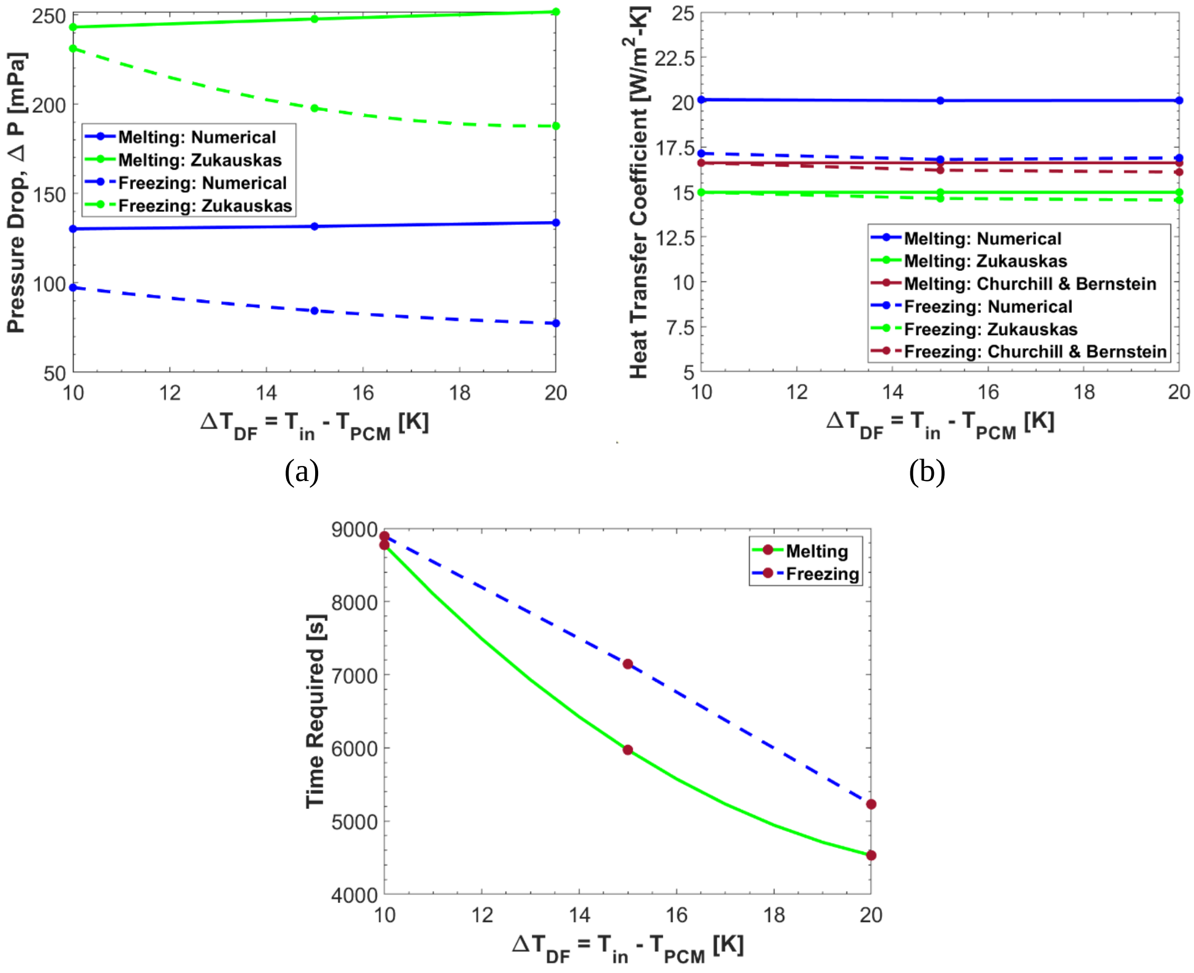

(a) (b)

(c)

Figure 2. 23. Melting and freezing performance parameters as a function of temperature driving force, ΔT_{DF}: (a) pressure drop across the tube, (b) average heat transfer coefficient, (c) time required for PCM melting/ freezing

Figure 2.23 depicts hydraulic and thermal performance parameters, including the pressure drop across the tube, average heat transfer coefficient, and melting/freezing time, as functions of temperature driving force under conjugate heat transfer boundary conditions. The numerical results of the pressure drop across the tube and average heat transfer coefficient were compared with those obtained from the experimental correlations provided by Zukauskas [82] and Churchill & Bernstein [84]. The numerical results are displayed in blue, while the correlation results are depicted in green (Zukauskas) and brown (Churchill & Bernstein). The solid line corresponds to the melting case, whereas the dotted line corresponds to the freezing case.

Figure 2.23a illustrates the pressure drop in relation to the temperature driving force during the melting/freezing process of PCM. As the temperature driving force increases, the pressure drop slightly rises during PCM melting. Conversely, during PCM freezing, the pressure drop decreases with the increase in temperature driving force. This variation in pressure drop is attributed to the change in the density of the incoming airflow with temperature. Figure 2.23b depicts that the heat transfer coefficient remains nearly constant and unaffected by changes in temperature driving force during PCM melting/freezing processes. Both pressure drop and heat transfer coefficient, as determined from the correlations, deviate from the results obtained through numerical analysis. It should be noted that these correlations entail uncertainties. Hence, the heat transfer coefficient calculated using the Churchill & Bernstein [84] correlation differs from that derived from the Zukauskas [82] correlation, albeit closely aligning with the numerical results for PCM freezing.

Figure 2.23c illustrates the time required for complete PCM melting and freezing in the tube as a function of temperature driving force. As mentioned earlier, with the increase in temperature driving force, the heat transfer rate between the PCM and air increases, resulting in faster melting and freezing. For temperature driving forces of 10, 15, and 20 K, it takes approximately 8700, 6000, and 4500 s, respectively, for PCM to completely melt. Similarly, it requires approximately 8800, 7000, and 5000 s, respectively, for PCM to entirely freeze under the same temperature driving forces.

2.8.4.3. Variation of outer diameter of the tube

Numerical analysis of PCM melting and freezing was conducted for different outer diameters of the tube (1″, 1.5″, and 2″) with a temperature driving force (ΔT_{DF}) of 10 K (ºC). Figures 2.24

and 2.25 illustrate PCM melting and freezing parameters, respectively: average liquid fraction and average PCM temperature as functions of time for the variation in outer diameter of the tube. Since the quantity of PCM increases with the increase in tube diameter, it requires more time for complete melting and freezing for a larger diameter tube. Similar to other cases, three distinct phases were observed during the melting and freezing processes of PCM.

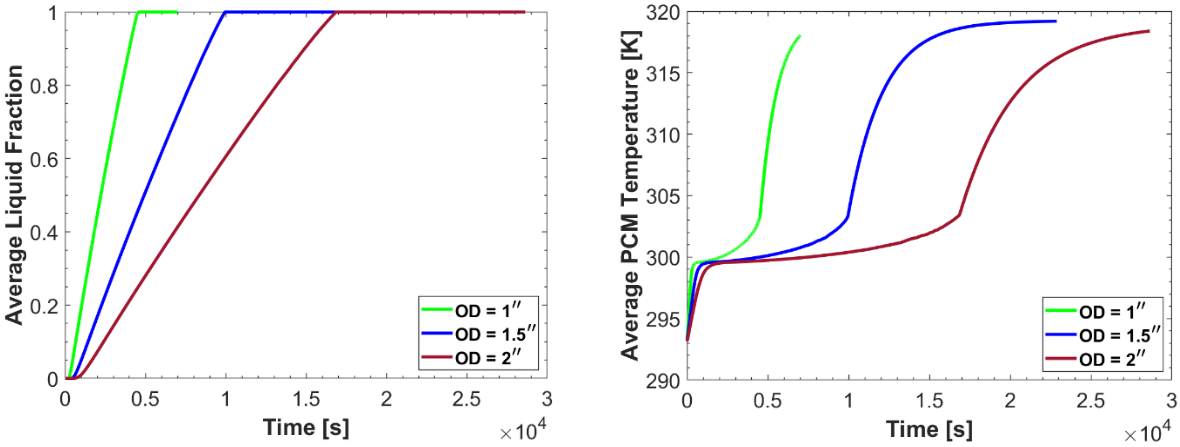

(a) (b)

Figure 2. 24. PCM melting parameters as a function of time for variation in outer diameter of the tube: (a) average PCM liquid fraction, (b) average PCM temperature

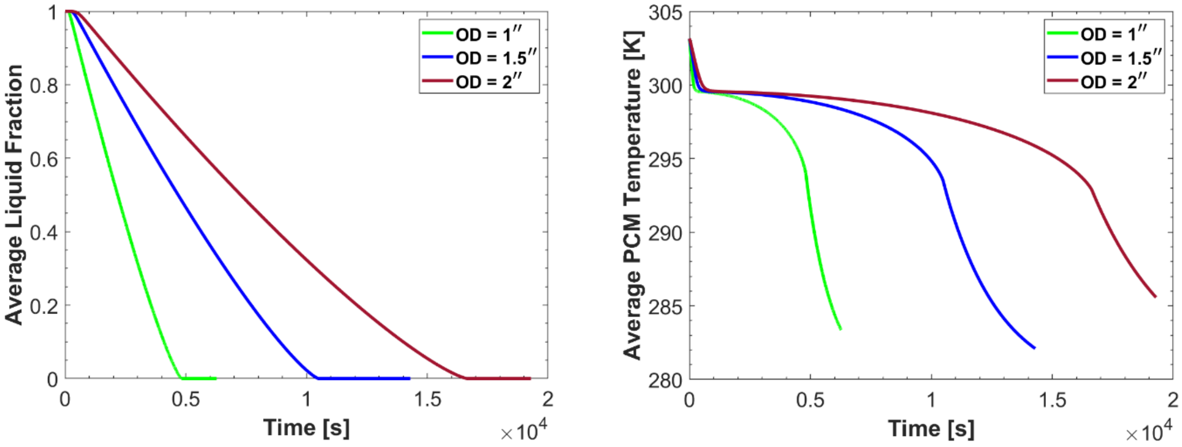

(a) (b)

Figure 2. 25. PCM freezing parameters as a function of time for variation in outer diameter of the tube: (a) average PCM liquid fraction, (b) average PCM temperature

Figure 2.26 illustrates the hydraulic and thermal performance parameters, which include the pressure drop across the tube, average heat transfer coefficient, and melting/freezing time, plotted against the outer diameter of the tube under conjugate heat transfer boundary conditions. Similar to previous cases, the numerical results for the pressure drop across the tube and average heat transfer coefficient were compared with those obtained from experimental correlations by Zukauskas [82] and Churchill & Bernstein [84]. Once again, the numerical results are represented in blue, while the correlation results are indicated in green (Zukauskas) and brown (Churchill & Bernstein). The solid line corresponds to the melting case, while the dotted line corresponds to the freezing case.

Figure 2.26a illustrates the pressure drop as a function of the outer diameter of the tube during the melting/freezing process of PCM. The pressure drop determined using the Zukauskas correlation [82] differs from the pressure drop obtained from numerical analysis and decreases with the increase in the outer diameter of the tube. Figure 2.26b shows the variation of the heat transfer coefficient as a function of the outer diameter of the tube. Again, as the tube diameter increases, the heat transfer coefficient decreases for both PCM melting and freezing. The heat transfer coefficients obtained from the correlations are lower than those of the numerically predicted results.

Figure 2.26c shows the time required for complete PCM melting and freezing in the tube as a function of the outer diameter of the tube. As previously mentioned, as the outer diameter of the tube increases, resulting in a greater quantity of PCM, both the melting and freezing processes take longer. During PCM melting, it takes approximately 4500, 10000, and 16800 s to complete the process for tube outer diameters of 1″, 1.5″, and 2″, respectively. Similarly, during PCM freezing, it requires approximately 5200, 10500, and 16600 s to complete the process for tube outer diameters of 1″, 1.5″, and 2″, respectively.

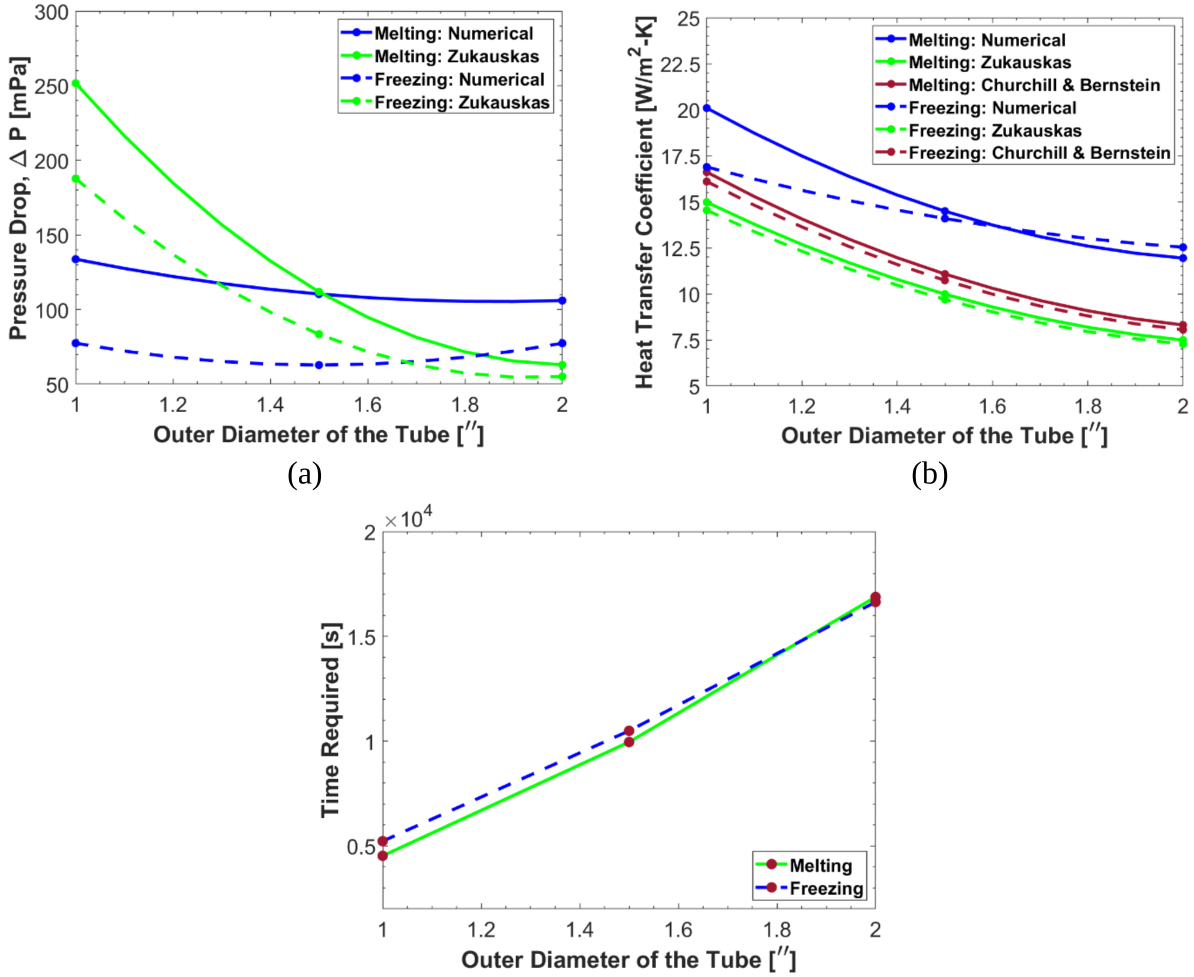

(a)

(b)

(c)

Figure 2. 26. Melting and freezing performance parameters as a function of outer diameter of the tube: (a) pressure drop across the tube, (b) average heat transfer coefficient, (c) time required for PCM melting/ freezing

2.9. Modeling of a single tube partially filled with PCM

A more thorough analysis was conducted by dividing the partially filled PCM tube into PCM and air zones, as depicted in Figure 2.27a using the Volume of Fluid (VOF) model. Each zone was discretized as illustrated in the figure. The VOF model utilizes the following expressions for the fluid volume fraction α:

$$\alpha_{PCM} + \alpha_{air} = 1 \tag{2.36}$$

The fluid volume fraction a in each cell varies between 0 (PCM only) to 1 (air only). Density is calculated from the following expression:

$$\rho = \rho_{PCM}\alpha_{PCM} + \rho_{air}\alpha_{air} \tag{2.37}$$

2.9.1. PCM melting process

A computational study was performed with a constant wall temperature (312 K) boundary condition on a tube partially (85%) filled with PCM, considering the actual latent heat of fusion (L_f), and compared with the literature by Assis et al [48]. A VOF model was used in the numerical model and paraffin wax was selected as PCM from the literature [48]. As shown in Figure 2.27b, there is an excellent agreement between the results published in reference [48] and those obtained in this study. There is virtually no difference between the results for the liquid fraction obtained from the 100% filled tube with a 15% lower L_f, the 85% filled tube with the actual L_f, and the numerical results from reference [48]. This comparison shows that the assumptions used in this study to simulate partially filled PCM tubes are realistic. However, experimental results obtained in reference [48] show that all numerical models considered in the analysis overpredict the liquid fraction. The authors of reference [48] attribute this difference to the assumption of high thermal conductivity of the tube wall (glass) in the numerical analysis, which results in faster melting of PCM and low heat losses at the wall. Reducing the thermal conductivity of the glass by approximately 30% results in excellent agreement between the predicted and measured values of the liquid fraction.

Further investigation was carried out to compare the results of the average PCM temperature obtained from the numerical analysis of a 100% PCM filled tube with a 15% lower L_f (in this case) with the temperature of the PCM-air mixture in the 85% PCM filled tube (see Figure 2.27c). As the results show, the agreement between these two cases is very good until approximately 90% of the PCM melts and the PCM volume fraction exceeds 93%. After approximately 28 min (1680 s), the predicted temperature in the 100% PCM filled tube with a 15% lower L_f is higher compared to the partially (85%) filled tube since the PCM liquid fraction is superheated. A very good agreement can be seen in the contour plot of the liquid fraction at 15 min (900 s), as shown in Figure 2.27d.

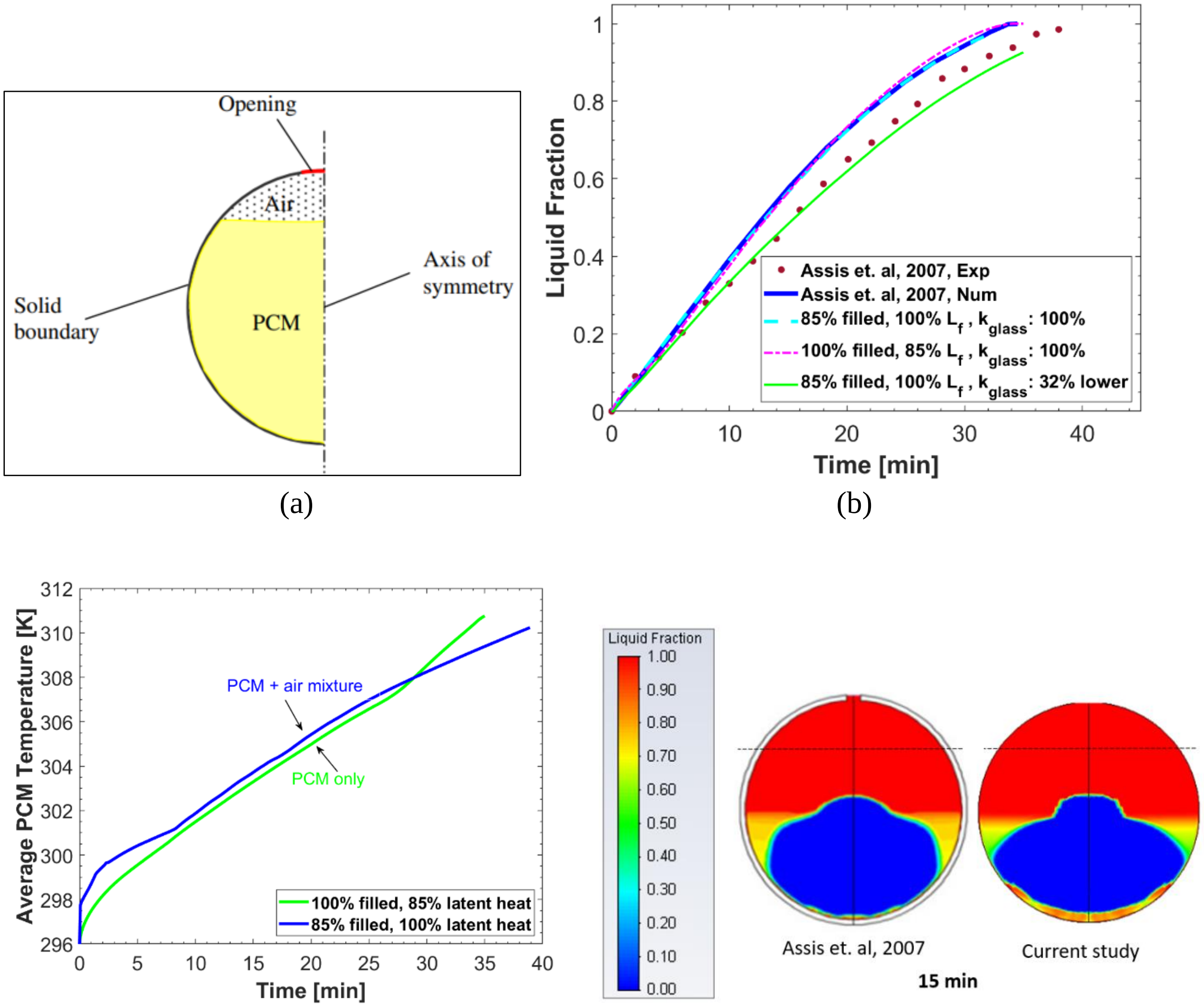

(a) (b)

(c) (d)

Figure 2. 27. (a) Computational domain from the reference [48] for the partially filled tube, (b) Model validation using the liquid fraction (c) Average PCM temperature, (d) Comparison of the liquid fraction contours of partially filled tube with the reference [48]

The contours predicting the liquid/solid fractions in a partially filled PCM tube and their corresponding variation of PCM density within the domain are shown in Figure 2.28, illustrating their evolution over time during the PCM melting process. In the case of the tube partially filled with PCM (85% in this instance), the PCM at the center of the tube remains solid for approximately 20 minutes (1200 seconds) after the simulation begins. With longer durations, the center transitions into a liquid phase, leading to liquid PCM experiencing superheating, as illustrated in Figure 2.27c. The density contours reveal an increase in PCM volume throughout the melting process. Consequently, in the investigated scenario, some air exits the tube through the opening section to accommodate the expanded volume of melted PCM.

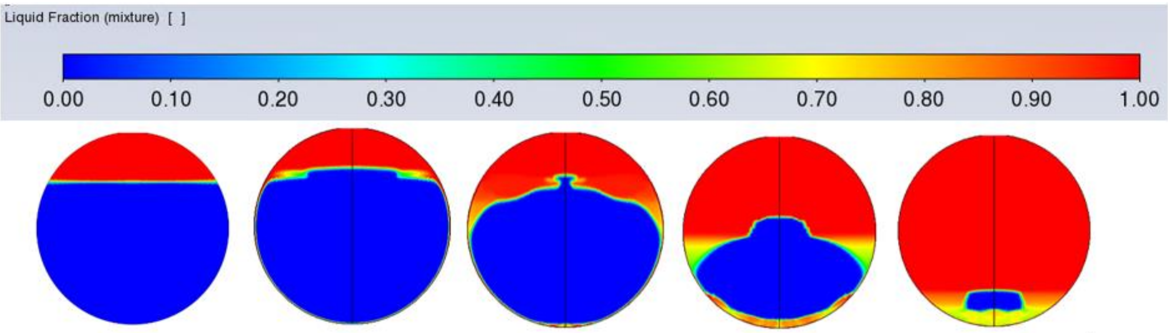

0 min, $\gamma = 1$ 1 min, $\gamma = 0.04$ 5 min, $\gamma = 0.2$ 15 min, $\gamma = 0.56$ 30 min, $\gamma = 0.97$

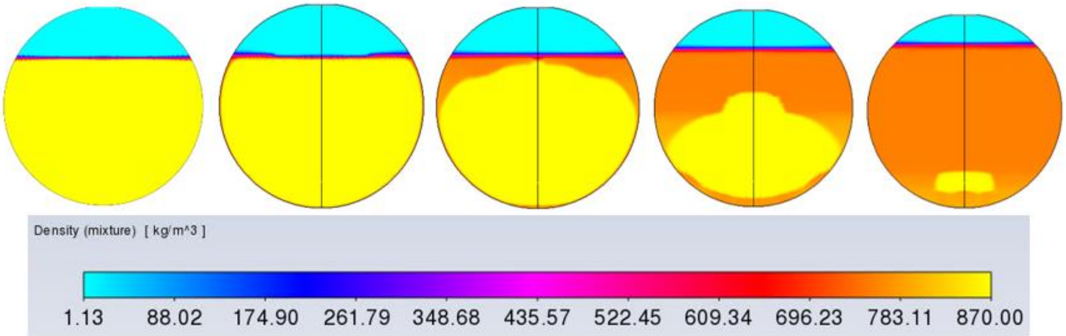

Figure 2. 28. Predicted contours of liquid/solid fractions and density in a partially (85%) filled PCM tube during PCM melting (current study)

2.9.2. PCM freezing process

Numerical analysis was performed for the PCM solidification process using a tube partially filled (98.5%) with PCM and validated with the literature by Assis et al. [49]. The same computational procedure was followed for the PCM melting process for a partially filled tube. Paraffin wax was used as the PCM, and a constant wall temperature (293 K) with a driving force 10 K lower than the PCM phase change temperature was used for the numerical analysis. Figure 2.29a shows excellent agreement between the numerical results of average liquid fraction obtained from the current study and the literature [49]. Figure 2.29b details the thermal stratification of PCM temperature within the tube. The local temperature in each location of the PCM inside the domain is different. Near the tube wall, PCM solidifies earlier compared to the center of the tube. As the PCM starts freezing, temperature keeps dropping till it reaches the temperature of the tube wall which takes longer than 1000 s. The average PCM temperature is presented with the black dotted line, which is completely different from the local temperature of each location.

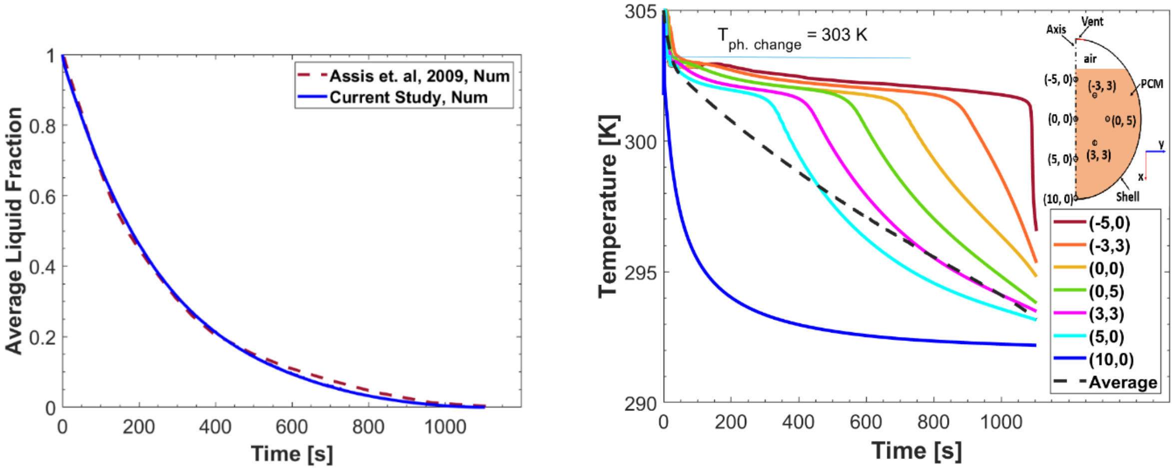

(a) (b)

Figure 2. 29. PCM freezing parameters as a function of time for partially filled tube: (a) Average liquid fraction, (b) Thermal stratification due to the variation of local PCM temperature

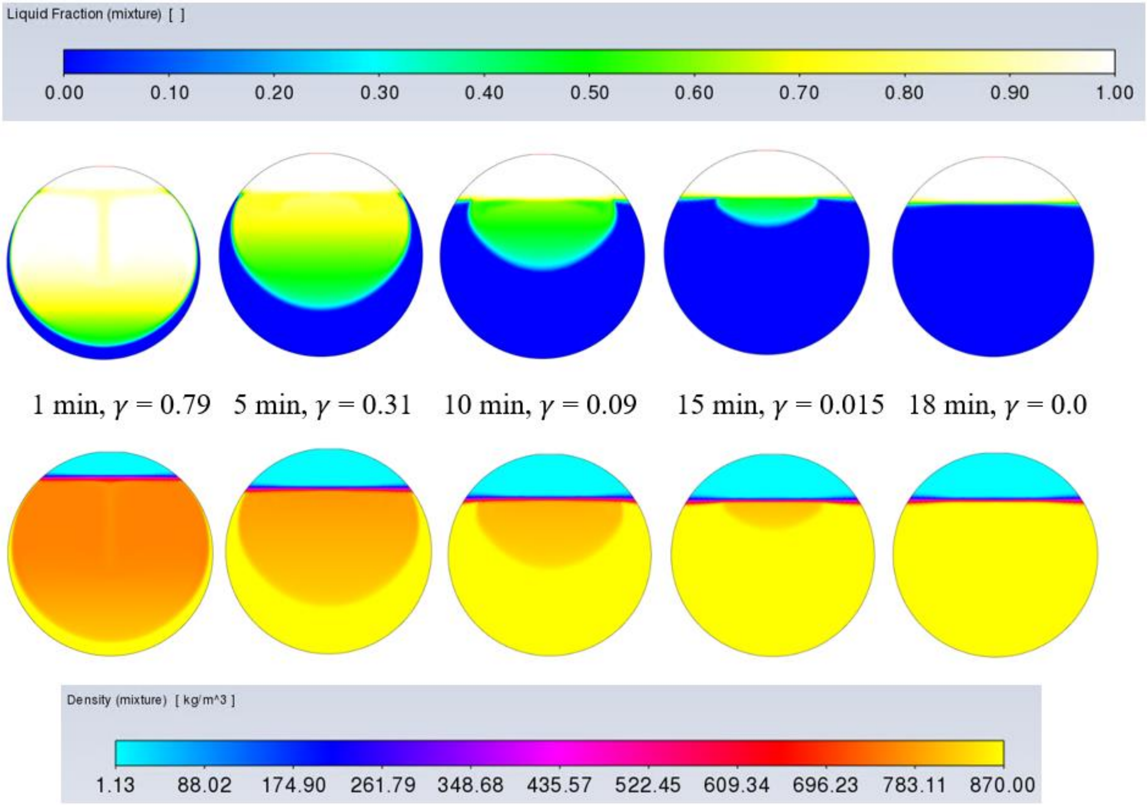

Figure 2. 30. Predicted contours of liquid/solid fractions and density in a partially (85%) filled PCM tube during PCM melting (current study)

The contours depicting liquid/solid fractions and the corresponding variation in density of the PCM or PCM-air mixture, in the initially partially filled PCM tube (98.5% filled in this instance), are illustrated in Figure 2.30 as they evolve over time during the PCM freezing process. The upper section of the tube is occupied by air, while freezing of the PCM begins at the bottom side of the tube, progressing inward from the tube wall towards the center. The center of the PCM zone remains in the liquid phase for approximately 10 min (600 s) after the simulation commences. Complete freezing of all PCM within the PCM zone occurs in approximately 18 min (1080 s). The density contours of the PCM-air mixture indicate a decrease in PCM volume during the freezing process, as the density of solid PCM is lower than that of liquid PCM.

2.10. Comparison of the numerical and experimental results

Tests were conducted to compare the numerical and experimental results of PCM temperatures and air temperature at the outlet of the test section across the tube. PCM melting tests were conducted using an inlet air velocity of 0.32 m/s with an incoming air temperature of 305 K (32°C). PCM freezing tests were conducted using an inlet air velocity of 0.25 m/s with an incoming air temperature of 291 K (18 °C). Transient behavior of the inlet air temperature due to the electric heater was incorporated into the numerical model using a user-defined function (UDF). All other numerical setups are the same as the conjugate heat transfer approaches. Lab-grade PCM was used for this test.

2.10.1. Experimental setup/ test facility

The test facility and other experimental setups are detailed in Chapter 4 for the lab-scale tube array. The same test facility was utilized for the single tube test. No further details are included in this section to avoid redundancy.

2.10.2. Comparison of the results

Numerical predictions were obtained by simulating partially (80%) filled PCM tubes. The simulation was performed using the latent heat of fusion (L_f), which was 20% lower compared to the actual L_f value of 170 kJ/kg, and assuming a 100% PCM filled tube. This simplification provides realistic results for the tube partially filled with PCM, with a relatively small difference between the predicted air outlet temperature, as shown in Figure 2.31a.

Figure 2.31b illustrates a comparison of the PCM temperature measured approximately in the center of the tube with the numerical prediction of PCM temperature in the center of the tube. Since a tube with partially filled (80%) PCM is used for the experiment, the air above the PCM increases the temperature of the PCM. Hence, there is no region of constant temperature during the phase change of PCM in the experiment; rather, a gradual increase in temperature is observed. However, the numerical analysis of a 100% filled tube with a 20% lower latent heat compared to the actual value shows a constant temperature for around 9000 s during the phase change of PCM since there is no effect of air on the PCM temperature. In the numerical analysis, three distinct phases of PCM temperature are observed: firstly, a rapid increase in temperature from the initial value (291 K), followed by a gradual increase, and finally, superheating until it reaches the inlet air temperature of 305 K.

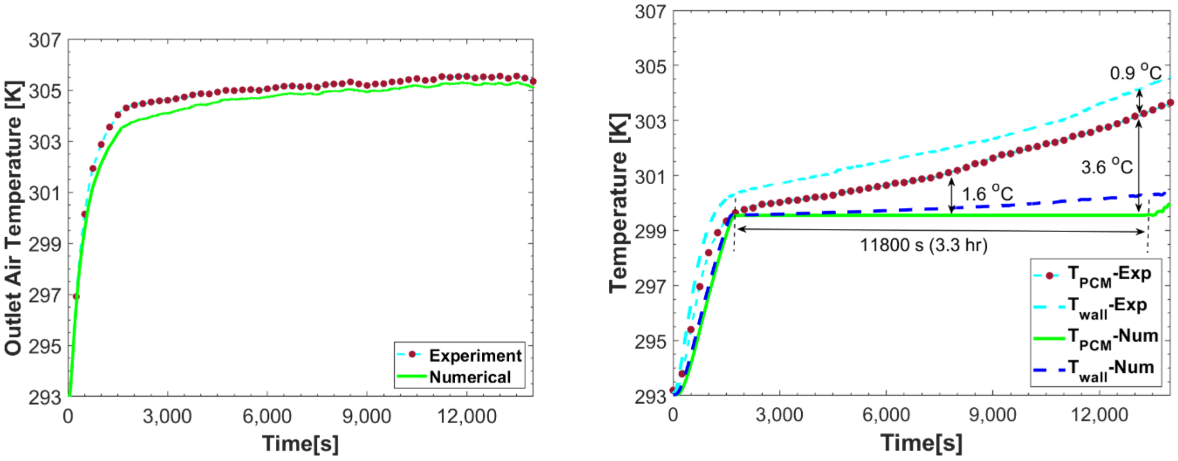

(a) (b)

Figure 2. 31. Comparison of the numerical and experimental results as a function of time during PCM melting process: (a) outlet air temperature, (b) PCM temperature

The difference between the PCM temperatures from the measurement and numerical prediction increases when the PCM is superheated. The maximum PCM temperature difference between the measurement and numerical prediction is 3.6 K or °C. Tube wall temperatures from the experiment and numerical prediction have been imposed in the same graph for a better understanding of the temperature difference between the numerical prediction and measurement. The tube wall temperature is slightly higher than the PCM temperature (see Figure 2.31b). Therefore, the effect of wall is less significant in contributing to the disparity between the experimental and numerical results of PCM temperature. The possible reasons behind this discrepancy are discussed later in this section.

Similar to the PCM melting process, numerical analysis was performed for the PCM freezing test simulating a partially filled tube considering a lower latent heat of fusion (L_f). As illustrated in Figure 2.32a, an excellent agreement was obtained between the predicted and experimental results of the outlet air temperature, with a relatively small difference.

Figure 2.32b presents a comparison between the measured and numerically predicted values of PCM temperature. The measured temperature indicates supercooling, which the numerical model fails to predict. Despite the addition of suppression additives, PCM supercooling still occurs. The maximum difference in PCM temperature between the measurement and numerical prediction is 8.3 K or °C. The PCM freezing process, akin to PCM melting, exhibited three distinct phases in the numerical predictions: initially, the superheated liquid PCM at 305 K or 32 ºC rapidly cools until the PCM temperature reaches the phase change temperature (299.55 K or 26.4 ºC), and ultimately, it reaches the temperature of the cooling air (291 K or 18 °C) at the inlet.

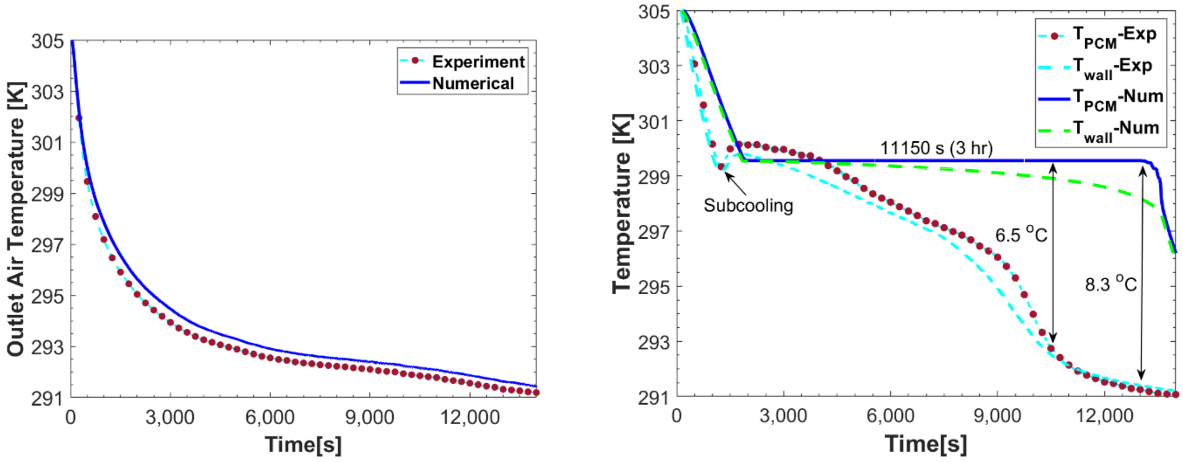

(a) (b)

Figure 2. 32 Comparison of the numerical and experimental results as a function of time during PCM freezing process: (a) outlet air temperature, (b) PCM temperature

It should be noted that the PCM temperature was measured using thermocouples ideally positioned at the center of the tube, while the numerical analysis provides the average temperature of the PCM in the tube. The misplacement of the thermocouple may result in a disparity between the measured and predicted PCM temperature, as the local temperature differs at each location, as presented earlier in Figure 2.29b.

Additionally, no heat loss from the wall was assumed for the computational analysis, while heat loss from the wall occurred during the experiment. However, the effect of heat loss from the wall is less significant with a larger storage capacity. Hence, heat loss from the wall should no longer be responsible for the discrepancy between the measured and predicted PCM temperature (Figures 2.31b and 2.32b).

The velocity measurement accuracy in the experiment was ± 4%. A comprehensive analysis of the average heat transfer coefficient (h_{avg}) was conducted, considering the uncertainty of velocity measurements, as presented in Table 2.10. The Zukauskas correlation (Zu) [83] for the Nusselt number was used for this analysis. It is worth noting that the correlation carries a 15% uncertainty [83].

The uncertainty in h_{avg}, considering the velocity measurement accuracy, is significantly low at around 2.4% during the PCM melting and freezing test (see Table 2.10). This indicates that neither h_{avg} nor velocity measurements are responsible for the discrepancy between the experiment and numerical results of PCM temperature, as shown in Figures 2.31b and 2.32b. However, there is a difference of around 18-30% between the numerical prediction of h_{avg} and the h_{avg} calculated using the correlation, possibly due to the 15% uncertainty associated with the correlation [83].

Table 2. 10 Calculation of the uncertainty in coefficient of heat transfer (h_{avg})

Cases	v_∞ (m/s)	h_{avg} (W/m^2-K)		
		Num	Zu [83] Correlation	% Difference
Melting	0.32	13.18	11.11	18.67
Solidification	0.25	13.18	9.93	32.76
Uncertainty (%)			2.4	

Another potential factor contributing to the discrepancy could be the accuracy of the thermocouples, as they were not calibrated during the measurements. A J-type thermocouple, with an accuracy of ± 2.2 °C, was used during the experiment. If the uncertainty from the thermocouple could be eliminated during the measurement by using a thermocouple with higher accuracy, the maximum discrepancy between the experiment and numerical prediction of PCM temperature (Figures 2.31b and 3.32b) would be around 1 °C at most, particularly when the PCM starts superheating/supercooling due to the hot/cold air above the PCM in the experiment, where a partially filled tube was used. Furthermore, numerical assumptions used to calculate density using the Boussinesq approximation, mushy zone constant, and constant values of thermal conductivity and specific heat may introduce some numerical error.

CHAPTER 3/ ARTICLE 1

Energy and exergy analysis of a laboratory-scale latent heat thermal energy storage (LTES) using salt-hydrate in a staggered tube arrangement

Mahfuja A. Khuda[1*], Lida Yan[2], Javad Khalesi[1], Nenad Sarunac[1],
Carlos Romero[2]

[1] Mechanical Engineering and Engineering Science, UNC Charlotte, Charlotte, NC 28223, USA. m12a34k5@charlotte.edu

[2] Energy Research Center, Lehigh University, Bethlehem, PA 18015, USA.

* Correspondence author

Highlights

- Numerical analysis of latent heat thermal energy storage system using PCM filled tubes was performed.
- PCM melting and solidification model was compared with the experiment.
- Energy and exergy analyses of the system were performed.

Abstract

The energy and exergy analyses were performed for a laboratory-scale latent heat thermal energy storage (LTES) using hexahydrate calcium chloride (CC6) as phase change material (PCM) in a staggered tube array configuration, placed horizontally. The PCM melting and solidification process within the tube array was investigated by performing a numerical analysis using transient two-dimensional Navier-Stokes equations and Realizable k-ε turbulence model to predict flow and heat transfer. The enthalpy-porosity technique was applied to model PCM melting and solidification. The accuracy of the numerical model was validated against experimentally obtained data where the numerically predicted and measured air temperature at the tube array outlet and PCM temperatures were compared. Additionally, the pressure drop in the array and the average peripheral heat transfer coefficient calculated from the numerical results were compared to the well-known Zukauskas correlation (Zu). The results show that the melting and solidification process of PCM in the tubes of the array is asymmetric in nature, with the PCM melting taking

slightly longer compared to the solidification process. It was also observed that the energy quantity was higher compared to the exergy quantity, as exergy considers entropy generation and accounts for irreversibility within the system.

Keywords: Melting, Solidification, Tube array, CFD, Turbulent flow, Conjugate heat transfer

3.1. Introduction

Thermal energy storage (TES) utilizing the latent heat of phase change materials (PCM) has garnered significant attention from researchers due to its numerous advantages, such as high energy storage density, nearly isothermal heat recovery, and chemical stability. The latent heat TES has become an essential component of HVAC systems and various applications due to increasing environmental concerns, energy demands, and the disparity between energy needs and supply [86]. It achieves energy savings by reducing thermal losses and improving the recovery efficiency of stored thermal energy. Additionally, TES enables the implementation of other conservation measures and enhances the performance of thermal systems by reducing energy supply and demand mismatches.

Thermal energy storage (TES) systems can be categorized into sensible heat storage [87, 88], latent heat storage [89, 90], and thermochemical energy storage systems [91, 92] . Sensible heat storage systems utilize heat directly, but their low energy density requires more space. Thermochemical storage offers higher energy density and storage duration, but its commercial application is limited due to the high temperatures, slow reactions, and costs involved [3]. On the other hand, latent heat storage using phase change materials (PCMs) provides high density energy storage through the phase change occurring at a specific temperature [4]. PCMs offer the advantage of tailoring temperature transitions, storage duration, and cycle consistency, making them a superior solution for low-temperature energy storage in industrial and commercial buildings [12].

While various configurations are employed for latent heat thermal energy storage (LTES), the shell and tube configuration has gained popularity due to its minimal heat loss and efficient cylindrical geometries [13, 14].

Two approaches are commonly used to evaluate the performance of latent heat storage units (LHSUs): energy analysis and exergy analysis. Energy analysis alone may not fully reveal thermal storage behavior, as it does not account for internal irreversibility [93]. Exergy analysis, on the other hand, quantifies the entropy generated, providing insight into the capability of LTES to store and discharge energy which allows designers to explore various design alternatives and identify performance trends, ultimately facilitating system enhancements and optimization. In other words, , exergy analysis assesses the entropy generated, which has led previous studies [86, 94-96] to report that exergy efficiency is lower compared to energy efficiency. Erek and Dincer [86] introduced a new approach to evaluate the energy and exergy analysis of a shell and tube type LTES for the charging (melting) process. Guelpa et al. [94] conducted a computational analysis to explore design enhancements for a shell-and-tube LTES system, considering entropy generation. Sari and Kaygusuz [95] performed an experimental study of semi-stratified energy storage to compute energy and exergy analyses of the system. Rezaei et al. [96] explored the energy, exergy, and economic analyses of various PCMs for solar heater applications. They found that the consideration of exergy concepts is crucial in system designs and policy making for achieving a more optimal design.

Numerous experiments and numerical analyses are described in the literature [5, 24, 97, 98]. Kalapala and Devanuri [5] conducted experiments to investigate the energy and exergy analysis for a shell and tube LTES with various orientations. The orientation of the LTES was found to have a significant influence on the natural convection phenomenon, which affects the melting behavior of PCM. Chen et. al [24] performed experiment and simulations to improve the performance of the LTES system by exploring various shapes of inner tubes including horizontal and vertical ellipse as well as triplex tube. Soni et. al [98] performed experimental and numerical investigation of solidification behavior of PCM using particle image velocimetry technique. They also computed energy discharge rate from the system. Rahdar et. al [99] conducted a comparative analysis of PCM and ice thermal energy storage for air conditioning systems in commercial building considering exergy efficiency and total cost rate of the systems.

The selection of the phase change material (PCM) is crucial in a latent heat TES system, as it significantly impacts the heat transfer mechanisms within the PCM [20] and operating temperature range. Some technically important PCMs include Glauber's salt, calcium chloride hexahydrate/ salt hydrate, sodium thiosulfate pentahydrate, sodium carbonate decahydrate, fatty acids, and paraffin waxes, which have been documented by Zalba et al. [21]. PCMs, in general, are advantageous for TES systems as they increase storage capacity and thus enhance the security of energy supply. Application of PCMs can be found in various areas, including solar collectors, greenhouses, and heating buildings [100-102]. Mahfuz et al. [103] conducted an experimental study to compute the energy and exergy, along with cost analyses of a shell-and-tube LTES system utilizing paraffin wax for solar water heating applications. Öztürk [104] evaluated experimentally the energy and exergy efficiency of LTES systems using paraffin wax for greenhouse heating applications. Koca et. al [22] used salt hydrate ($CaCl2 . 6H2O$) as PCM to perform energy and exergy analysis of LTES for a flat-plate solar collector. Pagkalos et al. [105] conducted numerical analysis using two different PCMs, water, and paraffin, to evaluate a better heat storage medium. Ghalambaz and Zhang [23] performed numerical analysis to evaluate the effect of transient heat flux pulse on heat sink filled with metal (Nickel) foam and PCM (paraffin wax).

Limited research has been conducted on the energy and exergy analyses of PCM-filled tube arrays. The main objective of this current study is to design a lab-scale LTES system with the vision of constructing a full-scale module in the future to reduce the temperature of incoming air for the Air Cooled Condenser (ACC). The smaller lab-scale module aims to providing insights into how LTES improves cooling effects of ACC. Therefore, a numerical study with a 4-row PCM-filled tube array was performed to guide the procedure for building the module. Flow conditions within the tube bank are significantly influenced by boundary layer separation effects and wake interactions, impacting the convection heat transfer within the PCM-filled tubes. To enhance heat transfer, a staggered arrangement of tube rows in a horizontal orientation was adopted in the direction of the flow, promoting a more tortuous flow. Numerical analysis of the PCM melting and solidification (freezing) process within the tube bank was conducted using ANSYS Fluent. Following the design obtained from numerical analysis, a smaller-scale module was built for experimentation. The numerical results were then compared against the experimental data. Energy and exergy analyses on the laboratory-scale (4-row) tube array were carried out to determine efficiency of the system. An uncertainty analysis was conducted to identify the reason for the discrepancy between the experimental and numerical results following the literature [39].

The article is structured as follows: Section 3.2.2 presents the computational approach used for simulating PCM melting and solidification processes in a 4-row tube array. In Section 3.3.1, validation of the numerical model for both the melting and solidification processes is explained. Section 3.3.2 provides a comprehensive overview of the various parameters involved in PCM melting and solidification. Section 3.3.3 investigates the energy and exergy analysis of the PCM-filled tube array, specifically focusing on the PCM melting and solidification processes. Lastly, Section 3.3.4 provides insight into possible reasons for the discrepancy between numerical and experimental results by conducting thermal loss analysis at the duct wall and uncertainty analysis during the measurements.

3.2. System description

3.2.1. Physical model

In the current study, performance of PCM melting and solidification within horizontal circular tubes in a staggered arrangement was analyzed. The tube array included thirty six 0.75" outer diameter (OD) tubes made of 304 stainless steel [106]. The tube thickness and length are 0.035" and 11", respectively. The tubes were partially (80% by volume) filled with PCM to allow volume expansion of PCM within the tubes. A schematic presentation of the physical model of a 4-row tube array is presented in Figure 3.1. The transverse tube spacing (S_T) of 1.2" and lateral (row) spacing (S_L) of 1.03", giving $S_T/D = 1.6$ and $S_L/D = 1.37$ were used. The tube-to-tube spacing (S) is 0.45". Partial tube fill was used to allow for the volume expansion of PCM during the phase change. The large tube spacing was used to allow the same tube array geometry to be used in other configurations investigated in the project.

Since the purpose of the project is to explore effective latent heat thermal energy storage (LTES) for residential and commercial applications, hexahydrate calcium chloride (CC6) was selected as the heat storage medium due to its low cost, stability, and melting/ solidification point at room temperature. A composite phase change material was prepared in the lab at Lehigh University using 95% $CaCl_2 \cdot 6H_2O$, 2% KCl, 3% $SrCl_2 \cdot 6H_2O$ to get a phase change temperature of 26.4 °C (299.55 K). A drop calorimeter was designed and constructed to measure the specific heat, latent heat of fusion and phase change temperature of PCM. A viscometer was used to measure the viscosity of the liquid PCM. Table 3.1 summarizes thermophysical properties of PCM used in the analysis.

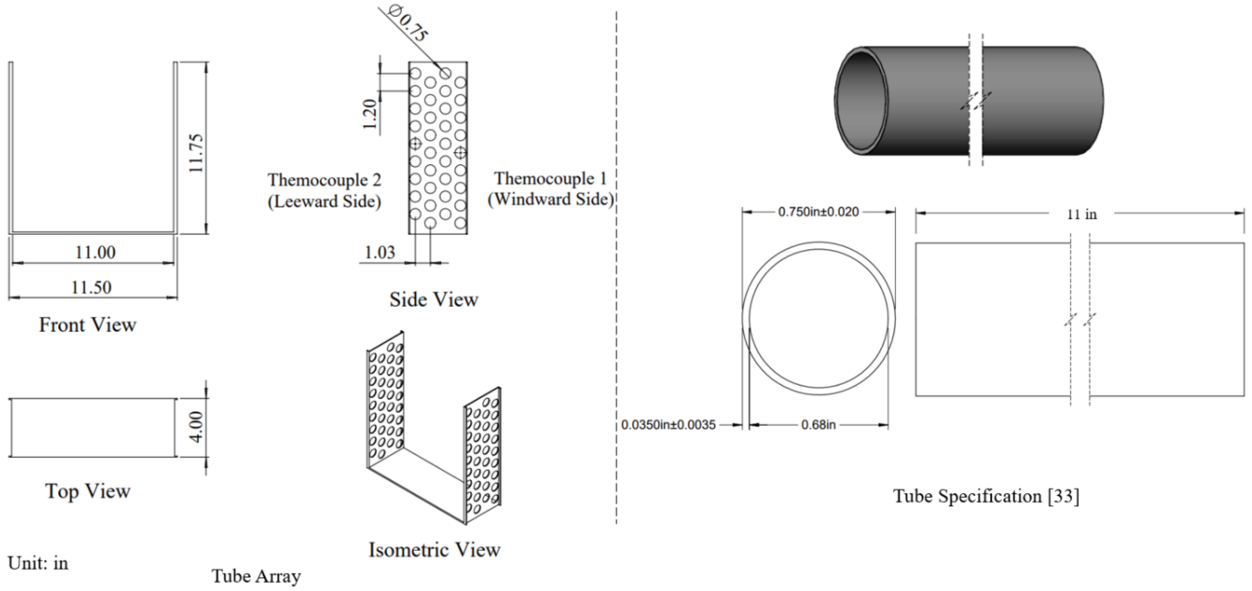

Figure 3. 1. Design of the laboratory scale (4-row) tube array in a staggered configuration

Table 3. 1 Thermophysical properties of PCM (CC6)

Property	Value
Melting/ solidification point [°C]	26.4
Density, ρ (solid/liquid) [kg/m^3]	1706/ 1538
Specific heat, C_p (solid/liquid) [J/kg.K]	2360/ 1560
Thermal conductivity, k (solid/liquid) [W/m.K]	1.09/ 0.546
Latent heat, L_f [kJ/kg]	170
Dynamic viscosity [mPa-s]	11.94
Thermal expansion coefficient [K^{-1}]	0.0005

The boundary conditions (B.C.s) used for the melting and solidifying study are presented in Table 3.2. The inlet air temperature was chosen, considering the impact of ambient conditions: specifically, daily air temperature, pressure, and humidity variations at several selected geographic locations, namely, Dallas, TX, Austin, TX, and Phoenix, AZ - on the performance of the ACC. Therefore, the temperature difference between the inlet air and the phase change temperature of the PCM is approximately 10 °C.

The solidification process took place during nighttime when the ambient temperature was sufficiently low, resulting in denser air. Additionally, the velocity for PCM solidification was deliberately kept lower than that for the melting process to prolong the freezing time. This led to a lower Reynolds number for the solidification process compared to the melting process.

Table 3. 2 Boundary conditions

B.C.s	Melting	Solidification
Velocity inlet, v_∞ (m/s)	1.10	0.79
Turbulence intensity at inlet (%)	5	5
Inlet air temperature, T_{in} (°C)	35	15
Pressure outlet (atm)	1	1
Mass flow rate, $\dot{m}$ (kg/s)	0.12	0.09
Re_D	1,285	985

Thermophysical properties of stainless steel used for the tubes were taken from the literature [40], density (ρ_s), specific heat (c_{P_s}) and thermal conductivity (k_s) as 8,000 kg/m^3, 500 J/kg-K and 21.5 W/m-K, respectively.

3.2.2. Computational procedure

A 2-D computational domain was chosen for the numerical analysis, given that the measurements are predominantly 1-D and the impact of oblique flow is negligible. Figure 3.2 represents a schematic presentation of a 2-D computational domain used for numerical analysis. The staggered tube arrangement was employed for the computation. Tubes in the array were labeled as PCM1 to PCM6 as shown in the figure. To avoid the effect of inlet and outlet boundaries on the numerical analysis and the results, the computational domain having the length of two times the tube diameter upstream of the tube bank and ten times the tube diameter downstream of the tube bank was used. The length of the upstream and downstream domains was sufficient to avoid the effect of entrance effects at the inlet and wake at the outlet. Symmetry B.C. was employed at the top and bottom of the computational domain.

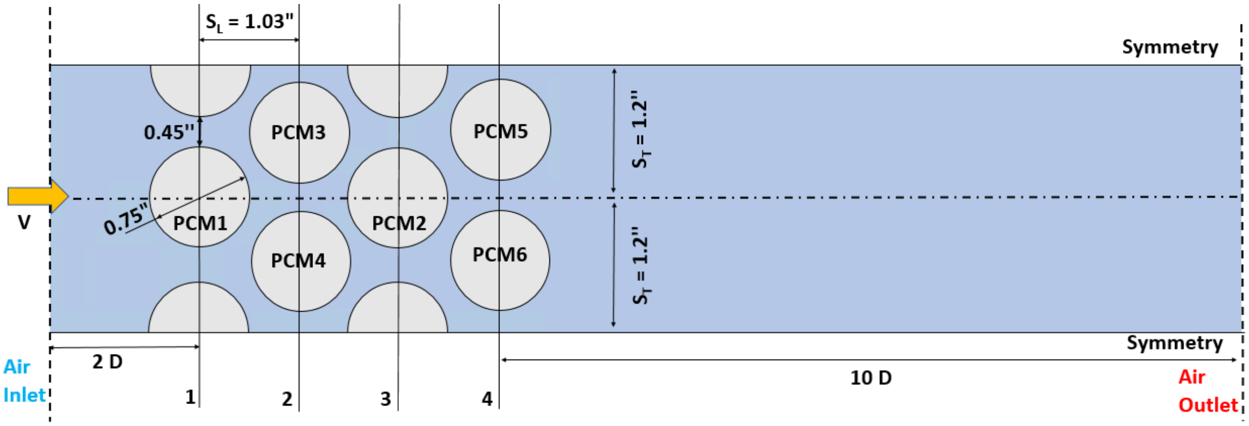

Figure 3. 2. A 2D computational domain for the tube bank

ANSYS Fluent 20.0 [81] was used to solve the governing Navier-Stokes equations for conservation of mass, momentum, and energy. The SIMPLE algorithm and the Implicit method were selected for coupling pressure and velocity in the computational approach. The second order upwind discretization scheme was used for both momentum and energy equations for higher accuracy. PRESTO! (PREssure STaggering Option) scheme was employed for the discretization of momentum equations since it gives more accurate results for the cases e.g., natural convection, porous media etc. by avoiding interpolation errors and pressure gradient assumptions on the boundaries. The value of 10^{-6} was specified as the convergence criterion for the RMS residuals for continuity, momentum, and energy equations. A transient model was employed to predict the melting and solidification process of the PCM as functions of time. In this study, a time step size of 0.5 s was used. Due to the selection of an Implicit time scheme, the numerical results are independent of the time step size. However, selection of time step size of 0.5 s reduces the computational cost by approximately 56% compared to a time step size of 0.1 s. The simulation of 1.7 physical hours (6000 s) of PCM melting/solidification in a lab-scale tube array required over two days (48 hours) of computational time on an HP Precision 5820 workstation equipped with 12 cores, 3.7/4.7 GHz, and 64 GB ECC memory.

The continuity, momentum, and energy conservation equations for the 2D PCM domain, shown in gray in Figure 3.2, are given by Eqns. (3.1)-(3.3) using the summation convention for repeated indexes:

$$\frac{\partial \rho}{\partial t} + \frac{\partial \rho u_i}{\partial x_i} = 0 \tag{3.1}$$

$$\frac{\partial(\rho u_i)}{\partial t} + \frac{\partial(\rho u_j u_i)}{\partial x_j} = \mu \frac{\partial^2 u_i}{\partial x_j \partial x_j} - \frac{\partial p}{\partial x_i} + \rho g_i + S_i \tag{3.2}$$

$$\frac{\partial(\rho h)}{\partial t} + \frac{\partial(\rho h_{latent})}{\partial t} + \frac{\partial(\rho u_i h)}{\partial x_i} = \frac{\partial}{\partial x_i}\left(k \frac{\partial T}{\partial x_i}\right) \tag{3.3}$$

where ρ represents density, u is the transverse velocity of the liquid PCM induced by density differences, μ is viscosity, p denotes pressure, g is gravitational acceleration, and ρg_i accounts for the buoyancy force resulting from density variation. The quantity h in the energy equation is the sensible enthalpy, defined as:

$$h = h_{ref} + \int_{T_{ref}}^{T} C_p\,(T)dT \tag{3.4}$$

Enthalpy-porosity method was used to calculate the latent portion of PCM:

$$\gamma = \left\{\begin{array}{c} \frac{h_{latent}}{L_f} = 0 \;\; if\; T < T_{solid} \\ \frac{h_{latent}}{L_f} = 1 \;\; if\; T > T_{liquid} \\ \frac{h_{latent}}{L_f} = \frac{T - T_{solid}}{T_{liquid} - T_{solid}} \quad if\; T_{solid} < T < T_{liquid} \end{array}\right\} \tag{3.5}$$

Source term S_i was used to model the effect of natural convection on phase change as follows:

$$S_i = -A_{mush} \cdot u_i \tag{3.6}$$

$$A_{mush} = \frac{C(1-\gamma)^2}{\gamma^3 + \delta} \tag{3.7}$$

where, δ = 0.001 and C is “mushy” zone constant ($10^5 - 10^7$). “mushy” zone refers to the portion of the domain with a liquid fraction (γ) between 0 and 1. For the present analysis, a value of 10^5 was used as mushy zone constant following the literature [41].

Boussinesq model was adopted to calculate density change due to the phase change and natural convection as presented in Eq. 3.8.

$$\rho = \rho_o[1 - \beta(T - T_o)] \tag{3.8}$$

where reference quantities ρ_o and T_o refer to density and temperature of the liquid PCM respectively, while β is thermal expansion coefficient of the PCM liquid phase. Other thermophysical properties of PCM were considered constant, using the average value of solid and liquid PCM properties.

The volume of fluid (VOF) model was used to model partially filled tube where the 2-D tube domain was divided into the air and PCM zones and discretized accordingly. The following expressions for the fluid volume fraction α were used in the VOF model.

$$\alpha_{PCM} + \alpha_{air} = 1 \tag{3.9}$$

The fluid volume fraction α in each cell varies between 0 (PCM only) to 1 (air only). Density is calculated from the following expression.

$$\rho_{cell} = \rho_{PCM}\alpha_{PCM} + \rho_{air}\alpha_{air} \tag{3.10}$$

3.2.2.1. Model verification

For verification of the melting/ solidification model, the numerical results of liquid fraction and temperature obtained from the current study were compared to the numerical results from Das et. al [59] as shown in Figure 3.3 c, d. Here, a horizontal annulus (Figure 3.3a) filled with n-eicosane as PCM was used for the geometry, where the inner wall was subjected to a constant temperature of 333 K (60 °C) and the outer wall was insulated (adiabatic). The disparity of around

7% in the liquid fraction (refer to Figure 3.3c) is attributed to the influence of density variations in the Boussinesq approximation, where knowledge of the operating temperature is crucial. However, the literature lacks clarification on the assumed operating temperature. A very good agreement was observed for the PCM temperature (Figure 3.3d). However, around the phase change temperature, a difference of around 5% is observed between the reference and the current study. As mentioned earlier, the literature does not provide enough information about the operating temperature assumed in the Boussinesq approximation, which may result in the disparity in both temperature and liquid fraction results. The temperature contours of PCM at 10800 s are almost identical (Fig 3.3b).

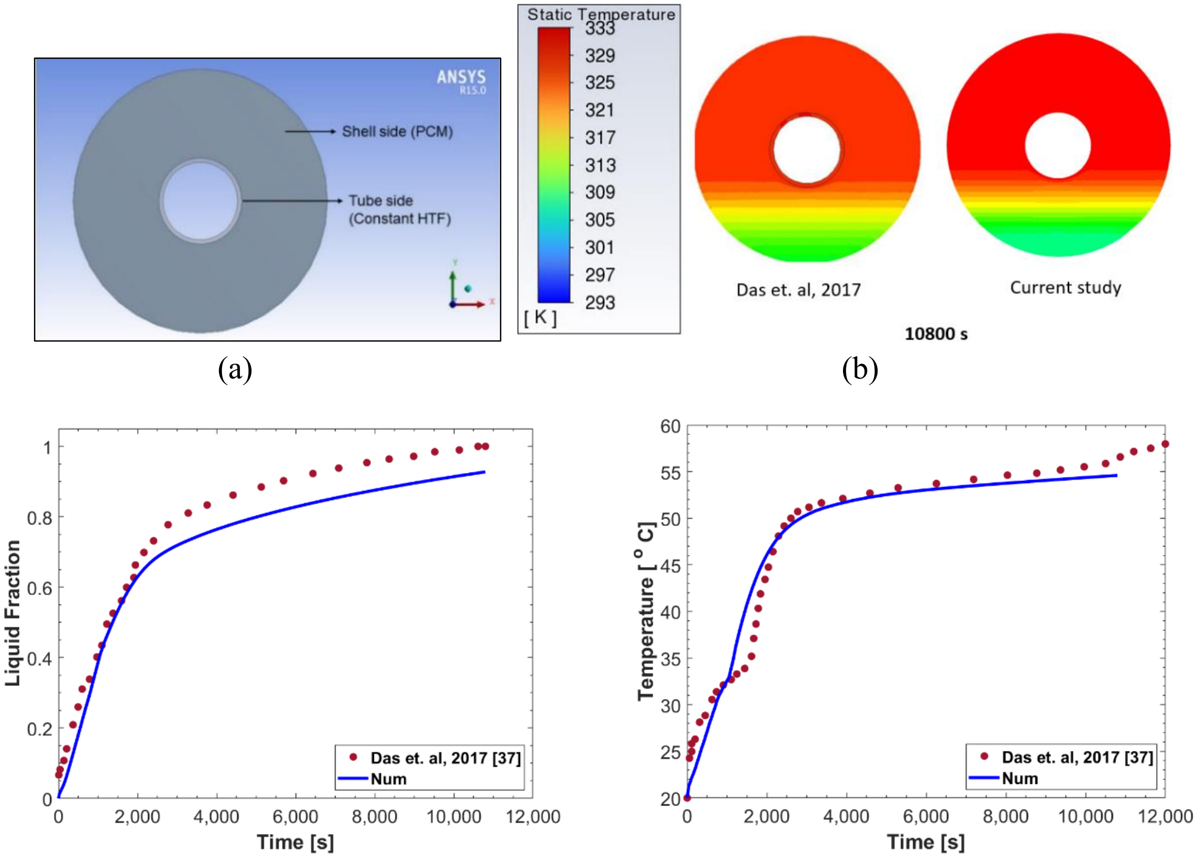

(a) (b)

(c) (d)

Figure 3. 3. (a) Computational domain from the reference [59], (b) comparison of the temperature contours with the reference [59], (c), (d) model verification using the liquid fraction and PCM temperature, respectively

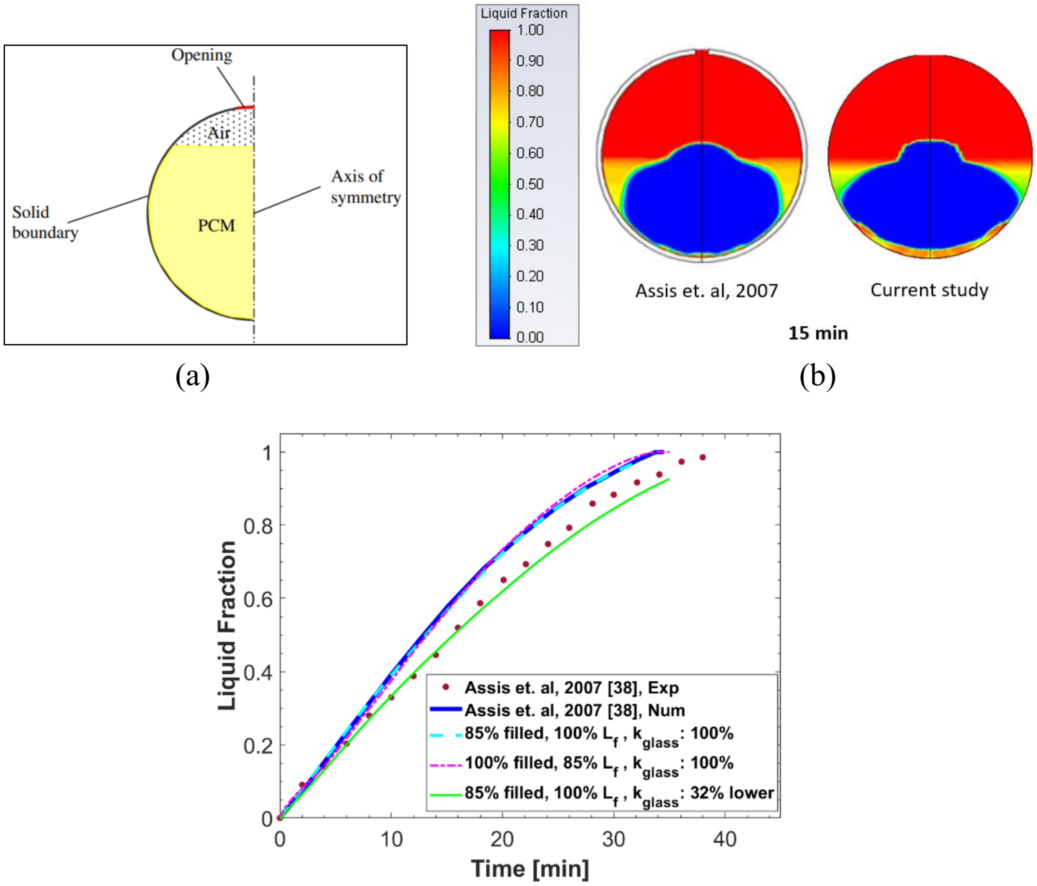

(a) (b)

(c)

Figure 3. 4. (a) Computational domain from the reference [48] for the partially filled tube, (b) comparison of the temperature contours with the reference [48], (c), model verification using the liquid fraction

Numerous references can be found on numerical modeling of PCM melting and solidification processes in a partially filled tube [48-50, 107]. The model for partially filled tube was validated with the numerical results obtained from Assis et. al [48]. To model a partially filled tube, the computational domain was divided into the air and PCM zones (Figure 3.4a) where the tube was 85% filled with PCM RT27 by volume. A constant wall temperature of 312 K (39 °C) was used which was 10 K higher than the phase change temperature. Figure 3.4c shows an excellent agreement between the numerical results from the reference [48] and the current study with a difference less than 1%. The authors from the reference [48] attribute the discrepancy (around 10%) between the numerical results and experimental measurement is due to prediction of the high thermal conductivity. The assumption of 32% lower thermal conductivity exhibits an excellent agreement between the numerical result and the experimental measurement (Figure 3.4c) with a difference of around 1%. A very good agreement in the contour plot of liquid fraction at 15 min was observed as shown in Figure 3.4b. Also, the comparison of average liquid fraction (Figure 3.4c) shows that there is virtually no difference between the predicted results from the current study and the literature when the tube is modeled assuming 100% filled with a PCM of 15% lower latent heat. However, assuming a 100% filled tube with a lower latent heat reduces the computation effort and time by approximately a factor three compared to the numerical model considering partially filled tube by using the VOF model.

3.2.2.2. Selection of turbulence model and grid sensitivity analysis

To select an appropriate turbulence model for modeling of flow through a tube array, three steps were followed. The velocity field was solved for the steady state conditions first, and then for the transient case without the PCM in the tubes. The experimental correlation for pressure drop (ΔP) across the tube bank developed by Zukauskas [83, 108] as Eq. 3.11 was used for verification of the numerical model.

$$\Delta P = N_L x \left(\frac{\rho_{air}\, v_{max}^2}{2}\right) f \tag{3.11}$$

where, N_L represents the number of tube rows. Friction factor f and correction factor x are derived from the graph presented in [83, 108] for the maximum velocity (v_{max}) in the tube bank, where (v_{max}) is computed using the following equation.

$$v_{max} = \frac{s_T}{s_T - D} v_\infty \tag{3.12}$$

where, S_T is the tube spacing in the transverse direction.

The energy equations at the interface of the PCM and fluid domain were solved next using the conjugate heat transfer approach for the transient flow model. The correlation of Nu number by Zukauskas [83, 108] was used for the verification (Eq. 3.13).

$$\overline{Nu}_D = C_1 C_2 R_{e_D}^m Pr^n \left(\frac{Pr}{Pr_s}\right)^{1/4} \tag{3.13}$$

where, $\left\{\begin{matrix} N_L \geq 20 \\ 0.7 \leq Pr \leq 500 \\ 10 \leq Re_{D_{max}} \leq 2 \times 10^6 \end{matrix}\right\}$

Coefficient of heat transfer (h_{Zu}) was calculated from Zukauskas correlation for Nu number using the following expression:

$$\overline{Nu}_D = \frac{h_{Zu} D}{k_{air}} \tag{3.14}$$

The average heat transfer coefficient (h_{num}) for the numerical analysis was computed from the log mean temperature difference (LMTD) method as presented in Eq. (3.15)

$$h_{num} = \frac{q''}{LMTD} \tag{3.15}$$

where, the peripheral average of wall heat-flux (q″) was determined from the Fourier's law as following:

$$q_w'' = -k_{air} \frac{\partial T_w}{\partial r}\bigg|_{r = r_0} = \frac{k_{air}}{r_0 - r_i}\left(T_{w,o} - T_{w,i}\right)$$

and, $LMTD = \frac{\Delta T_{in} - \Delta T_{out}}{ln(\Delta T_{in}/\Delta T_{out})} = \frac{(T_{w,i} - T_{in}) - (T_{w,i} - T_{out})}{\ln((T_{w,i} - T_{in})/(T_{w,i} - T_{out}))}$

Table 3.3 shows the comparison of the renowned turbulence models. The Realizable k-ε model was selected for its better prediction of Nu number and pressure drop (*Δ*P) compared to other considered models.

Table 3. 3 Selection of turbulence model for the transient flow analysis of the tube filled with PCM

Turbulence Models	ΔP_{Num} (Pa)	ΔP_{Zu} (Pa)	Difference, ΔP (%)	Nu_{avg}	Nu_{Zu}	Difference, Nu (%)
RNG k-ε	8.81	9.5	7.3	37.4	37.8	1.1
Realizable k-ε	9.32	9.5	1.9	36.5	37.8	3.4
Standard k-ε	9.35	9.5	1.6	36.7	37.8	2.9
SST k-ω	7.90	9.5	16.8	31.8	37.8	15.9
Standard k-ω	7.50	9.5	21.1	30.6	37.8	19.0

Navier-Stokes equations for the fluid domain (air) are as follows:

$$\frac{\partial \rho_{air}}{\partial t} + \frac{\partial \rho_{air} u_i}{\partial x_i} = 0 \tag{3.16}$$

$$\frac{\partial (\rho_{air} u_i)}{\partial t} + \frac{\partial (\rho_{air} u_i u_j)}{\partial x_j} = -\frac{\partial p}{\partial x_i} + \frac{\partial}{\partial x_j}\left[\mu_{air}\left(\frac{\partial u_i}{\partial x_j} + \frac{\partial u_j}{\partial x_i}\right) - \rho_{air}\overline{u_i' u_j'}\right] \tag{3.17}$$

$$\rho_{air}\frac{\partial T}{\partial t} + \rho_{air} u_j \frac{\partial T}{\partial x_j} = -\frac{\partial p}{\partial t} + \frac{\partial}{\partial x_j}\left(\frac{k_{air}}{Cp_{air}}\frac{\partial}{\partial x_j} - \rho_{air}\overline{u_j' T'}\right) \tag{3.18}$$

where, u_i, u_j denote mean flow velocity, u' denote velocity fluctuations due to turbulence and $\rho_{air}\overline{u_i' u_j'}$ represents Reynolds Stress term.

The transport equations for the turbulent kinetic energy (κ) and dissipation rate (ε) for Realizable κ-ε model are expressed as following [109]:

$$\frac{\partial (\rho_{air}\kappa)}{\partial t} + \frac{\partial}{\partial x_j}\left(\rho_{air}\kappa u_j\right) = \frac{\partial}{\partial x_j}\left[\left(\mu_{air} + \frac{\mu_t}{\sigma_k}\right)\frac{\partial k}{\partial x_j}\right] + G_k + G_b + S_k - \rho_{air}\varepsilon - Y_M \tag{3.19}$$

$$\frac{\partial (\rho_{air}\varepsilon)}{\partial t} + \frac{\partial}{\partial x_j}\left(\rho_{air}\varepsilon u_j\right) = \frac{\partial}{\partial x_j}\left[\left(\mu_{air} + \frac{\mu_t}{\sigma_\varepsilon}\right)\frac{\partial \varepsilon}{\partial x_j}\right] + S_\varepsilon + \rho_{air} C1 S_\varepsilon - \rho_{air} C_2 \frac{\varepsilon^2}{\kappa + \sqrt{\nu\varepsilon}} + C_{1\varepsilon}\frac{\varepsilon}{k} C_{3\varepsilon} G_b \tag{3.20}$$

where,

$$C_1 = \left[0 \cdot 43, \frac{\eta *}{\eta * + 5}\right], \qquad \eta * = S\frac{k}{\varepsilon}, \qquad S = \sqrt{2 S_{ij} S_{ij}}, \qquad S_{ij} = \frac{1}{2}\left(\frac{\partial u_j}{\partial x_i} + \frac{\partial u_i}{\partial x_j}\right)$$

G_k and G_b represent generation of turbulent kinetic energy due to the mean velocity gradient and buoyancy, respectively. Y_M stands for the extent to which the fluctuating dilatation contributes to the overall dissipation rate in the context of compressible turbulence. Quantities σ_k and σ_ε represent turbulent Prandtl number for κ and ε, respectively. S is the mean rate-of-strain tensor.

To obtain the appropriate grid fineness, a grid sensitivity analysis was carried out using the ANSYS meshing module [81]. Table 3.4 shows the comparison of the mesh independence test for different grid sizes. To precisely analyze changes in velocity and temperature near the tube wall within the boundary layer (see Figure 3.5), a highly refined grid was used close to the tube wall by adding an inflation layer. The inflation layer consists of 20 layers with a first layer thickness of 0.01 mm and growth ratio of 1.2 for all grid sizes. Grid 2 with 165878 quadrilateral elements was selected for its better prediction of pressure drop (ΔP) and lower computational time required compared to the Grids 1 and 3. Figure 3.5 shows the final grid used for further analysis.

Table 3. 4 Mesh independence study for steady state without PCM in the tube

Cases	Grid Size (mm)	Element Number	ΔP_{Num} (Pa)	ΔP_{Zu} [108] (Pa)	Difference, ΔP (%)
Grid 1: Coarse	1	31037	9.23	9.5	2.8
Grid 2: Medium	0.3	165878	9.32	9.5	1.9
Grid 3: Fine	0.2	243757	9.25	9.5	2.6

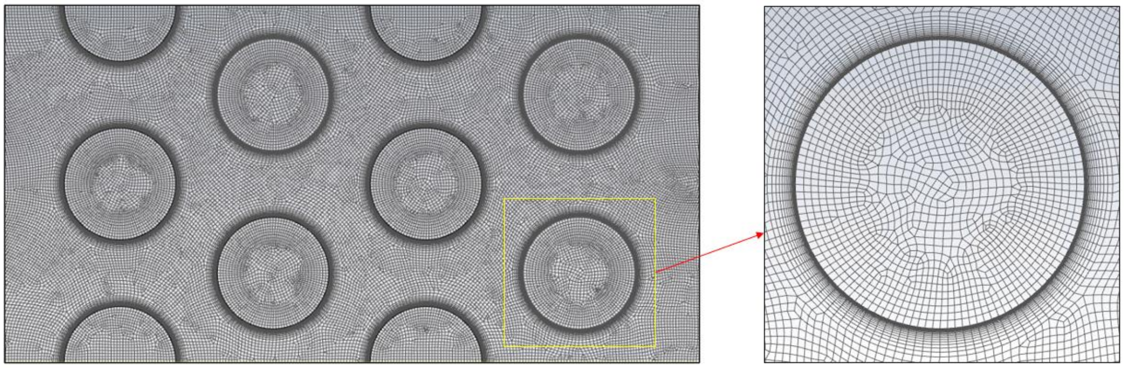

Figure 3. 5. Computational discretization (Grid 2) of the tube bank

3.2.3. Experimental setup

A custom-built, forced-air heat transfer setup was developed for determining the heat transfer in air flow through the latent heat storage module. The schematic of the setup, depicted in Figure 3.6, contains two main sections: the buffer and test sections.

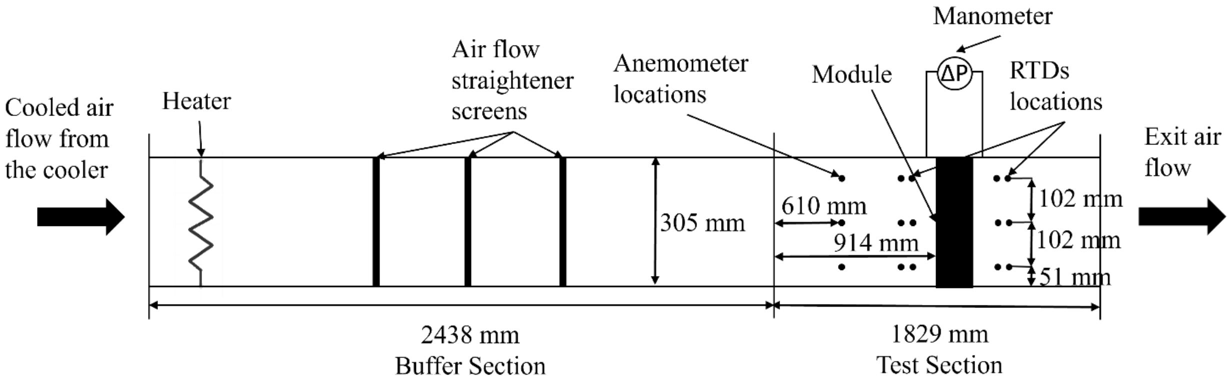

Figure 3. 6. A schematic diagram of the forced-air heat transfer apparatus.

The buffer section, whose function is to produce a fully developed air flow with specific temperatures and velocity, was made of a 2,438 mm long galvanized steel conduit with a 305×305 mm cross-sectional area. It incorporates an 8,920 BTU (2.6 kW) N407-TC portable air conditioner, a 10-kW finned tubular air electric duct heater, and three honeycomb cell air flow straightening screens.

Following the buffer section is the test section, housing the tested heat storage modules. The buffer section is constructed from the 1,829 mm length, 10-gauge carbon steel with an identical cross-sectional area to the buffer section. Three insertion points on the side, situated 610 mm downstream from the entrance, allow for a hot wire anemometer (Kanomax Climomaster 6501, 2% of reading or 15 mm/s accuracy, whichever is larger) to evaluate velocity distribution across the cross-section. Two drilled openings at the top wall function as pressure outlets for a differential manometer (accuracy: ± 0.025% full scale, range: 0 to 6895 Pa).

Figure 3.7 shows the photograph of the test section and associated instrumentation. The installation of the latent heat storage module is facilitated by the opening located on the top wall of the test section. The tested heat storage module is placed downstream of the anemometers. As shown in Figure 3.7b, two sets of PT100 RTD probes (accuracy: ± 0.15 °C), with each group containing nine probes are used to measure air temperature upstream and downstream of the tested heat storage module. The RTD probes are located at two different planes as presented by the black dots in Figure 3.6. The average readings of the upstream and downstream probes represent the inlet and outlet air temperatures, respectively. The testing section outlet is attached to a 7.5 HP high-output blower (model: 1953K55), regulated by a damper, to provide air flow for the tests.

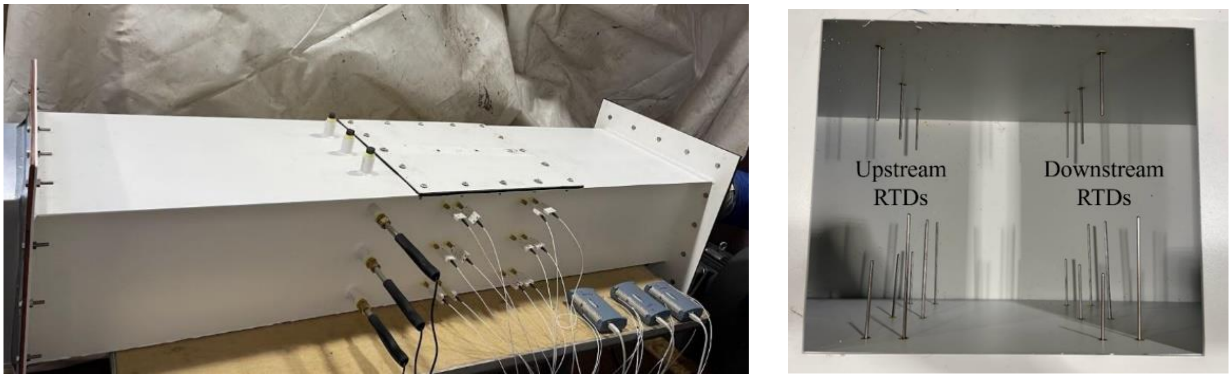

(a) (b)

Figure 3. 7. (a) Photograph of the test section, (b) The top opening in the test section.

Figures 3.8 (a-c) show the instrumentation setup where one tube in the first row (upstream of the flow direction) and one tube in the fourth row (downstream of the flow direction) was equipped with thermocouples to measure the tube wall temperature and the PCM temperature. Unfortunately, due to the limitations of the data acquisition system, the measured wall temperature values could not be recorded. Figure 3.8c, shows the photograph of the side view of the partially filled PCM tube, and the placement of a thermocouple (referred to as TC) at the center of the tube's span. TC1 is positioned at the center tube of the first row (upstream), while TC2 is inserted into the center tube of the fourth/last row, downstream from TC1. Type T thermocouple with an accuracy of ± 1 ºC was used for the temperature measurement. Figure 3.8d shows the photograph of a circular tube partially filled with frozen PCM (80% by volume while liquid) and an empty zone (air) above PCM.

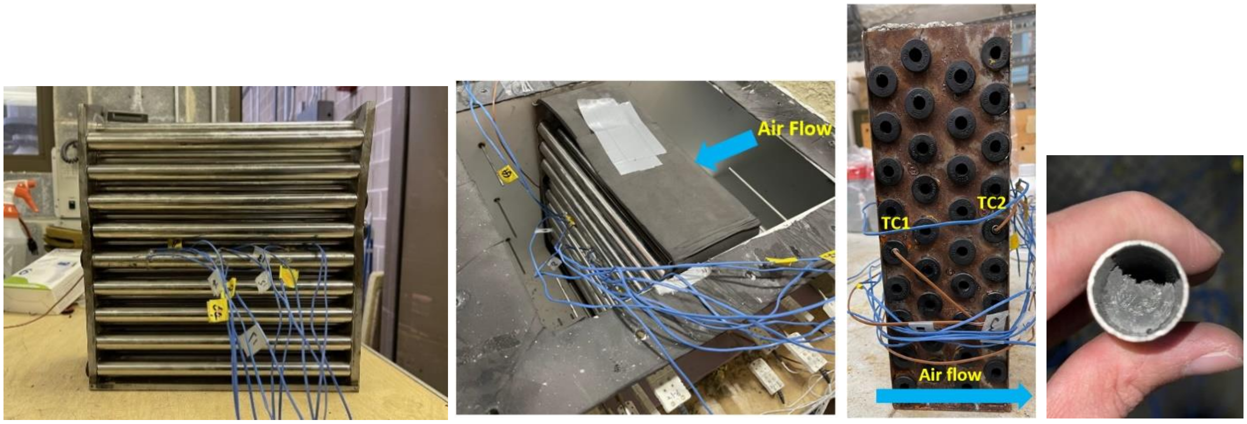

(a) Back view (b) Top view (c) Side view (d)

Figure 3. 8. (a), (b) Photograph of the laboratory-scale tube array showing thermocouples attached to the tube wall ; (c) Photograph of the side view of the tube array showing thermocouples attached at the center of the tube for PCM temperature measurement; (d) Photograph of partially filled tube with frozen PCM

The experimental procedure involved cycling between the charging (PCM melting) and discharging (PCM freezing) phases according to a defined protocol. The air cooling and flow systems were first activated to allow the entire experimental setup to reach a steady state bellow the PCM melting point temperature. With the air fan (blower) running, the heating phase starts by turning the heater on, which forces heated air flow through the heat storage module initially at the ambient temperature. At the end of the test when thermal equilibrium is obtained, the outlet and inlet air temperatures are the same indicating the end of the charging phase. With the fan running, the discharge phase begins by switching the heater off, which results in the ambient temperature (cold air) flow through the heat storage module, which begins to cool as stored heat is transferred to air. The test ends when the temperature of the outlet air matches inlet air temperature, signaling the end of the discharge phase. The operating temperature range of the LTES system is from 288 K or 15 °C (cold condition) to 308 K or 35 °C (hot condition). This range was selected based on the ambient air temperatures in various geographical regions of the USA, as mentioned earlier.

It is important to take into account measurement uncertainties and instruments accuracy while performing experiments. Table 3.5 summarizes the accuracy of the instruments used for measuring velocity, pressure, PCM properties, and temperatures at the PCM, as well as at the inlet and outlet of the tube array.

Table 3. 5 Uncertainties in the measurement and experimental setup

Instrument/ measurement	Accuracy
Drop calorimeter	± 5 %
Lab weighing scale	±0.3 mg
Anemometer	2 % of reading or 15 mm/s whichever is greater
Manometer	± 0.025 % full scale, range: 0 to 6895 Pa
RTD probe	± 0.15 °C
Thermocouple	± 1 °C
Inlet air velocity	± 0.05 m/s
Module heating temperature	± 0.3 °C
Module cooling temperature	± 1.1 °C
Steady state temperature	± 1.3 °C

3.3. Results and discussion

3.3.1. Comparison of the numerical and experimental results

The numerical model for the tube bank was validated against the experimental data using air temperature at the outlet of the tube bank and PCM temperature measured ideally at the center of the tube as functions of time. A user defined function (UDF) was employed in Fluent [81] code to provide the inlet B.C. (inlet air temperature) as a function of time, identical to the measurement.

Due to the transient behavior of the electric heater (thermal inertia), the setpoint temperature (308 K or 35 ºC) for the melting test was achieved approximately 2400 s after the heater was turned on (Figure 3.9a). The air velocity during the PCM melting test was 1.1 m/s. Figure 3.9 a, b show a very good agreement (less than 1 ºC difference) between the measured and numerically predicted values of air temperature at the tube array outlet. The computational analysis of the partially (80%) filled tube was carried out using the VOF model. The model was further simplified by assuming 100% filled tubes and using 20% lower latent heat of fusion (L_f) than the actual value. This simplification provides realistic results with a relatively small temperature difference between the numerical predictions and the measurements of air temperature at the tube array outlet. The benefit of numerical model simplification is a threefold reduction of computational time and effort. Therefore, the simplified model was used for analysis of PCM melting and freezing.

Figure 3.9a shows after the inlet air temperature reaches the setpoint value at around 1500 seconds (25 minutes) of the flow (test) time, the outlet air temperature stays almost constant for around 2400 seconds (40 minutes). After approximately 3960 seconds (66 minutes) of the flow time PCM in the tubes has completely melted and liquid PCM superheats approaching the inlet air temperature, the outlet air temperature follows the same trend, rapidly increases approaching the inlet air temperature till the end of the test (6120 seconds or 1.7 hours). Figure 3.9b shows the air temperature difference between the inlet and outlet of the domain. The numerical results using two different approaches to simulate 80% filled tube are almost identical. The results also demonstrate that the numerical model developed for the tube array is providing accurate and realistic results for PCM melting.

Figure 3.9c shows the comparison of the measured and predicted PCM temperature in the upstream and downstream tubes. As mentioned earlier, temperature of the PCM was measured by a TC ideally located at the center of the tube, while the average value of PCM temperature in the tube was reported from numerical analysis. The experimental results verify the dynamics of the PCM melting and solidification processes within the energy storage facility, aligning with the predicted outcomes from the numerical analysis. The agreement of predicted and measured values of PCM temperature is very good, with temperature difference between the measurement and numerical prediction being within 2 ºC. The agreement is better for the upstream tube compared to the downstream tube. The results show, temperature of the frozen PCM, initially at 288 K or 15 ºC, rapidly increases for the first 1000 s as solid PCM is heated until it reaches the phase change temperature. For the next 3700 s, PCM temperature stays almost constant as PCM is changing phase (melting). After all, PCM melts, the PCM temperature rapidly increases as liquid PCM superheats approaching the inlet air temperature as discussed above.

The test results in Figure 3.9 indicate that under the test conditions of PCM melting, utilizing a 4-row tube arrangement containing a relatively small amount of PCM (2.88 kg) leads to a reduction in outlet air temperature compared to the inlet. This setup sustains a cooling effect for a duration of approximately one hour. This relatively brief cooling duration can be attributed to the shallow array design (consisting of only 4 tube rows in the direction of flow) and the limited quantity of PCM (2.88 kg) within the tube array.

Following the PCM melting test, a PCM freezing test was performed by turning the heater off, turning the air chiller on, and maintaining a consistent air mass flow through the test setup, mirroring the conditions of the melting test. The air velocity during the PCM freezing test was 0.79 m/s, somewhat lower compared to the PCM melting test. As shown in Figure 10a, the initial inlet air temperature of 308 K (35 ºC) rapidly decreases within 600 seconds (10 minutes) to the chiller setpoint temperature of approximately 288 K (15 °C), thereafter remaining relatively constant.

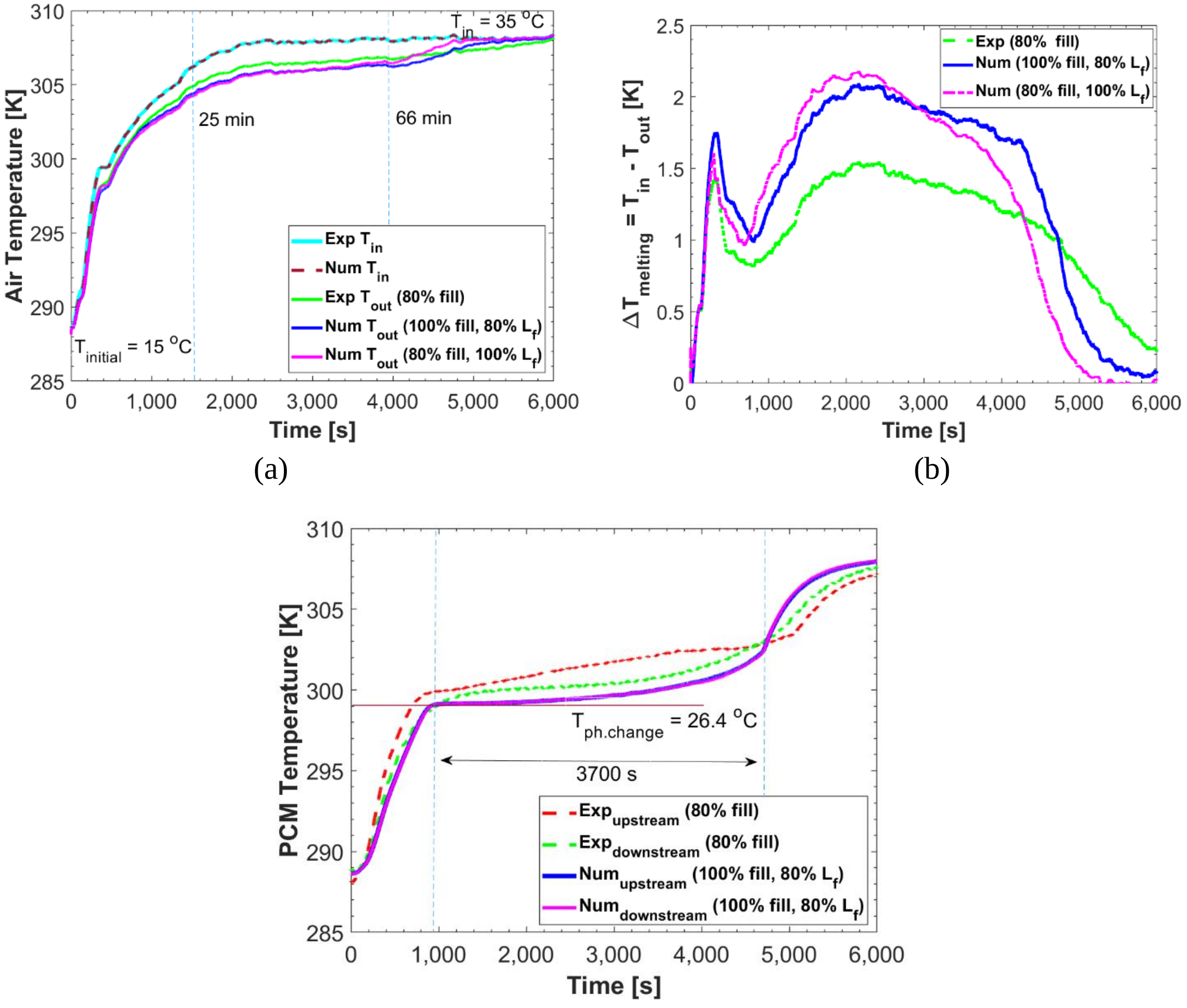

(a)

(b)

(c)

Figure 3. 9. Temperature as a function of time during the PCM melting test: (a) Inlet and outlet air temperature, (b) Temperature difference between inlet and outlet air temperatures, (c) PCM temperatures

Figures 3.10 a, b show the comparison between the measured and predicted values of air temperature at the array outlet. A very good agreement (less than 1 ºC difference) was obtained between the numerical prediction and the measurement. As previously mentioned, the numerical analysis was conducted by employing a latent heat of fusion (L_f) that was 20% lower compared to the true value, along with an assumption of complete PCM filling within the tubes. As demonstrated subsequently, this simplification yields realistic outcomes for the tubes partially filled with PCM.

As shown in Figure 3.10a, once the inlet air temperature reaches the setpoint temperature, the outlet air temperature remains nearly constant for roughly 2400 seconds (40 minutes). After 3000 seconds (50 minutes) of the flow time, the numerically predicted air temperature at the outlet starts to decline, ultimately reaching the setpoint temperature of the inlet air within about 1800 seconds (30 minutes). This temperature decrease occurs since the majority of PCM within the tubes solidifies. The experimental value of the outlet air temperature reaches the setpoint temperature of the inlet air approximately at the same time as numerical prediction, i.e., 5,000 seconds (1.39 hours) from the beginning of the PCM freezing test. Figure 3.10b shows the temperature difference between the outlet and the inlet air temperature. The numerical analysis provides realistic predictions of the temperature difference when compared to the actual measurements.

Figure 3.10c shows the comparison of the measured and numerically predicted values of PCM temperature in the upstream and downstream tubes. As mentioned earlier, the PCM temperature was measured by the thermocouples located ideally at the center of the tube, while the numerical analysis provides the average temperature of PCM in the tube. The numerical prediction of PCM temperature agrees very well with the measurement until it reaches supercooling since numerical model is unable to predict PCM supercooling. PCM supercooling occurs despite the addition of suppression additives. Supercooling occurs a few minutes earlier in the upstream tube compared to the downstream tube, due to propagation of the freezing front in the direction of the flow.

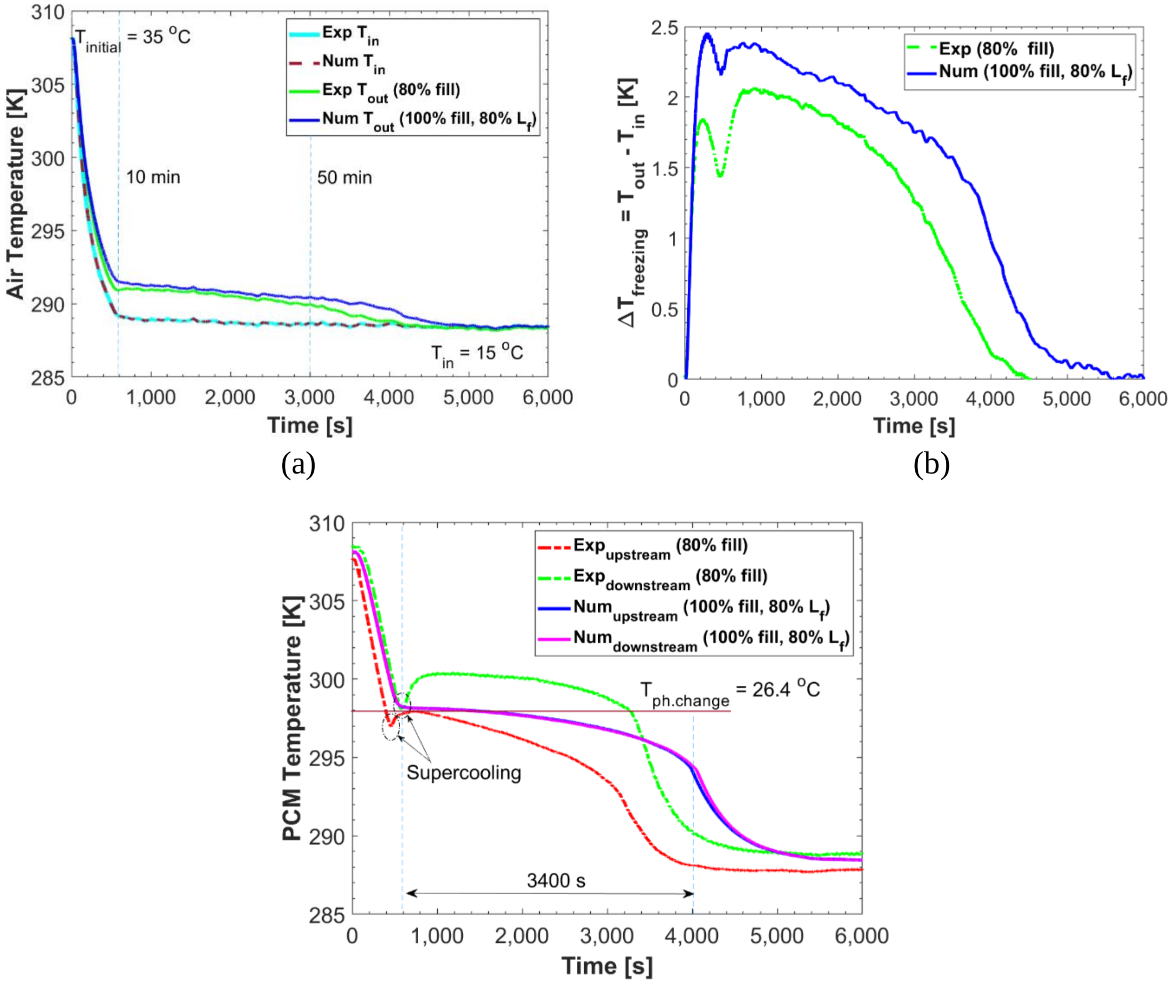

(a) (b)

(c)

Figure 3. 10. Temperature as a function of time during the PCM freezing test: (a) Inlet and outlet air temperature, (b) Temperature difference between inlet and outlet air temperatures, (c) PCM temperature in the upstream and downstream tubes

The numerically predicted values for the upstream and downstream tubes are virtually identical (Figure 3.10c). In the beginning of the test, the superheated liquid PCM at 308 K or 35 ºC rapidly cools within 600 seconds (10 minutes) till the temperature of PCM reaches the phase change temperature (299.55 K or 26.4 ºC). As the temperature of PCM approaches the fusion temperature, the temperature decrease follows approximately linear pattern, and the freezing accelerates, causing the temperature to decrease steeply until it asymptotically reaches the cooling air temperature (around 288 K or 15 °C) at the inlet.

Overall, the measurements and predictions of the PCM temperature correspond closely until the occurrence of supercooling. The PCM temperature measured at the center of the upstream tube experiences a more rapid decline over time compared to the numerical prediction, reaching the air inlet temperature of 288 K (15 °C) approximately 4,200 seconds (1.17 hours) into the test. The numerically predicted average PCM value within the upstream tube is relatively higher and decreases more gradually than the observed value, eventually reaching the air inlet temperature setpoint value at around 5,200 seconds (1.44 hours) after the beginning of the test. This discrepancy might stem from the assumptions integrated into the numerical model or potentially due to the fact that the PCM temperature is measured at a single point in the center of the tube, while the numerical prediction represents the average PCM temperature across the cross-section of the tube.

A similar trend follows in the downstream tube as for the upstream tube where the temperature was measured at the center of the downstream tube. However, its value tends to be higher compared to both the numerical prediction and measurements in the upstream tube. Since it is implausible for the PCM temperature in the downstream tube to be consistently 4 K (or °C) higher compared to the upstream tube (except for the early stages of freezing), it's reasonable to suspect experimental errors in measuring temperatures of the PCMs. Potential causes for such errors include the location of the thermocouples not being at the center of the tube and non-uniform airflow throughout the tube array. In the case of a partially filled PCM tube, the variance between the center-located temperature measurement and the average temperature of PCM could also lead to the observed temperature discrepancy. Furthermore, the measured PCM temperature within the downstream tube falls short of reaching the inlet air temperature of 288 K or 15 °C but rather reads approximately 1 °C higher, likely due to differences in thermocouple calibration. The numerically predicted average PCM temperature values are roughly 0.5 °C higher compared to the outlet temperature setpoint, primarily due to the resistance to heat transfer between the PCM inside the tube and the surrounding airflow. This illustrates the considerable challenge associated with conducting precise tests at low temperatures.

It can be deduced from Figure 3.10 that under the test conditions of PCM freezing, the 4-row tube array affects the outlet air temperature for approximately 2988 seconds (0.83 hours), i.e., maintaining the outlet air temperature in proximity to the phase change temperature. Subsequently, it reaches the inlet air temperature setpoint value in around 4,600 seconds (1.3 hours). This relatively short duration stems from the shallow configuration of tube array consisting of only 4 rows and the limited mass of PCM (2.88 kg) within the air flow direction.

Table 3.6 presents a comparison between the numerically predicted values of the pressure drop through the tube array and the peripherally averaged convection heat transfer coefficient to the values obtained from the literature (Zukauskas [83, 108]), for the PCM melting and freezing scenarios. The results show a very good agreement between the predicted values and the published data with a difference of less than 5%. The experimentally obtained value of the pressure drop through the array during PCM melting is 9.7 Pa, while for PCM freezing, it is 8.7 Pa. The difference between the numerically predicted and measured values of pressure drop is less than 5% for the PCM melting test, while for the solidification (freezing) test, the difference between the measured and numerically predicted valued of pressure drop is higher due to the difficulty in measurement of low values of pressure drop at a very low velocity.

Table 3. 6 Comparison of numerical predictions and experimental correlations

Cases	v_∞ (m/s)	ΔP (Pa)			$h_{avg.}$ (W/m^2-K)	
		Exp	Num	Zu [108] Correlation	Num	Zu [83] Correlation
Melting	1.10	9.7	9.32	9.5	50.28	52.00
Solidification	0.79	8.7	6.7	6.8	50.69	52.00

3.3.2. Detailed analysis of PCM melting/ solidification

A detailed analysis of the dynamics of flow and heat transfer within the tubes in an array with staggered tube arrangement was conducted for the melting and solidification processes. Figures 3.11 and 3.12 show the changes in liquid fraction, tube temperature, and average wall heat-flux in tubes 1 to 6 (see Figure 3.2) in the array as functions of time. Since the convection rates on tubes 3, 4 and 5, 6 (see Figure 3.2) are the same, only resuls for tubes 4 and 6 are shown for clarity while skipping tubes 3 and 5.

The PCM liquid fraction in tubes 1 to 6 is shown as a function of time in Figure 3.11a, while Figure 3.11b presents the average PCM temperature and corresponding tube wall temperature in these tubes. A liquid fraction of zero ($\gamma = 0$) indicates that the PCM is entirely frozen, whereas a liquid fraction of one ($\gamma = 1$) indicates that the PCM is completely melted.

Initially, the solid PCM in all tubes (1 to 6) is at 288 K (15 °C). As the heater is turned on, PCM temperature rapidly increases until it reaches the phase change temperature of 299.5 K (26.4 °C) in about 1000 seconds (Figure 3.11b). During this phase change from solid to liquid (melting), the average PCM temperature increases linearly as heat is added through the tube walls until all solid PCM melts. During the phase transition, the average temperature of PCM increases gradually and after around 3700 s, PCM in the first row tube (upstream) starts to superheat (see Figure 3.11b). Once the PCM in a tube has melted, the average PCM temperature rapidly increases, reaching the temperature of the tube wall (approx. equal to air inlet temperature), as shown in Figure 3.11b. The difference between the tube wall and average PCM temperature during the phase chnage is approximately 1 °C during the PCM melting.

Due to thesecondary flows on tubes 2 and 4, the heat transfer rate in tubes 2 and 4 is higher compared to tubes 1 and 6, which results in faster melting in tube 4, followed by tube 2 (Figure

3.11a). Melting process in tubes 1 and 6 is longer compared to the other tubes. The PCM melting process in tubes 1 and 6 occurs almost simultaneously.

According to the results presented in Figure 3.11b, it is evident that for the analyzed tube array geometry and operating conditions, a relatively constant air temperature at the array outlet can be maintained for approximately 2400 s (40 minutes). Beyond this duration, the outlet air temperature begins to rise due to the increase in average PCM temperature in the tubes and tube wall temperature, caused by the melting of a significant portion (more than 80%) of the solid PCM in the tube.

The results also show that the air temperature at the array outlet (see Figure 3.9a) is approximately 3.5 K (or °C) higher than the PCM phase change temperature at the beginning of PCM melting. This temperature difference is attributed to the thermal resistance to heat transfer due to convection on the tube wall and conduction through the tube wall. As the average PCM temperature increases during the PCM melting, the average tube wall temperature rises (see Figure 3.11b) as mentioned earlier. Consequently, temperature of the air leaving the array will be higher than the PCM phase change temperature. For the specific tube array analyzed, this temperature difference increases with the time taken for the PCM melting.

Figure 3.11c shows peripherally averaged wall heat-flux (q'') on the tube wall as a function of time. The wall heat-flux (q'') was computed from the Fourier’s law as mentioned earlier and averaged along tube periphery. The negative value of the heat-flux indicates the heat-flux is inwards and heat transfer is occurring across the tube wall to increase the temperature of the frozen (solid) PCM. The average wall heat flux is initially zero. As heat transfer by convection and conduction takes place, the heat flux increases and after reaching maximum value at approximately

2,000 s, q˝ starts to decrease reaching zero once all frozen PCM in the tube is melted and its temperature reaches the inlet air temperature eliminating driving force for heat transfer.

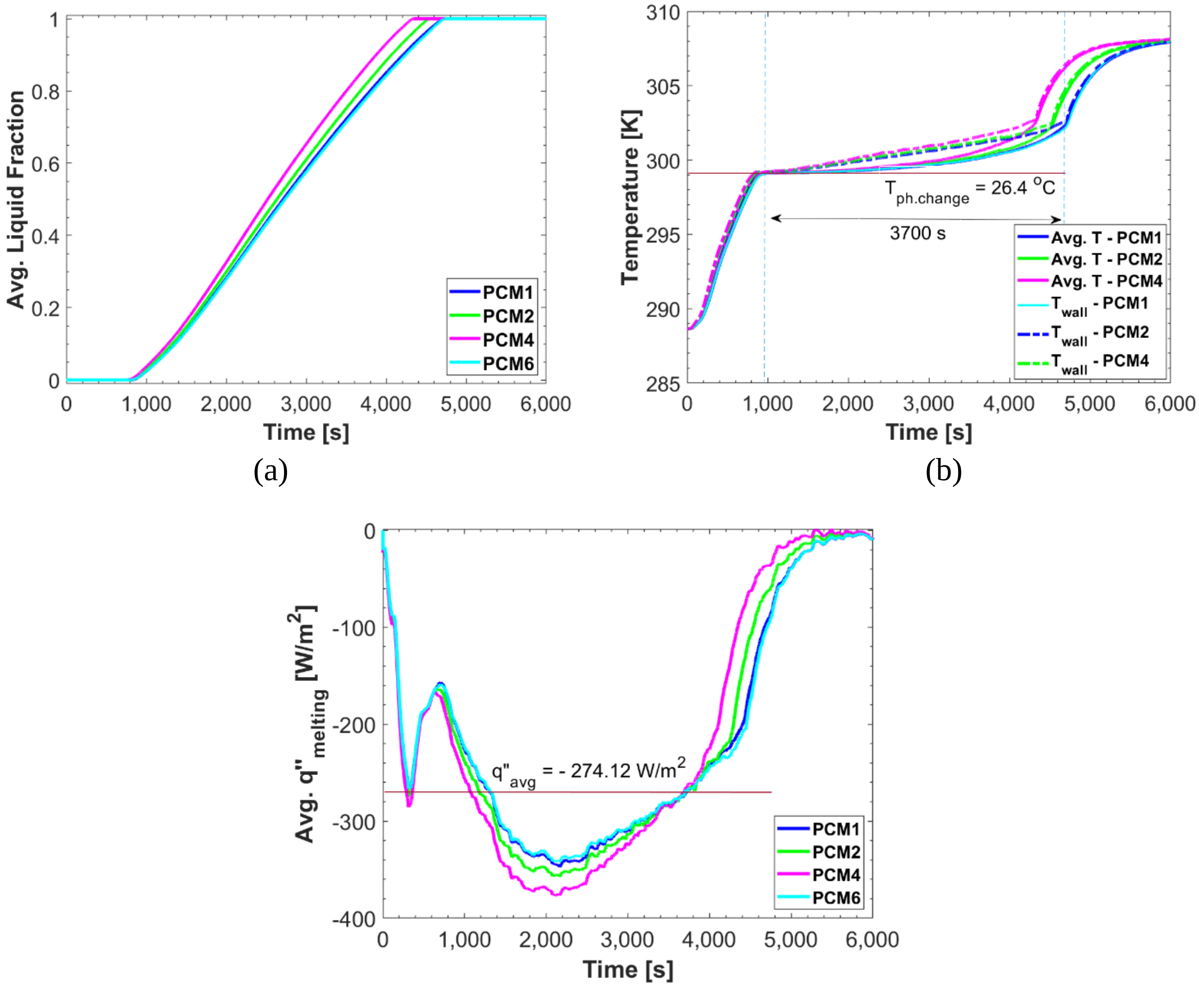

(a) (b)

(c)

Figure 3. 11. Melting parameters as a function of time: (a) Evolution of average liquid fraction of PCMs, (b) Temperature of PCM and tube wall, (c) Peripherally averaged wall heat flux (q˝)

Higher wall heat-flux means higher melting rates which result in shorter melting time. As illustrated in Figure 3.11c, the average wall heat flux is higher for the tubes in the second row (tube 4) compared to other tubes. Therefore, the melting process is faster for tube 4 compared to tubes 1 (first row) and 6 (last row), as discussed before. The average value of wall heat-flux in all tubes is 274.12 W/m^2 for the PCM melting process.

Similar to the analysis conducted for the PCM melting process, a comprehensive investigation of various freezing parameters was carried out for the PCM freezing process and is shown in Figure 3.12. Figure 3.12a presents changes in the average PCM liquid fraction in the tubes as a function of time, while Figure 3.12b shows variations in the average PCM temperature and corresponding tube wall temperature with time during the freezing process for tubes 1 to 6 (see Figure 2).

The liquid superheated PCM ($\gamma = 1$) in all tubes (1 to 6) initially at 308 K (35 °C) is rapidly cooled until it reaches the phase change temperature of 299.5 K (26.4 °C) in about 500 seconds (Figure 3.12b). During this phase change from liquid to solid (freezing), the average PCM temperature decreases linearly as heat is removed from the tube walls until all liquid PCM has frozen. After approximately 3400 seconds, the PCM in the first-row tube (upstream) starts to subcool (see Figure 3.12b). Once the PCM in the tube has frozen completely, the average PCM temperature rapidly decreases, reaching the temperature of the tube wall (approximately equal to the air temperature). The temperature difference between the tube wall and PCM during the freezing process is approximately 1 °C.

Similar to the PCM melting process, the heat transfer rate during freezing process is higher in tubes 2 and 4 due to the effect of secondary flows on these tubes, resulting in faster freezing in tube 4 followed by tube 2 (Figure 3.12a). Tubes 1 and 6 experience a longer freezing process, which occurs almost simultaneously in both tubes.

Based on the results shown in Figure 3.12b, it is evident that the analyzed tube array geometry and operating conditions can maintain a relatively constant air temperature at the array outlet for approximately 2400 s (40 minutes). Beyond this duration, the outlet air temperature starts to decrease due to a decrease in both the tube wall temperature and the average PCM temperature in the tube, caused by the freezing of a significant portion (more than 80%) of the liquid PCM (see Figure 3.12a).

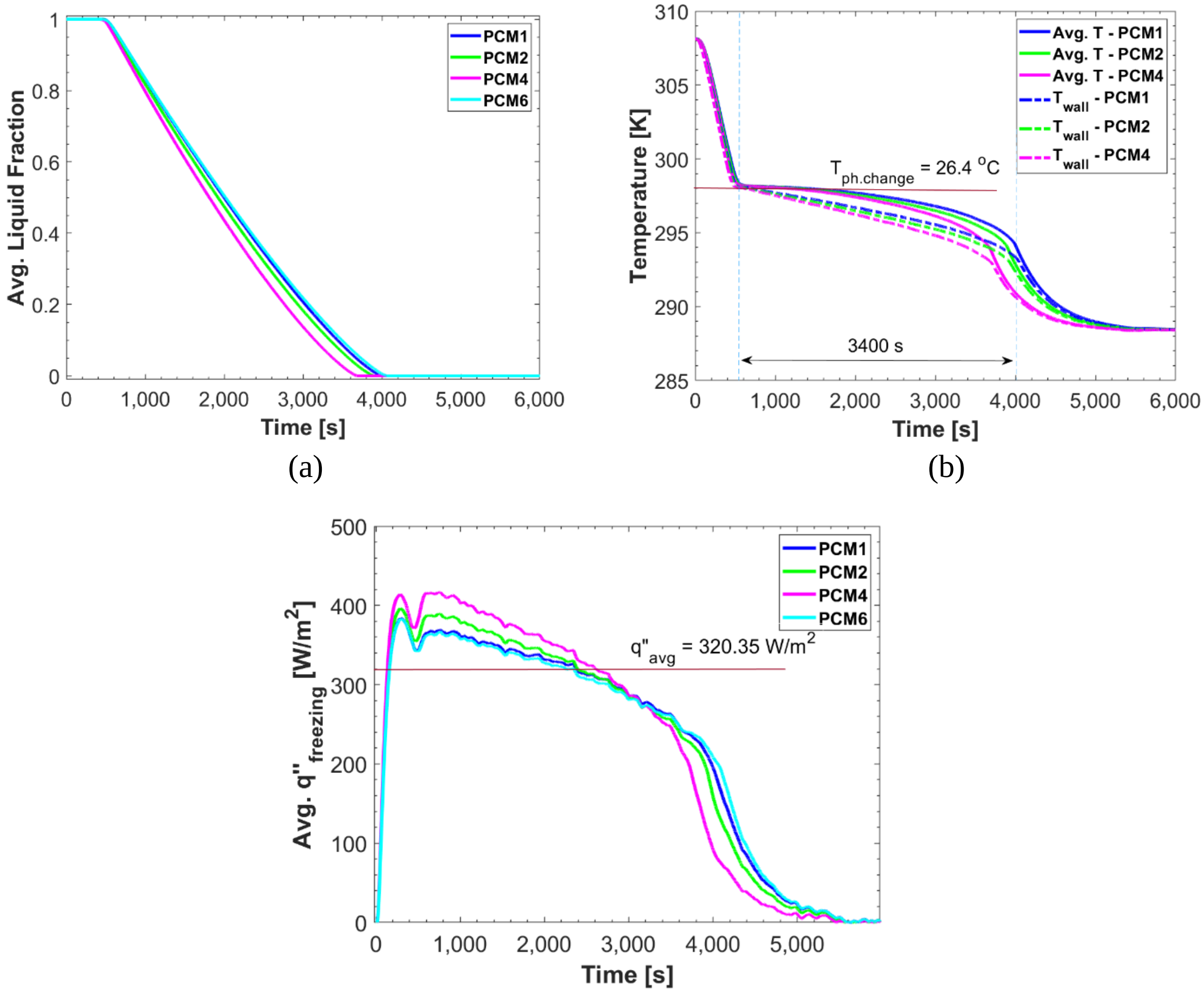

(a) (b)

(c)

Figure 3. 12. Solidification parameters as a function of time: (a) Evolution of average liquid fraction of PCMs, (b) Temperature of PCM and tube wall, (c) Peripheral average of wall heat flux (q″)

The results also show that the air temperature at the array outlet (see Figure 3.10a) is approximately 7.5 K (or °C) lower than the PCM phase change temperature at the beginning of the PCM freezing. This temperature difference is caused by the resistance to heat transfer, both the convection on the tube wall and conduction through the tube wall. As the average PCM temperature decreases during the PCM freezing, the average tube wall temperature also decreases (see Figure 3.12b), resulting in a lower air temperature leaving the array compared to the PCM phase change temperature . This temperature difference increases as the PCM freezing increases.

Figure 3.12c displays the distribution of the peripherally averaged wall heat-flux (q″) along the tube wall over time, where q" was calculated using Fourier's law, as mentioned earlier. A positive value of the heat-flux indicates outward heat transfer from the tube wall, leading to a decrease in temperature of the liquid PCM.

Initially, q″ is zero, but it starts to increase as heat conduction takes place through the tube wall, resulting in a decrease in the PCM temperature. Once all the liquid PCM in the tube has frozen completely, the heat transfer across the tube wall stops, and wall heat-flux returns to zero. Higher wall heat-flux signifies higher freezing rates, which result in shorter freezing times. As shown in Figure 3.12c, the peripheral average wall heat-flux is higher for the tubes in the second row (tube 4) compared to the other tubes. Consequently, the freezing process is faster for tube 4 in comparison to tube 1 (first row) and tube 6 (last row), as discussed earlier. The average value of wall heat-flux for all tubes during the freezing process is 320.35 W/m².

Table 3. 7 Comparison of heat transfer coefficient (h_{num}) for individual PCM filled tubes in the flow direction

Tube No.	h_{num} (W/m^2-K)	
	Melting	Solidification
PCM 1	47.00	48.00
PCM2	50.00	51.00
PCM4	57.27	55.69
PCM6	47.27	47.53

Table 3.7 summarizes the heat transfer coefficient values for the tubes PCM1, PCM2, PCM4, and PCM6 for the PCM melting and freezing. In the staggered tube array, the flow is tortuous even for small Re_D number ($Re_D \leq 100$) [83], which enhances the heat transfer within the

tubes. As indicated in Table 3.7, the heat transfer coefficient is the highest for the tubes in the second row (tubes 3 and 4, Figure 3.2) for both the PCM melting and freezing, while tubes in the first row and last rows (see Figure 3.2) have the lowest heat transfer coefficients, due to small changes in flow as it progresses downstream through the tube array.

Figure 3.13 shows the PCM melting and freezing times for the tubes in the direction of the flow for a staggered tube bank. As discussed before, since the heat transfer rate is higher for the tubes in the second row (tube 3 and 4, see Figure 3.2), the melting/ freezing rate is faster for these tubes. On average, the melting process takes approximately 1.2 hours to complete, while the freezing process takes approximately 1.08 hours.

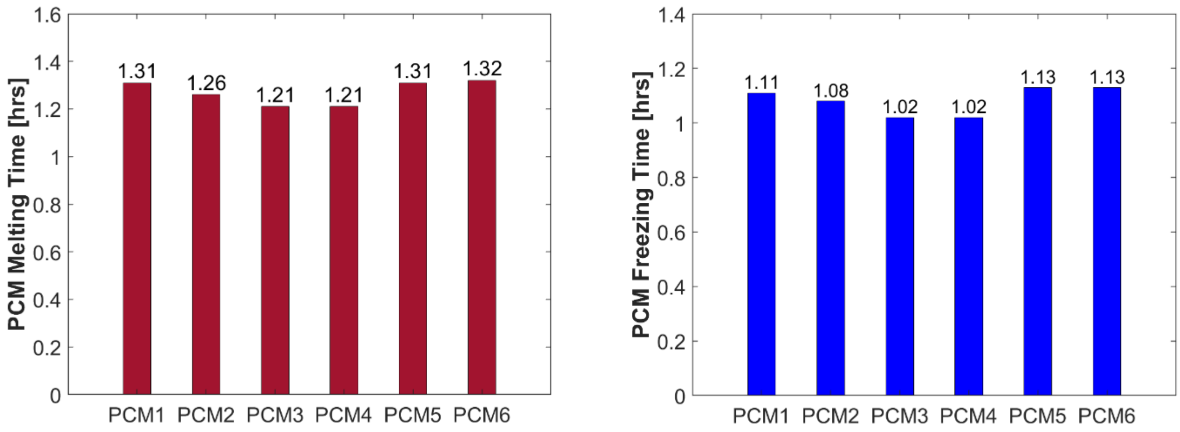

(a) (b)

Figure 3. 13. Comparison of time required for PCM melting and freezing in the 4-row tube array in the direction of the flow: (a) melting, (b) freezing.

Figures 3.14 and 3.15 show the predicted contours of PCM liquid fraction within the tubes and temperature of the air surrounding the array of tubes for the conditions corresponding to the PCM melting and freezing, respectively. The time intervals considered are 600 seconds (10 minutes) during PCM melting for freestream air velocities of 1.1 m/s and 0.79 m/s during PCM freezing.

In the legend for liquid fraction, the red color represents a liquid fraction of one, indicating complete melting, while the blue color denotes frozen PCM with a liquid fraction of zero. For PCM melting, the temperature legend uses red color to represent 308 K or 35 °C (inlet air temperature) and blue to represent temperatures lower than the PCM phase change temperature, such as 293 K or 20 °C. A thin green-yellow ring around the solid PCM indicates the mushy zone. The melting of PCM initiates on the tube periphery and proceeds inwards.

The results presented in Figure 3.14 illustrate dynamics of the PCM melting in the 4-row PCM array. As heat is transferred from the air flowing around the tubes to the PCM in the tubes, the PCM temperature rises, and melting commences. This process begins in the first row of tubes and advances to the downstream tube rows. After approximately 3,000 seconds, a substantial amount of PCM in the front end of the array has melted, while a small quantity of solid PCM remains in the back of the array. By approximately 4,200 seconds, almost all of the PCM in the tubes has melted, with very little solid PCM remaining in the back rows. The dynamics of PCM melting elucidates the time variation of air temperature at the array outlet and PCM temperature in tubes 1 (upstream) and 5 (downstream), as discussed earlier and shown in Figure 3.9 a, c.

Figure 3.15 illustrates dynamics of the PCM freezing in the 4-row PCM array. Heat is transferred from the PCM inside the tubes to the cold air flowing around the tubes, resulting in a decrease in the PCM temperature, and the onset of PCM freezing. Similar to the melting process, freezing initiates in the first row of tubes and progresses downstream. After approximately 3,600 seconds, almost all of the PCM in the array has frozen, with a small amount of liquid PCM remaining in the centers of the PCM tubes. By approximately 4,200 seconds, all PCM in the tubes has frozen. The dynamics of PCM freezing explains the time variation of air temperature at the array outlet and PCM temperature in tubes 1 (upstream) and 5 (downstream), as discussed earlier and shown in Figure 3.10 a, c.

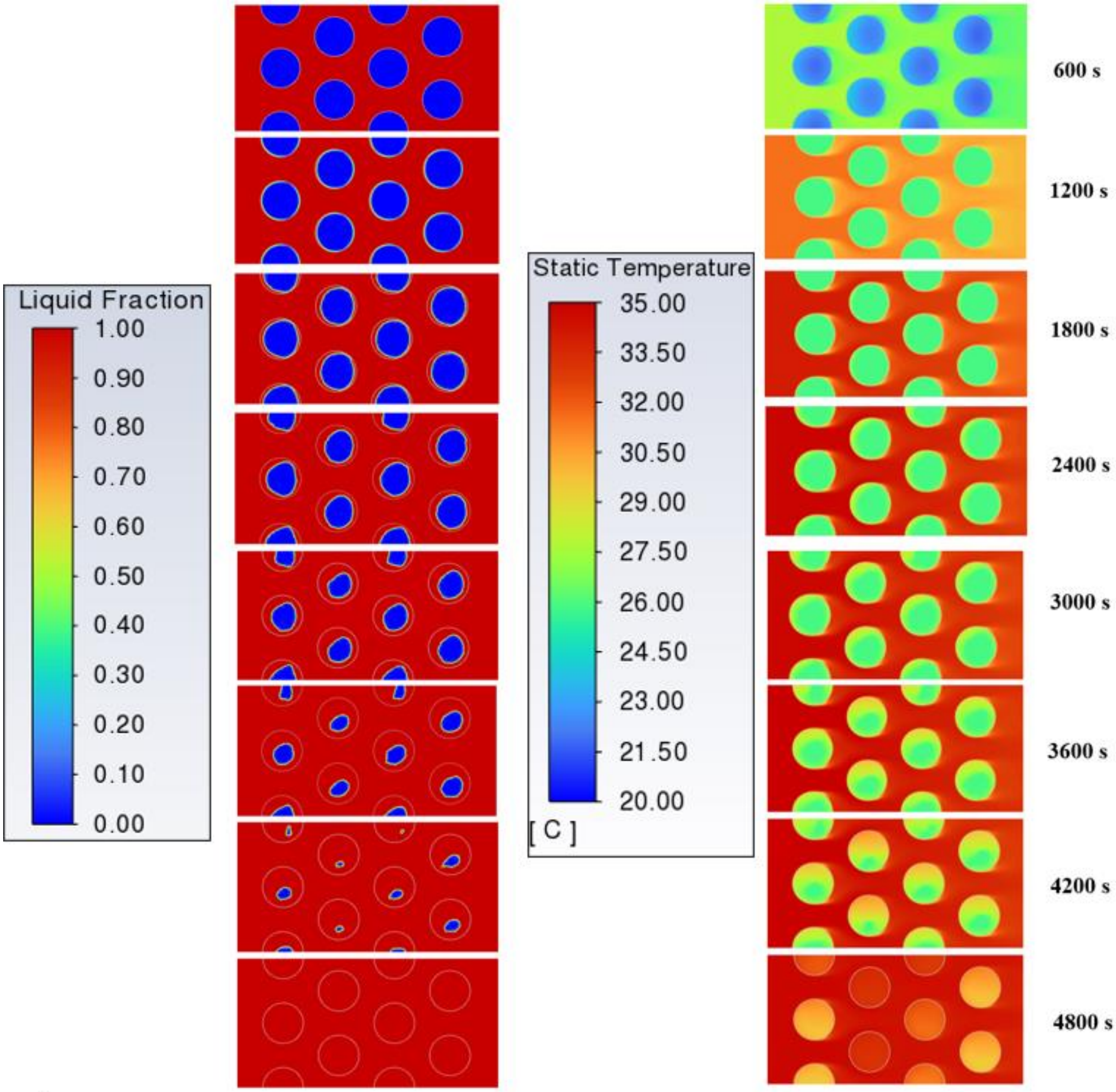

Figure 3. 14. Contours of PCM liquid fraction in tubes and air temperature in the 4-row tube array during PCM melting as functions of time for freestream air velocity of 1.1 m/s.

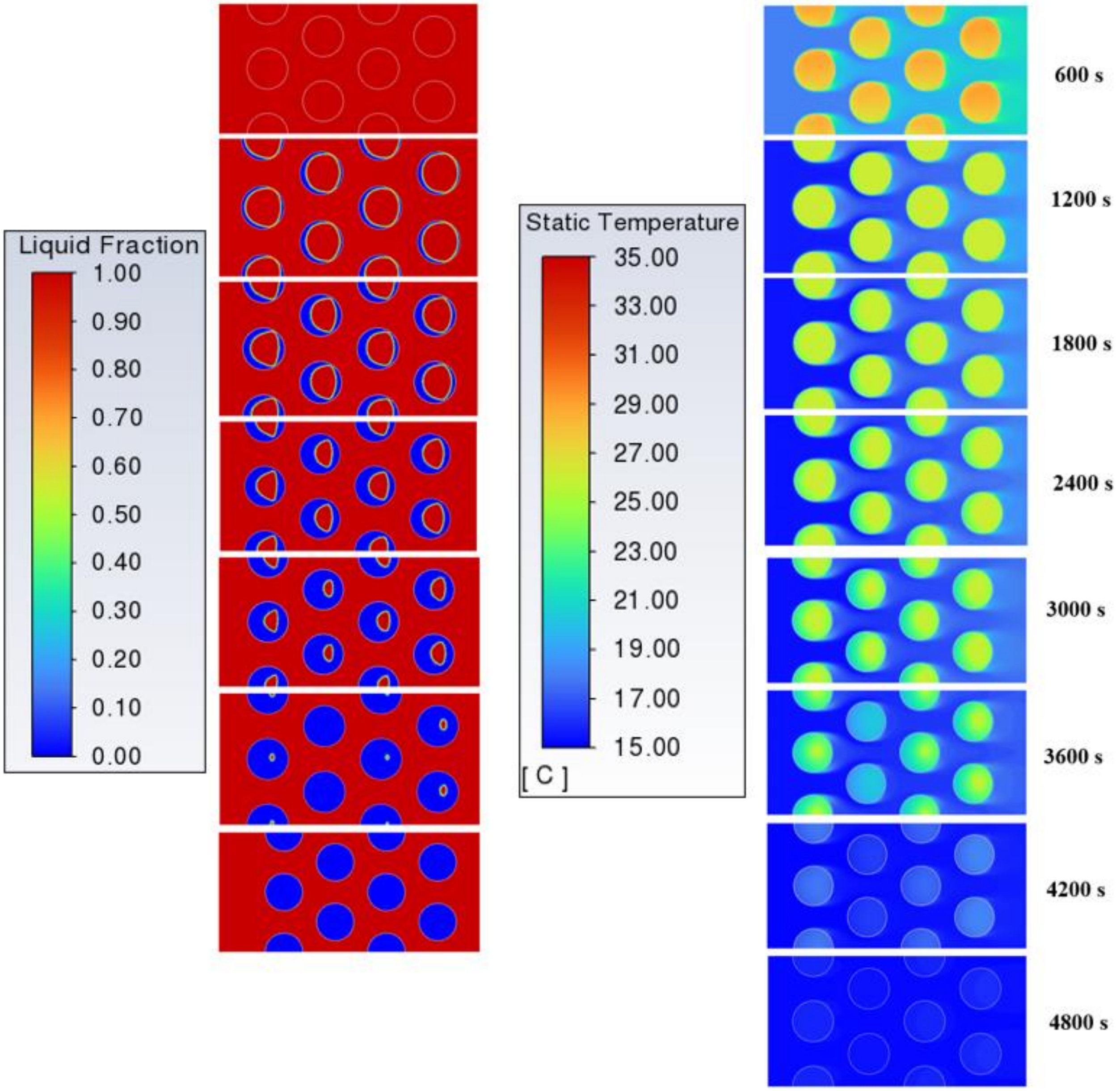

Figure 3. 15. Contours of liquid fractions of PCM in tubes and air temperature in the 4-row tube array during PCM solidification as functions of time for freestream air velocity of 0.79 m/s.

Figure 3.16 presents the details of the PCM melting and freezing processes one hour (3,600 seconds) after the initiation of the test. The contours of the PCM liquid and solid fractions indicate that one hour into the PCM melting test, PCM near the tube center is frozen, while in the freezing test, PCM in the region near the tube center is in a liquid state. The temperature difference between the solid and liquid states being of the order of 1 to 2 °C accounts for difference between the measured PCM temperature at the tube center and the average PCM temperature in the tube and explains a significant part of the observed difference between the experimental data and numerical predictions (see Figures 3.9c, 3.10c).

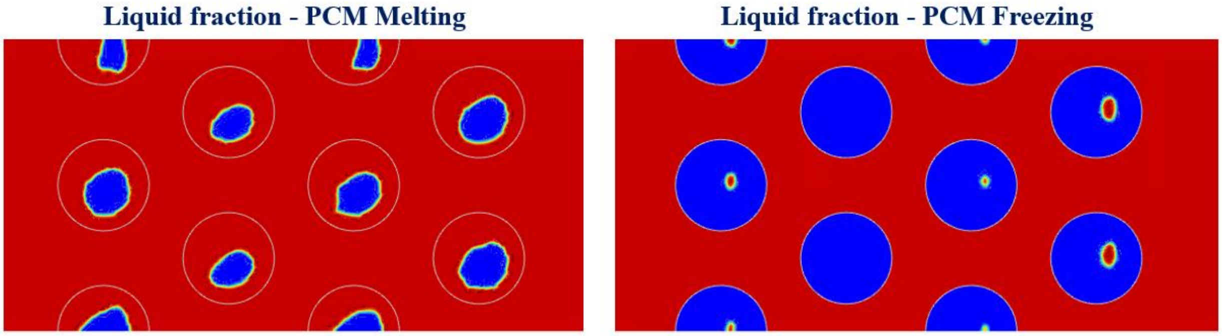

Figure 3. 16. Contours of liquid fraction of PCM in the tube array 1 hour (3600 s) after beginning of the PCM melting and freezing tests

Figure 3.17 displays the contours of the predicted air velocity fields within the tube array for the PCM melting and freezing tests. In the PCM melting tests, the air velocity increases from the inlet value of 1.1 m/s to approximately 3 m/s as the flow accelerates while passing through the minimum area between the tubes. As the flow passes through the staggered tube arrangement, it decelerates as flow area increases. The flow accelerates again when passing through the next minimum flow area between the tubes. Consequently, the air flow through the tube array undergoes a series of accelerations and decelerations. Upon exiting the array, the flow further decelerates, reaching the superficial air velocity of 1.1 m/s.

During the PCM freezing, the air velocity follows a similar pattern. It increases from the inlet value of 0.79 m/s to 2.11 m/s as it accelerates through the minimum cross-sectional area. Similar to the PCM melting, the air flow within the tube array experiences a series of accelerations and decelerations.

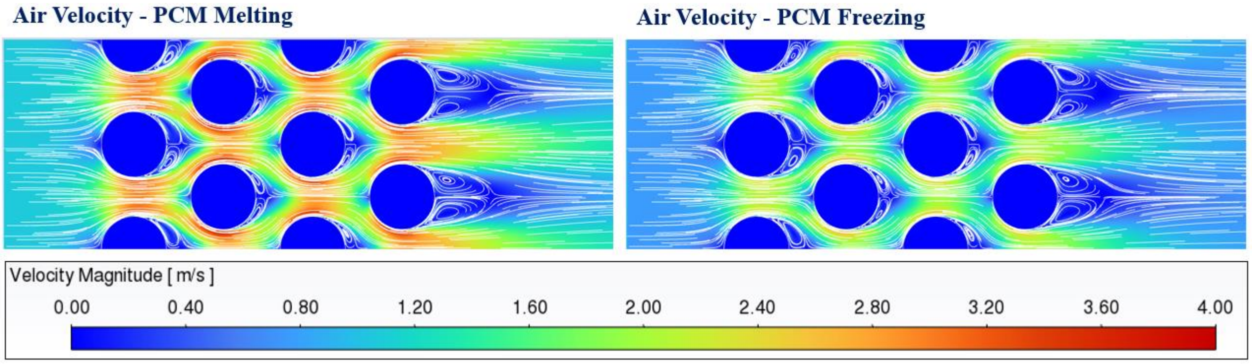

Figure 3. 17. Contours of numerical prediction of air velocities in the 4-row tube array for freestream air velocities of 1.1 m/s (PCM melting) and 0.79 m/s (PCM solidification)

3.3.3. Energy and exergy analysis

The energy and exergy analyses were performed for the laboratory scale (4-row tube array) LTES to evaluate the efficiency and effectiveness of the system. The energy transfer across the tube bank over a period of time was calculated following the traditional heat transfer analysis from the literature [5, 40] as shown in Eq. 3.21:

$$E_{in} = \int_0^t \dot{m}_{air} C_{P_{\mathrm{air}}} (T_{in} - T_{out})\, \mathrm{d}t \tag{3.21}$$

The average value of energy stored in all PCMs is calculated considering the liquid fraction (γ) and the average PCM temperature as presented in Eq. 3.22 [5]:

$$E_{st} = \frac{1}{N} \sum_0^N m \left[\int_{T_{low}}^{T_{melt}} Cp_{solid} (1 - \gamma)\, dT + \gamma L_f + \int_{T_{melt}}^{T_{high}} Cp_{liquid}\, \gamma\, dT \right] \tag{3.22}$$

where, N is the number of the tubes. Cp_{solid} and Cp_{liquid} are the specific heat of the frozen and melted PCM, respectively.

As the experiment does not provide data on the liquid fraction, linear variation was assumed. Therefore, PCM temperature exhibits nearly linear change during the phase transition (as shown in Figures 3.7c and 3.8c), also, an average value of the specific heat of PCM was employed to compute the energy stored in the PCM-filled tubes for the experimental results.

From an energy perspective, only heat generation through viscous dissipation was considered as a loss, resulting in very high overall efficiencies [110]. The energy efficiency (η) of the system is derived from the ratio of the stored energy and energy transfer to the system (Eq. 3.23):

$$\eta = \frac{E_{st}}{E_{in}} \tag{3.23}$$

Since the energy balance does not consider the internal or external losses in the system, exergy balance over a period was carried out to take into account the entropy losses and calculate the useful work in the system following the expression Eq. (3.24)

$$Ex_{in} = \int_0^t \dot{m}_{air} C_{P_{\mathrm{air}}} \left[(T_{in} - T_{out}) - T_o \ln\left(\frac{T_{in}}{T_{out}}\right) \right] \mathrm{d}t \tag{3.24}$$

The exergy stored in the PCM using the ambient temperature (T_o) was computed from the Eq. (3.25)

$$Ex_{st} = E_{st} \left[1 - \frac{T_o}{T_{PCM}} \right] \tag{3.25}$$

The exergy efficiency ($\boldsymbol{\Xi}$) of the system is derived from the ratio of the exergy stored and exergy transfer to the system (Eq. 3.26):

$$\boldsymbol{\Xi} = \frac{Ex_{st}}{Ex_{in}} \tag{3.26}$$

The maximum possible energy can be stored when the average PCM temperature equals the inlet temperature of the heat transfer fluid (air). Eqs. (3.27), (3.28) were used to calculate the maximum energy and maximum exergy that could be stored in the system, respectively.

$$E_{st_{\max}} = \int_{T_{PCM}}^{T_{in}} m\, Cp_{avg.}\, dT + \, mL_f \tag{3.27}$$

$$Ex_{max} = E_{st_{\max}} \left[1 - \frac{T_o}{T_{in}} \right] \tag{3.28}$$

To investigate the effectiveness of the system, the energy efficiency and exergy effectiveness were calculated from the ratio of the actual energy/ exergy stored to the maximum energy/ exergy that could be stored as shown by Eq. (3.29) and (3.30), respectively.

$$\epsilon = \frac{E_{st}}{E_{st_{\max}}} \tag{3.29}$$

$$\chi = \frac{Ex_{st}}{Ex_{\max}} \tag{3.30}$$

The energy and exergy parameters were outlined as a function of the dimensionless parameter, Fourier number (Fo), dimensionless time, calculated from Eq. (3.31)

$$Fo = \frac{\alpha_d t}{D^2} \tag{3.31}$$

where, thermal diffusivity, $\alpha_d = \frac{k_{air}}{\rho_{air} C_{p_{air}}}$

3.3.3.1. Melting process of PCM

Figure 3.18a shows the comparison between the energy variation over dimensionless time, the Fo number, during the PCM melting in the 4-row tube array. This comparison is also made between the experimental and numerical analyses. For the numerical prediction (solid line), the energy transfer in the storage moduleis higher compared to the experiment (dotted line). This discrepancy arises because the numerical analysis simulates an ideal case, neglecting ambient effects on the storage (Figure 3.18a). The stored energy (heat) increases as long as there is a temperature difference between the inlet and outlet of the array, until the phase change material (PCM) in the tubes completely melts and starts superheating. The maximum energy transferred to the system during charging is approximately 885 kJ for the numerical prediction and 755 kJ for the experimental results.

The numerically and experimentally obtained values of energy stored in the PCM-filled tube are almost identical, with a difference of less than 5%. As indicated in Figure 3.18a, the maximum energy that could be stored during the melting process is higher compared to the actual stored energy. Achieving the maximum storage is practically impossible, as it would require the average PCM temperature to be equal to the inlet air temperature, or a tube of infinite length. For both the numerical and experimental results, the quantity of the maximum possible energy that could be stored is approximately the same. All energy parameters continue to increase until they reach a maximum value and remain constant, signifying that the PCM in the tubes has started to superheat (Figure 3.18a).

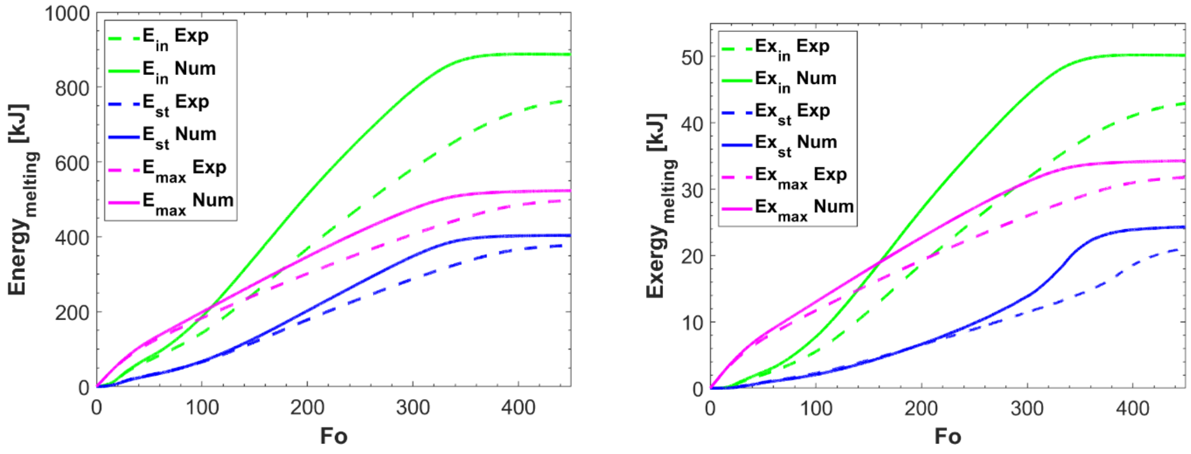

(a) (b)

Figure 3. 18. (a), (b) Comparison of experiment and numerical results of energy and exergy analysis in the laboratory scale (4-row tube array) LTES during melting as functions of the Fo number, respectively.

The variation of exergy quantities with the Fo number for the melting process is presented in Figure 3.18b. Exergy is an important parameter in the analysis as it assesses the entropy generation in the system caused by the irreversibility associated with heat transfer. When the temperature driving force is higher, it leads to increased entropy generation and higher exergy destruction. In this case, with T_{in} = 308 K or 35 ºC, the inlet air temperature is about 10 ºC higher compared to the fusion temperature of PCM ($T_{ph.change}$ = 299.55 K or 26.4 ºC), resulting in a significantly lower exergy quantities compared to energy quantities for the PCM melting process. As time progresses, the exergy stored in the system increases due to an increase in the average PCM temperature, which can be identified as convection dominant zone. The increase in temperature difference between the inlet and outlet (as shown earlier in Figure 3.9b) causes higher exergy input and higher maximum exergy. Once the PCM gets melted completely, the exergy becomes almost constant since conduction becomes the predominant mode of heat transfer. The exergy during the melting process is significantly lower than the energy, mainly due to both internal and external irreversibilities. It is crucial to minimize factors like heat gain to enhance overall performance.

In Figure 3.19, the energy and exergy efficiency and effectiveness during the melting process are presented. The relatively low thermal conductivity of stainless-steel limits the heat transfer through the tube wall, leading to low energy efficiency (Figure 3.19a). The maximum energy efficiency is achieved when the PCM starts to superheat. Since the amount of transferred heat predicted by numerical analysis is higher compared to the experiment with almost the same amount of energy stored as measured in the experiment, the energy efficiency is slightly lower for the numerical results ($\eta = 0.45$) compared to the experiment ($\eta = 0.49$) (Figure 3.19a).

Figure 3.19a shows that the exergy efficiency increases in the beginning as the average temperature of the PCM increases during the melting process (Figure 3.9c). As the conduction mode of heat transfer becomes more dominant during the phase change period, the efficiency decreases until around 4700 s (see Figure 3.9c), and then it starts to increase again to reach the maximum value ($\boldsymbol{\Xi} = 0.49$) during the PCM superheating, as demonstrated in Figure 3.19a. During the phase change period, the experimentally obtained value of exergy efficiency is slightly higher than the numerical one but becomes the same during PCM superheating.

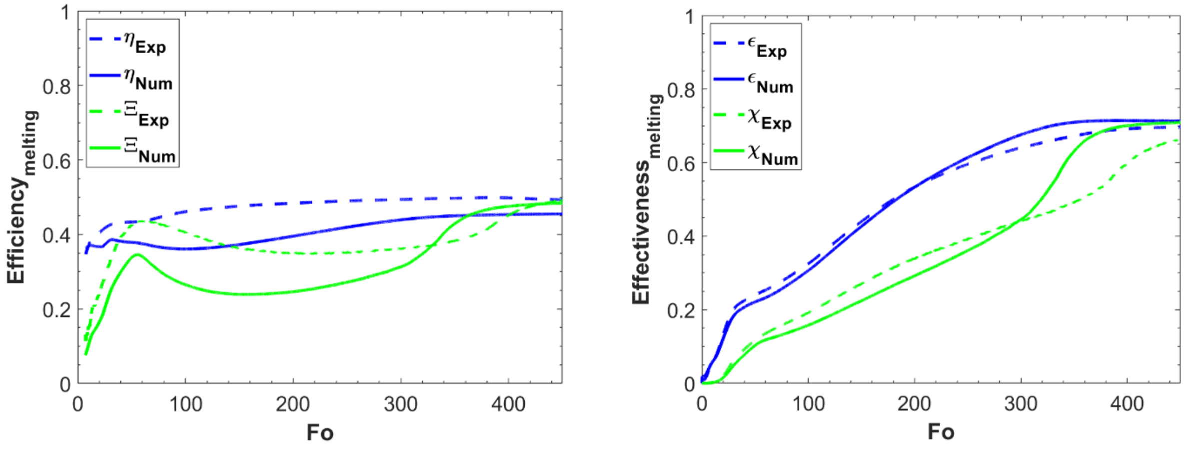

(a) (b)

Figure 3. 19. (a), (b) Comparison of experiment and numerical results of efficiency and effectiveness of the laboratory scale (4-row tube array) LTES during melting as functions of the Fo number, respectively.

In summary, to determine the storage effectiveness during the charging (melting) process, the study introduced energetic (ϵ) and exergetic (χ) effectiveness, , i.e., the ratio of stored energy/exergy to the maximum energy/exergy that could be stored, presented as functions of the Fo number as shown in Figure 19b. The energetic and exergetic efficiency/effectiveness exhibit similar trends during the PCM melting process. As the effectiveness increases, the melting time decreases. Figure 3.19b shows that the effectiveness continuously increases over the examined period (as the Fo number increases). The numerical and experimental results show almost identical values for the two effectiveness parameters. The maximum exergetic effectiveness calculated from the measurements is 0.66, while it is 0.7 for the numerical results during the melting process. The maximum value of energetic effectiveness and exergetic effectiveness (0.7) (see. Fig 3.19b) is higher compared to the energetic and exergetic efficiencies (0.49) (see. Fig 3.19a) during PCM melting process.

3.3.3.2. Solidification process of PCM

Figure 3.20a presents a comparison of the energy variation with respect to a dimensionless time, Fo number, during the PCM freezing. Similar to the PCM melting, the comparison was made between the experimental and numerical analyses and results. Similar to the melting, the numerical prediction (solid line) of the energy transfer is higher compared to the experimental results (dotted line). As discussed before, this disparity arises because the numerical analysis simulates an ideal scenario, neglecting ambient effects on the storage (Figure 3.20a). As long as there is a temperature difference between the inlet and outlet air temperature to/from the tube array, the amount of stored thermal energy increases until the PCM in the tubes completely freezes and starts to subcool. The maximum amount of thermal energy transferred to the system during the PCM freezing obtained numerically is approximately 745 kJ, while experimental results give 535 kJ.

As presented in Figure 3.20a the numerical analysis predicts higher amounts of stored energy in the PCM-filled tube array during the PCM freezing compared to the experiment. The maximum energy, calculated from the experimental data, that could be stored during the freezing is higher compared to the actual stored energy, which is expected due to the heat losses to the ambient. The numerical results predict nearly the same amount of maximum energy that could be stored during freezing as the experiments. The amounts of stored energy and the maximum energy that could be stored in the PCM-filled tube obtained in numerical analysis are identical in the numerical analysis since no heat losses to the environment were considered in the model. All energy parameters continued to increase until they reach a maximum value and remain constant. This indicates that PCM temperature and air temperature are the same, thus there is no heat transfer. Heat transfer can continue in the PCM subcooled or superheated regions because of the conduction predominance mode.

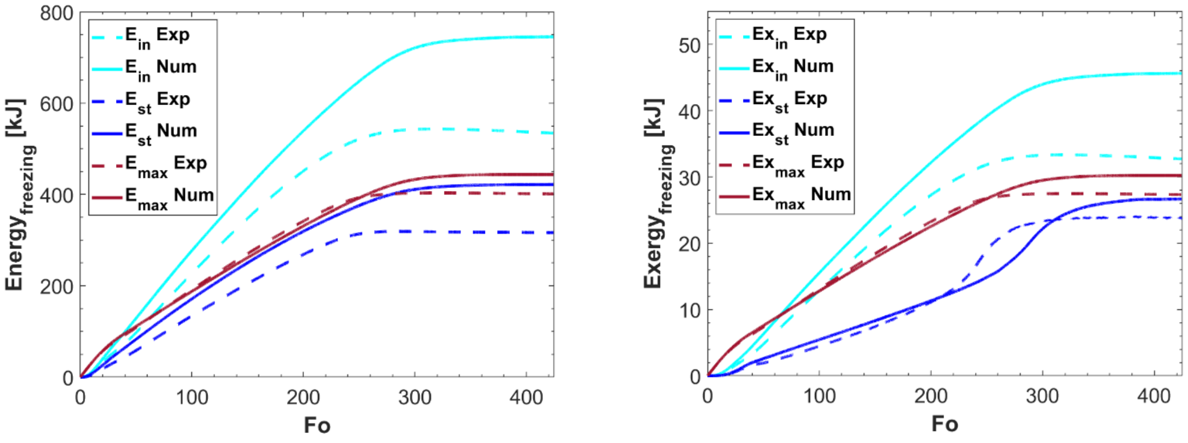

(a) (b)

Figure 3. 20. (a), (b) Comparison of experimental and numerical results of energy and exergy analysis in the laboratory scale (4-row tube array) LTES during solidification as functions of the Fo number, respectively.

Similar to the melting process, the variation of exergy quantities with respect to the dimensionless time (Fo number) for the freezing process is illustrated Figure 3.20b. The entropy generation increases with the increase in temperature driving force which results in higher exergy destruction. In this case, with T_{in} = 288 K or 15 ºC, lower than the PCM fusion temperature of 299.55 K (26.4 ºC) the temperature driving force is approximately 10 K (or ºC), than the fusion temperature of the PCM ($T_{ph.change}$ = 299.55 K or 26.4 ºC), resulting in lower values of exergy quantities compared to the energy quantities for the freezing process. As time progresses and Fo increases, the exergy increases since the difference between inlet air temperature and PCM solidification temperature decreases during the PCM freezing because of the convective heat transfer.

The energy efficiency and exergy effectiveness during the PCM freezing process are presented in Figure 3.21 as functions of dimensionless time, Fo number. The relatively low thermal conductivity of stainless-steel limits the heat transfer through the tube wall, resulting in low energy efficiency (Figure 3.21a). The energy efficiency decreases as the PCM starts to subcool because conduction becomes the dominant mode of heat transfer. The efficiency values computed from the experimental data and numerical analysis are almost identical. The energy efficiency, η determined from the numerical results is 0.57 while for the experiment, it is 0.59 (Figure 3.21a).

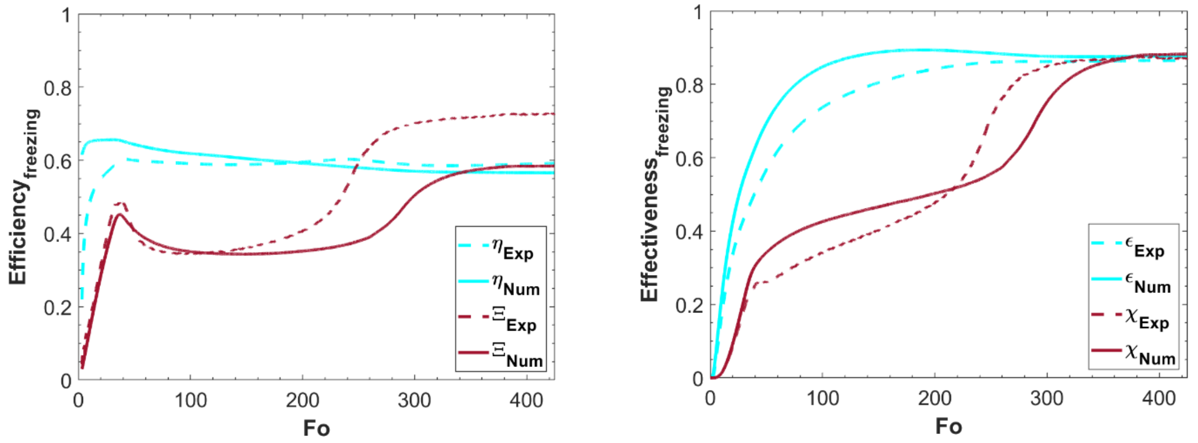

(a) (b)

Figure 3. 21. (a), (b) Comparison of experiment and numerical results of efficiency and effectiveness of the laboratory scale (4-row tube array) LTES during solidification as functions of the Fo number, respectively.

Figure 3.21a shows that the exergy efficiency ($\boldsymbol{\Xi}$) initially increases as the difference between PCM average temperature and inlet air temperature decreases during the freezing process (Figure 10), as discussed earlier. However, during the phase change period, as the conduction mode of heat transfer becomes more dominant, the numerically predicted value of efficiency gradually decreases until around 4000 seconds (see Figure 3.10c) corresponding to Fo number of 283. Afterwards, the exergy efficiency starts to increase again, reaching the maximum value of 0.58 during PCM subcooling, as shown in Figure 3.21a. For the freezing process, the experimental exergy efficiency is higher than the numerically predicted with a maximum value of 0.72. The results presented in Figure 3.21a show that for the experimental results the exergy efficiency is higher than the energy efficiency which is practically impossible since exergy accounts for the internal and external irreversibility. This is an indication of experimental error during the freezing test as discussed before in section 3.3.1 (referred to Figure 3.10c).

In summary, to evaluate the storage efficiency and effectiveness during the PCM freezing, energetic effectiveness (ϵ) and exergetic effectiveness (χ) were determined. The results are presented as functions of the Fo number, as shown in Figure 3.21b. As the heat storage effectiveness increases, the freezing time decreases. The experimental and numerical results show a similar trend for energetic effectiveness. The same trends are observed for the exergetic effectiveness calculated from the experimentally obtained and numerically predicted results.

Figure 3.21b shows that the storage effectiveness continuously increases over the examined period as the Fo number increases. The numerical and experimental results show nearly identical values for the two effectiveness parameters. During the solidification process of PCM, the energetic effectiveness and exergetic effectiveness parameters exhibit different trends from each other. However, the trends converge to the same value during subcooling. For solidification process, the maximum value of energetic effectiveness and exergetic effectiveness is 0.87 for numerical and experimental results.

3.3.4. Thermal loss and uncertainty analyses

To enhance the accuracy of the energy balance approach, it is essential to consider the heat lost between the air and the duct wall. Furthermore, examining the thermal loss within the system during the experiment provides insight into potential reasons for the observed discrepancy between numerical and experimental results discussed in earlier sections. The calculation for the thermal energy exchanged between the air and the wall (Q_{wall}) is as follows:

$$Q_{wall} = \int_0^t \dot{Q}_{wall}\,\mathrm{d}t = m_{wall} C_{P_{\text{wall}}} \left(T_{wall,initial} - T_{wall,final}\right) \tag{3.32}$$

where, m_{wall} and $C_{P_{\mathrm{wall}}}$ denote the mass and specific heat of the wall surrounding the module, and for all cases, these values are 9.50 kg and 0.49 kJ/kg.K, respectively. The initial ($T_{wall,initial}$) and final ($T_{wall,final}$) wall temperatures are identical to the initial and final inlet air temperatures.

The heat loss between the air and the duct wall, computed using Eq. 3.32, is approximately 90 kJ. Since the initial and final temperature difference is approximately the same for both melting and solidification processes, the same amount of heat is lost at the duct wall during both processes, accounting for approximately 15% of the transferred heat to the system.

Uncertainty analysis was performed, considering the uncertainties during the measurement (see Table 3.5), which is another probable reason for the discrepancy between the numerical and experimental results. Analyses of uncertainty for the energy transferred through the system and the energy stored in the system were conducted using the following expression [39]:

$$w_R = \left[\left(\frac{\partial R}{\partial x_1} w_1\right)^2 + \left(\frac{\partial R}{\partial x_2} w_2\right)^2 + \cdots + \left(\frac{\partial R}{\partial x_n} w_n\right)^2\right]^{1/2} \tag{3.33}$$

where, w_R is the uncertainty in the result, R and w_1, w_2, …, w_n are the uncertainties in the independent variables x_1, x_2, …, x_n.

Following the expression in Eq. 3.33, the uncertainty for the stored energy is found to be approximately 5.5 kJ, equivalent to 2%, while the uncertainty for the energy transferred through the system is approximately 0.2 kJ, or 0.03%, during the experiment.

3.4. Conclusions

A lab-scale (4-row) tube array was designed to analyze the performance of the LTES system in cooling down the incoming air to the ACC. Numerical analysis of PCM melting and solidification in a staggered tube configuration, oriented horizontally, was conducted to guide the design procedure. This paper also presents energy and exergy analyses of the system. Thermal loss at the duct wall and measurement uncertainty analyses were performed to address the discrepancy between the numerical and experimental results. Key findings and conclusions from the study include:

- The PCM melting and solidification process in the tube array is asymmetric, where the second row of PCM-filled tubes experiences faster melting/freezing due to secondary flows, enhancing heat transfer.
- The corresponding design, consisting of 2.88 kg of PCM, can maintain a cooling effect for approximately 3,960 seconds during melting, while it can sustain the phase change temperature for approximately 3,000 seconds during freezing.
- The maximum energy efficiency achieved for the corresponding design is 49% and 59% during the PCM melting and freezing processes, respectively. The maximum exergy efficiency, considering entropy generation, is 49% and 58% during the melting and freezing processes, respectively.
- The maximum energy and exergy effectiveness achieved during the PCM melting process for the laboratory-scale tube array are 70% and 66%, respectively, while during the PCM solidification process, the maximum energy and exergy effectiveness reach 87%. This provides insight into the system's performance.
- For the tested system, the heat loss between the air and the duct wall accounts for approximately 15% of the transferred heat to the system, while measurement uncertainties contribute to approximately 5.5 kJ, or a 2% discrepancy in stored energy, and approximately 0.2 kJ, or a 0.03% discrepancy in energy transferred.

Author contributions

Mahfuja A. Khuda: Numerical analysis, Investigation, Methodology, Software, Verification & Validation, Post-processing, Writing – original draft.

Lida Yan: PCM preparation, Experiment, CAD model, Writing – Experimental setup.

Javad Khalesi: Software, Methodology, Verification.

Nenad Sarunac: Conceptualization, Project administration, Resources, Supervision, Writing - review & editing.

Carlos Romero: Conceptualization, Project administration, Resources, Supervision.

Conflict of interest

The authors declare no conflict of interest.

Acknowledgement

The paper is based upon work supported by the U.S. Department Office of Fossil Energy FE-1 under Award Number DE-FE0031886.

Disclaimer

This paper was prepared as an account of work sponsored by an agency of the United States Government. Neither the United States Government nor any agency thereof, nor any of their employees, makes any warranty, express or implied, or assumes any legal liability or responsibility for the accuracy, completeness, or usefulness of any information, apparatus, product, or process disclosed, or represents that its use would not infringe privately owned rights. Reference herein to any specific commercial product, process, or service by trade name, trademark, manufacturer, or otherwise does not necessarily constitute or imply its endorsement, recommendation, or favoring by the United States Government or any agency thereof. The views and opinions of authors expressed herein do not necessarily state or reflect those of the United States Government or any agency thereof.

CHAPTER 4/ ARTICLE 2

Design, analysis, and testing of a prototype-scale latent heat thermal energy storage (LTES) system

Mahfuja A. Khuda[1*], Lida Yan[2], Nenad Sarunac[1],
Carlos Romero[2]

[1] Mechanical Engineering and Engineering Science, UNC Charlotte, Charlotte, NC 28223, USA. m12a34k5@charlotte.edu

[2] Energy Research Center, Lehigh University, Bethlehem, PA 18015, USA.

* Correspondence author

Highlights

- Parametric analysis was performed numerically to design prototype scale module using a 13-row tube array.
- Numerical results of PCM melting and solidification model was compared with the experiment.
- The proposed design met the performance criteria of cooling effect of 4 °C for a duration of 4 hours.
- The pressure drop across the tube array satisfies the pressure drop requirement of 100 Pa or less.

Abstract

A parametric analysis was performed to design a prototype-scale latent heat thermal energy storage (LTES) system using commercial grade hexahydrate calcium chloride as phase change material (PCM) in a staggered tube array configuration, placed horizontally. The study involved numerical analysis of melting and solidification processes of the PCM within the tube array, considering transient two-dimensional Navier-Stokes equations and a Realizable k-ε turbulence model to predict fluid flow and heat transfer. The enthalpy-porosity technique was used to model PCM melting and solidification. The study included a comparison between numerically predicted and experimentally obtained air temperatures at the tube array outlet, as well as PCM temperatures. This comparison revealed an excellent level of agreement. Additionally, the study compared the pressure drop within the array and the average peripheral heat transfer coefficient calculated from the numerical results to the well-established Zukauskas correlation. The resulting design successfully met the predefined performance criteria: achieving a cooling effect of 4 °C for a four-hour duration while maintaining a pressure drop of less than 100 Pa. The proposed prototype-scale tube array design can be efficiently cooled down and PCM frozen overnight. The energy storage density of the system falls within the range of 22 to 27 kWh/m^3.

Keywords: Melting, Solidification, Tube array, CFD, Turbulent flow, Conjugate heat transfer

4.1. Introduction

There is an urgent demand for expediting the progress and implementation of cutting-edge clean energy technologies to tackle the worldwide issues of energy security, climate change, and sustainable development [111]. Thermal energy storage (TES) that exploits the latent heat of phase change materials (PCM) has attracted considerable attention from researchers. This is because it offers numerous advantages, including high energy storage density, nearly isothermal heat recovery, and chemical stability. The use of latent heat TES has now become an indispensable component in HVAC systems, solar powerplants, solar heating systems etc., primarily in response to growing environmental concerns, increased energy demands, and the widening gap between energy supply and demand [86, 112, 113]. It accomplishes energy savings by mitigating thermal losses and enhancing the efficiency of recovering stored thermal energy.

Thermal energy storage (TES) systems can be classified into three main categories: sensible heat storage [87, 88], latent heat storage [89, 90], and thermochemical energy storage systems [91, 92]. Sensible heat storage systems use sensible heat, but their lower energy density necessitates more space. Thermochemical storage offers higher energy density and longer storage durations, but its commercial application is constrained by high operating temperatures, slow reactions, and cost considerations [3].

In contrast, latent heat storage, which utilizes phase change materials (PCMs), provides high-density energy storage by capitalizing on phase changes occurring at specific temperatures [4]. PCMs offer the advantage of tailoring temperature transitions, storage durations, and cycle consistency, rendering them an excellent choice for low-temperature energy storage in industrial and commercial buildings [12]. Among the various configurations used for latent heat thermal energy storage (LTES), the shell and tube configuration has gained popularity due to its minimal heat loss and efficient cylindrical geometries [13, 14].

The choice of the phase change material (PCM) plays a critical role in latent heat thermal energy storage (TES) systems by increasing storage capacity, thereby enhancing the security of energy supply [20]. Some noteworthy PCMs, which have been documented by Zalba et al. [21], include Glauber's salt, calcium chloride hexahydrate/salt hydrate, sodium thiosulfate pentahydrate, sodium carbonate decahydrate, fatty acids, and paraffin waxes. Koca et al. [22] used salt hydrate ($CaCl_2 \cdot 6H_2O$) as a PCM to conduct an energy and exergy analysis of latent heat thermal energy storage in a flat-plate solar collector. Ghalambaz and Zhang [23] conducted a numerical study to examine how the use of a transient heat load influences the phase change behavior of a PCM in metal foams.

It is crucial to design an efficient LTES system tailored for HVAC applications. Several studies have focused on improving heat transfer and enhancing the design of LTES systems [15-18]. For example, Guo and Zhang [15] conducted a numerical study to assess the impact of heat exchanger geometry and thermal boundary conditions on the energy storage performance of a vertical shell-and-tube LTES. Wang et al. [16] examined how the temperature difference between the Heat

Transfer Fluid (HTF) and the melting point of PCM, as well as the inlet mass flow rate, affect the charging performance of a horizontal shell-and-tube LTES. Freeman et al. [19] discussed various thermal energy storage solutions for a residential-scale solar combined heat and power (CHP) system to fulfill both heat and electricity requirements during the night, although the authors did not consider its heat transfer performance under dynamic inlet parameters. Numerous experiments and numerical analyses [24, 97, 98, 105, 114] can be found in the literature. Uddin et al. investigate how the direction of HTF flow influences the intensity and duration of natural convection in PCM within a vertical cylindrical shell-and-tube container [114].

LTES system analyzed in this work is envisioned to be used to reduce the temperature of the cooling air entering the ACC (Air Cooled Condenser). The application of ACC in a coal-fired power plant is used to reduce water consumption compared to a wet-cooled condenser or wet cooling tower. However, the performance of dry cooling technology using ACC depends on ambient conditions. A lower inlet air temperature results in lower condenser pressure, higher turbine power output, and better power plant performance. The latent heat of PCM stored in the LTES system during the nighttime is discharged during the hottest period of the day to cool the inlet air to the air-cooled condenser (ACC). The design criteria of the LTES system analyzed in this study are to achieve a cooling effect of 4 °C for a duration of four hours while maintaining a pressure drop of less than 100 Pa and cooling down the system to freeze PCM overnight.

The current study extends the previous investigation of a laboratory-scale (4-row) tube array [115] to develop a prototype-scale LTES system with improved heat transfer performance. Similar to the design of the laboratory-scale tube array, a staggered arrangement of tube rows in a horizontal orientation was adopted in the direction of the air flow. A parametric study was conducted, considering various inlet boundary conditions to meet the final design requirements, as mentioned earlier. A dimensionless tube spacing in lateral and transverse directions of 1.25 was chosen to meet the pressure drop and storage density criteria. Numerical analysis of the phase change process (melting and solidification) of the PCM within the tube array was performed using ANSYS Fluent and then compared with experimental results.

The article is organized as follows: Section 4.2.2 presents the computational approach used to simulate the PCM melting and solidification processes within a 13-row tube array. Section 4.2.3 provides a description of the test facility and the experimental setup. Section 4.3.1 offers a comparison between the numerical and experimental results related to PCM melting and solidification. Finally, Section 4.3.2 includes the numerical prediction of liquid fraction, temperature, and velocity contours within the tube array during the PCM melting and solidification processes.

4.2. System description

4.2.1. Physical model

Figure 4.1 shows the design of a prototype tube array. A parametric numerical study was conducted for different tube diameters and inlet air velocities to design the prototype tube array that meets the performance criteria. The tube array comprises 208 tubes, each with an outer diameter (OD) of 1.75", constructed of carbon steel. The tubes have a thickness of 0.065" and a length of 35". These tubes were filled to 90% of their volume with a commercial-grade phase change material (PCM) to allow for PCM expansion during the phase change process. The total mass of PCM in the prototype tube array used for testing was 323.2 kg, equivalent to 1.553 kg in each tube. For the tube arrangement, a transverse tube spacing (S_T) and lateral (row) spacing (S_L) of 55.56 mm was used, resulting in dimensionless S_T/D and S_L/D ratios of 1.25. The tube-to-tube spacing (S) was set at 11.11 mm.

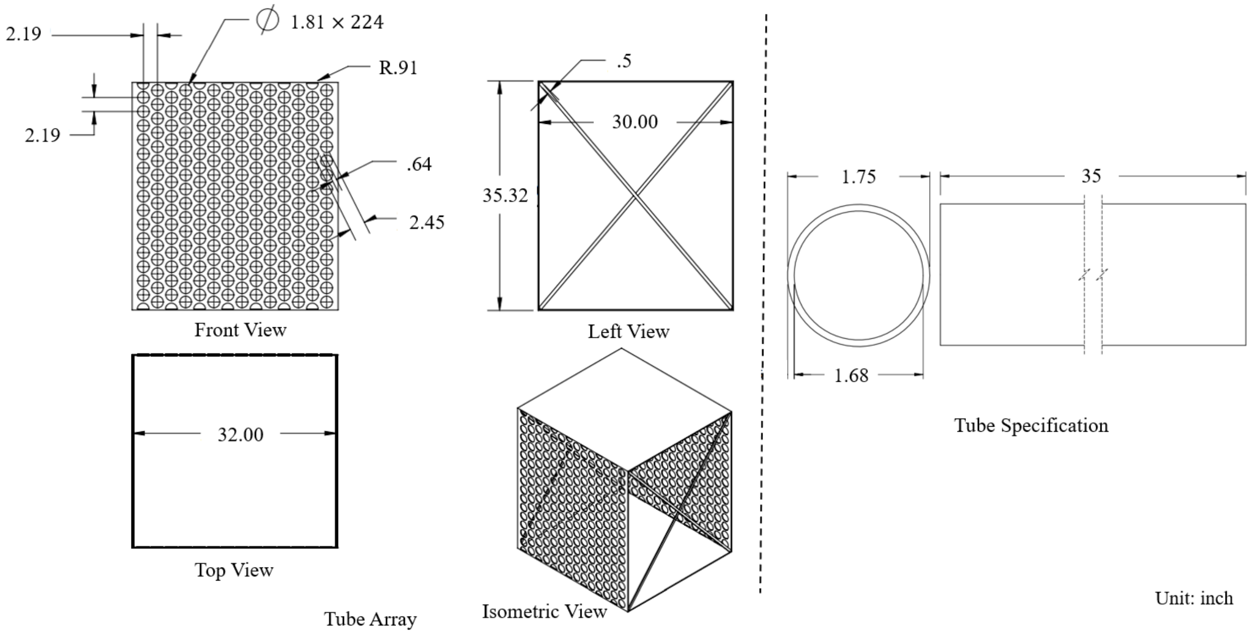

Figure 4. 1. Design of the protype scale (13-row) tube array in a staggered configuration

A commercial-grade phase change material, specifically hexahydrate calcium chloride ($CaCl_2{\cdot}6H_2O$ or CC6), was chosen as the heat storage medium for its affordability, stability, and its ability to melt and solidify at room temperature. Nucleation agents have been added to the commercial PCM in the laboratory to suppress supercooling. Thermal cycling tests, as described in the previous literature [116, 117], were conducted to check the stability of the PCM. The resulting phase change temperature of CC6 is 298 K or 25 °C. Table 4.1 provides a summary of the thermophysical properties of the commercial-grade PCM used in the test. Table 4.2 represents the boundary conditions (B.C.s) employed for the melting and solidification study.

The thermophysical properties of the carbon steel employed for the tubes were: density (ρ_s), specific heat (c_{P_s}), and thermal conductivity (k_s) as 7,870 kg/m³, 500 J/kg-K, and 45 W/m-K, respectively.

Table 4. 1 Thermophysical properties of PCM (CC6)

Property	Value
Melting/ solidification point [°C]	25
Density, ρ (solid/liquid) [kg/m^3]	1706/ 1538
Specific heat, C_p (solid/liquid) [J/kg.K]	2540/ 1680
Thermal conductivity, k (solid/liquid) [W/m.K]	1.09/ 0.546
Latent heat, L_f [kJ/kg]	150
Dynamic viscosity (solid/liquid) [mPa-s]	11.94/ 18.50
Thermal expansion coefficient [K^{-1}]	0.0005

Table 4. 2Boundary conditions

B.C.s	Melting	Solidification
Velocity at inlet, v_∞ (m/s)	0.82	0.82
Turbulence intensity at inlet (%)	5	5
Inlet air temperature, T_{in} (°C)	35	14.5
Pressure outlet (atm)	1	1
Mass flow rate, $\dot{m}$ (kg/s)	0.77	0.82
Re_D	2,241	2,388

4.2.2. Computational procedure

Figure 4.2 illustrates a schematic representation of a 2-D computational region employed for numerical analysis. The computational setup involved a staggered tube arrangement, with the tubes in the array designated as PCM1 to PCM7, as shown in the figure. To mitigate the impact of inlet and outlet boundaries on the numerical analysis and its outcomes, a computational domain with a length of 1.5 times the tube diameter upstream of the tube bank and ten times the tube diameter downstream of the tube bank was used. This extended length for the upstream and downstream domains was adequate to minimize the influence of entrance effects at the inlet and the wake at the outlet. Free-stream velocity was set at the inlet, and pressure conditions were imposed at the outlet. Symmetry boundary conditions were enforced on the top and bottom boundaries of the computational domain. Assumptions used for tube array modeling are as follows:

- Buoyancy force was considered due to density change during the phase transition.
- Heat transfer occurs by conduction in the solid PCM.
- The liquid PCM was assumed to be incompressible, flow regime is laminar, and heat transfer occurs by natural convection.
- The enthalpy-porosity method was applied for the PCM domain using a constant value of latent heat.
- The air was assumed to be incompressible fluid, with uniform inlet velocity.
- The air flow was assumed to be turbulent.
- No body force or heat source was considered in the air domain.
- Thermal resistance at the duct wall was neglected.

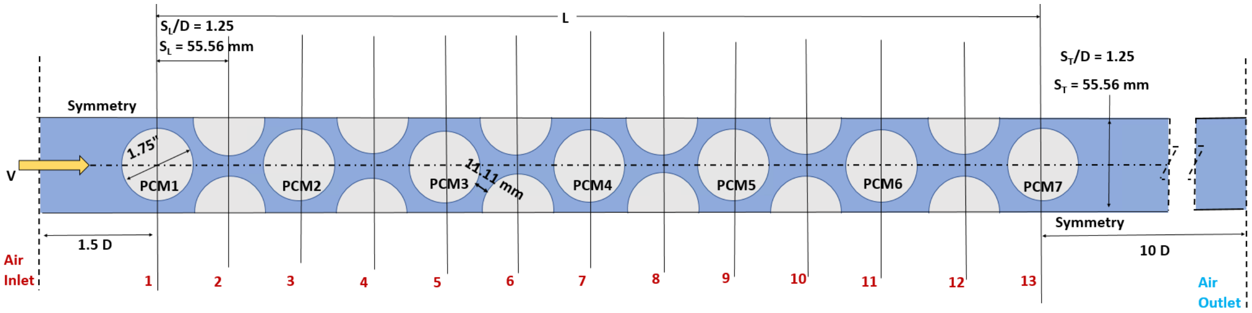

Figure 4. 2. A 2D computational domain for the tube bank

The simulation was conducted using ANSYS Fluent 20.0 [81] to solve the governing Navier-Stokes equations, which account for the conservation of mass, momentum, and energy. Realizable κ-ε turbulence model was selected for the fluid domain from the previous literature [115]. In the computational approach, the SIMPLE algorithm and the Implicit method were chosen to couple pressure and velocity. To enhance precision, a second-order upwind discretization scheme was applied to both the momentum and energy equations. For the discretization of momentum equations, the PRESTO! (PREssure STaggering Option) scheme was utilized. This choice is particularly beneficial for cases involving natural convection, porous media, etc., as it helps avoid interpolation errors and pressure gradient assumptions at boundaries. The convergence criterion for the RMS residuals for continuity, momentum, and energy equations was set to 10^{-6}. In order to predict the melting and solidification process of the PCM over time, a transient model was implemented. A time step size of 0.5 seconds was employed for this study. The model was validated, and a grid sensitivity analysis was conducted in previous literature [115]. A finer grid size was chosen near the tube wall to accurately capture changes in velocity and temperature in a boundary layer near the tube wall (see Figure 4.3). A total number of 614146 elements were generated for the current prototype-scale model in the numerical analysis. The simulation of nine physical hours of PCM melting in a tube array required over nine days (216 hours) of computational time on Orion HPC cluster, equipped with a Dual 32-Core AMD EPYC 7542 CPU, 2.9/3.4 GHz and 4TB RAM.

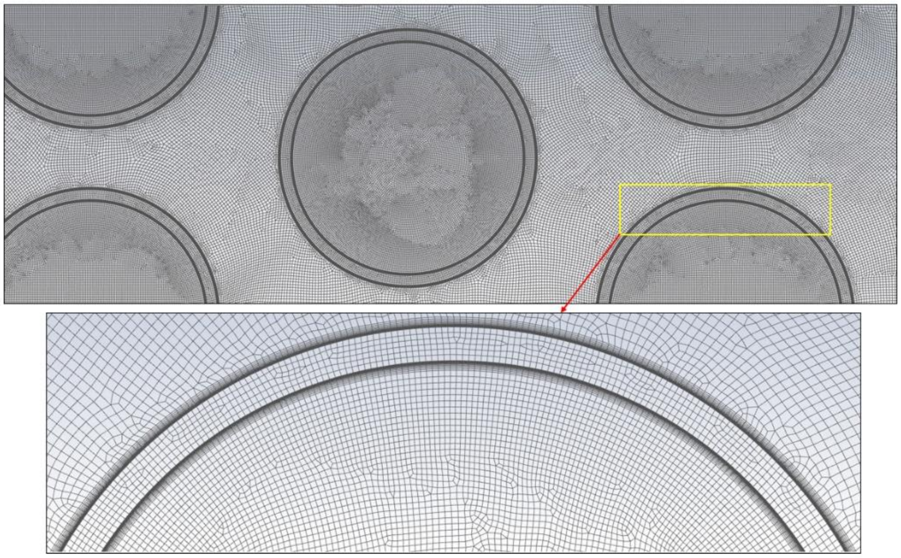

Figure 4. 3. Numerical grid of prototype-scale model

The continuity, momentum, and energy equations for the 2D PCM domain, showed in gray in Figure 4.2, are given by Eqns. (4.1)-(4.3) using the summation convention for repeated indexes:

$$\frac{\partial \rho}{\partial t} + \frac{\partial \rho u_i}{\partial x_i} = 0 \tag{4.1}$$

$$\frac{\partial(\rho u_i)}{\partial t}+\frac{\partial(\rho u_j u_i)}{\partial x_j}=\mu\frac{\partial^2 u_i}{\partial x_j\partial x_j}-\frac{\partial p}{\partial x_i}+\rho g_i+S_i \tag{4.2}$$

$$\frac{\partial(\rho h)}{\partial t}+\frac{\partial(\rho h_{latent})}{\partial t}+\frac{\partial(\rho u_i h)}{\partial x_i}=\frac{\partial}{\partial x_i}\left(k\frac{\partial T}{\partial x_i}\right) \tag{4.3}$$

where, ρ represents the density, u signifies the velocity of liquid PCM in the transverse direction driven by density variations, μ stands for viscosity, p denotes pressure, g corresponds to gravitational acceleration, and ρg_i represents the buoyancy force due to density discrepancies. The quantity h refers to the sensible enthalpy in the energy equation, and it is defined as follows:

$$h=h_{ref}+\int_{T_{ref}}^{T}C_p\,(T)dT \tag{4.4}$$

The enthalpy-porosity method was used to calculate the latent portion of PCM:

$$\gamma=\left\{\begin{array}{c}\frac{h_{latent}}{L_f}=0\ \ if\ T<T_{solid}\\ \frac{h_{latent}}{L_f}=1\ \ if\ T>T_{liquid}\\ \frac{h_{latent}}{L_f}=\frac{T-T_{solid}}{T_{liquid}-T_{solid}}\quad if\ T_{solid}<T<T_{liquid}\end{array}\right\} \tag{4.5}$$

Source term S_i was used to model the effect of natural convection on phase change as follows:

$$S_i=-A_{mush}\cdot u_i \tag{4.6}$$

$$A_{mush}=\frac{C(1-\gamma)^2}{\gamma^3+\delta} \tag{4.7}$$

where, δ is set to 0.001, C represents the constant associated with the "mushy" zone, typically falling within the range of 10^5 to 10^7. The term "mushy" zone pertains to the segment of the domain where the liquid fraction (γ) ranges from 0 to 1. For this particular analysis, a value of 10^5 was adopted as the mushy zone constant, consistent with previous literature by Pan et. al [41].

Boussinesq model was used to calculate density change due to the phase change and natural convection:

$$\rho=\rho_o[1-\beta(T-T_o)] \tag{4.8}$$

where reference quantities ρ_o and T_o pertain to the density and temperature of the liquid PCM, respectively, while β represents the thermal expansion coefficient of the liquid phase of the PCM.

The energy equation for the solid domain (tube wall) for transient condition is given by the following expression:

$$\rho_s c_{P_s} \frac{\partial T}{\partial t} = k_s \left(\frac{\partial^2 T}{\partial x^2} + \frac{\partial^2 T}{\partial y^2} \right) \tag{4.9}$$

where ρ_s, c_{P_s} ,and k_s are density, specific heat, and the thermal conductivity of the solid domain, respectively.

Navier-Stokes equations using the summation convention for repeated indexes for the 2D fluid domain (air) are as follows:

$$\frac{\partial \rho_{air}}{\partial t} + \frac{\partial \rho_{air} u_i}{\partial x_i} = 0 \tag{4.10}$$

$$\frac{\partial(\rho_{air} u_i)}{\partial t} + \frac{\partial(\rho_{air} u_i u_j)}{\partial x_j} = -\frac{\partial p}{\partial x_i} + \frac{\partial}{\partial x_j}\left[\mu_{air}\left(\frac{\partial u_i}{\partial x_j} + \frac{\partial u_j}{\partial x_i}\right) - \rho_{air}\overline{u_i' u_j'}\right] \tag{4.11}$$

$$\rho_{air} \frac{\partial T}{\partial t} + \rho_{air} u_j \frac{\partial T}{\partial x_j} = -\frac{\partial p}{\partial t} + \frac{\partial}{\partial x_j}\left(\frac{k_{air}}{C_{p_{air}}}\frac{\partial T}{\partial x_j} - \rho_{air}\overline{u_j' T'}\right) \tag{4.12}$$

where, u_i, u_j denote mean flow velocity, u' denote velocity fluctuations due to turbulence and $\rho_{air}\overline{u_i' u_j'}$ represents Reynolds Stress term.

The transport equations for the turbulent kinetic energy (κ) and dissipation rate (ε) for Realizable κ-ε model are expressed as following [109]:

$$\frac{\partial(\rho_{air}\kappa)}{\partial t} + \frac{\partial}{\partial x_j}\left(\rho_{air}\kappa u_j\right) = \frac{\partial}{\partial x_j}\left[\left(\mu_{air} + \frac{\mu_t}{\sigma_k}\right)\frac{\partial k}{\partial x_j}\right] + G_k + G_b + S_k - \rho_{air}\varepsilon - Y_M \tag{4.13}$$

$$\frac{\partial(\rho_{air}\varepsilon)}{\partial t} + \frac{\partial}{\partial x_j}\left(\rho_{air}\varepsilon u_j\right) = \frac{\partial}{\partial x_j}\left[\left(\mu_{air} + \frac{\mu_t}{\sigma_\varepsilon}\right)\frac{\partial \varepsilon}{\partial x_j}\right] + S_\varepsilon + \rho_{air} C1 S_\varepsilon - \rho_{air} C_2 \frac{\varepsilon^2}{\kappa + \sqrt{\nu\varepsilon}} + C_{1\varepsilon}\frac{\varepsilon}{k} C_{3\varepsilon}\, G_b \tag{4.14}$$

where,

$$C_1 = \left[0 \cdot 43, \frac{\eta *}{\eta * +5}\right], \qquad \eta * = S\frac{k}{\varepsilon}, \qquad S = \sqrt{2S_{ij}S_{ij}}, S_{ij} = \frac{1}{2}\left(\frac{\partial u_j}{\partial x_i} + \frac{\partial u_i}{\partial x_j}\right)$$

G_k and G_b signify the production of turbulent kinetic energy stemming from the mean velocity gradient and buoyancy, respectively. Y_M denotes the degree to which fluctuating dilatation contributes to the total dissipation rate in the context of compressible turbulence. The variables σ_k and σ_ε represent the turbulent Prandtl numbers for κ and ε, respectively. S is the mean rate-of-strain tensor.

Zukauskas [83, 108] experimental correlation for pressure drop (ΔP) across the tube array is as follows:

$$\Delta P = N_L x \left(\frac{\rho_{air}\, v_{max}^2}{2}\right) f \tag{4.15}$$

where, N_L represents the number of tube rows. The friction factor f and the correction factor x are determined from the graph provided in the references [83, 108] for the maximum velocity (v_{max}) within the tube bank, which is calculated using the following equation.

$$v_{max} = \frac{s_T}{s_T - D} v_\infty \tag{4.16}$$

where, S_T is the tube spacing in the transverse direction.

The correlation of Nu number by Zukauskas [83, 108] was used as follows (Eq. 4.17):

$$\overline{Nu}_D = C_1 C_2 R_{e_D}^m Pr^n \left(\frac{Pr}{Pr_s}\right)^{1/4} \tag{4.17}$$

where, $\left\{\begin{matrix} N_L \geq 20 \\ 0.7 \leq Pr \leq 500 \\ 10 \leq Re_{D_{max}} \leq 2 \times 10^6 \end{matrix}\right\}$

Coefficient of heat transfer (h_{Zu}) was calculated from Zukauskas correlation for Nu number using the following expression [40]:

$$\overline{Nu}_D = \frac{h_{Zu}D}{k_{air}} \tag{4.18}$$

The log mean temperature difference (LMTD) method was used to compute the average heat transfer coefficient (h_{num}) for the numerical analysis as presented in Eq. (4.19).

$$h_{num} = \frac{q''}{LMTD} \tag{4.19}$$

where, the peripheral average of wall heat-flux (q″) was determined from the Fourier's law as following:

$$q_w'' = -k_{air}\frac{\partial T_w}{\partial r}\bigg|_{r=r_0} = \frac{k_{air}}{r_0 - r_i}\left(T_{w,o} - T_{w,i}\right)$$

and, $LMTD = \frac{\Delta T_{in} - \Delta T_{out}}{ln(\Delta T_{in}/\Delta T_{out})} = \frac{(T_{w,i} - T_{in}) - (T_{w,i} - T_{out})}{\ln((T_{w,i} - T_{in})/(T_{w,i} - T_{out}))}$

Performance of an energy storage system may be determined by the combined effect of Colburn factor *j* and friction factor *f* as follows [29]:

$$j = \frac{Nu}{Re\,.\,Pr^{1/3}} \tag{4.20}$$

$$f = \frac{2 \times \Delta P}{\rho v_\infty^{\,2}} \times \frac{D}{L} \tag{4.21}$$

The factor *j/f* is defined as goodness factor that indicates the heat transfer per unit flow rate.

4.2.2.1. Effect of tube size, tube spacings and inlet air conditions

The dimensionless tube spacings (S_T/D and S_L/D) were determined by applying the Zukauskas correlation [108] for pressure drop. Although smaller tube spacing increases energy storage density, it also increases the pressure drop. Hence, the spacing was adjusted systematically to achieve a pressure drop (ΔP) of less than 100 Pa. The dimensionless tube spacings, S_T/D and S_L/D, both were set to 1.25. The tube diameter was established through numerical simulations of the tube array, covering a range of tube diameters and air velocities of interest to attain the necessary level of air cooling for a duration of at least 4 hours during the PCM melting process.

Numerical simulations were also conducted for PCM freezing to confirm that the PCM within the tube array can be completely frozen during nighttime operation. Since the PCM melting front propagates in the direction of the air flow, increasing the number of tube rows downstream of the tube bank does not necessarily increase the duration of the cooling effect (constant air outlet temperature). The total number of tube rows in the array was set to 13 for the prototype-scale model.

Figure 4.4 and 4.5 summarize the numerical results obtained for the PCM melting for the inlet air temperatures of 303 K (30 °C) and 308 K (35 °C), inlet air velocity in the 0.4 to 1 m/s range, tube diameter of 1", 1.5", 1.75", and 2", commercial grade PCM and 80% tube fill. To ensure PCM is fully frozen at the beginning of the simulation, the initial temperature of PCM and tubes was assumed 293 K (20 °C), i.e., 5 K (5 °C) lower compared to the PCM phase change temperature. It needs to be mentioned that the dimensionless tube spacing used for 1" outer diameter tube was S_T/D and S_L/D of 1.59 and 1.38, respectively to show the effect of variation of tube spacing (black dotted line in Figure 4.4).

Figure 4.4 shows the outlet air temperature is maintained approximately constant for a period of several hours. As PCM melts, the outlet air temperature increases, asymptotically approaching the inlet air temperature. Air temperature at the array outlet is lower compared to the inlet air temperature since the array of PCM filled tubes is lowering temperature of the inlet air as latent heat of PCM melting is provided by the air flow.

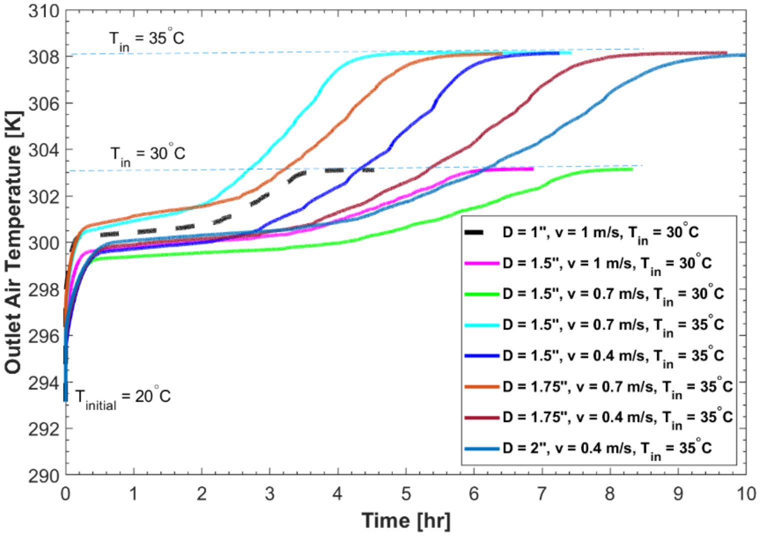

Figure 4. 4. Air temperature leaving the prototype-scale tube array as a function of time, air velocity, and tube diameter for inlet air temperature of 30 °C and 35 °C

Figure 4.5 displays the magnitude of air cooling, which is the difference between the air temperature at the inlet and outlet of the tube array. This cooling effect varies based on the tube diameter and operating parameters, and it increases as the inlet air temperature rises.

When the inlet air temperature is 303 K or 30 °C (5 °C higher than the phase change temperature of 25 °C) and the initial PCM temperature is 293 K or 20 °C, the air temperature at the outlet is initially 6 to 7 °C lower than the inlet air temperature. As the PCM temperature increases and reaches the phase change temperature, the outlet air temperature remains relatively constant, resulting in a temperature difference ($\Delta T_{\text{melting}}$) in the range of 3 to 4 °C for about 4 hours, until the PCM in the tubes melts. After the solid PCM melts, its temperature quickly rises, and $\Delta T_{\text{melting}}$ decreases.

For a higher inlet air temperature of 308 K or 35 °C (10 °C higher than the phase change temperature of 25 °C) and an initial PCM temperature of 293 K or 20 °C, the air temperature at the array outlet is initially 11 to 12 °C lower than the inlet air temperature. Once the PCM temperature increases from the initial value and reaches the phase change temperature, the outlet air temperature remains constant, resulting in a temperature difference ($\Delta T_{melting}$) in the range of 8 to 9 °C for approximately four hours, until the PCM in the front rows of the array melts. After the PCM melts, its temperature rapidly approaches the inlet air temperature, and $\Delta T_{melting}$ decreases.

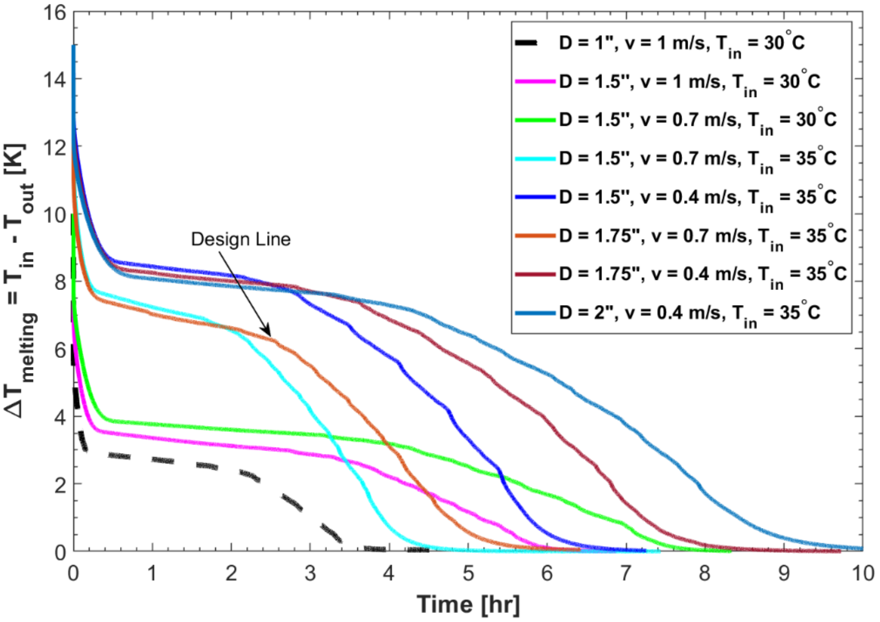

Figure 4. 5. Magnitude of air cooling (temperature difference) $\Delta T_{melting}$ for the prototype-scale tube array as a function of time, air velocity, and tube diameter for inlet air temperature of 30 °C and 35 °C

The Area Goodness Factor (*j/f*) is employed to assess the compactness of an energy storage system, as depicted in Figure 4.6. For an inlet air temperature of 308 K or 35 °C, tube diameters of 1.5" and 1.75" exhibit a higher goodness factor compared to 2" OD tubes primarily due to their low pressure drop, which is directly associated with low pumping power required. Moreover, these two tube sizes have comparable heat transfer coefficients, as detailed in Table 4.3. Since tube spacing for 1" tube array is different compared to other tube diameters, the area goodness factor for the tube array with 1" OD tubes is not presented in Figure 4.6.

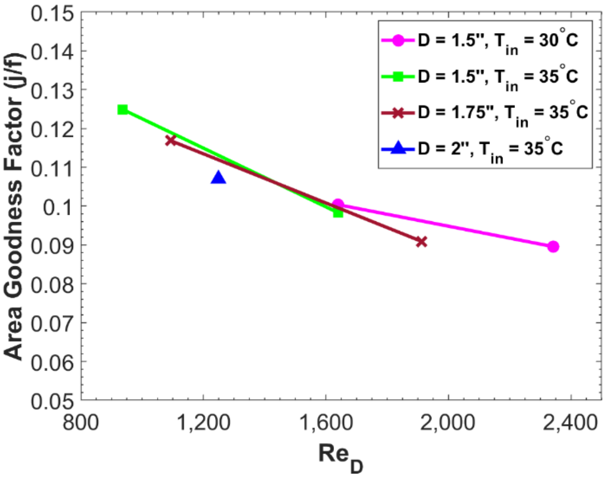

Figure 4. 6. Area goodness factor as a function of Re_D for different tube diameter and inlet air temperature of 30 °C and 35 °C

As discussed earlier, the duration of the cooling effect extends as the tube diameter increases due to a greater amount of PCM and longer heat diffusion pathways through the PCM. Additionally, a lower inlet air temperature and reduced velocity contribute to a longer cooling duration. The results from the numerical simulations presented earlier indicate that a tube array consisting of thirteen rows of 1.75" OD tubes in a staggered arrangement, operating with an inlet air temperature between 303 K (30 °C) and 308 K (35 °C) and an air velocity ranging from 0.4 to 0.7 m/s, can offer the desired cooling effect for a period of 4 hours (see Figure 5).

Additionally, for the examined geometry and operational conditions, the average cooling magnitude ($\Delta T_{melting}$) approximates a factor of the difference between the inlet air temperature (T_{in}) and the PCM phase change temperature ($T_{ph.change}$) as follows:

$$\Delta T_{melting} = C \times \left(T_{in} - T_{ph.change}\right) \tag{4.22}$$

where, C is a constant. For the numerical results, C is 0.8, while for the experimental results shown below C is 0.4 to 0.6, depending on the air velocity.

This study also involved a numerical analysis of PCM freezing in a tube array consisting of 13 rows of 1.75" diameter tubes, each 80% filled with commercial-grade PCM. The analysis considers various inlet air velocities ranging from 0.7 to 1.6 m/s, aiming to determine the time required for complete PCM freezing within the tube array. It is crucial for the PCM to freeze entirely during nighttime when ambient temperatures are below the PCM phase change temperature. Incomplete freezing would result in reduced cold energy storage capacity.

The results indicate that, under prototype operating conditions (inlet air velocity around 1 m/s), all PCM within the array freezes in approximately 3.8 to 7.1 hours, depending on the initial temperature. Lower inlet air temperatures (288 K or 15 °C) significantly reduce freezing time, nearly halving it in comparison to higher inlet air temperatures (298 K or 20 °C). At low inlet air velocities and high air inlet temperatures (298 K or 20 °C), freezing time increases significantly. Conversely, operating at high inlet air velocities (around 1.6 m/s) notably shortens the freezing time to 2.9 to 5.4 hours, dependent on the inlet air temperature. Since the prototype-scale LTES system will operate within the range of 0.5 m/s to 1 m/s of inlet air velocities, freezing time primarily depends on the air temperature.

Figure 4.7a illustrates the average PCM temperature in the tube labeled PCM6, located in the 12th row of the array, over time for inlet air velocities ranging from 0.7 to 1.6 m/s. During PCM freezing, the average PCM temperature rapidly decreases from the initial temperature (T_{init}) to the phase change temperature. As PCM gradually freezes, the average PCM temperature remains approximately constant. After PCM is fully frozen, the average PCM temperature rapidly decreases, approaching the inlet air temperature (T_{ain}). Lower inlet air temperature results in shorter freezing times.

Figure 4.7b presents the outlet air temperature just downstream from the tube array during PCM freezing as a function of time for various inlet air velocities and temperatures, with initial temperatures ranging from 303 K to 308 K (or 30 to 35 °C). The results show that the outlet air temperature follows similar trends as the average PCM temperature: it decreases rapidly as PCM cools to the phase change temperature, remains relatively constant during freezing, and drops rapidly after PCM is completely frozen, approaching the inlet air temperature. These findings suggest that the outlet air temperature can serve as an indicator of PCM freezing, with PCM considered fully frozen when the outlet air temperature matches the inlet air temperature (assuming the inlet air temperature is below the phase change temperature).

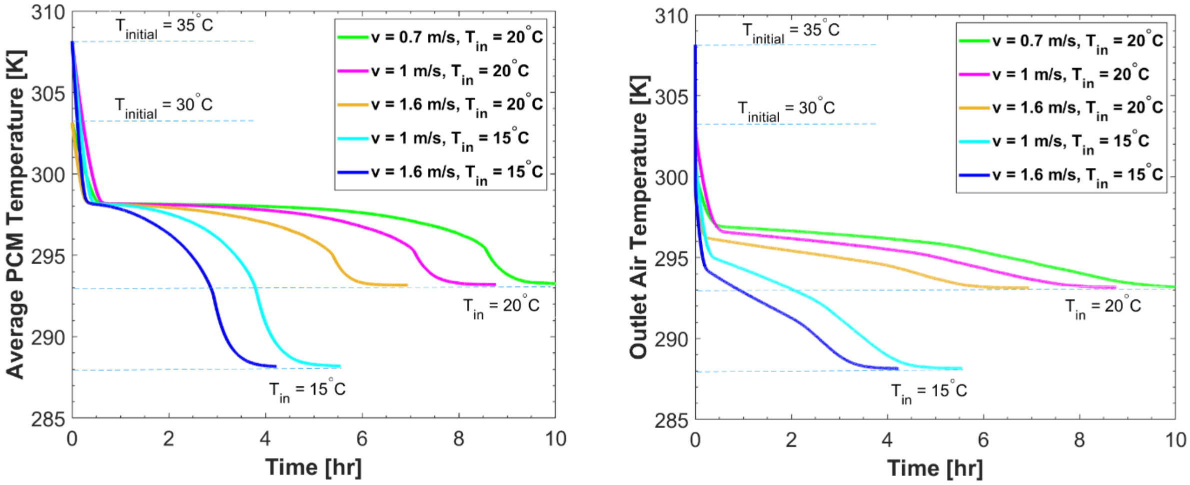

(a) (b)

Figure 4. 7. (a) Average PCM temperature and (b) Outlet air temperature as a function of time during PCM freezing

Table 4.3 provides a comparison of the predicted hydraulic and thermal performance of the analyzed tube array geometry for PCM melting and freezing and results obtained from experimental correlations for pressure drop and heat transfer by Zukauskas [83, 108]. The numerically predicted values of ΔP are in excellent agreement with the values obtained from experimental correlation. A very good agreement between the numerically predicted and experimentally obtained values of the average heat transfer coefficient (h_{avg}) is obtained from the numerical analysis. The deviation between the numerical results and the experimental correlation is less than 10% for the selected design with 1.75" OD tubes in the array during both PCM melting and freezing. It should be noted that the results for the tube array 1" OD tube was obtained for the dimensionless tube spacing of $S_T/D = 1.59$ and $S_L/D = 1.38$ which are different from the other.

Table 4. 3 Comparison of numerical predictions and experimental correlations for the tube array

Phase	D	T_{in}	v_∞	ΔP		h_{avg}	
		°C	m/s	Pa		W/m^2-K	
				Num	Zu [108] Correlation	Num	Zu [83] Correlation
PCM Melting	1.0"	30	1	22.5	24.0	43.5	46.7
	1.5"	30	1.0	77.9	77.6	58.3	58.5
			0.7	44.7	44.0	53.6	47.2
		35	0.7	44.7	44.0	52.5	47.2
			0.4	17.7	17.1	46.1	33.8
	1.75"	35	0.7	42.8	43.1	46.8	44.4
			0.4	16.9	16.6	41.1	31.8
	2"	35	0.4	16.4	16.0	37.0	30.1
PCM Freezing	1.75"	20	0.7	41.4	43.1	51.4	44.4
			1.6	162.5	185.5	69.2	72.9
			1.0	72.9	69.0	60.5	55.0
		15	1.0	72.9	69.0	59.0	55.0

4.2.3. Test facility and experimental setup

Figure 4.8 illustrates the schematic of the experimental setup. An electric heater (TUTCO, model EDHS-36H/36W-35kW-480V-3P) was positioned 3 feet from the inlet of the test rig and controlled by a PID controller (Omega, model CN08D3-L-AC). Two identical sets of resistance temperature sensors (RTDs) (Evolution Sensors and Controls, model P4B3-TF22-26S-PX-008-PFXX-72-STWL) were placed 12" (305 mm) apart, both upstream and downstream of the test module to measure airflow temperature. Each RTD set consisted of 24 RTDs.

In line with previous literature on laboratory-scale tests [115, 116], a stratification of air temperature was observed in the vertical direction. As a result, the RTD layout was evenly divided into eight vertical sections and three horizontal sections. All RTDs were calibrated by measuring the room temperature, resulting in a standard deviation of less than 0.1 °C. Air velocity was measured using a Kanomax Climomaster 6501 Multi-Function Hot-Wire Anemometer, and air flow was determined using the Equal Area Method (EAM). Velocity measurements were taken at 4" × 6" (width × height) equal areas across the cross-section.

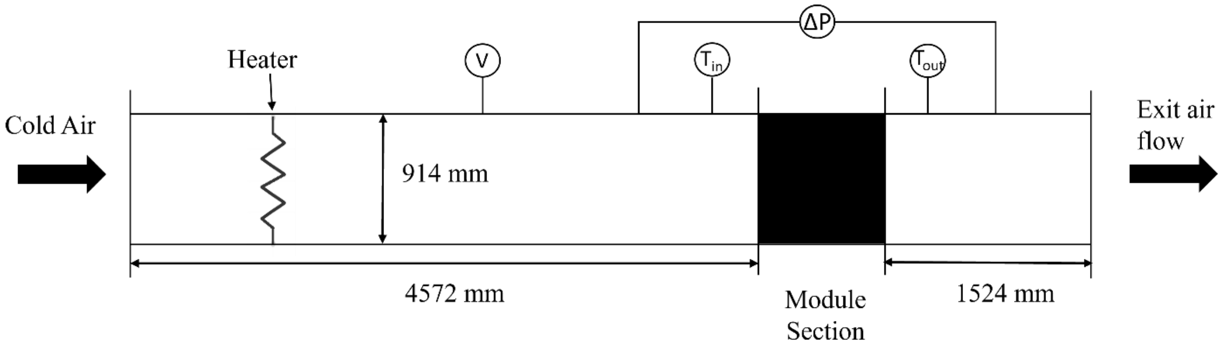

Figure 4. 8. A schematic diagram of the forced-air heat transfer test apparatus. The symbols V, T, and ΔP represent the measurement of air velocity, temperature and pressure drop, respectively.

Figure 4.9a displays the prototype-scale experimental test facility. The test section, located downstream of the heating elements, was insulated to prevent heat loss. Figure 4.9b shows the assembly of the array, featuring PCM tubes inserted into tube sheets. A photograph of the tube array inserted into the duct is presented in Figure 4.9c. To enhance structural rigidity, a cross brace has been added. Figures 4.9d and 4.9e present a side view and an isometric view of the 16 × 13 tube array, respectively, with plugs inserted into the tubes. The array comprises 208 circular tubes, each with an outer diameter of 1.75". Every tube is filled with 1.553 kg of PCM, constituting 90% of its volume, as depicted in Figure 4.9f, which showcases a cross-section of a 0.75"OD tube filled with crystalized commercial grade PCM.

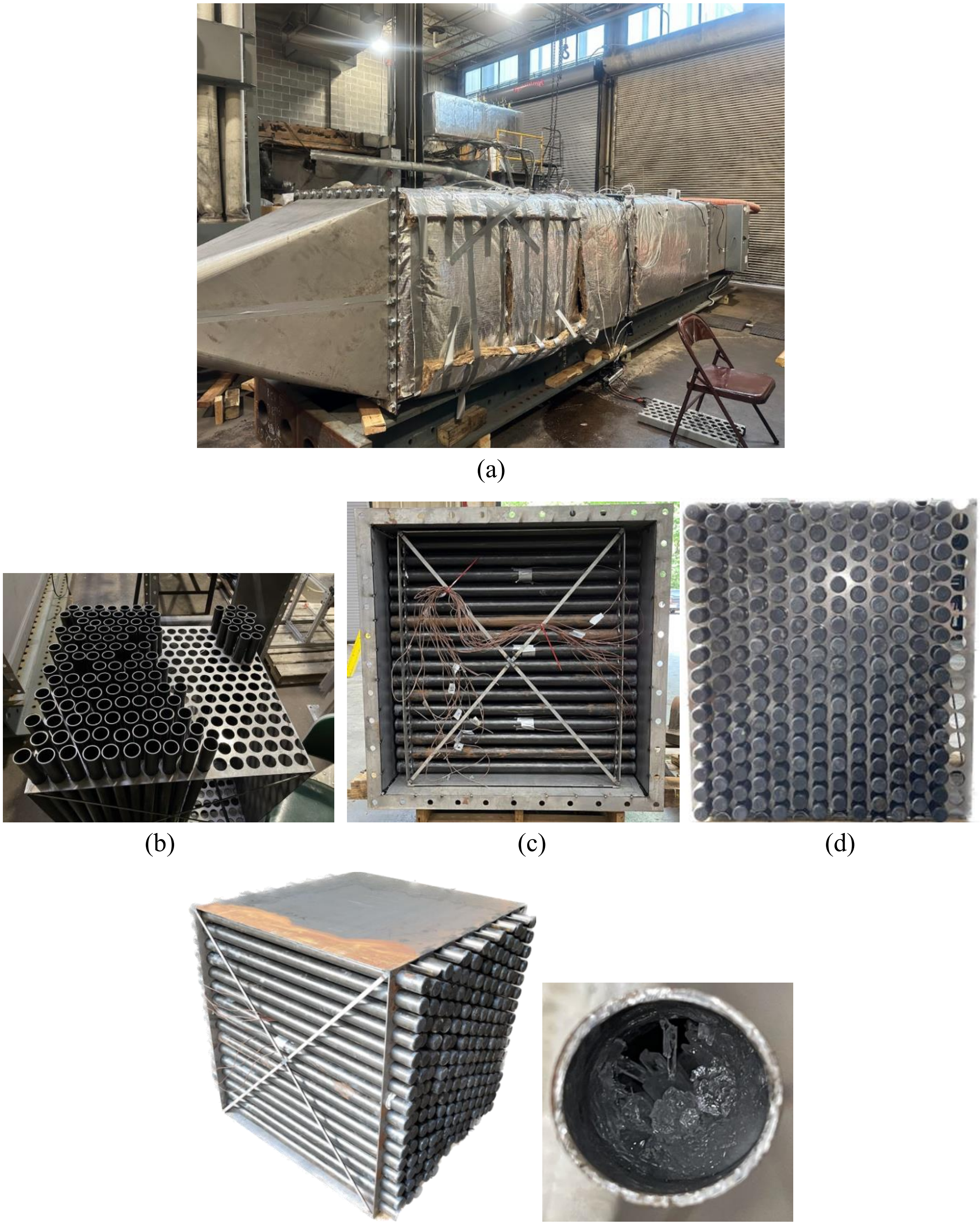

(a)

(b) (c) (d)

(e) (f)

Figure 4. 9. (a) Assembled prototype-scale test rig; (b) Tube array assembly; (c) Tube array inserted in the duct; (d), (e) Side view and isometric view of 16 × 13 tube array, respectively; (f) Photograph of a tube partially filled with a commercial grade PCM.

To measure the PCM temperature, six tubes (numbered 1 to 6) located within the tube bank were equipped with T-type thermocouples placed at the center of each tube. Additionally, thermocouples were welded on the outer surface of the tubes at four locations around the tube periphery to enable the measurement of tube wall temperatures. Since these thermocouples were affixed to the surface of the tubes and exposed to the airflow, they measured temperatures within the range of both the tube wall and the surrounding air temperatures. The location of these instrumented tubes is depicted in Figure 4.10. To ensure their accuracy, the thermocouples were calibrated in an ice water bath, resulting in a reported accuracy of ±0.5 °C.

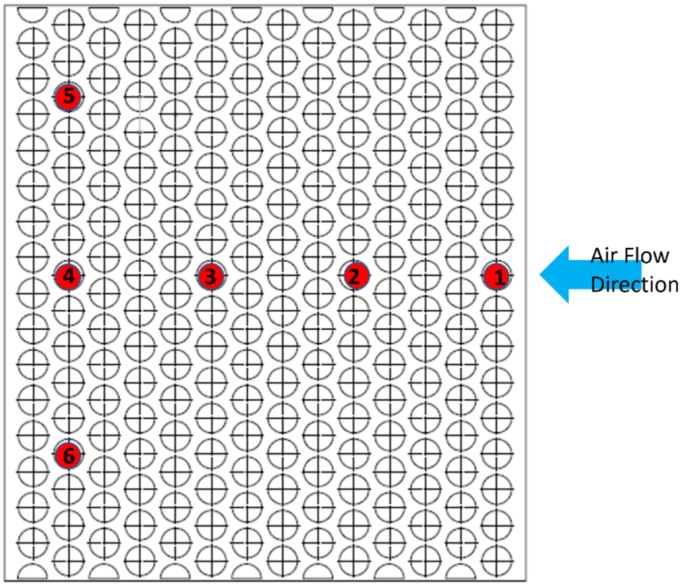

Figure 4. 10. Locations of the thermocouples in the tubes within the tube array

To induce airflow through the ductwork and test module, a centrifugal blower was utilized. The airflow through the blower was regulated by a manually operated damper, allowing for adjustments to system resistance. The maximum airflow velocity of 0.81 m/s was achieved with the damper fully open. Most of the tests were conducted at this maximum airflow velocity, although some tests were performed at a lower airflow velocity of 0.5 m/s. The PCM freezing tests were conducted at the maximum superficial inlet air velocity to expedite the freezing process.

4.2.3.1. Test matrix

The test matrix is detailed in Table 4.4, comprising five series of tests conducted under both PCM freezing and melting conditions. Freezing tests occurred at night to solidify the PCM within the tube array, while melting tests followed by activating an electric heater.

Table 4. 4 Test Matrix: a 16×13 tube array (tests conducted at Lehigh University, Bethlehem, PA)

Date, 2023	**PCM Phase**	**Test Conditions**	**Test Time [hrs]**	**Remarks/ Comments**
31-May to 1-Jun	**Test 1** (Melting)	$V = 0.8$ m/s, $T_{ain} = 35$°C, $T_{init} = 16$°C	9	Successful test, PCM melting dynamics was established.
				Velocity measurement
2-Jun to 6-Jun				No test/ Test error
7-Jun	**Test 1** (Freezing)	$V = 0.8$ m/s, $T_{ain} = 14.5$°C, $T_{init} = 35$°C	8	Successful test, PCM freezing dynamics was established.
	Test 2 (Melting)	$V = 0.8$ m/s, $T_{ain} = 35$°C, $T_{init} = 16$°C	9	Repeat of Melting Test 1. Successful test repeatability.
8-Jun	**Test 2** (Freezing)	$V = 0.8$ m/s, $T_{ain} = 14.5$°C, $T_{init} = 35$°C	7	Repeat of Freezing Test 1. Successful test repeatability.
	Melting Test	$V = 0.8$ m/s, $T_{ain} = 35$°C, $T_{init} = 16$°C		Test error
9-Jun to 12-Jun				No test due to poor air-quality (Canadian wildfire)
13-Jun	**Test 3** (Melting)	$V = 0.5$ m/s, $T_{ain} = 35$°C, $T_{init} = 16$°C	14	Successful test, PCM melting dynamics was established.
14-Jun	Freezing Test	$V = 0.8$ m/s, $T_{ain} = 17$°C, $T_{init} = 35$°C		Test error
15-Jun	**Test 4** (Melting)	$V = 0.5$ m/s, $T_{ain} = 35$°C, $T_{init} = 18$°C	12	Repeat of Melting Test 3. Successful test repeatability.
29-Jun	**Test 5** (Melting)	$V = 0.8$ m/s, $T_{ain} = 30$°C, $T_{init} = 20$°C	18	Successful test, PCM melting dynamics was established.

Most tests, apart from Tests 3 and 4, were performed at a maximum inlet air velocity of 0.8 m/s, whereas Tests 3 and 4 were performed at a reduced inlet air velocity of 0.5 m/s to obtain data for lower air velocity conditions. To ensure the reliability of the results, some tests were repeated to assess experimental uncertainty and repeatability.

Despite most tests taking place in the first half of June, the nighttime ambient air temperature was sufficiently low to facilitate PCM freezing during these conditions. However, one freezing test had to be halted due to adverse air quality caused by smoke from Canadian wildfires and unseasonably high nighttime ambient air temperatures. The melting tests maintained an inlet air temperature of 308 K or 35°C, with the exception of Test 5, which utilized an inlet air temperature of 303 K or 30°C to simulate lower maximum air temperature conditions.

4.2.3.2. Test results

The test results are presented in this section, following the sequence in which the tests were performed. As previously mentioned, these tests were carried out to assess the performance of the test module under varying operating conditions, including differences in inlet air velocity and temperature. Some tests were repeated to evaluate experimental uncertainty and repeatability.

Focusing on melting Tests 1 and 2, performed at the maximum inlet air velocity of 0.8 m/s, an inlet air temperature of 308 K or 35°C, and an initial temperature of 289 K or 16°C, their results are depicted in Figures 4.11(a-c), detailing their variations over time. Figure 4.11a highlights the excellent consistency in inlet air temperature, with a maximum temperature difference of only 2 K (°C). The minor fluctuations in inlet air temperature, indicated by the thin solid lines, can be attributed to the dead band of the PID controller responsible for regulating the electric heater. The thicker solid lines represent moving averages.

Comparing the outlet air temperatures for melting Tests 1 and 2 at an inlet air velocity of 0.8 m/s and an inlet air temperature of 308 K or 35°C (Figure 4.11b), the trends mirror those observed during the parametric numerical study, which was conducted to determine the tube array design, as previously discussed. The rapid initial rise in outlet air temperature is due to the swift heating of the initially frozen PCM within the tubes. This is followed by an almost linear increase as the PCM continues to melt, culminating in a nearly constant temperature as the melted PCM approaches the inlet air temperature. The test results exhibit strong repeatability, with a maximum temperature difference of approximately 1 K (°C).

The air-cooling effect of the PCM tube array, denoted as $\Delta T_{melting}$ (the difference between the air temperature at the tube array inlet and outlet), is portrayed in Figure 4.11c. Under the conditions of an inlet air temperature of 308 K or 35°C, which is 10 K (°C) higher than the phase change temperature (298 K or 25°C), and an inlet air velocity of 0.8 m/s, the air temperature at the array outlet is initially 10°C lower than the inlet air temperature, given that the PCM is initially frozen at 289 K or 16°C.

As the PCM temperature rises and reaches the phase change temperature, the outlet air temperature increases (refer to Figure 4.11b), leading to a reduction in the air temperature difference ($\Delta T_{melting}$). This difference remains within the range of 4 to 6 K (°C) (40 to 60% of the driving force, $\Delta T_{DF} = T_{in} - T_{ph.change}$) for approximately 4 hours. Following the complete melting of the solid PCM, $\Delta T_{melting}$ gradually diminishes and approaches zero after 8 hours.

The results illustrated in Figure 4.11c confirm that the selected PCM tube array configuration, operating at an inlet air velocity of 0.8 m/s and an inlet air temperature of 308 K or 35°C, meets the performance criteria of the design regarding the magnitude and duration of the cooling effect. Furthermore, the results showcase a high level of repeatability, with the maximum difference in $\Delta T_{melting}$ between Melting Tests 1 and 2 falling within the 1 K (°C) range, and the average difference being even smaller.

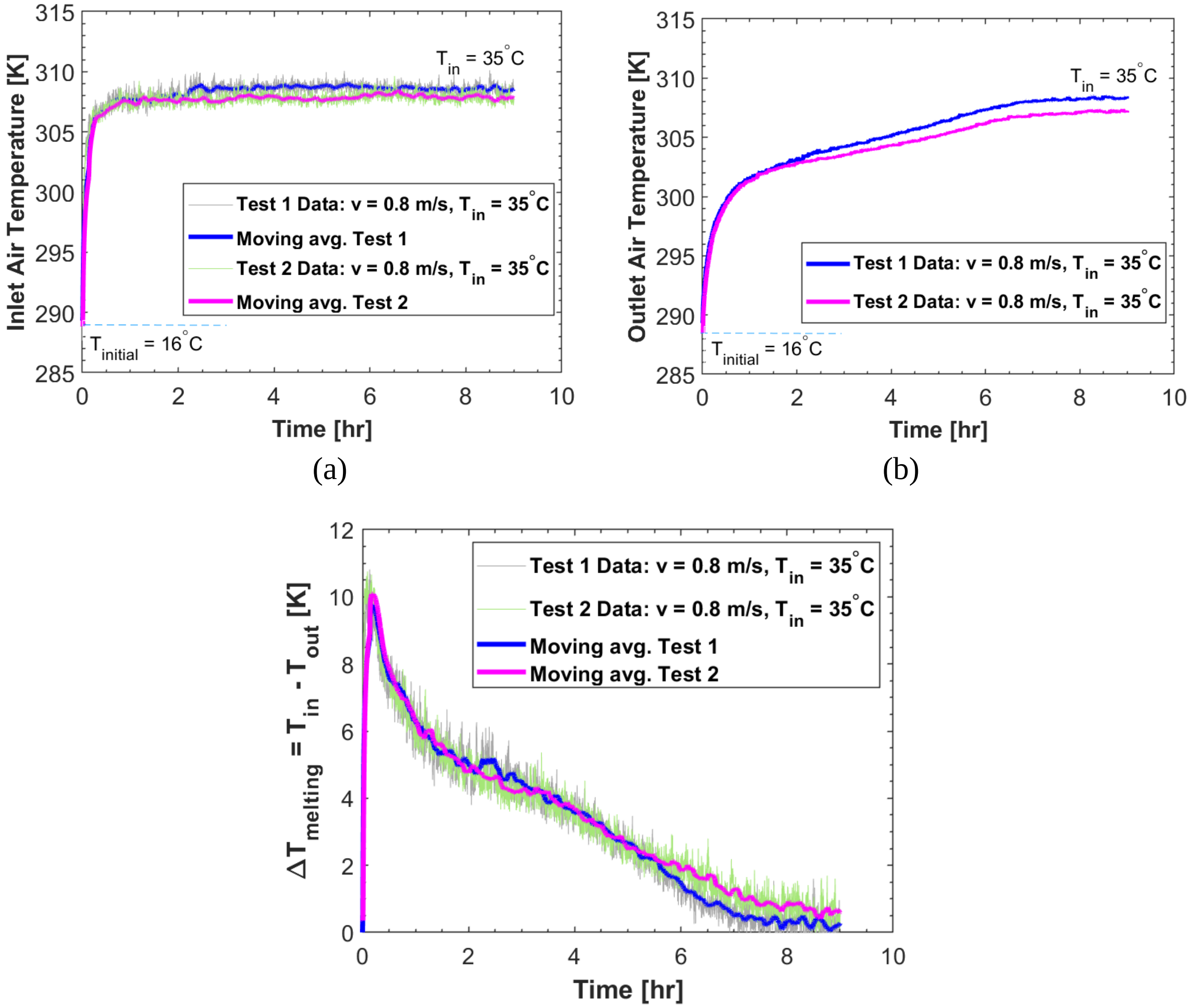

(a) (b)

(c)

Figure 4. 11. Comparison of melting Test1 and 2 (a) inlet air temperature, (b) outlet air temperature and (c) temperature difference as a function of flow time

The comparison of results obtained for inlet air temperatures of 303 K or 30 and 308 K or 35°C is presented in Figures 4.12(a-c). In melting Tests 1 and 5, the inlet air temperature was kept constant at 308 K or 35°C and 303 K or 30°C, respectively, as indicated in Figure 4.12a and b. The smaller temperature difference, representing the driving force, between the air stream and the phase change temperature had a noticeable impact on the performance of tube array. With the reduced driving force resulting from the 303 K or 30°C inlet air temperature, the PCM melting process occurred at a significantly slower rate, leading to an extended melting time of over 15 hours, in contrast to the 8-hour melting period for the 308 K or 35°C inlet air temperature.

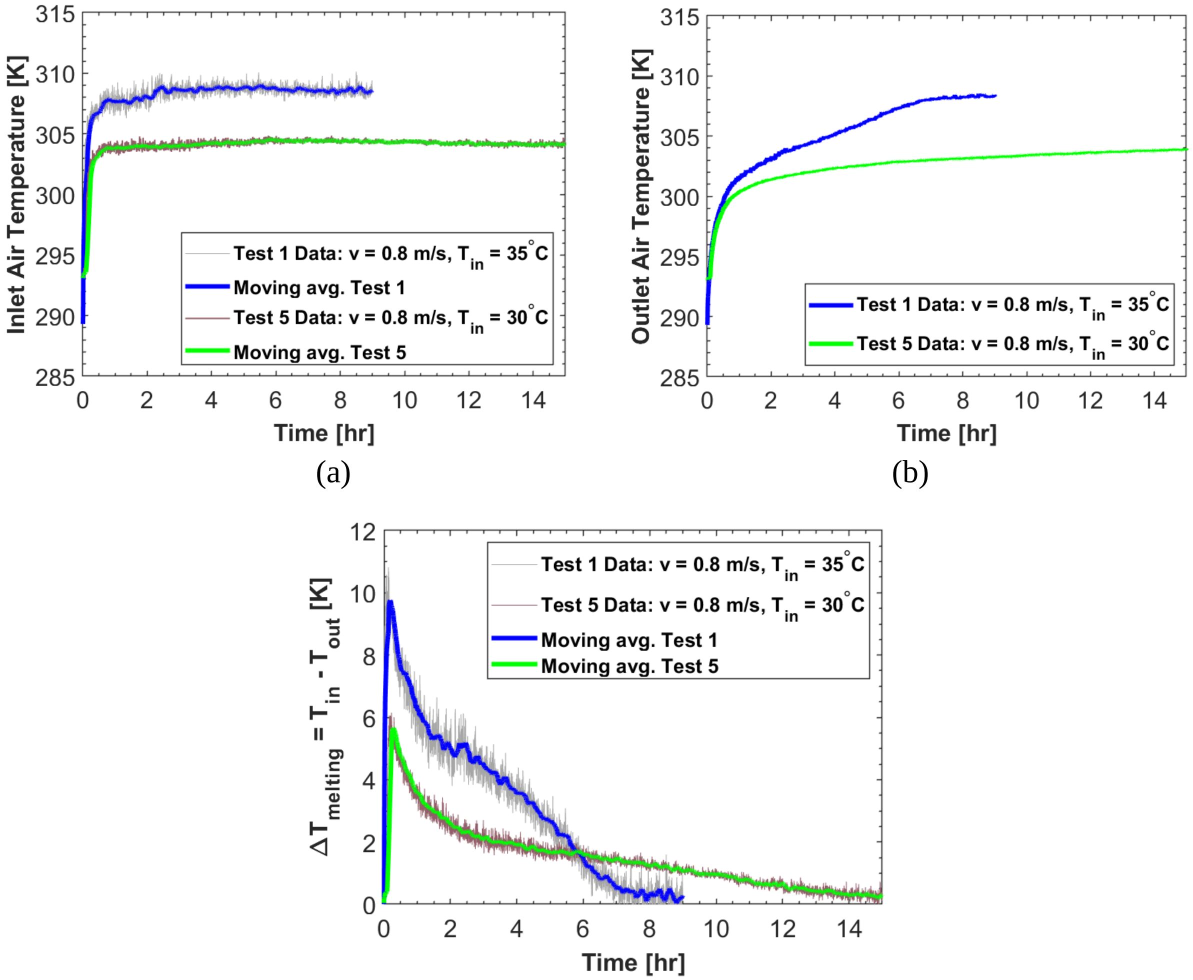

(a) (b)

(c)

Figure 4. 12 Comparison of melting Tests 1 and 5 (a) inlet air temperature, (b) outlet air temperature, (c) temperature difference as a function of flow time

The comparison of the performance of tube array, characterized by the magnitude and duration of the cooling effect, is depicted in Figure 4.12c across different stages of flow (test) time. As evident from the results, a reduced driving force corresponds to a smaller magnitude and a prolonged duration of the cooling effect. In the case of a 5 K (°C) driving force, the air temperature difference ($\Delta T_{melting}$) remains above 2°C (equivalent to 40% of the driving force) for 4 hours before gradually declining. Conversely, for a driving force of 10 K (°C), $\Delta T_{melting}$ remains above 4 K (°C) for a duration of four hours.

The tests were also conducted at an inlet air velocity of 0.5 m/s to gather experimental data under conditions of lower air velocity. During these tests, a minor glitch with the PID controller regulating the power input to the electric heater caused fluctuations in the recorded inlet air temperature. This led to a sudden change in temperature, typically in the range of 2 to 3°C, occurring between 3 and 4 hours of the testing period.

The results from melting Tests 3 and 4 exhibited excellent repeatability, with the maximum temperature difference being approximately 2 °C. As anticipated, the observed trends were similar to those depicted in Figure 4.11 for higher inlet air velocities (0.8 m/s). However, the rate of temperature increase in the outlet air was slightly slower, attributed to the reduced thermal capacity of the air stream. This slower increase in temperature led to a longer duration for the melting process.

In summary, the cooling effect generated by the tested tube array is roughly equivalent to 40% to 60% of the driving force ($\Delta T_{DF} = T_{in} - T_{ph.change}$), dependent on the air velocity, as mentioned earlier in Eq. 4.21. This implies that the PCM tube array has a more significant impact on the performance of the air-cooled condenser (ACC) when the ambient air temperatures are higher, as opposed to lower air temperatures.

As previously mentioned, the PCM freezing tests were conducted during the nighttime when the ambient air temperature was lower, typically around 288 K or 15°C for most of the freezing tests. This was in contrast to the PCM phase change temperature at the inlet air velocity of 0.8 m/s. The results for freezing Tests 1 and 2 are illustrated in Figures 4.13(a-b).

In Figure 4.13a, the inlet air temperature recorded during PCM freezing Tests 1 and 2 is depicted. The data reveals that the ambient air temperature was nearly identical during these tests and gradually decreased throughout the night, reaching its lowest point in the early morning. Similar to the previous figures, slight fluctuations in the inlet air temperature are indicated by the thin solid lines, while the thicker solid lines represent moving averages.

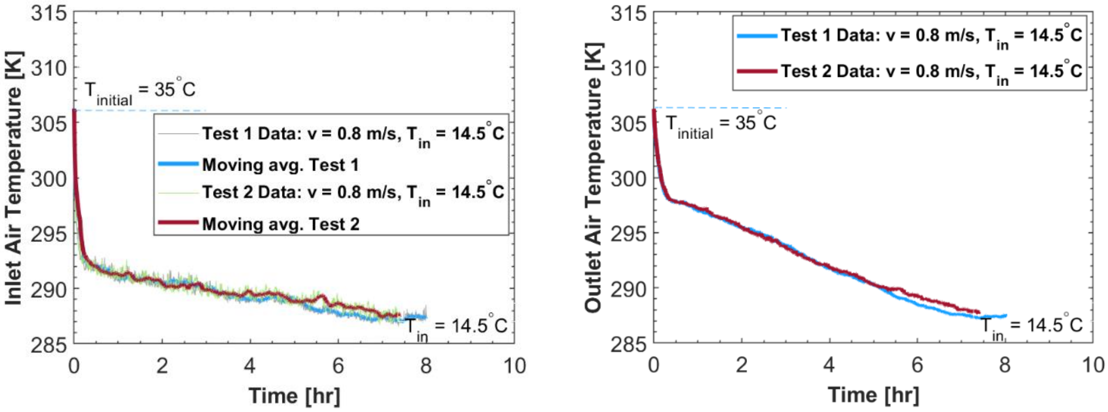

(a) (b)

Figure 4. 13. Comparison of freezing Tests 1 and 2 (a) inlet air temperature, (b) outlet air temperature as a function of flow time

Figure 4.13b presents a comparison of the outlet air temperatures for PCM freezing Tests 1 and 2, conducted with an inlet air velocity of 0.8 m/s and an initial PCM temperature of 308 K or 35°C. The sharp drop in outlet air temperature at the test's onset is a result of the rapid cooling of the molten PCM in the tubes. This is followed by an almost linear decrease during the PCM freezing process, and eventually, the temperature remains relatively constant as the frozen PCM undergoes subcooling, gradually approaching the inlet air temperature. The PCM freezing is considered complete when the outlet air temperature aligns with the inlet air temperature, which typically occurs approximately 7 hours after the initiation of the freezing test. These test results indicate very good repeatability, with a maximum temperature difference of less than 1°C.

The pressure drop within the tube array was measured upstream and downstream of the tube array, encompassing the core pressure drop as well as the pressure losses at the inlet and outlet caused by changes in flow velocity. At a superficial inlet air velocity of 0.8 m/s, the measured pressure drop was 70 Pa, aligning with the prescribed pressure drop threshold of 100 Pa. When the air velocity was reduced to 0.5 m/s, the pressure drop decreased to 30 Pa.

For the given test conditions during parametric study, the energy storage density within the tube bank was evaluated to be 28.0 kWh/m³ during PCM melting and 26.3 kWh/m³ during PCM freezing. The slight variation in energy storage between the melting and freezing experiments primarily results from the temperature differences applied in these two phases, impacting the sensible heat component of the heat storage capacity. The thermal storage capacity of the tube array, as determined in both PCM melting and freezing trials, ranges from 15.1 to 18.3 kWh. The specific details regarding the performance of tube array are presented in Table 4.5.

Table 4. 5 Summary of experimental results for the 16 × 13 tube array

Operating condition	**Melting Test - 1**	**Freezing Test - 1**	**Melting Test - 2**	**Melting Test - 3**
Initial temperature, $T_{initial}$ (°C)	16.0 ± 0.2	33.1 ± 0.0	18.0	20.0
Final temperature, T_{in} (°C)	35.0 ± 0.4	14.2 ± 0.2	36.7	30.8
Air velocity, v_∞ (m/s)	0.81	0.81	0.50	0.81
Pressure drop, ΔP (Pa)	70	70	30	70
Total stored energy, E_{st} (kWh)	18.3 ± 0.7	15.7 ± 0.6	17.3	15.1
Total stored energy density, (kWh/m^3)	27.0 ± 1.1	23.1 ± 0.8	25.4	22.3

4.3. Results and discussion

4.3.1. Comparison of experimental and numerical results

The numerical model used to analyze the melting and solidification of PCM in the tube array is described in Section 4.2.2. A realizable k-ε turbulence model was used to model turbulence within the fluid domain (air) of the tube array as mentioned earlier. A partially filled tube was simulated by assuming the tube was 100% filled with a PCM having 10% lower latent heat of fusion. Operating conditions corresponding to the prototype scale tests were applied to perform the computational analysis. To account for the transient behavior of the electric heater, variations in the inlet air temperature were simulated using UDF (User Defined Function).

The comparison of the results for Melting Test 1, as depicted in Figure 4.14a, demonstrates a strong agreement between the measured and numerically predicted values of the air temperature at the array outlet. This agreement is particularly evident at the beginning and end of the test. However, in the middle of the test, the numerical model exhibits a slight underprediction of the outlet air temperature by approximately 2 K (°C). As the test progresses, with over 4 hours of flow time, the predicted values start to exceed the measurements. The measured values show a gradual increase, while the numerical model suggests a linear temperature rise during the PCM melting phase, followed by a further increase after complete PCM melting. Approximately 3 hours after the commencement of the test, the model predicts a phase where the molten PCM experiences superheating, suggesting three distinct phases of phase transition: (a) heating of the solid PCM, (b) PCM melting (phase change), and (c) superheating where temperature of the molten PCM approaches the inlet air temperature. On the other hand, the measurements indicate a more gradual temperature increase.

Several factors may contribute to this disagreement, including the utilization of the enthalpy-porosity model/technique, measurement locations, and instrumentation. Recent literature suggests that better predictions for this geometry may be achieved by employing the specific heat capacity-porosity method, as proposed by Iten et. al. [43]. Additionally, the thermal resistance and inertia of the tube wall and the method of obtaining the average outlet air temperature play a role. The average outlet air temperature was determined through an array of RTDs using the Equal Area Method for measurements, while the numerically obtained average value represents the mass average. Although the thermal resistance and inertia of the tube wall do contribute to the difference, their effect is deemed relatively minor.

As mentioned earlier, the PCM temperature within the tube was measured using a thermocouple placed in the center of selected tubes (see Figure 4.10). The comparison between the measured and predicted values of PCM temperature in the upstream and downstream PCM tubes (PCM tubes 01 and 04) is presented in Figure 4.14b for Melting Test 1, plotted against the test (flow) time. The numerical model accurately predicts the duration of the heating phase of the solid PCM at the test's outset. However, during the PCM melting phase, the numerical model assumes a constant PCM temperature, while experimental data show a gradual increase followed by an almost constant temperature plateau. This disparity can be attributed to the assumption of a constant solidification/melting temperature in the numerical approach using the enthalpy-porosity technique. In reality, the phase change temperature may not remain constant due to impurities in the commercial PCM, as noted by Iten et. al. [43]. Consequently, the heat capacity of the PCM may not be constant, as assumed in the numerical analysis employing the enthalpy-porosity technique. As previously discussed, the specific heat capacity-porosity method may offer more accurate predictions in such cases.

Furthermore, the numerical model predicts a shorter melting time compared to the experimental results. It indicates approximately 3 hours for the PCM in the tubes upstream of the tube bank, while the experimental data show that PCM melting takes around 4.5 hours. This discrepancy may be related to the placement of the thermocouples. Additionally, it is worth noting that the numerical model provides an average temperature for the PCM, while the thermocouples measure the temperature of the PCM at a single point at the center of the tube.

It is important to note that the PCM in the upstream tube melts approximately 2 hours earlier compared to the downstream tube. This discrepancy is due to the melting front propagating through the tube array in the direction of the flow, and the temperature of the inlet air decreases as it progresses downstream. Moreover, the trend observed in the melting temperatures of the PCM aligns with findings in the literature [118], which employed a natural convection boundary condition approach.

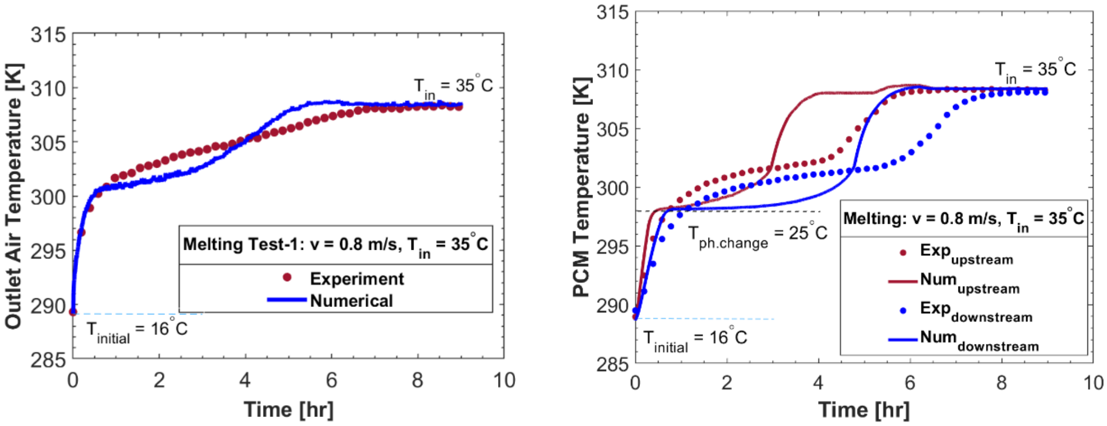

(a) (b)

Figure 4. 14. (a) Outlet air temperature and (b) PCM temperature as a function of flow time during the PCM melting test for inlet air velocity and temperature of 0.8 m/s and 35°C and initial temperature of 16°C.

Figure 4.15 shows the comparison of experimental and numerical analysis of Freezing Test 1. The analysis of the air temperature at the outlet of the tube array, as depicted in Figure 4.15a, reveals a high level of agreement between the measured and numerically predicted values, with a maximum temperature difference within a 1 K (°C) range. Similar to the PCM melting process, the freezing of PCM unfolds in three distinct stages: (a) the cooling of the molten PCM, (b) the phase change as PCM freezes, and (c) subcooling, where the temperature of the solidified PCM approaches the inlet air temperature. As previously mentioned, numerical simulations and prototype-scale tests were conducted to determine the duration required for PCM to freeze within the tube array during nighttime when ambient air temperatures are lower than the phase change temperature. Consequently, simulating PCM freezing and conducting PCM freezing tests constitute crucial components of the design process.

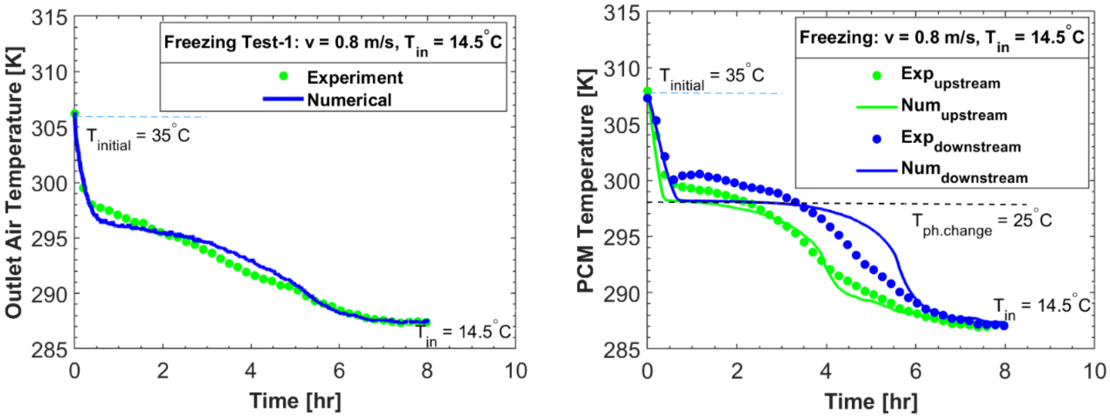

(a) (b)

Figure 4. 15. (a) Outlet air temperature and (b) PCM temperature as a function of flow time during PCM freezing for inlet air velocity and temperature of 287.5 K or 14.5^{o}C and 0.8 m/s and initial PCM temperature of 308 K or 35^{o}C.

The comparison of PCM temperature, as illustrated in Figure 4.15b, demonstrates a good agreement between numerical predictions and actual measurements with a difference less than 3 °C. PCM freezing temperatures follow a similar pattern to freezing temperatures found in literature [118], which used natural convection conditions. Also, PCM in tubes closer to the airflow freezes quicker than those farther away because the freezing moves with the airflow. Under the specific test conditions and with the chosen tube array geometry, the complete freezing of PCM within the tube array is achieved in less than 7 hours (as shown in Figure 4.15a). The three stages of the PCM freezing process are visually represented in Figure 4.15b.

Table 4.6 illustrates a comparison between numerical predictions and experimental correlations regarding the hydraulic and thermal performance. The results reveal a strong agreement between the numerical predictions and the Zukauskas correlation [108]. The measured pressure drop in the experiment was higher due to cold ambient conditions, resulting in a denser air. Furthermore, the correlation was derived from a tube array with more tube rows, which aided in streamlining the flow, coupled with an inlet flow straightener to ensure flow uniformity.

For the investigated range of superficial (freestream) inlet air velocities, the measured pressure drop (ΔP) across the 13-row circular PCM tube array is significantly lower, ranging from 30 to 70 Pa depending on the air velocity. This is in contrast to the maximum target value of 100 Pa. The numerically predicted values of ΔP and the average heat transfer coefficient closely match the experimental correlation, demonstrating excellent agreement with less than 10% difference.

Table 4. 6 Comparison of numerical predictions and experimental correlations

Cases	v_∞ (m/s)	ΔP (Pa)			$h_{avg.}$ (W/m^2-K)	
		Exp	Num	Zu [108] Correlation	Num	Zu [83] Correlation
Melting	0.82	70 ± (2-3)	56.34	60.30	51.27	48.30
Solidification	0.82	70 ± (2-3)	58.61	64.30	48.63	50.10

4.3.2. Contours of PCM melting/ solidification

Figures 4.16 and 4.17 display the anticipated contours of the liquid fraction of PCM within the tubes and the air temperature during the melting of PCM, respectively, at a freestream air velocity of 0.8 m/s. In the liquid fraction legend, the red color signifies a liquid fraction of one, while the blue color represents frozen PCM (a liquid fraction of zero). In the temperature legend, the red color corresponds to an air temperature of 308 K or 35 °C (the inlet air temperature), while the blue color indicates air temperature close to the PCM phase change temperature. A narrow green-yellow ring encircling the solid PCM signifies the mushy zone.

These results provide insight into the dynamic process of PCM melting within a tube array. As heat transfers from the air to the PCM inside the tubes, the PCM temperature rises, initiating the melting process. PCM melting commences in the initial row of tubes and progresses downstream as a melting front. After approximately 9,600 seconds (2.7 hours), a significant portion of the PCM at the front end of the array has melted, while the rear portion of the array still contains solid PCM. Due to the secondary wake within the tube array, the PCM in the second row of tubes melts more quickly than in the first row. By the time 12,000 seconds have elapsed (3.33 hours), nearly all the solid PCM in tubes 1 to 6 has melted, with only a small amount of solid PCM remaining in the rear rows of tubes. This dynamic process of PCM melting accounts for the variation in air temperature at the array outlet over time, as discussed earlier and depicted in Figure 4.14a. Specifically, the air outlet temperature remains relatively constant as long as there is solid PCM in the tubes located at the front of the tube array. However, as the melting front advances downstream in the direction of the air flow, the air outlet temperature increases due to the superheating of the liquid PCM.

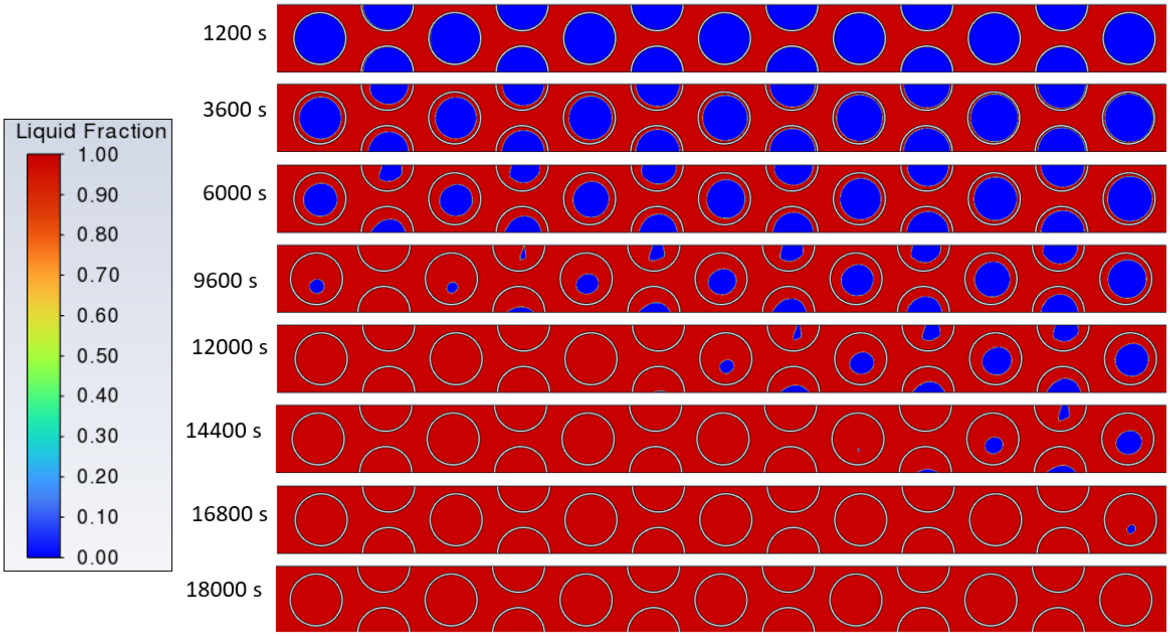

Figure 4. 16. Liquid fraction contours during PCM melting in 1.75" PCM tubes, 90% filled with commercial-grade PCM in the 13-row tube array as functions of time for air velocity of 0.8 m/s

Figure 4.17 illustrates the predicted temperature of the air stream as it flows through the array during the PCM melting process. As previously mentioned, the variation in air temperature leaving the array mirrors the dynamics of PCM melting.

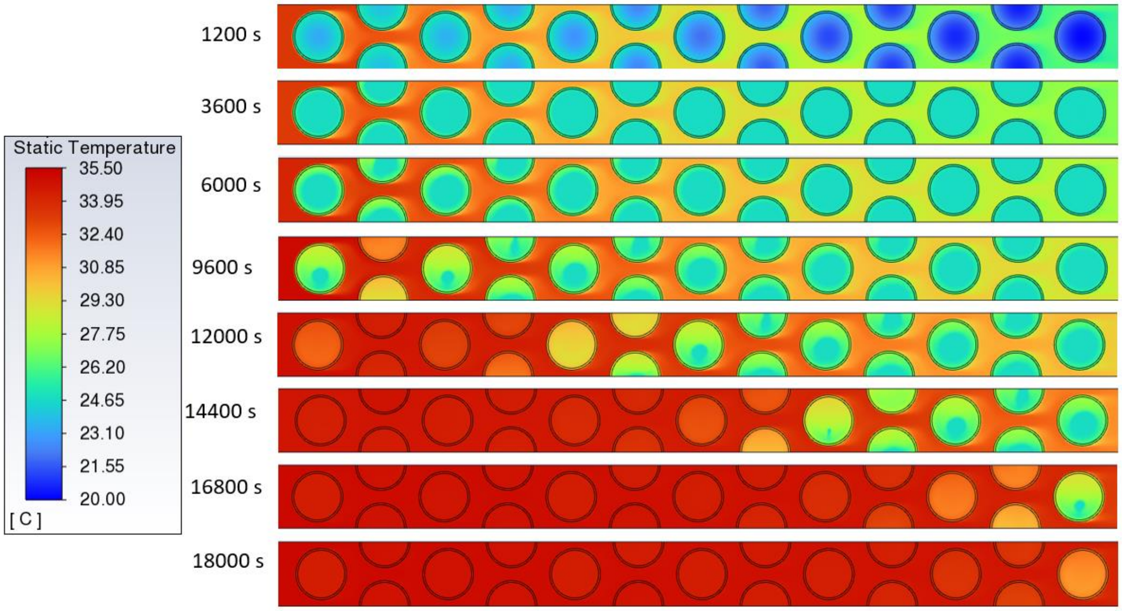

Figure 4. 17 Temperature of air flowing through the array as a function of time for freestream air velocity of 0.8 m/s during PCM melting

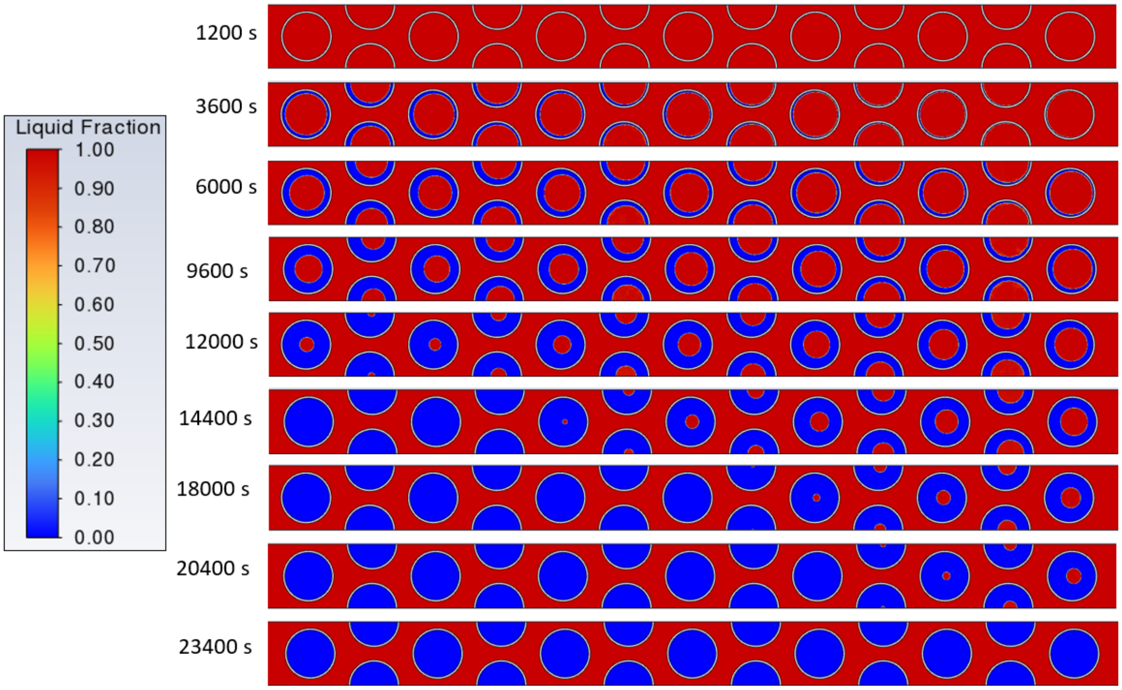

Figure 4. 18 Liquid fraction contours during PCM freezing in 1.75" PCM tubes, 90% filled with commercial-grade PCM in the 13-row tube array as functions of time for air velocity of 0.8 m/s

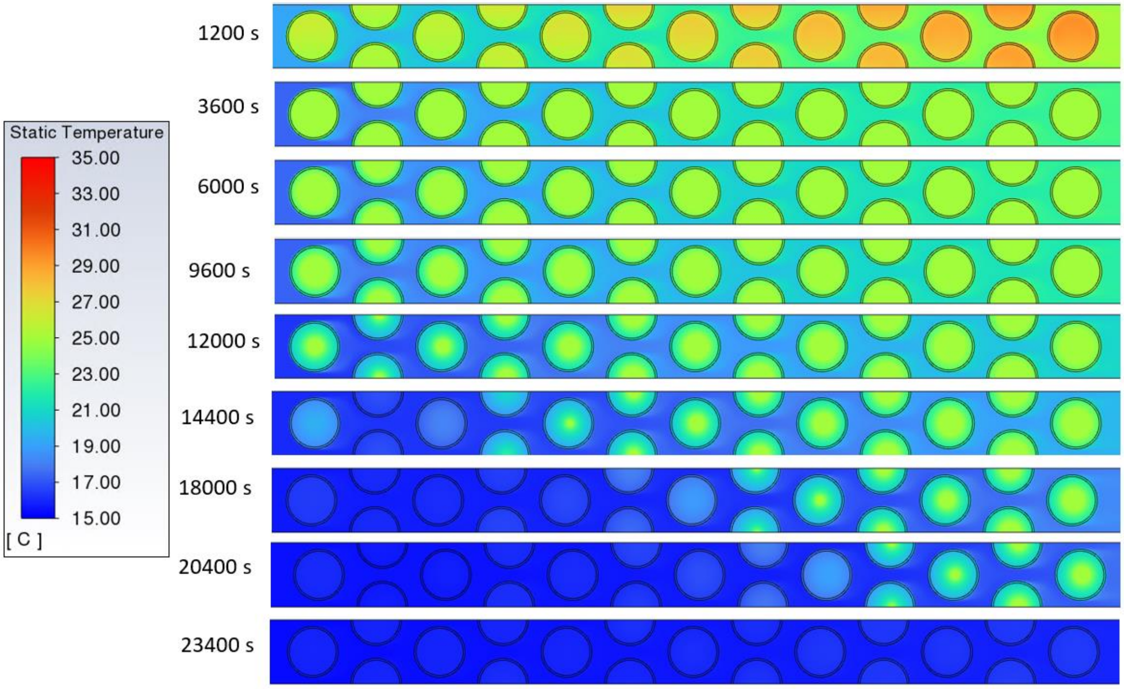

Figure 4. 19 Temperature of air flowing through the array as a function of time for freestream air velocity of 0.8 m/s during PCM freezing

Similar to the PCM melting process, the liquid fraction and air temperature contours depicted in Figures 4.18 and 4.19 respectively, provide insight into the dynamics of PCM freezing within the 13-tube array. This simulation was conducted under conditions of an inlet air velocity of 0.8 m/s, an initial air temperature of approximately 288 K or 15°C, and an initial PCM temperature of 308 K or 35°C, assuming a partial (90%) tube fill by assuming a 10% lower latent heat of fusion.

As illustrated in Figure 4.18, PCM initially freezes along the periphery of the tubes, with freezing progressing inward toward the center of the tubes. Additionally, freezing initiates in the front rows of the array, and the freezing front advances in the direction of the air flow. Roughly 14,400 seconds (4 hours) into the process, the PCM in the first six rows of the array is fully frozen. By 20,400 seconds (5.7 hours), only a small amount of solid PCM remains at the downstream end of the array. Complete freezing of the PCM within the tube array occurs at approximately 21,600 seconds (6 hours). This indicates that with the corresponding design, the cooling of the storage can be effectively accomplished during nighttime hours.

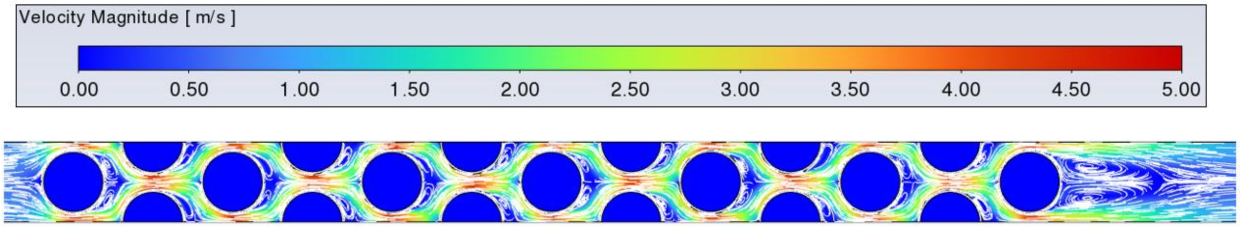

Figure 4. 20. The predicted air velocities in a 13-row tube array for freestream air velocity of 0.8 m/s

Figure 4.20 displays the predicted air velocities within the tube array. As anticipated, the simulations indicate the presence of wakes trailing behind the tubes. The air velocity experiences a transition from the inlet value of 0.8 m/s to approximately 4 m/s as it accelerates while passing through the narrowest gap between the tubes. Subsequently, as the flow progresses through the staggered tube arrangement, it decelerates in response to the expanded flow area. The flow re-accelerates upon passing through the subsequent narrowest flow area between the tubes. This leads to a series of alternating accelerations and decelerations within the air flow through the tube array. Upon exiting the array, the flow gradually decelerates, ultimately reaching the superficial air velocity of 0.8 m/s. The pressure drop, as predicted by the Zukauskas correlation [108], is related to the maximum velocity in the tube array. Vortices develop downstream of the tubes. The acceleration and deceleration of velocity within the array result in a pressure drop between the inlet and outlet of the tube array.

4.4. Conclusions

This paper provides a detailed design of the prototype-scale module for a Latent Heat Thermal Energy Storage (LTES) system. The tests were conducted at the Lehigh University prototype-scale test facility in May and June of 2023, and this study involves a comparison between numerical and experimental results. The key findings are summarized as follows:

- The tested PCM tube array geometry consists of 1.75" OD tubes, 90% filled with commercial-grade PCM, operating at an inlet air velocity of 0.8 m/s and an inlet air temperature of 308 K or 35 °C. It meets or exceeds the performance criteria of the design regarding the magnitude (4 °C) and duration (4 hours) of the cooling effect. Furthermore, the proposed design can be cooled down overnight.
- The measured temperatures exhibit excellent repeatability, with the maximum difference in $\Delta T_{melting}$ between the repeated tests within a 1 K (°C) range.
- The cooling performance of the tested tube array accounts for roughly 40 to 60% of the driving force ($\Delta T_{DF} = T_{in} - T_{ph.change}$), depending on the air velocity. This implies that the PCM tube array exerts a more significant influence on ACC performance in elevated ambient air temperatures as opposed to lower temperatures.
- The numerical results of the temperature at the tube array outlet demonstrate a very good agreement with the measurements.
- The discrepancy between the numerical prediction of PCM temperatures and the measurements is attributed to the assumption of a constant phase change temperature of the commercial PCM, which may be influenced by impurities in the PCM. Using the specific heat capacity method instead of the enthalpy-porosity technique to model melting and solidification process of PCM could lead to a better prediction [43].
- The pressure drop through the tube array, measured at the array inlet and outlet, falls in the range of 30 to 70 Pa, depending on the superficial inlet air velocity (0.5 or 0.8 m/s), and it satisfies the pressure drop requirement of 100 Pa or less.
- The proposed design was used to perform a comparative study using cylindrical and elliptical tubes to continue improving the system performance.

- Numerical predictions of pressure drop, and the pressure drop calculated using the Zukauskas correlation [108] exhibit a very good agreement. The measured pressure drop in the experiment was higher due to cold ambient conditions, resulting in denser air.
- The thermal storage capacity of the tube array under test conditions ranges from 15 to 18 kWh, depending on the test mode (PCM melting or freezing) and operating conditions (inlet air temperature). The corresponding energy storage density is in the range of 22 to 27 kWh/m^3.

Author contributions

Mahfuja A. Khuda: Numerical analysis, Investigation, Methodology, Software, Verification & Validation, Post-processing, Experiment, Writing – original draft.

Lida Yan: PCM preparation, Experiment, CAD model, Writing - review & editing.

Nenad Sarunac: Conceptualization, Project administration, Resources, Supervision, Writing - review & editing.

Carlos Romero: Conceptualization, Project administration, Resources, Supervision.

Conflict of interest

The authors declare no conflict of interest.

Acknowledgement

The paper is based upon work supported by the U.S. Department Office of Fossil Energy FE-1 under Award Number DE-FE0031886.

Disclaimer

This paper was prepared as an account of work sponsored by an agency of the United States Government. Neither the United States Government nor any agency thereof, nor any of their employees, makes any warranty, express or implied, or assumes any legal liability or responsibility for the accuracy, completeness, or usefulness of any information, apparatus, product, or process disclosed, or represents that its use would not infringe privately owned rights. Reference herein to any specific commercial product, process, or service by trade name, trademark, manufacturer, or otherwise does not necessarily constitute or imply its endorsement, recommendation, or favoring by the United States Government or any agency thereof. The views and opinions of authors expressed herein do not necessarily state or reflect those of the United States Government or any agency thereof.

CHAPTER 5: ENERGY AND EXERGY ANALYSIS OF A PROTOTYPE-SCALE LATENT HEAT THERMAL ENERGY STORAGE (LTES) SYSTEM

5.1. Overview

This section provides energy and exergy analyses of a prototype-scale Latent Heat Thermal Energy Storage (LTES) system. The design, presented in the previous chapter, features a prototype-scale LTES system that uses commercial-grade hexahydrate calcium chloride as a phase change material (PCM) in a staggered tube array configuration placed horizontally. The energy stored in each PCM tube during the tests was compared with the numerical analysis for the corresponding tubes. Exergy analysis was performed to account for entropy losses and compute usefulness of the system. Thermal loss and measurement uncertainties are presented at the end of this chapter.

5.2. Energy and exergy of the system

The energy and exergy analyses were performed for the prototype scale (13-row tube array) LTES to evaluate the efficiency and effectiveness of the system. The energy transfer across the tube bank over a period of time was calculated following the traditional heat transfer analysis from the literature [5, 40] as shown in Eq. 5.1:

$$E_{in} = \int_0^t \dot{m}_{air} C_{P_{\mathrm{air}}} (T_{in} - T_{out})\, \mathrm{d}t - Q_{loss} \tag{5.1}$$

where, Q_{loss} accounts for the heat loss from the system, no heat loss is considered during numerical analysis. However, heat loss does occur during the test, either at the duct wall or through the system.

The average value of energy stored in all PCMs is calculated considering the liquid fraction (γ) and the average PCM temperature as presented in Eq. 5.2 [5]:

$$E_{st} = \frac{1}{N} \sum_0^N m \left[\int_{T_{low}}^{T_{melt}} Cp_{solid} (1-\gamma)\, dT + \gamma L_f + \int_{T_{melt}}^{T_{high}} Cp_{liquid}\, \gamma\, dT \right] \tag{5.2}$$

where, N is the number of the tubes. Cp_{solid} and Cp_{liquid} are the specific heat of the frozen and melted PCM, respectively.

As the experiment does not provide data on the liquid fraction, linear variation was assumed. Therefore, PCM temperature exhibits nearly linear change during the phase transition (as shown in Figures 5.7c and 5.8c), also, an average value of the specific heat of PCM was employed to compute the energy stored in the PCM-filled tubes for the experimental results.

From an energy perspective, only heat generation through viscous dissipation was considered as a loss, resulting in very high overall efficiencies [110]. The energy efficiency (η) of the system is derived from the ratio of the stored energy and energy transfer to the system (Eq. 5.3):

$$\eta = \frac{E_{st}}{E_{in}} \tag{5.3}$$

Since the energy balance does not consider the internal or external losses in the system, exergy balance over a period was carried out to take into account the entropy losses and calculate the useful work in the system following the expression Eq. (5.4)

$$Ex_{in} = \int_0^t \dot{m}_{air} C_{P_{\text{air}}} \left[(T_{in} - T_{out}) - T_o \ln\left(\frac{T_{in}}{T_{out}}\right) \right] \mathrm{d}t \tag{5.4}$$

The exergy stored in the PCM using the ambient temperature (T_o) was computed from the Eq. (5.5)

$$Ex_{st} = E_{st} \left[1 - \frac{T_O}{T_{PCM}} \right] \tag{5.5}$$

The exergy efficiency ($\boldsymbol{\Xi}$) of the system is derived from the ratio of the exergy stored and exergy transfer to the system (Eq. 5.6):

$$\boldsymbol{\Xi} = \frac{Ex_{st}}{Ex_{in}} \tag{5.6}$$

The maximum possible energy can be stored when the average PCM temperature equals the inlet temperature of the heat transfer fluid (air). Eqs. (5.7), (5.8) were used to calculate the maximum energy and maximum exergy that could be stored in the system, respectively.

$$E_{st_{\max}} = \int_{T_{PCM}}^{T_{in}} m\, Cp_{avg.}\, dT + mL_f \tag{5.7}$$

$$Ex_{max} = E_{st_{\max}}\left[1 - \frac{T_o}{T_{in}}\right] \tag{5.8}$$

To investigate the effectiveness of the system, the energy efficiency and exergy effectiveness were calculated from the ratio of the actual energy or exergy stored to the maximum energy or exergy that could be stored as shown by Eq. (5.9) and (5.10), respectively.

$$\epsilon = \frac{E_{st}}{E_{st_{\max}}} \tag{5.9}$$

$$\chi = \frac{Ex_{st}}{Ex_{\max}} \tag{5.10}$$

The energy and exergy parameters were outlined as a function of the dimensionless parameter, Fourier number (Fo), dimensionless time, calculated from Eq. (5.11)

$$Fo = \frac{\alpha_d t}{D^2} \tag{5.11}$$

where, thermal diffusivity, $\alpha_d = \frac{k_{air}}{\rho_{air} Cp_{air}}$

5.3. Energy and exergy analyses of PCM melting

Energy and exergy analyses were performed during the system discharging process (PCM melting) in the daytime, with an inlet velocity of 0.8 m/s and an incoming air temperature of 308 K (35°C) at the inlet. Figure 5.1a shows the comparison of temperature differences between the inlet and outlet as a function of Fo number, which is used to determine the energy transfer through the system using Eq. 5.1. Both the numerical predictions and the measured data were plotted on the same graph for comparison. As time progresses, all PCMs in the tube melt completely, resulting in a steady-state condition with a temperature difference between the inlet and outlet close to 0 K. The numerical results and the test results both initially and at the final state agree well, with a temperature difference of approximately 2 K in the middle. This may result in different values for heat transfer through the system in numerical and experimental results.

Figure 5.1b illustrates the comparison of the temperature differences between the PCMs in the tubes and the temperature at the inlet as a function of the Fo number for both numerical and test results. Since the PCM melting front progresses in the direction of the flow, the PCMs in the downstream tube melt later compared to those in the upstream tube (see Figure 5.1b). Additionally, there is a discrepancy between the numerically predicted results (solid lines) and the measured PCM temperatures (dotted lines). It should be noted that the inlet temperature was the same for both the numerical predictions and the measurements. The mean values of PCM temperatures and the liquid fractions of PCM in the tubes were used to determine the energy stored in the system during the PCM melting process using Eq. 5.2.

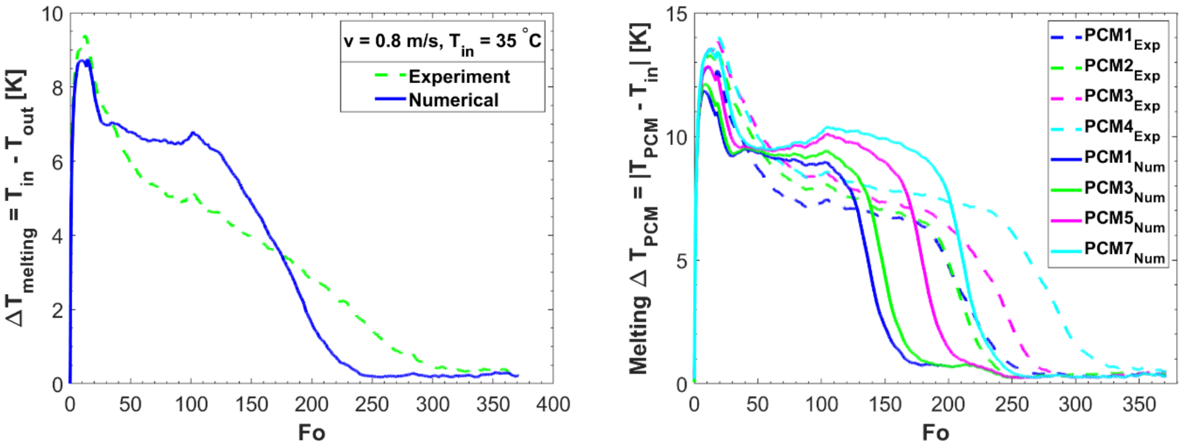

(a) (b)

Figure 5. 1 Comparison of temperature differences: (a) between inlet and outlet, and (b) between PCM and inlet, as a function of the Fo number during PCM melting process within a prototype-scale LTES module.

Figure 5.2a presents a comparison of energy variation over the dimensionless time, represented by the Fo number, during PCM melting in a 13-row tube array. The comparison is made between experimental and numerical analyses. In the numerical prediction (represented by a solid line), the energy transfer in the storage module is higher by approximately 4.5 MJ or 10% compared to the experimental results (represented by a dotted line). This discrepancy arises because the numerical analysis simulates an ideal case, neglecting ambient effects on storage and heat loss in the system.

As the temperature difference between the inlet and outlet of the array persists, the stored energy (heat) increases until the PCM in the tubes completely melts and begins superheating. The maximum energy transferred to the system during discharging/PCM melting is approximately 51.8 MJ for the numerical prediction and 48.5 MJ for the experimental results, as shown in Figure 5.2a.

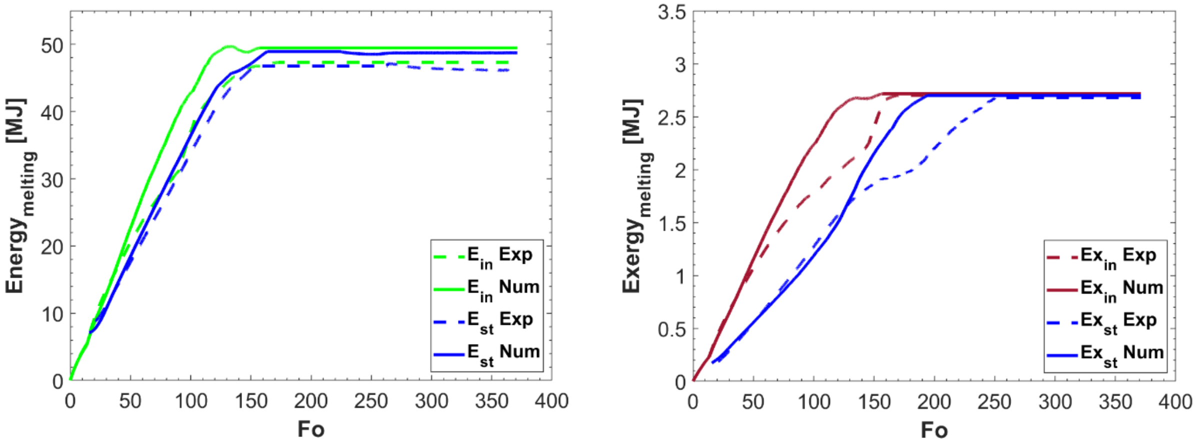

(a) (b)

Figure 5. 2. Comparison of experimental and numerical results for (a) energy and (b) exergy analyses in the prototype-scale LTES system during PCM melting, presented as functions of the Fo number.

From the energy balance equation, the energy transferred to the system should equal the energy stored in the system. Therefore, the maximum energy that could be stored in the system is approximately equal to the transferred energy at the equilibrium state, which is 48.9 MJ for the numerical results and 47.2 MJ for the measurements (refer to Figure 5.2a). The very small discrepancy between the energy transfer through the system and the energy stored within the system accounts for the sensible heat gain at the tube wall, which is neglected in the calculations. All energy parameters continue to increase until they reach a maximum value and then remain constant, indicating that the PCM in the tubes has started to superheat.

Figure 5.2b presents the variation of exergy quantities with the Fo number during the PCM melting process. Exergy is a critical parameter in the analysis as it quantifies the entropy generation in the system, which results from the irreversibility associated with heat transfer. When the temperature driving force is greater, it leads to increased entropy generation and, consequently, higher exergy destruction. In this scenario, with an inlet temperature (T_{in}) of 308 K or 35 ºC, which is 10 ºC higher than the fusion temperature of PCM ($T_{ph.change}$ = 298 K or 25 ºC), the exergy quantities are significantly lower compared to the energy quantities for the PCM melting process.

As time progresses, the exergy stored in the system increases due to a rise in the average PCM temperature, entering what can be identified as the convection dominant zone (see Figure 5.2b). The increase in the temperature difference between the inlet and outlet, as shown earlier in Figure 5.1a, leads to higher exergy input and thus a higher maximum exergy. Once the PCM has completely melted, the exergy levels off and becomes almost constant, as conduction becomes the predominant mode of heat transfer.

The exergy during the melting process is significantly lower than the energy, primarily due to both internal and external irreversibilities. It is crucial to minimize factors such as heat gain to enhance the overall performance. The maximum exergy stored/transferred in the system is approximately 2.7 MJ for both the numerical and experimental results after the equilibrium state is reached (refer to Figure 5.2b).

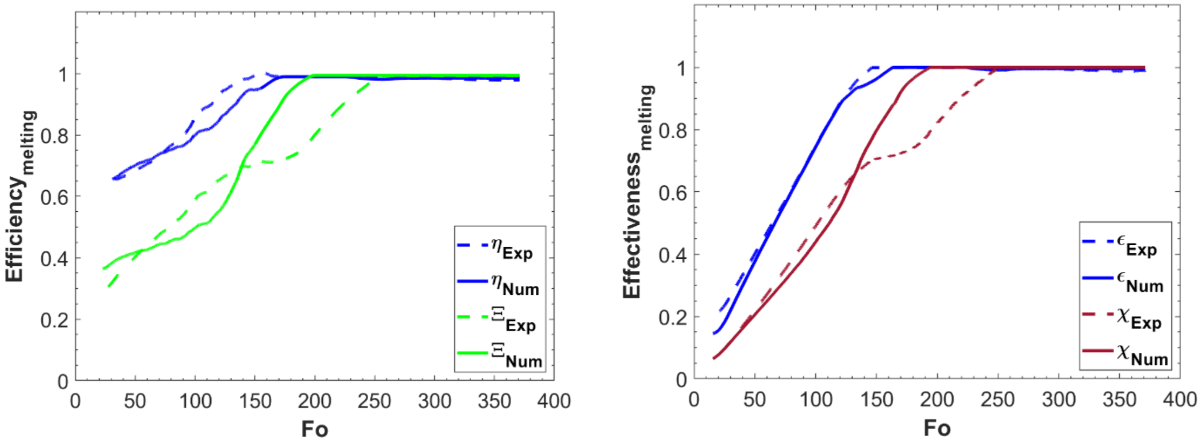

Figure 5. 3. Comparison of experimental and numerical results of (a) efficiency and (b) effectiveness of the prototype-scale (13-row tube array) LTES system during melting, as functions of the Fo number.

Figure 5.3 illustrates the energy and exergy efficiency and effectiveness during the PCM melting process, as a function of the Fo number. The trends for energy (η) and exergy (Ξ) efficiencies are similar, as shown in Figure 5.3a. During the phase change period, the experimentally obtained values of energy and exergy efficiencies are slightly higher than the numerical ones but become the same during PCM superheating. Figure 5.3a shows that energy and exergy efficiency increases from the beginning to the phase change period as the average temperature of the PCM increases during the melting process (refer to Figure 4.14b) and becomes constant once all the PCM in the tubes has completely melted and begins to superheat. The maximum energy (η ~ 0.98) and exergy (Ξ ~ 0.99) efficiencies are achieved when the PCM starts to superheat (Figure 5.3a).

Energetic (ϵ) and exergetic (χ) effectiveness were calculated from the ratio of stored energy/exergy to the maximum energy/exergy that could be stored to determine the storage effectiveness and were presented as a function of the Fo number in Figure 5.3b. Energetic effectiveness (ϵ) increases linearly during the phase transition and becomes constant once all the PCM in the tubes has melted for both numerical and experimental results. On the other hand, exergetic effectiveness (χ) increases almost linearly during the phase transition for numerical results, while for the experimental results, the trend is similar to the exergy efficiency (Ξ) of the experiments. The maximum energetic and exergetic effectiveness (χ) is close to 1 for both numerical and experimental results.

5.4. Energy and exergy analyses of PCM solidification/ freezing

Similar to the PCM melting process, the energy and exergy during the system charging process (PCM solidification) were analyzed at night. An inlet velocity of 0.8 m/s and an air temperature of 287.5 K (14.5 °C) were used at the inlet. In Figure 5.4a, the temperature differences between the inlet and outlet over time are compared, aiding in the understanding of energy transfer through the system as outlined in Eq. 5.1. Both numerical predictions and actual measurements are included on the graph for comparison. Over time, all PCMs in the tube are solidified completely, resulting in a temperature difference between the inlet and outlet that approaches zero. The numerical results are shown to closely match the test results, with a very small temperature difference of less than 1 K noted in the middle.

Figure 5.4b presents a comparison of temperature differences between the PCM in the tubes and the inlet temperature, plotted as a function of the Fo number for both numerical and experimental results. As the PCM freezing front moves in the direction of flow, PCM in the tubes downstream solidifies later than in those upstream (refer to Figure 5.4b). Additionally, there is a very slight mismatch between the numerically predicted results (solid lines) and the actual measured PCM temperatures (dotted lines), particularly in the range of Fo numbers from 50 to 100. Given that the inlet temperature remained consistent for both numerical predictions and measurements, the amount of energy stored in the system during the PCM solidification process is influenced by the average temperatures of the PCM and the average liquid fraction in the PCM-filled tubes.

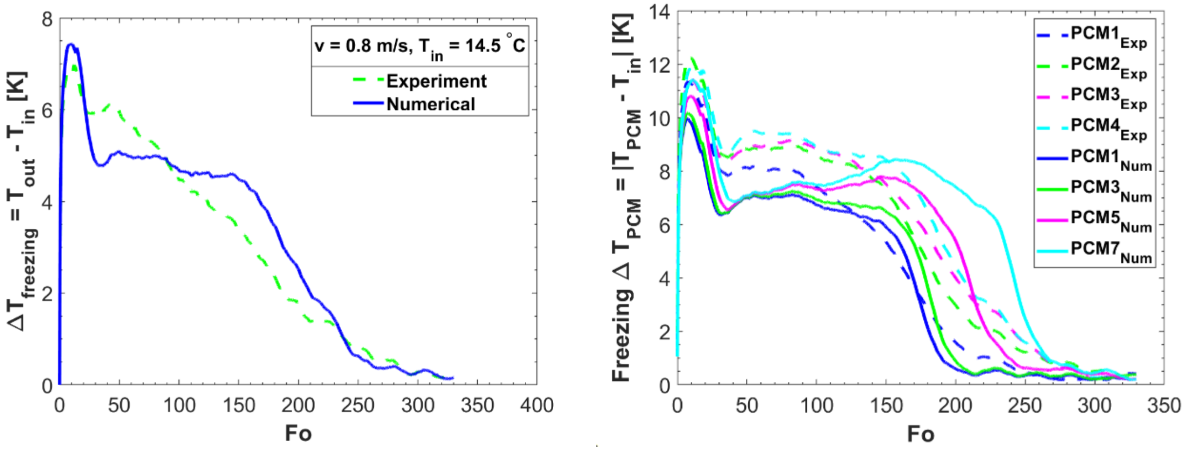

Figure 5. 4 Comparison of temperature differences: (a) between inlet and outlet, and (b) between PCM and inlet, as a function of the Fo number during PCM freezing process within a prototype-scale LTES module.

Figure 5.5a presents a comparison of energy variation over dimensionless time, represented by the Fo number, during PCM freezing in a 13-row tube array. The comparison is made between experimental and numerical analyses. Since the test for system charging was conducted at night with the system exposed to the cold ambient air, there is no heat loss from the system. Instead, heat is released from the PCMs to warm the incoming cold air. The numerically predicted results of energy (solid line) are almost equal to the energy calculated from the measurements, with a very small discrepancy of around 2%.

As the temperature difference between the inlet and outlet of the array continues, the energy released by the system increases until the PCM in the tubes fully freezes and starts to supercool. The peak energy transferred to the system during discharging or PCM melting reaches about 51.6 MJ according to the numerical prediction, and 50.5 MJ based on the experimental results, as depicted in Figure 5.5a.

As mentioned earlier, the energy transferred to the system should equal the energy stored in the system from an energy balance perspective. Therefore, the maximum energy that could be released (E_{st}) from the system during PCM freezing is approximately equal to the transferred energy at the equilibrium state, which is 49.7 MJ for both numerical and experimental results (refer to Figure 5.5a). Sensible heat release from the tube wall accounts for the small discrepancy between the energy transferred and the energy (heat) released from the PCMs, which is neglected in the calculations. All energy parameters continue to increase until they reach a maximum value and then remain constant, indicating that the PCM in the tubes has frozen and started to subcool.

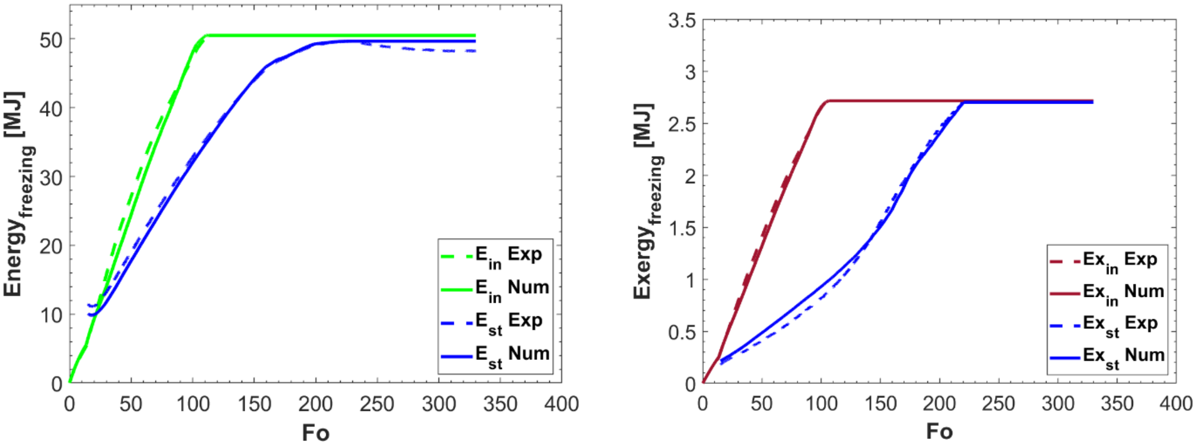

Figure 5. 5. Comparison of experimental and numerical results for (a) energy and (b) exergy analyses in the prototype-scale LTES system during PCM freezing, presented as functions of the Fo number.

Figure 5.5b presents the variation in exergy quantities with the Fo number during the PCM solidification process. As previously mentioned, entropy generation was considered for the exergy analysis. When the temperature driving force is greater, it leads to increased entropy generation and, consequently, higher exergy destruction. In this scenario, with an inlet temperature (T_{in}) of 287.5 K or 14.5 ºC, which is 10 ºC lower than the fusion temperature of PCM ($T_{ph.change}$ = 298 K or 25 ºC), the exergy quantities are significantly lower compared to the energy quantities during the PCM freezing process.

As time progresses, the exergy stored in the system increases due to a decrease in the average PCM temperature, shifting into the convection dominant zone (see Figure 5.5b). The widening temperature difference between the inlet and outlet, as previously shown in Figure 5.4a, results in higher exergy input and thus a higher maximum exergy. Once the PCM is fully frozen, exergy levels off and remains nearly constant as conduction becomes the dominant mode of heat transfer. The numerical predictions and experimental results for exergy closely align. The maximum exergy released or transferred to the system is approximately 2.7 MJ for both numerical and experimental results (refer to Figure 5.5b). After about 19440 seconds (Fo = 222), the exergy release from the system reaches its maximum value.

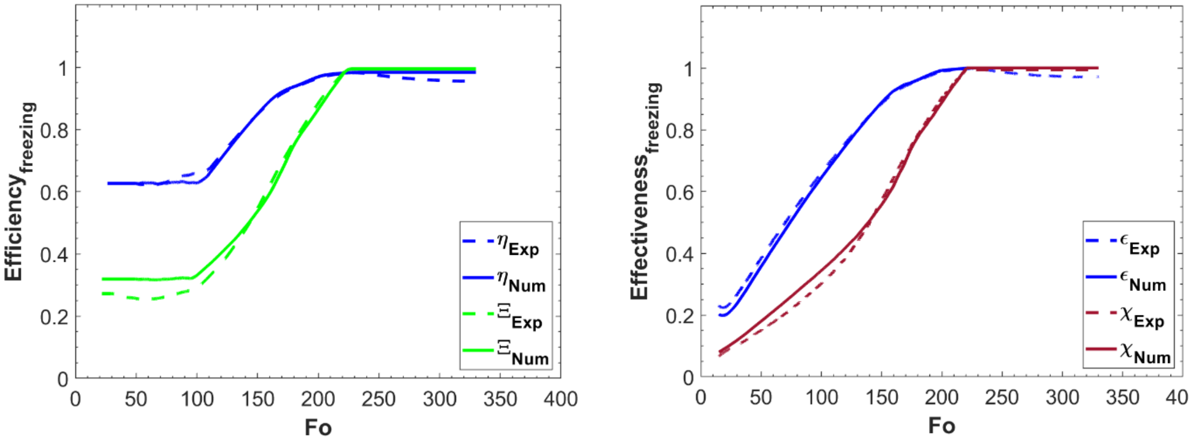

Figure 5. 6. Comparison of experimental and numerical results of (a) efficiency and (b) effectiveness of the prototype-scale (13-row tube array) LTES system during freezing, as functions of the Fo number.

Figure 5.6 illustrates the energy and exergy efficiency and effectiveness during the PCM solidification process, as a function of the Fo number. The trends for energy (η) and exergy (Ξ) efficiencies are similar, as shown in Figure 5.6a. There is an overlap between the numerical and experimental results for energy and exergy efficiencies. During the phase change period, the exergy remains lower than the energy until the Fo number reaches 222. Figure 5.6a indicates that energy and exergy efficiency increase from the beginning of the phase change period as the average temperature of the PCM decreases during the freezing process (refer to Figure 4.15b) and remain constant once all the PCM in the tubes has completely frozen and begins to subcool. The maximum energy (η ~ 0.96) and exergy ($\varXi$ ~ 0.99) efficiencies are achieved when the PCM begins to subcool (Figure 5.6a).

Similar to PCM melting, energetic (ϵ) and exergetic (χ) effectiveness were calculated and presented as a function of the Fo number in Figure 5.6b for the PCM solidification process. Both energetic (ϵ) and exergetic (χ) effectiveness increase almost linearly during the phase transition and become constant once all the PCM in the tubes has frozen for both numerical and experimental results. Additionally, the results for numerical and experimental analysis overlap. The maximum energetic and exergetic effectiveness (χ) is close to 1 for both sets of results.

5.5. Analysis of thermal loss at the duct wall

To improve the precision of the energy balance approach, it is crucial to account for the heat loss between the air and the duct wall. Additionally, analyzing the thermal losses within the system during the experiment offers valuable insights into potential causes for the discrepancies observed between the numerical and experimental results, as discussed in previous sections. The calculation for the thermal energy exchanged between the air and the wall (Q_{wall}) is as follows:

$$Q_{wall} = \int_0^t \dot{Q}_{wall}\,\mathrm{d}t = m_{wall} C_{P_{\text{wall}}} \left(T_{wall,initial} - T_{wall,final}\right) \tag{5.12}$$

where, m_{wall} and $C_{P_{\text{wall}}}$ denote the mass and specific heat of the wall surrounding the module, and for all cases, these values are 146 kg and 0.49 kJ/kg.K, respectively. The initial ($T_{wall,initial}$) and final ($T_{wall,final}$) wall temperatures are identical to the initial (289 K) and final (308 K) inlet air temperatures.

The heat loss between the air and the duct wall, calculated using Eq. 5.12, amounts to approximately 1386 kJ, which accounts for approximately 3% of the transferred heat to the system during the PCM melting (system discharging) process. As previously noted, during the PCM freezing (system charging) process, there is no heat loss from the system since the module was exposed to the cold ambient air at night, allowing the PCM in the tubes to release heat.

5.6. Measurement uncertainties analysis

When conducting experiments, it is crucial to consider measurement uncertainties and the accuracy of the instruments used. Table 5.1 provides a summary of the accuracies for the instruments utilized to measure velocity, pressure, PCM properties, and temperatures both within the PCM and at the inlet and outlet of the tube array.

Table 5. 1 Uncertainties in the measurement and experimental setup

Instrument/ measurement	Accuracy
Drop calorimeter	± 5 %
Lab weighing scale	±0.3 mg
Anemometer	2 % of reading or 15 mm/s whichever is greater
Manometer	± 0.025 % full scale, range: 0 to 6895 Pa
RTD probe	± 0.15 ℃
Thermocouple	± 1 ℃
Inlet air velocity	± 0.05 m/s
Module heating temperature	± 0.3 ℃
Module cooling temperature	± 1.1 ℃
Steady state temperature	± 1.3 ℃
Latent heat measurement	± (2-3) kJ/kg.K

The uncertainty in the energy transferred through the system and the energy stored in the system was analyzed using the specified expression [39]:

$$w_R = \left[\left(\frac{\partial R}{\partial x_1} w_1\right)^2 + \left(\frac{\partial R}{\partial x_2} w_2\right)^2 + \cdots + \left(\frac{\partial R}{\partial x_n} w_n\right)^2\right]^{1/2} \tag{5.13}$$

where, w_R is the uncertainty in the result, R and w_1, w_2, …, w_n are the uncertainties in the independent variables x_1, x_2, …, x_n. According to Eq. 5.13, the uncertainty in the stored energy is determined to be approximately 1300 kJ, or 3%, whereas the uncertainty in the energy transferred through the system is about 112 kJ, or 0.3%, during the experiment.

CHAPTER 6/ ARTICLE 3

A comparative study of latent heat thermal energy storage (LTES) system using cylindrical and elliptical tubes in a staggered tube arrangement

Mahfuja A. Khuda[1*], Nenad Sarunac[1]

[1] Mechanical Engineering and Engineering Science, UNC Charlotte, Charlotte, NC 28223, USA. m12a34k5@charlotte.edu

* Correspondence author

Highlights

- Numerical analysis of a prototype-scale latent heat thermal energy storage (LTES) system was conducted using horizontal elliptical tubes.
- Numerical results were compared with those of the corresponding design using circular tubes.
- The results showed similar dynamics of melting and freezing for both circular and elliptical tube shapes.
- The pressure drop is significantly lower for elliptical tubes compared to the circular tube geometry.

Abstract

Numerical analysis was performed to compare the thermal and hydraulic performance of the elliptical and circular tube geometries in the prototype-scale latent heat thermal energy storage (LTES) system. A staggered tube array configuration was used for the analysis where the tubes were placed horizontally. Commercial grade hexahydrate calcium chloride (CC6) was selected as a phase change material (PCM) due to its phase change occurring at room temperature. The study included a numerical analysis of the melting and solidification processes of the PCM within the tube array for both tube shapes, employing transient two-dimensional Navier-Stokes equations and a Realizable k-ε turbulence model to predict fluid flow and heat transfer. The enthalpy-porosity technique was used to model PCM melting and solidification. Numerical predictions indicate that the thermal performance for both tube shapes is almost indistinguishable during the melting and freezing processes. However, due to the aerodynamic shape of the elliptical tube, the pressure drop across the horizontal elliptical tube array is approximately 80% lower compared to that of the circular geometry. This reduced pressure drop implies that less pumping power will be required to achieve the desired flow rate across the tube bank, leading to economic advantages for the horizontal elliptical tube array. The proposed design can be used as a dry cooling technique employing an Air Cooled Condenser (ACC) in a thermal power plant.

Keywords: Thermal energy storage, Phase change material (PCM), Computational fluid dynamics (CFD), Turbulent flow, Conjugate heat transfer

6.1. Introduction

The global surge in economic development is swiftly progressing, creating a substantial need for a consistent energy supply. To reduce environmental impacts, scientists and engineers are actively exploring innovative technologies to enable increased usage of renewable energy sources. A pivotal technology integral to the widespread adoption of renewable energies is the advancement of energy storage systems. The unpredictable and fluctuating disparity between the supply and demand for various types of renewable energy can be mitigated by embracing responsive, resilient, and efficient energy storage solutions.

Thermal energy can be stored through three methods: sensible heat, latent heat, and thermo-chemical heat storage. Among these, latent heat storage, facilitated by a wide range of phase change materials (PCMs), stands out as a highly promising option due to its high thermal energy storage density and operation under nearly isothermal conditions. In this process, thermal energy is stored in a material as latent heat during the melting phase, and the stored energy can later be utilized by solidifying the material when needed. PCMs also find use in various engineering applications, such as electronic cooling technology, enhancing thermal comfort in buildings , waste heat recovery, textiles, and heating, ventilation, and air conditioning (HVAC) [6, 115, 119].

The melting of phase change material (PCM) is a transient process that is significantly influenced by factors such as the container's shape, orientation, the position of the heat source, and the mode of heat transfer. Dhaidan and Khodadadi [6] reviewed the melting process of PCM in containers of various shapes, including rectangular, spherical, cylindrical, and annular enclosures. Kalapala and Devanuri [5] conducted experiments to explore the energy and exergy analysis of a shell and tube latent thermal energy storage (LTES) system with different orientations. Both numerical and experimental investigations have been carried out on melting and solidification in enclosures of different shapes, such as rectangular [66, 120], triangular [121], sphere [49, 50, 78], elliptical [24, 53, 65, 73], trapezoidal [68], hexagonal [70], horizontal cylindrical/circular tube [79, 122, 123], and hemicylindrical cell [124]. Chen et al. conducted both experimental and numerical analyses on the melting and freezing processes of Phase Change Material (PCM) within a cylindrical tube, examining various filling rates [24]. The authors extended their numerical analysis to include horizontal ellipses, vertical ellipses, and circular geometries to enhance the efficiency of the cylindrical unit during both charging and discharging phases. Some authors have performed numerical analyses on concentric annuli with combinations of circular and elliptical tubes in horizontal or vertical orientations to examine the impact of aspect ratio (AR) and orientations on the melting front and flow field within the tube for heat transfer [56, 125]. Khedher et. al [25] investigated various shapes of PCM container frames, including smooth, arc-shaped, reverse arc-shaped, and zigzag-shaped structures, to assess their impact on the melting performance of a vertical latent heat double-pipe heat exchanger. The findings indicate that the reverse arc-shaped structure enhances the thermal energy storage performance the most. Chatterjee et. al [26] performed numerical studies to analyze the influence of angular variation of trapezoidal containers and the position of the tubes on the melting behavior of three distinct PCMs. Their findings suggest that modifying the cavity shape and ensuring the correct placement of the inner tube can significantly impact the melting process, resulting in a notable improvement in the charging rate.

Numerical and experimental analyzes were conducted to examine the flow and heat transfer characteristics of a crossflow heat exchanger using various tube shapes [27-31]. Horvat et al. [27] conducted detailed transient numerical simulations of fluid and heat flow, investigating heat exchanger segments with cylindrical, ellipsoidal, and wing-shaped tubes arranged in a staggered configuration. Mangrulkar et al. [28] performed a combined numerical and experimental investigation focusing on heat transfer and friction characteristics of in-line elliptical tubes, exploring different aspect ratios (AR) across a range of Reynolds numbers (Re) to enhance thermal performance. Mohanan et al. [29] carried out numerical investigations of heat transfer and fluid flow in a crossflow heat exchanger with elliptical tubes, studying the impact of varying longitudinal and transverse pitch-to-diameter ratios, different aspect ratios of elliptical tubes, and tube arrangements (inline and staggered) on the overall performance of the crossflow heat exchanger. Jang and Yang [31] conducted experiment and 3D numerical analysis to investigate the hydraulic and thermal performance in elliptic finned-tube heat exchangers for different tube arrangements and compared the results with those of corresponding circular-finned tube heat exchangers.

Swain and Das [32] conducted a numerical investigation to assess the impact of elliptical and flattened tube bundle geometries (both staggered and inline configurations) on convective heat transfer and pressure drop for various pitch-to-diameter ratios across a laminar Reynolds number range, aiming to design a compact and efficient single-phase shell and tube heat exchanger. Jodaei and Zamzamian [33] conducted a 3D numerical investigation to assess the performance of a heat exchanger utilizing cam-shaped tube banks. The study involved comparing this configuration in both aerodynamic and inverse aerodynamic directions in crossflow air with that of elliptical tube banks for a range of Reynolds numbers and a constant tube surface temperature. The results reveal that elliptical tube banks exhibit superior heat transfer performance compared to cam-shaped tube banks, regardless of the flow direction (inverse aerodynamic or aerodynamic) in both configurations. Numerical investigations were conducted in the literature [34, 35] to examine the thermal and hydraulic performance of heat exchangers utilizing mixed tube bundles, incorporating both circular and elliptical tubes in various orientations, arranged in both staggered and inline configurations. The study found that while transitioning from circular to elliptical tube bundles, and maintaining a constant inlet velocity and pitch-to-diameter ratio, the heat transfer coefficient decreases [34].

Ding et. al [36] conducted numerical analyses to study heat transfer and fluid flow in various types of latent heat storage units, including shell-and-tube, rectangular, and cylindrical configurations. These units were filled with the same amount of PCM but packed in differently shaped containers. Their research revealed that the shell-and-tube configuration offers the highest exergy efficiency for the thermal storage-release cycle. Fabrykiewicz et. al [37] conducted numerical and experimental analyses of a latent heat storage unit to compare three organic PCMs in a cylinder and seven tube bundles arranged in a staggered tube configuration inside the cylinder, where the heat transfer fluid (HTF) flows through the tubes, and the cylinder wall maintains a constant temperature. Rana et. al [38] conducted a two-dimensional computational study on the melting process of PCM and the heat transfer properties of a shell-and-tube heat exchanger, where circular, rectangular, and elliptical tubes were used at a constant wall temperature. The findings indicate that the PCM melts the fastest in heat exchangers with rectangular tubes, followed by those with elliptical tubes and circular tubes, respectively.

Despite the research conducted by other authors on shell-and-tube heat exchangers, gaps persist in understanding the impacts of different tube shapes in LTES systems that use PCM and employ tube array geometry with a conjugate heat transfer boundary condition approach. The objective of the work presented in this paper was to design an LTES system to lower the temperature of the incoming air to the Air Cooled Condenser (ACC). The design requirements for the LTES system include achieving a cooling effect of 4 °C over a four-hour period, maintaining a pressure drop of less than 100 Pa, and effectively cooling the system to freeze PCM during overnight operation. This study focuses on the hydraulic and heat storage performance of an elliptic tube array with horizontal tubes arranged in a staggered configuration. The choice of elliptic tube geometry aims to reduce the pressure drop of the heat transfer fluid flowing through the array compared to the circular tube geometry. Numerical predictions for elliptical tubes were compared with the numerical and experimental results obtained for circular tubes, as published in the literature [119]. The purpose of the proposed design is to enhance the dry cooling technique of a thermal power plant using ACC, suitable for Dallas, TX, Phoenix, AZ, and Las Vegas, NV.

The structure of the article is as follows: In Section 6.2.2, the computational approach used for simulating the melting and solidification processes of phase change material (PCM) within a 13-row tube array is outlined. Model validation for the melting and solidification processes in both circular and elliptical tubes is presented in Section 6.2.3. Moving on to Section 6.3.1, a comparison is provided between the numerical results of PCM melting and solidification in circular and elliptical tube arrays. Section 6.3.2 presents the numerical prediction of liquid fraction, temperature, and velocity contours within the circular and elliptical tube arrays throughout the PCM melting and solidification processes.

6.2. System description

6.2.1. Physical model

Figure 6.1 displays the design of a prototype-scale tube array, as derived from prior literature [119]. The design was selected to meet the design criteria, which was determined through a parametric study conducted in the literature [119] for different tube spacings and sizes under different inlet boundary conditions. The array comprises 208 circular tubes, each manufactured from carbon steel with an outer diameter (OD) of 1.75". The tubes have a thickness of 0.065" and are 35" long. The circular tube arrangement, analyzed in Reference [119], employed a transverse tube spacing (S_T) and lateral (row) spacing (S_L) of 55.56 mm, yielding dimensionless tube spacing S_T/D and S_L/D ratios of 1.25. The tube-to-tube spacing (S) was established at 11.11 mm. These circular tubes were filled to 90% of their volume with a commercial-grade phase-change material (PCM) to facilitate PCM expansion during the phase-change process. The overall mass of PCM in the prototype circular tube array amounted to 323.2 kg, equating to 1.553 kg within each tube.

The horizontal elliptical tubes were designed with an aspect ratio of 2.5:1 between the major and minor radii (a = 1.38" and b = 0.55"), ensuring that each elliptical tube consists of the same amount of PCM as a circular tube (see Figure 6.1). Also, the heat transfer area of the elliptical tubes is nearly the same as that of circular tubes. Table 6.1 summarizes the comparison of the PCM mass and tube area for the two analyzed tube shapes. The tube-to-tube spacing for elliptical tubes, both in the transverse (S_T) and lateral (S_L) directions, is maintained the same as for circular tubes, resulting in dimensionless tube spacing S_T/D and S_L/D ratios of 1.98. Here, D is the minor axis for the elliptical tube, defined as:

$$D = 2b \tag{6.1}$$

The hydraulic diameter of the elliptical tubes is defined as:

$$D_h = \frac{4ab(64-16E^2)}{(a+b)(64-3E^4)} \tag{6.2}$$

where, $E = \frac{(a-b)}{(a+b)}$

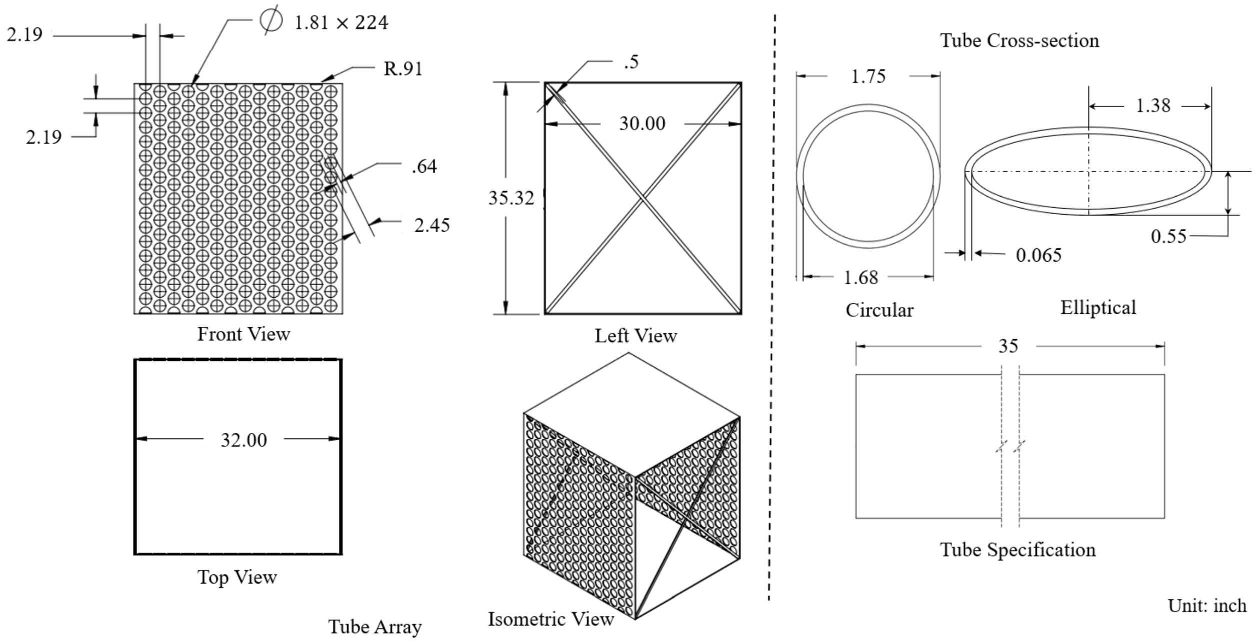

Figure 6. 1. Design of the protype scale (13-row) tube array in a staggered configuration

Table 6. 1 Comparison of circular and elliptical tube geometry

Tube Shape	D or D_h	PCM mass/ tube [kg]	A_{in} [m^2]	A_{out} [m^2]
Circular	1.75"	1.55	0.00133	0.00155
Elliptical	1.5"	1.59	0.00129	0.00154
Ratio (elliptical/ circular)	0.857	0.995	0.973	0.992

A commercially available phase-change material, namely hexahydrate calcium chloride (CC6), was selected as the heat storage medium following the previous literature [119]. The thermophysical properties of the commercial-grade PCM utilized in the experiment are summarized in Table 6.2. Additionally, Table 6.3 outlines the boundary conditions (B.C.s) applied for the study of melting and solidification. The solidification was performed during the night when the ambient temperature was low, resulting in denser air. This leads to a higher mass flow rate ($\dot{m}$) and Reynolds number (Re_D) compared to the melting process (see Table 6.2).

Table 6. 2 Thermophysical properties of PCM (CC6) [119]

Property	Value
Melting/ solidification point [°C]	25
Density, ρ (solid/liquid) [kg/m^3]	1706/ 1538
Specific heat, C_p (solid/liquid) [J/kg-K]	2540/ 1680
Thermal conductivity, k (solid/liquid) [W/m-K]	1.09/ 0.546
Latent heat, L_f [kJ/kg]	150
Dynamic viscosity [mPa-s]	11.94
Thermal expansion coefficient [K^{-1}]	0.0005

Table 6. 3 Boundary conditions [119]

B.C.s	Melting	Solidification
Velocity inlet, v_∞ (m/s)	0.82	0.82
Turbulence intensity at inlet (%)	5	5
Inlet air temperature, T_{in} (°C)	35	14.5
Pressure outlet (atm)	1	1
Mass flow rate, $\dot{m}$ (kg/s)	0.77	0.82
Re_D	2,241	2,388

The thermophysical characteristics of the carbon steel utilized in the tubes were as follows [119, 126]: density (ρ_s) of 7,870 kg/m³, specific heat (c_{P_s}) of 500 J/kg-K, and thermal conductivity (k_s) of 45 W/m-K.

6.2.2. Computational procedure

Due to the nearly symmetrical flow along the tube length, a two-dimensional domain was employed for the numerical analysis (refer to Figure 6.2). Figure 6.2a illustrates the 2-D computational layout for a circular tube array, while Figure 6.2b depicts the same for an elliptical tube array. The computational configuration featured a staggered arrangement of tubes, labeled

PCM1 to PCM7 in the figure. To minimize the influence of inlet and outlet boundaries on the numerical analysis and its results, a computational domain was established with a length 1.5 times the tube diameter upstream of the tube bank and ten times the tube diameter downstream of the tube bank. This extended length for the upstream and downstream domains proved sufficient in reducing the impact of entrance effects at the inlet and the wake at the outlet. Free-stream velocity at the inlet and pressure at the outlet boundary conditions were used. Symmetry boundary conditions were applied to the top and bottom of the computational domain. Following the previous literature [119], simulation for the partially filled tubes was conducted assuming them to be completely filled with a phase change material (PCM) having a latent heat of fusion 10% lower than that reported in Table 6.2. Assumptions used for tube array modeling are as follows:

- Buoyancy force was considered due to density change during the phase transition.
- Heat transfer occurs by conduction in the solid PCM.
- The liquid PCM was assumed to be incompressible, flow regime is laminar, and heat transfer occurs by natural convection.
- The enthalpy-porosity method was applied for the PCM domain using a constant value of latent heat.
- The air was assumed to be incompressible fluid, with uniform inlet velocity.
- The air flow was assumed to be turbulent.
- No body force or heat source was considered in the air domain.
- Thermal resistance at the duct wall was ignored.

The ANSYS Fluent 20.0 software package [81] was utilized for the simulation, employing the solution of the governing Navier-Stokes equations that satisfy mass, momentum, and energy conservation. The Realizable κ-ε turbulence model, sourced from previous literature [115], was chosen for the fluid domain. Within the computational framework, the SIMPLE algorithm and the Implicit method were selected to couple pressure and velocity. Precision was enhanced by employing a second-order upwind discretization scheme for both the momentum and energy equations. The PRESTO! (PREssure STaggering Option) scheme was employed for the discretization of momentum equations, proving advantageous in scenarios like natural convection and porous media by preventing interpolation errors and assumptions about pressure gradients at boundaries.

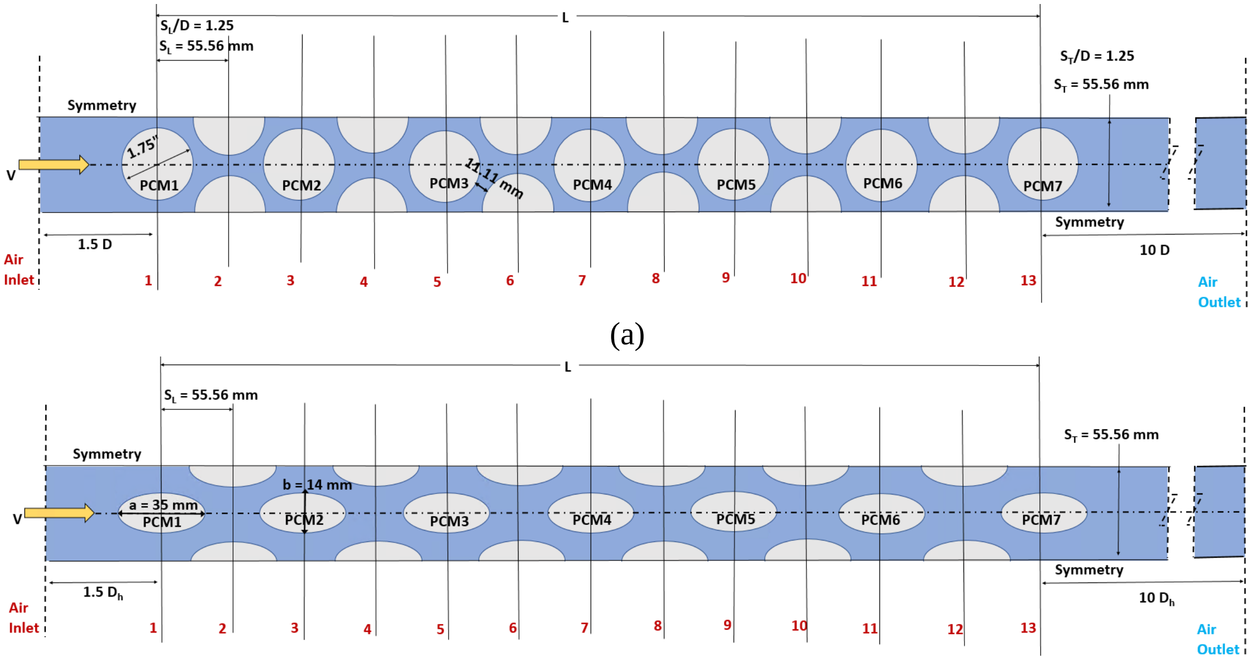

(a)

(b)

Figure 6. 2. A schematic of 2-D computational domain for the tube bank: (a) circular, (b) elliptical

The convergence criterion for the RMS residuals in continuity, momentum, and energy equations was set at 10^{-6}. To model the melting and solidification process of the Phase Change Material (PCM) over time, a transient model was implemented. Because of the selection of Implicit time scheme, the numerical results are independent of the time step size. A time step size of 0.5 seconds was adopted for this study. A UDF (User Defined Function) was used to account for the transient behavior of the inlet air temperature.

The validation of the model and a grid sensitivity analysis were conducted in a prior study [115] focusing on the circular tube array. To accurately determine variations in velocity and temperature within the boundary layer near the tube wall (see Figure 6.3), a very fine grid was employed near the tube wall. The numerical analysis utilized a total of 614146 elements for the circular prototype-scale model and 626783 elements for the elliptical prototype-scale model.

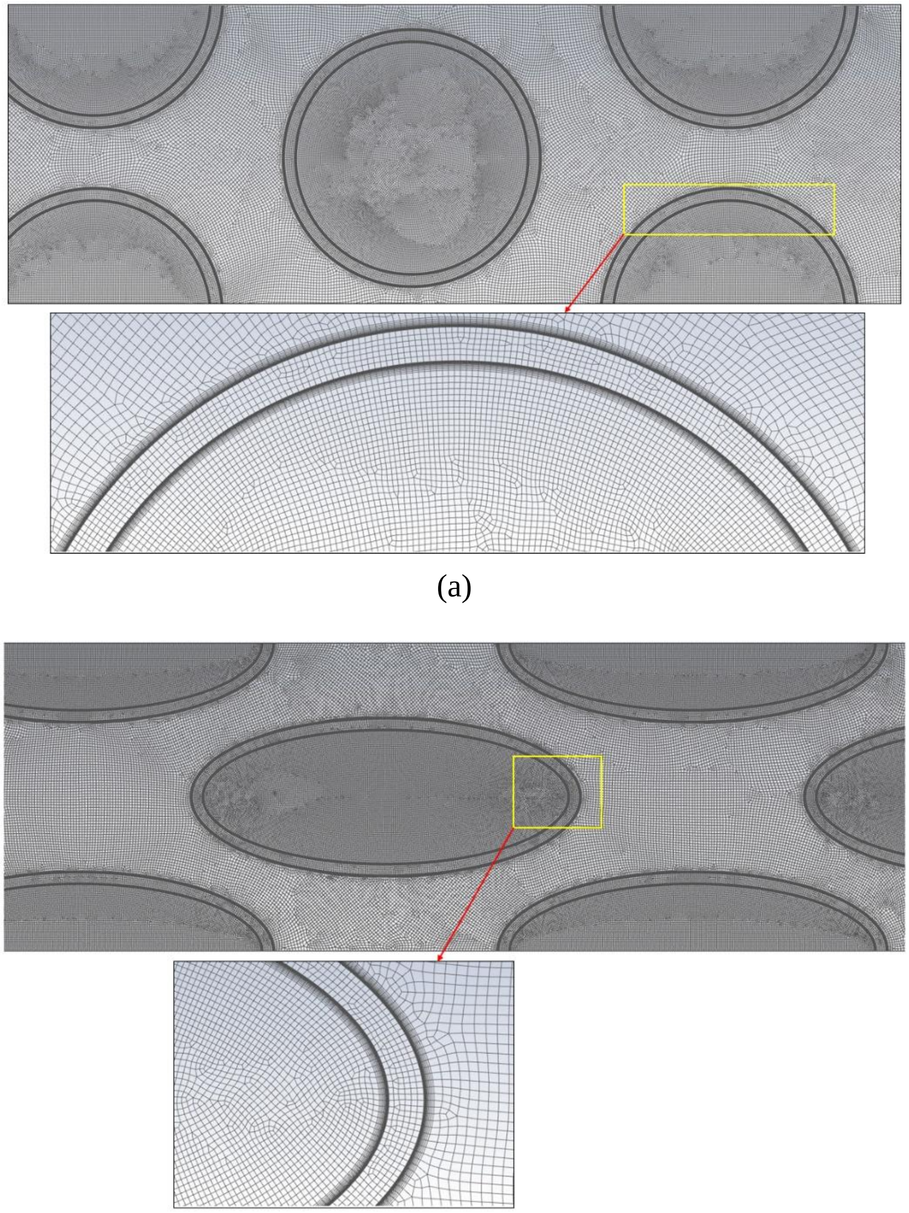
(a)

(b)

Figure 6. 3. Numerical grid of prototype-scale model: (a) circular, (b) elliptical

The simulation of nine physical hours of PCM melting in a tube array was a significant computational effort which required over nine days (216 hours) of computational time on Orion HPC cluster for both circular and elliptical prototype scale model. The cluster is equipped with a Dual 32-Core AMD EPYC 7542 CPU, 2.9/3.4 GHz and 4TB RAM. Table 4 summarizes the data on computational grid number and time required for both circular and elliptical prototype scale model.

Table 6. 4 Computational grid number and time

Tube shape	Circular	Elliptical
Number of elements	614146	626783
Computational time	nine days (216 hours)	nine days (216 hours)

The continuity, momentum, and energy conservation equations for the 2D PCM domain, shown in gray in Figure 6.2, are given by Eqns. (6.3)-(6.5) using the summation convention for repeated indexes:

$$\frac{\partial \rho}{\partial t} + \frac{\partial \rho u_i}{\partial x_i} = 0 \tag{6.3}$$

$$\frac{\partial (\rho u_i)}{\partial t} + \frac{\partial (\rho u_j u_i)}{\partial x_j} = \mu \frac{\partial^2 u_i}{\partial x_j \partial x_j} - \frac{\partial p}{\partial x_i} + \rho g_i + S_i \tag{6.4}$$

$$\frac{\partial (\rho h)}{t} + \frac{\partial (\rho h_{latent})}{\partial t} + \frac{\partial (\rho u_i h)}{\partial x_i} = \frac{\partial}{\partial x_i}\left(k \frac{\partial T}{\partial x_i}\right) \tag{6.5}$$

where ρ represents density, u is the transverse velocity of the liquid PCM induced by density differences, μ is viscosity, p denotes pressure, g is gravitational acceleration, and ρg_i accounts for the buoyancy force resulting from density variation. The quantity h in the energy equation is the sensible enthalpy, defined as:

$$h = h_{ref} + \int_{T_{ref}}^{T} C_p\,(T) dT \tag{6.6}$$

The enthalpy-porosity method was used to calculate the latent portion of PCM:

$$\gamma = \left\{ \begin{array}{c} \frac{h_{latent}}{L_f} = 0 \;\; if\, T < T_{solid} \\ \frac{h_{latent}}{L_f} = 1 \;\; if\, T > T_{liquid} \\ \frac{h_{latent}}{L_f} = \frac{T - T_{solid}}{T_{liquid} - T_{solid}} \quad if\, T_{solid} < T < T_{liquid} \end{array} \right\} \tag{6.7}$$

The source term S_i was used to model the effect of natural convection on phase change as follows:

$$S_i = -A_{mush} \cdot u_i \tag{6.8}$$

$$A_{mush} = \frac{C(1-\gamma)^2}{\gamma^3 + \delta} \tag{6.9}$$

where δ equals 0.001, and C represents the constant for the "mushy" zone (ranging from 10^5 to 10^7), the term "mushy" zone pertains to the domain section with a liquid fraction (γ) spanning from 0 to 1. For the current analysis, a value of 10^5 was employed as the mushy zone constant, aligning with literature [41].

Boussinesq model was applied to calculate density change due to the phase change and natural convection:

$$\rho = \rho_o[1 - \beta(T - T_o)] \tag{6.10}$$

where reference quantities ρ_o and T_o refer to density and temperature of the liquid PCM respectively, while β is thermal expansion coefficient of the PCM liquid phase. Other thermophysical properties were assumed to remain constant, utilizing the average values of solid and liquid PCM properties.

The energy conservation equation for the solid domain (tube wall) for transient condition is given by the following expression:

$$\rho_s c_{P_s} \frac{\partial T}{\partial t} = k_s \left(\frac{\partial^2 T}{\partial x^2} + \frac{\partial^2 T}{\partial y^2} \right) \tag{6.11}$$

where ρ_s, c_{P_s} ,and k_s are density, specific heat, and the thermal conductivity of the solid domain, respectively.

Navier-Stokes equations using the summation convention for repeated indexes for the 2D fluid domain (air) are as follows:

$$\frac{\partial \rho_{air}}{\partial t} + \frac{\partial \rho_{air} u_i}{\partial x_i} = 0 \tag{6.12}$$

$$\frac{\partial(\rho_{air} u_i)}{\partial t} + \frac{\partial(\rho_{air} u_i u_j)}{\partial x_j} = -\frac{\partial p}{\partial x_i} + \frac{\partial}{\partial x_j}\left[\mu_{air}\left(\frac{\partial u_i}{\partial x_j} + \frac{\partial u_j}{\partial x_i}\right) - \rho_{air}\overline{u_i' u_j'}\right] \tag{6.13}$$

$$\rho_{air}\frac{\partial T}{\partial t} + \rho_{air} u_j \frac{\partial T}{\partial x_j} = -\frac{\partial p}{\partial t} + \frac{\partial}{\partial x_j}\left(\frac{k_{air}}{c_{p_{air}}}\frac{\partial T}{\partial x_j} - \rho_{air}\overline{u_j' T'}\right) \tag{6.14}$$

where, u_i, u_j denote mean flow velocity, u' denote velocity fluctuations due to turbulence and $\rho_{air}\overline{u_i' u_j'}$ represents Reynolds Stress term.

The transport equations for the turbulent kinetic energy (κ) and dissipation rate (ε) for Realizable κ-ε model are expressed as following [109]:

$$\frac{\partial(\rho_{air}\kappa)}{\partial t} + \frac{\partial}{\partial x_j}\left(\rho_{air}\kappa u_j\right) = \frac{\partial}{\partial x_j}\left[\left(\mu_{air} + \frac{\mu_t}{\sigma_k}\right)\frac{\partial k}{\partial x_j}\right] + G_k + G_b + S_k - \rho_{air}\varepsilon - Y_M \tag{6.15}$$

$$\frac{\partial(\rho_{air}\varepsilon)}{\partial t} + \frac{\partial}{\partial x_j}\left(\rho_{air}\varepsilon u_j\right) = \frac{\partial}{\partial x_j}\left[\left(\mu_{air} + \frac{\mu_t}{\sigma_\varepsilon}\right)\frac{\partial \varepsilon}{\partial x_j}\right] + S_\varepsilon + \rho_{air} C1 S_\varepsilon - \rho_{air} C_2 \frac{\varepsilon^2}{\kappa + \sqrt{\nu\varepsilon}} + C_{1\varepsilon}\frac{\varepsilon}{k} C_{3\varepsilon}\, G_b \tag{6.16}$$

where,

$$C_1 = \left[0 \cdot 43, \frac{\eta *}{\eta * + 5}\right], \qquad \eta * = S\frac{k}{\varepsilon}, \qquad S = \sqrt{2 S_{ij} S_{ij}}, \qquad S_{ij} = \frac{1}{2}\left(\frac{\partial u_j}{\partial x_i} + \frac{\partial u_i}{\partial x_j}\right)$$

G_k and G_b represent the generation of turbulent kinetic energy resulting from the mean velocity gradient and buoyancy, respectively. Y_M indicates the extent to which fluctuating dilatation contributes to the overall dissipation rate in the context of compressible turbulence. The variables σ_k and σ_ε denote the turbulent Prandtl numbers for κ and ε, respectively. S is the mean rate-of-strain tensor.

Zukauskas experimental correlation [83, 108] for pressure drop (ΔP) across the tube array is as follows:

$$\Delta P = N_L x \left(\frac{\rho_{air}\, v_{max}^2}{2}\right) f \tag{6.17}$$

where N_L denotes the number of tube rows, the friction factor f and the correction factor x are obtained from the graph presented in references [83, 108]. This graph refers to the maximum velocity (v_{max}) within the tube bank, which is calculated using the following equation.

$$v_{max} = \frac{s_T}{s_T - D} v_\infty \tag{6.18}$$

where, S_T is the tube spacing in the transverse direction.

The correlation for Nu number by Zukauskas [83, 108] was used as follows (Eq. 6.19):

$$\overline{Nu}_D = C_1 C_2 R_{e_D}^m Pr^n \left(\frac{Pr}{Pr_s}\right)^{1/4} \tag{6.19}$$

where, $\left\{\begin{matrix} N_L \geq 20 \\ 0.7 \leq Pr \leq 500 \\ 10 \leq Re_{D_{max}} \leq 2 \times 10^6 \end{matrix}\right\}$

The coefficient of heat transfer (h_{Zu}) was calculated from Zukauskas correlation for Nu number using the following expression [40]:

$$\overline{Nu}_D = \frac{h_{Zu} D}{k_{air}} \tag{6.20}$$

The log mean temperature difference (LMTD) method was used to compute the average heat transfer coefficient (h_{num}) for the numerical analysis as presented in Eq. (6.21).

$$h_{num} = \frac{q''}{LMTD} \tag{6.21}$$

where, the peripheral average of wall heat-flux (q″) was determined from the Fourier's law as following:

$$q_w'' = -k_{air} \frac{\partial T_w}{\partial r}\bigg|_{r=r_0} = \frac{k_{air}}{r_0 - r_i}\left(T_{w,o} - T_{w,i}\right)$$

and, $$LMTD = \frac{\Delta T_{in} - \Delta T_{out}}{ln(\Delta T_{in}/\Delta T_{out})} = \frac{(T_{w,i} - T_{in}) - (T_{w,i} - T_{out})}{\ln((T_{w,i} - T_{in})/(T_{w,i} - T_{out}))}$$

6.2.3. Model validation

To validate the melting/solidification model for circular geometry (partially filled), the liquid fraction and temperature numerical results obtained in this study were compared with those from Assis et al. [48], where the tube was partially filled with air and PCM. To simulate a partially filled tube, the 2-D computational domain was divided into air and PCM zones (see Figure 6.4a), with the tube being 85% filled with PCM RT27 by volume. The Volume of Fluid (VOF) model was used to simulate the partially filled tube, which utilized the following expressions for the fluid volume fraction α:

$$\alpha_{PCM} + \alpha_{air} = 1 \tag{6.22}$$

The fluid volume fraction α in each cell varies between 0 (PCM only) to 1 (air only). Density is calculated from the following expression.

$$\rho_{cell} = \rho_{PCM}\alpha_{PCM} + \rho_{air}\alpha_{air} \tag{6.23}$$

A constant wall temperature of 312 K or 39 °C was maintained, which was 10 °C higher than the phase change temperature. Figure 6.4b demonstrates a remarkable agreement between the numerical results from the reference [48] and the present study. The authors in reference [48] attribute the discrepancy between the numerical results and experimental measurements to the assumption of high thermal conductivity of glass (tube wall). Adjusting for a 32% lower thermal conductivity leads to an excellent agreement between the numerical results and experimental measurements (refer to Figure 6.4b).

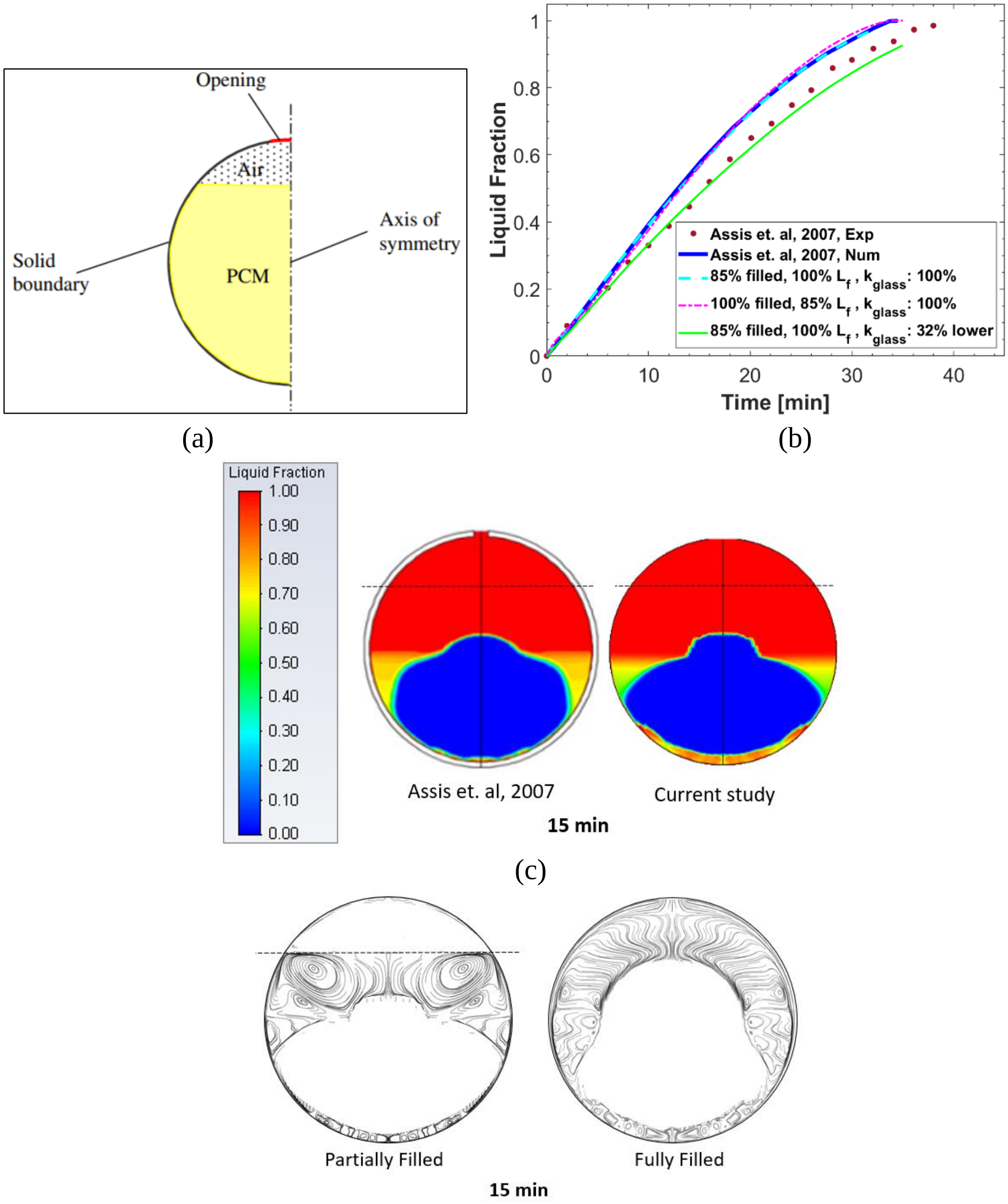

(a) (b)

(c)

(d)

Figure 6. 4. (a) Computational domain from the reference [48] for the partially filled tube, (b) model validation using the liquid fraction (c) comparison of the liquid fraction contours of partially filled tube with the reference [48], and (d) vortices in current study for partially and fully filled tube

Additionally, the comparison of average liquid fraction (Figure 6.4b) reveals virtually no difference between the predicted results from the current study and the literature when the tube was modeled assuming 100% filled with PCM with a 15% lower latent heat. However, assuming a 100% filled tube with lower latent heat reduces the computational effort and time by approximately a factor of three compared to the numerical model considering a partially filled tube using the Volume of Fluid (VOF) model.

The contours of liquid fraction are illustrated in Figure 6.4c. A very good agreement in liquid fraction contours at 15 minutes was observed, as depicted in Figure 6.4c. When the Rayleigh number (Ra_L) exceeds 1708, heat transfer becomes convection dominant, and fluid motion manifests as regularly spaced roll cells [83]. Consequently, vortices are formed at the top of the solid PCM, as indicated in Figure 6.4d. These vortices are recognized as Rayleigh-Bénard convection [83].

Similar to the circular geometry, the melting/solidification model for elliptical geometry (fully filled) was validated for the liquid fraction and temperature contours using results published by Benbrika et al. [53], where n-eicosane was used as the phase change material (PCM). Figure 6.5a shows the computational domain used for the numerical analysis, adopted from the literature [53]. An excellent agreement was observed between the current study and the literature for the liquid fraction, as shown in Figure 6.5b.

After 500 seconds, identical liquid fraction contours and streamlines were observed, as depicted in Figure 6.5c. Similar to the circular tube case, Rayleigh-Bénard cells are evident, indicating the dominance of natural convection. The occurrence of counter-rotating vortices at the upper part of the tube and weaker vortices at the bottom is attributed to the confinement of liquid PCM between the warmer enclosure wall and the colder melting front [53].

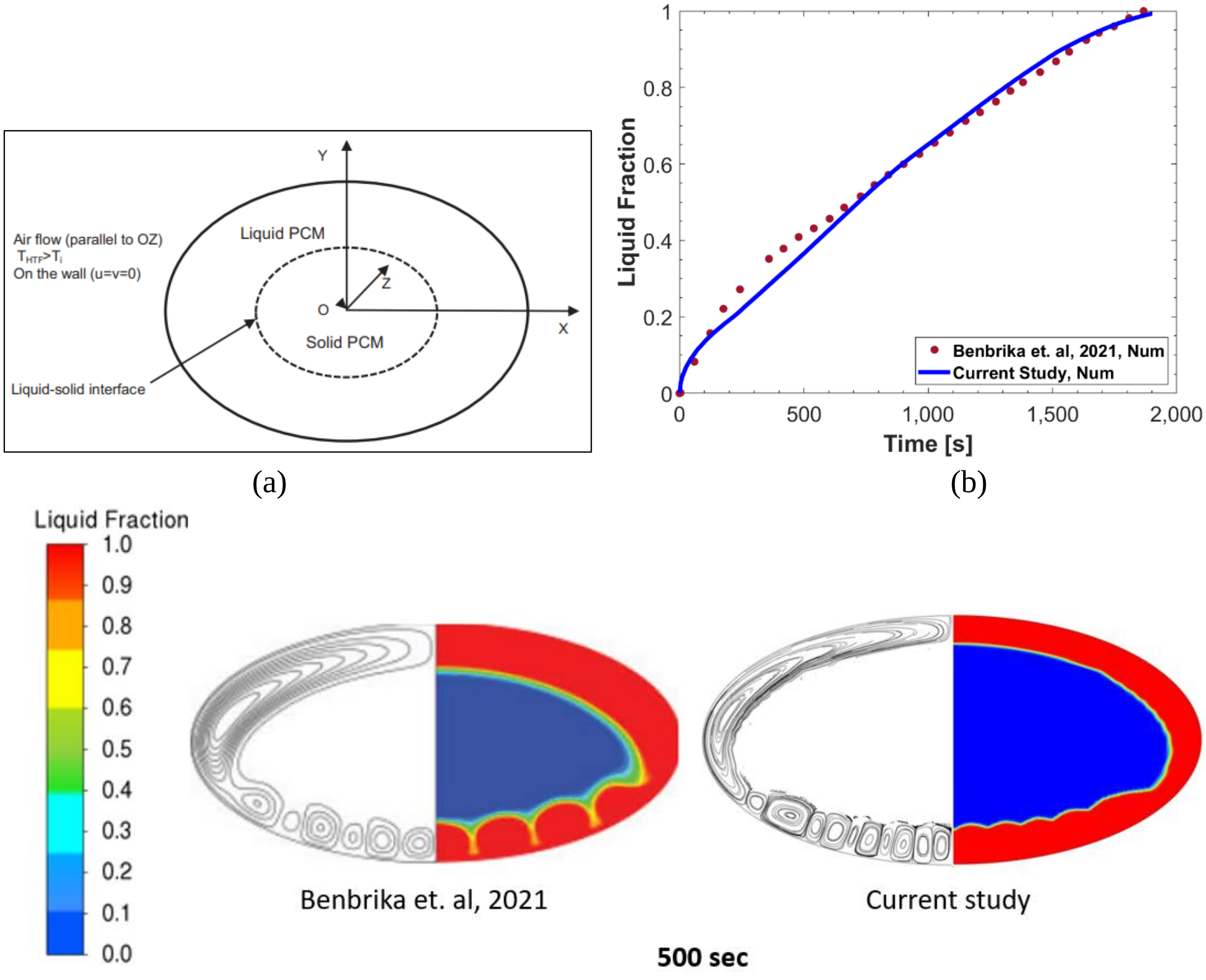

(a) (b)

(c)

Figure 6. 5. (a) Schematic of computational domain from the reference [53] for the elliptical tube, (b) model validation using the liquid fraction (c) comparison of the vortices and liquid fraction contours with the reference [53].

6.3. Results and discussion

In this section, the numerical results obtained for different performance parameters, i.e., liquid fraction of PCM, outlet air temperature, and PCM temperature, were compared for the circular and elliptical geometries. Additionally, the numerical results obtained for the circular tube geometry were compared to the experimental data.

6.3.1. Comparison of numerical results of circular and elliptical tube array

The comparison of numerical results obtained for the fully filled circular and elliptical tube shapes and upstream (up) and downstream (down) tubes is depicted in Figures 6.6a-c. The findings indicate that melting patterns of the phase change material (PCM) in the circular and elliptical tube arrays are virtually identical.

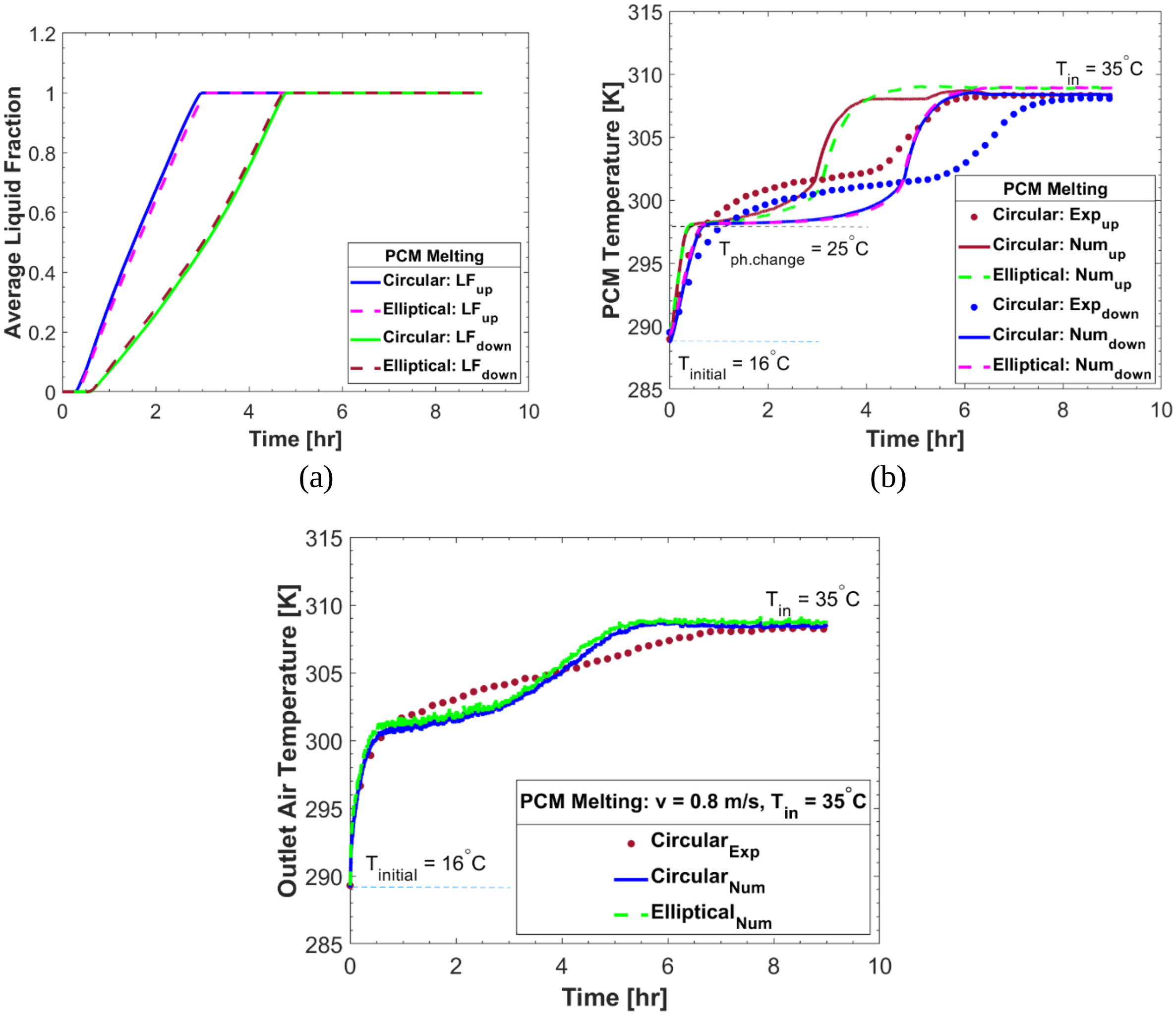

(a) (b)

(c)

Figure 6. 6 Comparison of (a) Average liquid fraction, (b) PCM temperature and (c) Outlet air temperature as a function of flow time during the PCM melting test for inlet air velocity and temperature of 0.8 m/s and 35 °C and initial temperature of 16 °C

Figure 6.6a displays the liquid fraction of PCM in the tubes. Throughout the transition from frozen to molten PCM, the PCM temperature (Figure 6.6b) and outlet air temperature (Figure 6.6c) remain relatively constant. Once all PCMs in the tube have completely melted, the PCM temperature and outlet air temperature increase rapidly. Consequently, approximately 3 hours after the initiation of the PCM melting process, the model predicts superheating of molten PCM (Figure 6.6b). The numerical prediction outlines three distinct phases of phase transition: (a) heating of the solid PCM, (b) PCM melting (phase change), and (c) superheating, where the temperature of the molten PCM approaches the inlet air temperature. A cooling effect ($\Delta T_{melting} = T_{in} - T_{out}$) of 4 °C was maintained for a duration of 4 hours for both tube shapes.

The numerical results of PCM temperature (Figure 6.6b) and outlet air temperature (Figure 6.6c) were also compared against the melting test results of a prototype-scale tube array with circular geometry derived from the literature [119]. The variation in the outlet air temperature (Figure 6.6c) is attributed to the transient behavior of the electric heater, which causes variation of inlet air temperature with time [119]. The moving average value of the measured outlet air temperature for the circular tube array is presented in Figure 6.6c for better representation and is compared with the numerical results for the circular and elliptical tube arrays. The results show a good agreement between the measured and numerically predicted values of the air temperature at the array outlet at the beginning and end of the test. However, as shown in Fig 6.6c, in the middle of the test, the numerical model exhibits a slight underprediction of the outlet air temperature by approximately 2 °C. As mentioned in the literature [119], the discrepancy between the test results and the numerical prediction is attributed to the PCM modeling technique using the enthalpy-porosity model/technique [43] and/or a difference in measurement locations, along with instrumentation error. Impurities in the commercial PCM may also contribute to the disparity between the numerical predictions of PCM temperature and the measurements, as discussed in the literature [119].

It is noteworthy that the PCM in the upstream (up) tube melts approximately 2 hours earlier compared to the downstream (down) tube for both tube shapes. This difference is attributed to the melting front propagating through the tube array in the direction of the flow, and the temperature of the inlet air decreases as it progresses downstream. Additionally, the trend in PCM melting temperatures shows consistency with the literature [118], where natural convection boundary condition approach was used.

Figures 6.7a-c present a comparison of numerical results obtained for PCM freezing for circular and elliptical tube arrays. In the elliptical tube array, the PCM freezes slightly later than in the circular tube array, as indicated in Figure 6.7a. Nevertheless, there is no significant difference in the numerically predicted outlet air temperatures for both tube shapes, as depicted in Figure 6.7c. Similar to the PCM melting process, the freezing of PCM unfolds in three distinct stages, as illustrated in Figure 6.7b: (a) the cooling of the molten PCM, (b) the phase change as PCM freezes, and (c) subcooling, where the temperature of the solidified PCM approaches the inlet air temperature.

The freezing test results of PCM temperature (Figure 6.7b) and outlet air temperature (Figure 6.7c) using a circular tube array were compared against the numerical predictions. The comparison of PCM temperature, as shown in Figure 6.7b, demonstrates a good agreement between numerical predictions and actual measurements. Similarly, the analysis of the air temperature at the outlet of the tube array, depicted in Figure 6.7c, reveals a high level of agreement between the measured and numerically predicted values, with a maximum temperature difference within a 1 °C range. Similar to PCM melting, the trend in PCM freezing temperatures is consistent with the literature [118] using the natural convection boundary condition approach. Additionally, the PCM in the upstream tube rows freezes faster compared to the downstream tube rows due to the propagation of the freezing front through the tube array in the direction of the air flow.

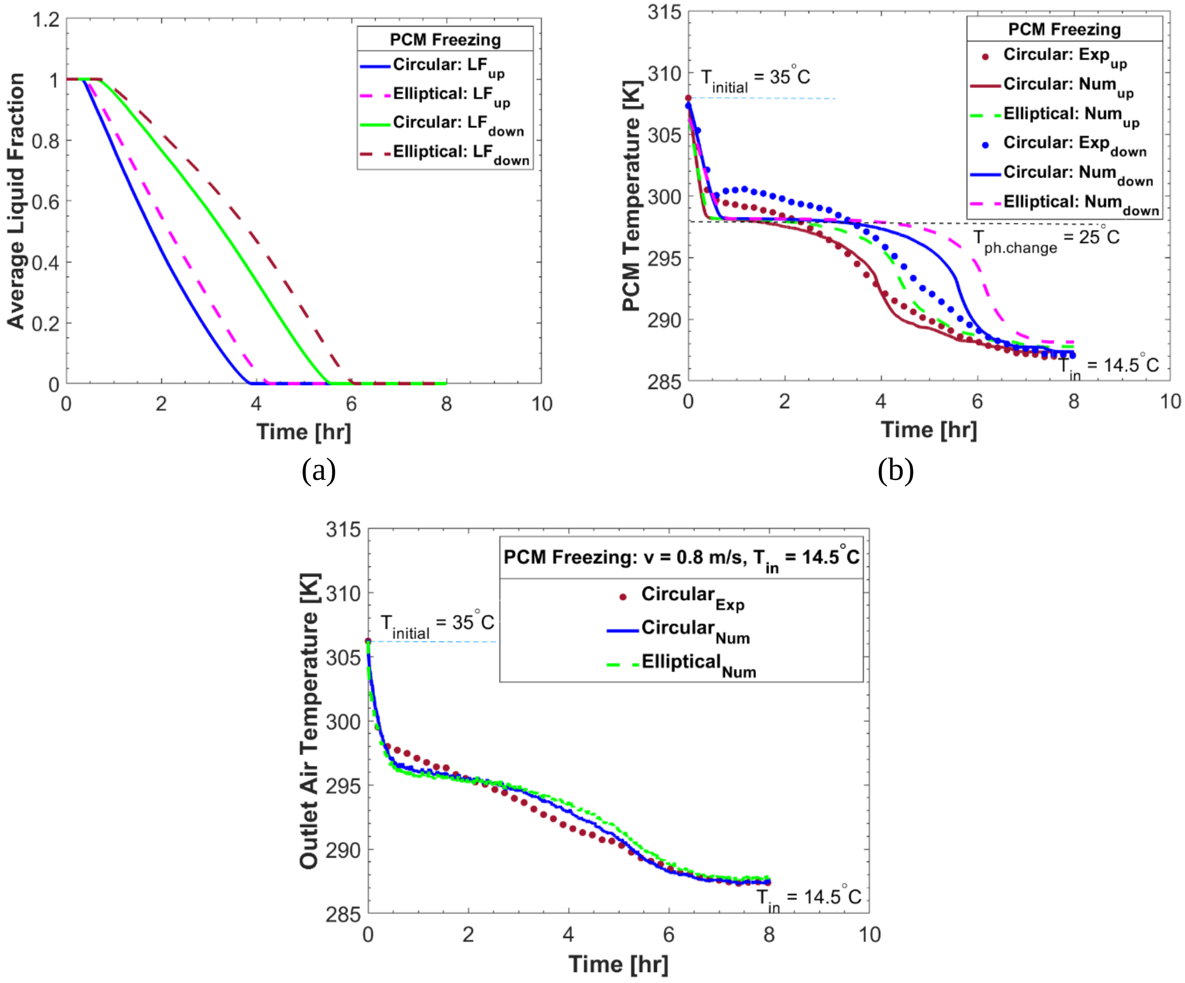

(a) (b)

(c)

Figure 6. 7 Comparison of (a) Average liquid fraction, (b) PCM temperature and (c) Outlet air temperature as a function of flow time during PCM freezing for inlet air velocity and temperature of 14.5 °C and 0.8 m/s and initial PCM temperature of 35 °C

Under the specific test conditions for both circular and elliptical tube array geometries, complete freezing of PCM within the tube array is achieved in less than 7 hours, as shown in Figure 6.7c. This demonstrates that the PCMs in the elliptical tube array can be solidified during the nighttime when the ambient air temperature is lower than the phase change temperature, making this information crucial for the design process.

Table 6.5 summarizes the numerical predictions for the hydraulic and thermal performance of circular and elliptical tube array geometries. Aligned with the findings in the literature [34] for shell and tube heat exchangers, the heat transfer coefficient decreases from circular to elliptical tube arrays. Despite the numerically predicted heat transfer coefficient being lower for the elliptical tube array compared to the circular tube array, this difference does not affect the overall melting/freezing performance in the elliptical tube geometry. This is attributed to its aerodynamic shape (refer to Figures 6.6 and 6.7). However, the aerodynamic shape of elliptical tubes reduces the wake (recirculation region) behind the tube, resulting in a lower pressure drop compared to that of circular tubes, as the circular geometry is more bluff. Consequently, less pumping power will be required for the horizontal tube array to achieve the desired flow rate across the tube bank, which is also economically advantageous.

Table 6. 5 Comparison of numerical predictions of pressure drop and heat transfer coefficient

Cases	ΔP (Pa)				$h_{avg.}$ (W/m^2-K)		
	Circular			Elliptical	Circular		Elliptical
	Exp	Zu [108] Correlation	Num	Num	Zu [83] Correlation	Num	Num
Melting	70 ±3	60.30	56.34	11.41	48.30	51.27	33.20
Solidification	70 ±3	64.30	58.61	11.41	50.10	48.63	35.09

Table 6.5 also presents a comparison between numerical predictions and experimental correlations of pressure drop and heat transfer coefficient within the circular tube array. The results demonstrate a good agreement between the numerical predictions and the Zukauskas correlation [108]. The experimentally measured pressure drop was higher due to low ambient temperature,

resulting in denser air. Furthermore, the correlation was derived from a tube array with more tube rows compared to the prototype array, contributing to streamlined flow.

6.3.2. Contours of PCM melting/ solidification

Figures 6.8 and 6.9 show the predicted contours of the liquid fraction of PCM within the tubes and the air temperature during the PCM melting process at a freestream air velocity of 0.8 m/s for both circular and elliptical tube geometries. In the legend for the liquid fraction, the red color indicates a liquid fraction of one, while the blue color represents frozen PCM (a liquid fraction of zero). In the temperature legend, the red color corresponds to an air temperature of 35 °C (the inlet air temperature), while the blue color indicates air temperature below the PCM phase change temperature. A narrow green-yellow ring surrounding the solid PCM signifies the mushy zone.

These findings offer insights into the dynamic process of PCM melting within a tube array. There is virtually no distinction in the dynamics of PCM melting process between the circular and elliptical tube arrays. As heat is transferred from the air to the PCM inside the tubes, the PCM temperature rises, initiating the melting process. PCM melting begins in the initial row of tubes and progresses downstream as the melting front advances in the direction of the flow.

Around 9,600 seconds (2.7 hours) into the process, a significant portion of the PCM at the front end of the array has melted for both tube shapes, while the rear portion of the array still contains solid PCM (see Figures 6.8a-b). Due to the wake within the tube array, the PCM in the second row of tubes melts more rapidly than in the first row. By 12,000 seconds (3.33 hours), nearly all the solid PCM in tubes 1 to 6 in the front rows has melted, with only a small amount of solid PCM remaining in the rear rows of tubes. The dynamics of the melting process contributes to the variation in air temperature at the array outlet over time, as discussed earlier and presented in Figure 6.6c. Specifically, the air outlet temperature remains relatively constant as long as there is solid PCM in the tubes at the front of the array. However, as the melting front advances downstream in the direction of the air flow, the air outlet temperature increases due to the superheating of the liquid PCM.

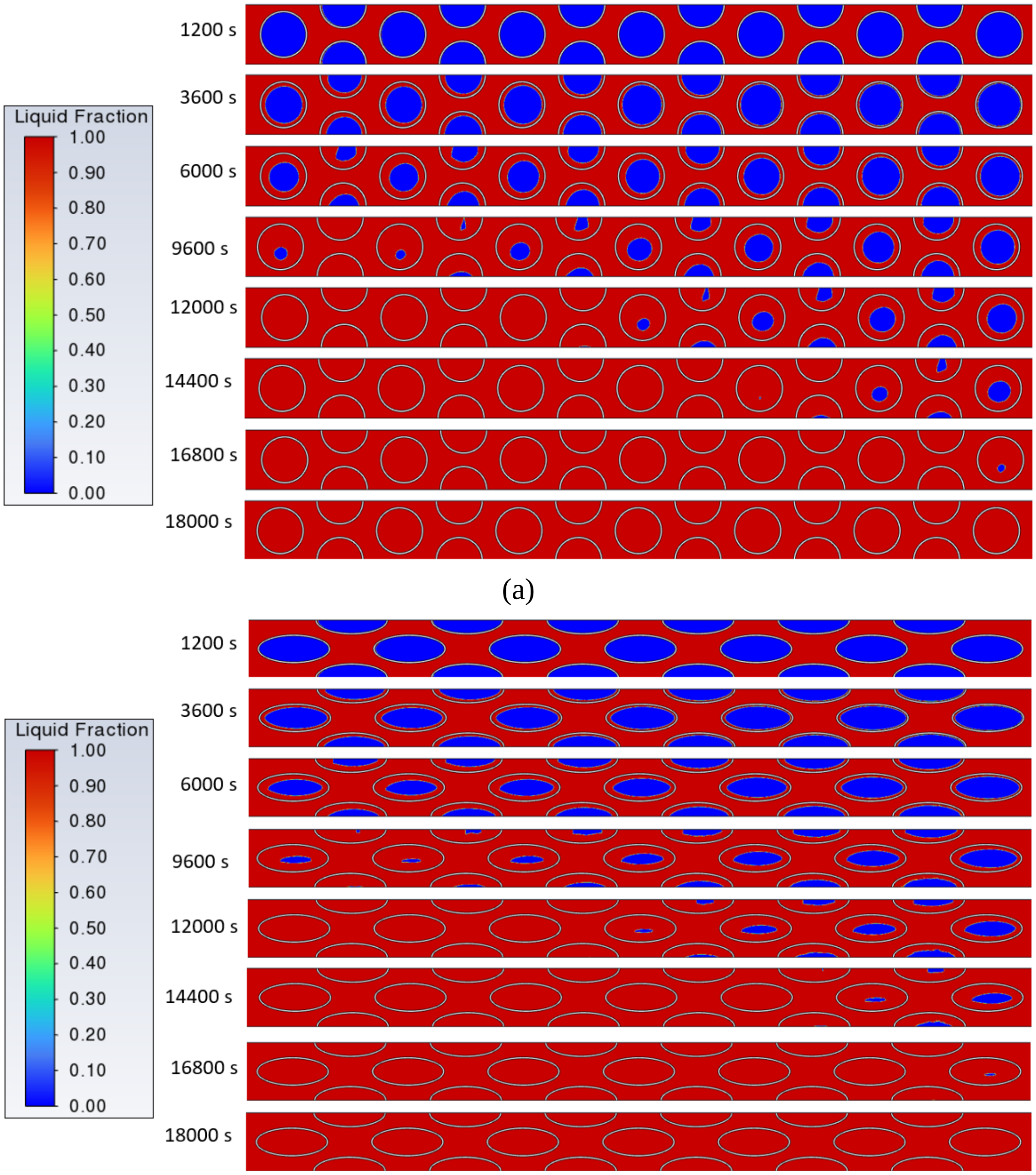

(a)

(b)

Figure 6. 8. Liquid fraction contours during PCM melting in PCM tubes, 90% filled with commercial-grade PCM in the 13-row tube array as functions of time for air velocity of 0.8 m/s: (a) Circular, (b) Elliptical

Figures 6.9 a-b illustrate the predicted temperature of the air stream as it flows through the circular and elliptical tube array, respectively, during the PCM melting process. As mentioned earlier, the variation in air temperature leaving the array mirrors the dynamics of PCM melting.

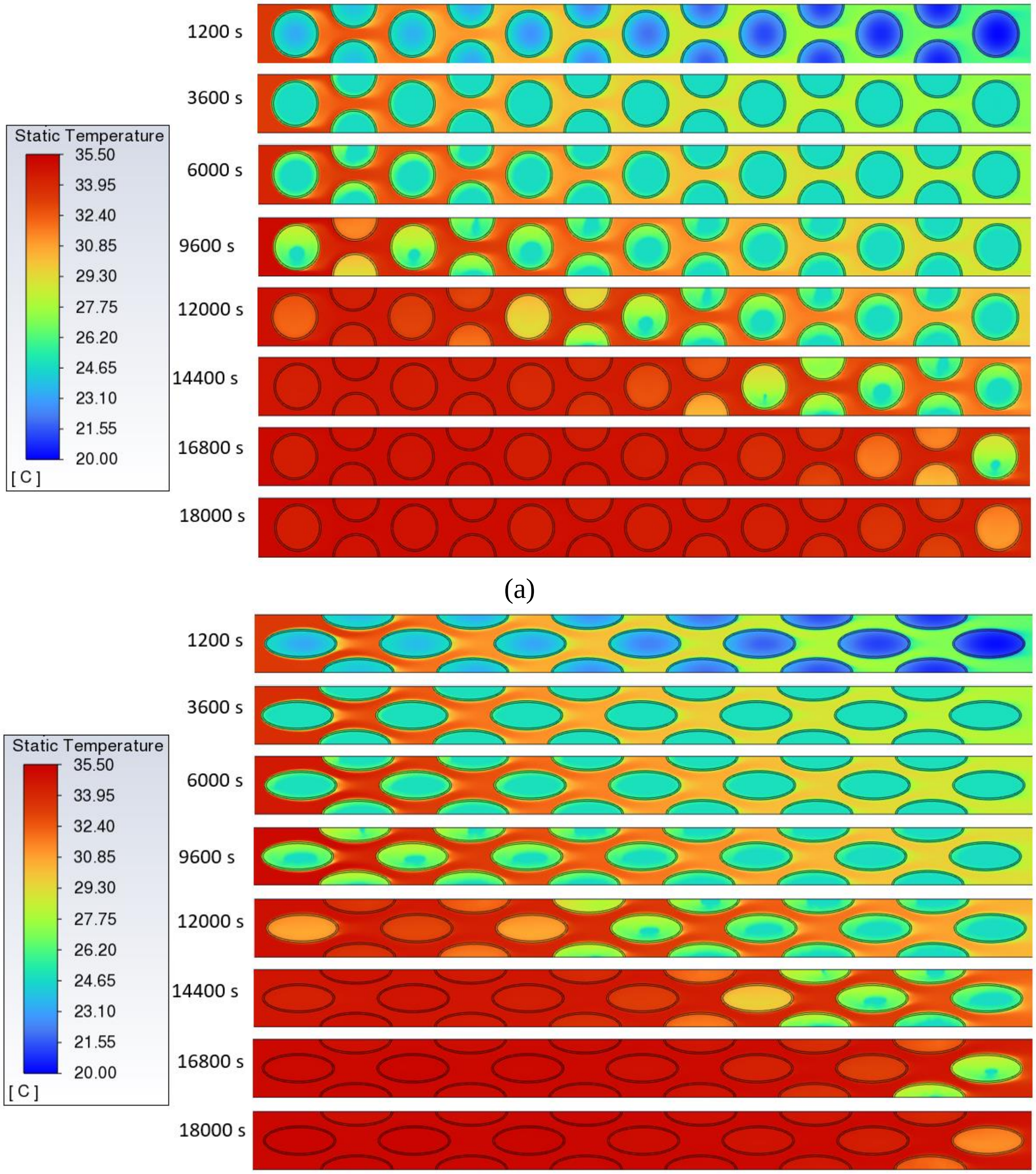

Figure 6. 9 Temperature of air flowing through the array as a function of time for freestream air velocity of 0.8 m/s during PCM melting: (a) Circular, (b) Elliptical

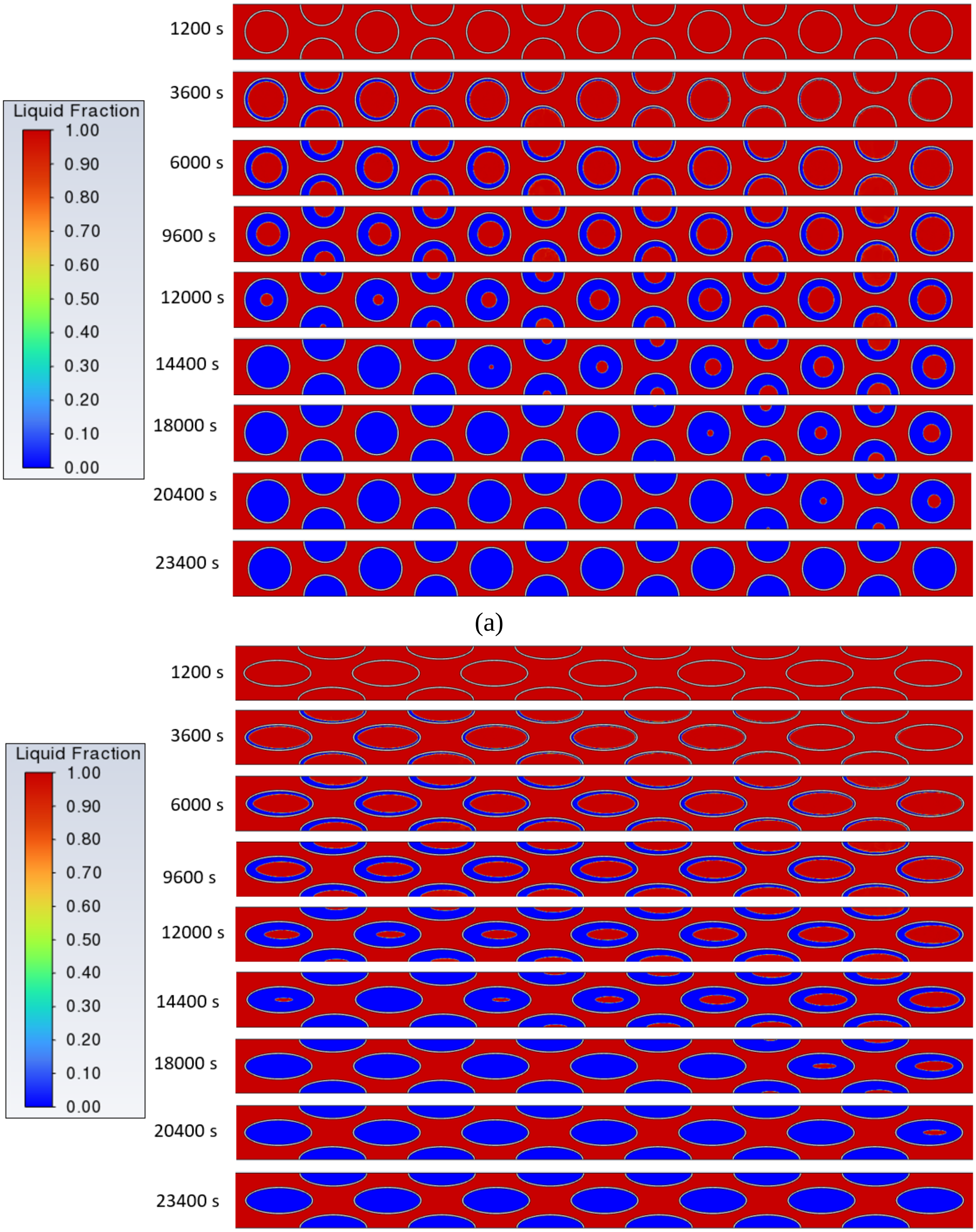

(a)

(b)

Figure 6. 10 Liquid fraction contours during PCM freezing in PCM tubes, 90% filled with commercial-grade PCM in the 13-row tube array as functions of time for air velocity of 0.8 m/s: (a) Circular, (b) Elliptical

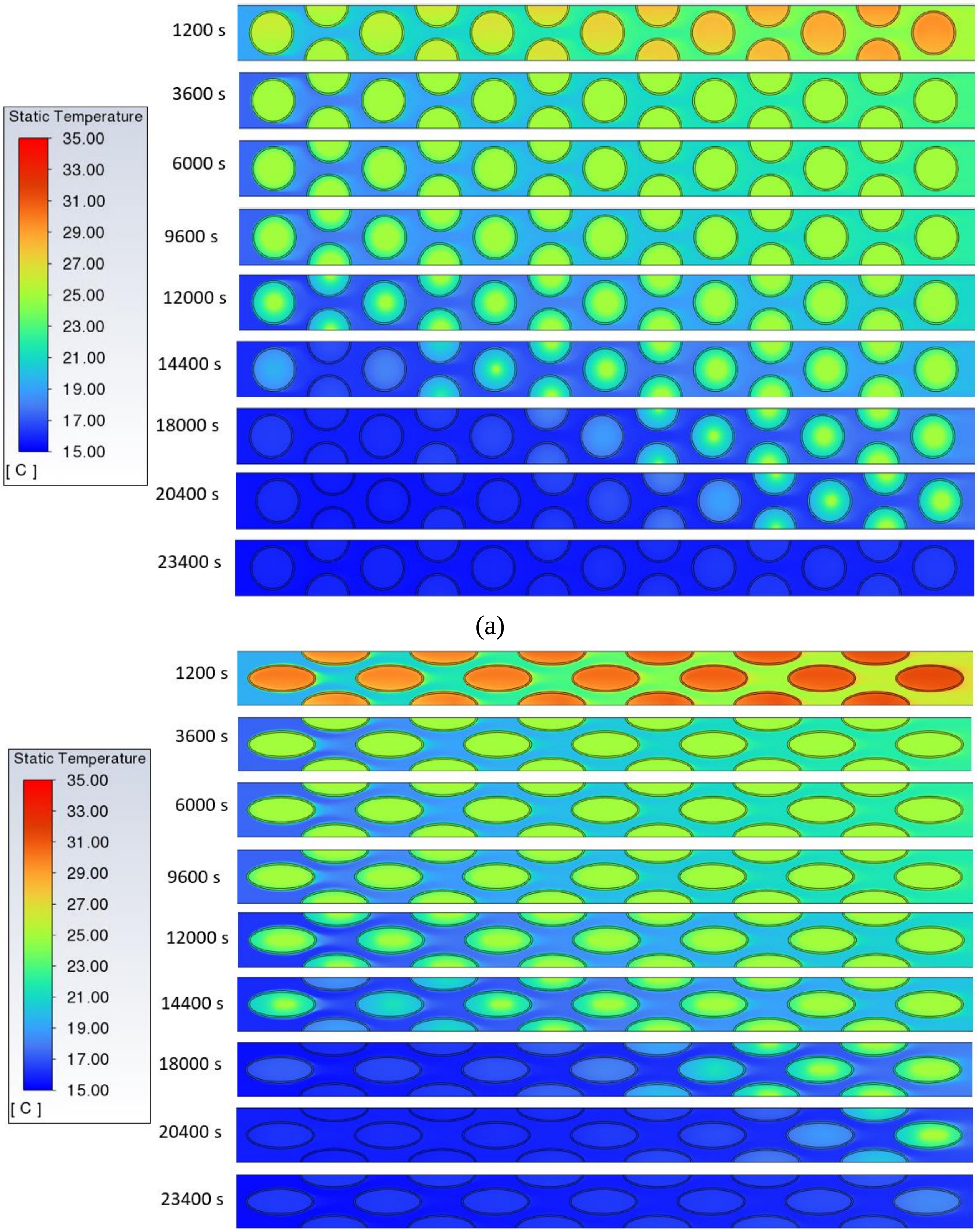

(a)

(b)

Figure 6. 11 Temperature of air flowing through the array as a function of time for freestream air velocity of 0.8 m/s during PCM freezing; (a) Circular, (b) Elliptical

Similar to the PCM melting process, the liquid fraction and air temperature contours depicted in Figures 6.10 and 6.11, respectively, offer insights into the dynamics of PCM freezing within the 13-tube array for both circular and elliptical tube shapes. This simulation was carried out under conditions of an inlet air velocity of 0.8 m/s, an initial air temperature of around 288 K or 15 °C, and an initial PCM temperature of 308 K or 35 °C. The simulation assumes a partial (90%) tube fill, considering a 10% lower latent heat of fusion.

Similar to the PCM melting process, there is virtually no distinction between the freezing process in circular and elliptical tube arrays. As shown in Figures 6.10 a-b, PCM initially freezes along the periphery of the tubes, with freezing progressing inward toward the center. Freezing begins in the front rows of the array, and the freezing front advances in the direction of the air flow. Approximately 14,400 seconds (4 hours) into the process, the PCM in the first six rows of the circular tube array is completely frozen, while there is still a small amount of PCM at the center of the front row tube in the elliptical tube array. By 20,400 seconds (5.7 hours), only a small amount of solid PCM remains at the downstream end of the array for both tube shapes. Complete freezing of the PCM within the tube array occurs at approximately 21,600 seconds (6 hours) for both tube geometries (see Figure 6.7a). This suggests that, with the appropriate design, effective cooling of the thermal energy storage system can be achieved during nighttime hours for both tube shapes.

Figure 6.12 illustrates the predicted air velocities within the tube array for the circular and elliptical tube shapes. As expected, numerical simulation reveals the presence of wakes (flow recirculation zones) behind the tubes in the circular geometry. In the case of elliptical geometry, the wakes are much smaller, and the flow is less turbulent due to better aerodynamics [28, 97, 127].

For the circular tube shape, the air velocity accelerates from the inlet value of 0.8 m/s to a maximum velocity of approximately 4 m/s. For the elliptical tube shape and the same inlet air velocity, the maximum air velocity is around 2.6 m/s as the flow accelerates while passing through the narrowest gap between the tubes. The flow through a staggered tube array may be described as a series of accelerations and decelerations. Upon exiting the tube array, the flow gradually decelerates, ultimately reaching a superficial air velocity of 0.8 m/s.

The pressure drop, as predicted by the Zukauskas correlation [108], is linked to the maximum velocity in the tube array. Thus, the pressure drop for the elliptical tube array predicted by the Zukauskas correlation (~ 11 Pa) is significantly lower compared to the circular tube array (~ 58 Pa), as presented in Table 6.5.

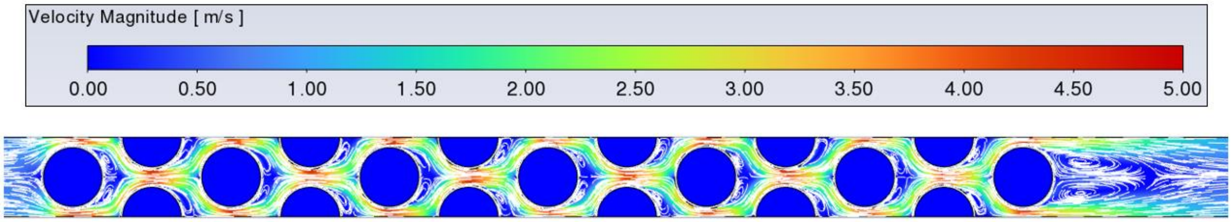

Circular Shape

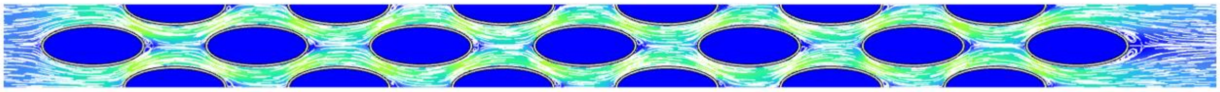

Elliptical Shape

Figure 6. 12 The predicted air velocities in a 13-row tube array for freestream air velocity of 0.8 m/s

6.4. Conclusions

This paper provides a comparison of the performance of the prototype-scale module of the LTES system using circular and horizontal elliptical tubes. The elliptical geometry was designed with almost the same amount of PCM in the tubes and the same heat transfer area as that of the circular geometry. The tube-to-tube spacing, and pitch-to-hydraulic diameter ratio were kept the same for both geometries. The numerical predictions of the thermal performance for both tube shapes are almost identical during the melting and freezing processes. The results demonstrate a similar trend in the melting and freezing process consistent with the literature [118], where natural convection boundary condition approach was used. Additionally, the results show faster melting/ freezing of PCM in the upstream tube compared to the downstream tube for both tube shapes due to the melting/ freezing front propagating through the tube array in the direction of the air flow. However, due to better aerodynamics of the elliptic tube, the pressure drop across the horizontal elliptical tube array is significantly (80%) lower compared to that of the circular geometry. This lower pressure drop implies that less pumping power will be required to achieve the desired flow rate across the tube array, making the horizontal elliptical tube array economically beneficial. The numerical results of the PCM freezing process show that the PCM in the elliptical tubes can be solidified overnight, and a cooling effect with a magnitude of 4 °C can be maintained for a duration of 4 hours during daytime when energy demand is high. This outcome meets the design criteria for constructing a prototype-scale module to lower the temperature of incoming airflow to the ACC. The proposed design offers an alternative approach to reduce the temperature and pressure of the exhaust steam from the turbine of a coal power plant by implementing dry cooling technique using ACC. For the future work, Artificial Intelligence (AI) can be used to predict the performance of the system instead of commercial software to reduce the computational time.

Author contributions

Mahfuja A. Khuda: Numerical analysis, Investigation, Methodology, Software, Verification & Validation, Post-processing, Experiment, Writing – original draft.

Nenad Sarunac: Conceptualization, Project administration, Resources, Supervision, Writing - review & editing.

Conflict of interest

The authors declare no conflict of interest.

Acknowledgement

The paper is based upon work supported by the U.S. Department Office of Fossil Energy FE-1 under Award Number DE-FE0031886.

Disclaimer

This paper was prepared as an account of work sponsored by an agency of the United States Government. Neither the United States Government nor any agency thereof, nor any of their employees, makes any warranty, express or implied, or assumes any legal liability or responsibility for the accuracy, completeness, or usefulness of any information, apparatus, product, or process disclosed, or represents that its use would not infringe privately owned rights. Reference herein to any specific commercial product, process, or service by trade name, trademark, manufacturer, or otherwise does not necessarily constitute or imply its endorsement, recommendation, or favoring by the United States Government or any agency thereof. The views and opinions of authors expressed herein do not necessarily state or reflect those of the United States Government or any agency thereof.

CHAPTER 7: EFFECT OF TUBE MATERIAL ON SYSTEM COOLING AND WEIGHT REDUCTION

7.1. Overview

In this section, the effect of different tube materials on cooling the Latent Heat Thermal Energy Storage (LTES) system and reducing the weight of the prototype-scale module designed in previous chapters is discussed. The reduction of system weight by using lighter tube materials would also result in reduced construction costs. Poly Vinyl Chloride (PVC) was selected as the non-metallic tube material for the analysis. Numerical analysis was performed for PVC and compared with experimental and numerical results obtained for metallic tubes (carbon steel) from Chapter 4.

7.2. Numerical analysis

The computational domain (Figure 4.2) and computational grid (Figure 4.3) mentioned in the previous chapter (Chapter 4) were utilized for the numerical analysis. The thermophysical properties (Table 4.1) of PCM (CC6), governing equations, and the boundary conditions for PCM melting (Table 4.2) were also identical for both PVC and carbon steel. The thermophysical properties of the tube materials are detailed in Table 7.1.

Table 7. 1 Thermophysical properties of tube materials

Tube material	ρ_s [kg/m^3]	C_{P_s} [J/kg.K]	k_s [W/m.K]
Carbon Steel	7870	500	45
PVC	1500	850	0.15

7.3. Results and discussion

The numerical results obtained for fully filled circular PVC tubes, following the same computational procedure as mentioned in Chapter 4, were compared to the numerical results obtained for fully filled circular carbon steel tubes. Experimental results using carbon steel tubes were included in the analysis for comparison.

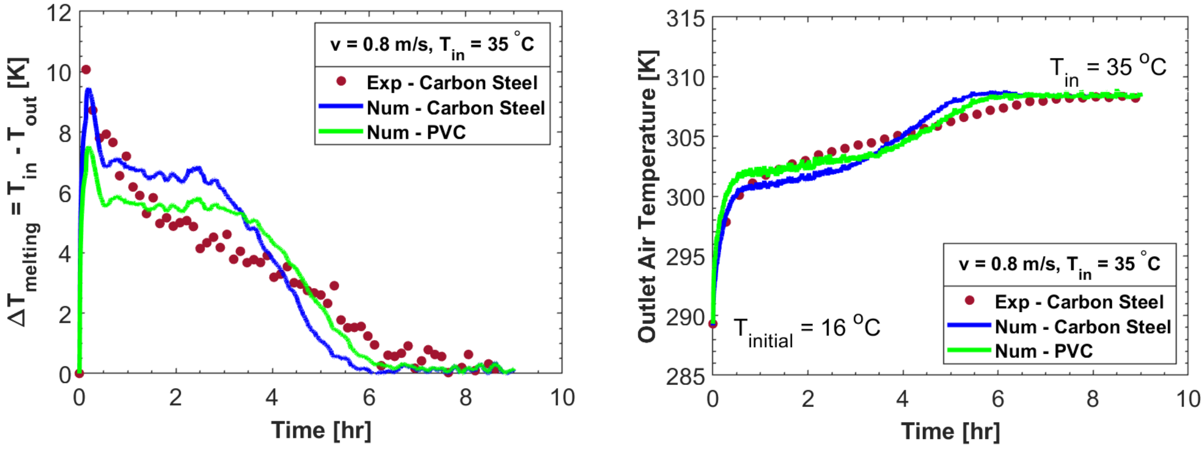

(a) (b)

Figure 7. 1 Comparison of (a) temperature difference ($\Delta T_{melting}$) for system cooling, (b) outlet air temperature as a function of flow time during the PCM melting test with inlet air velocity and temperature of 0.8 m/s and 308 K or 35 °C and initial temperature of 289 K or 16 °C

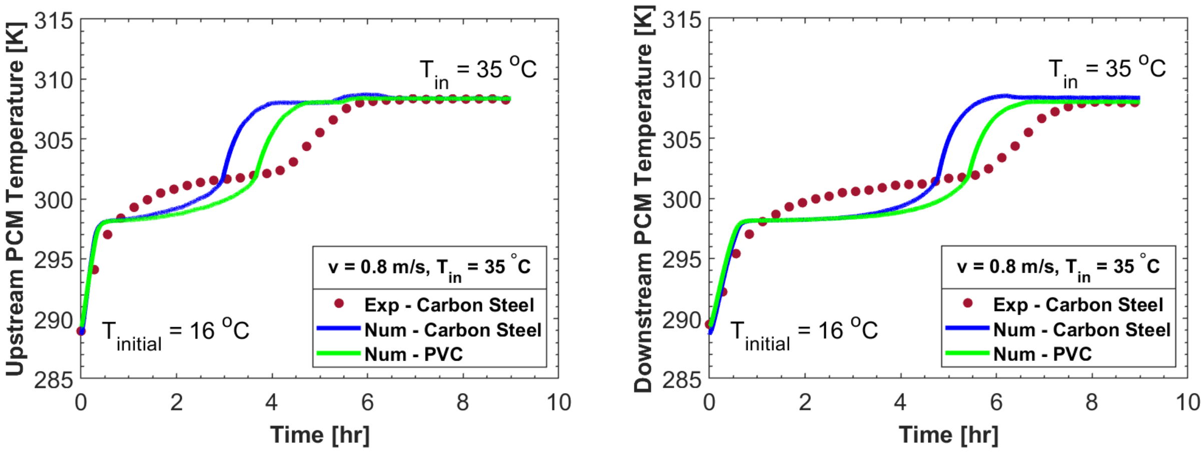

(a) (b)

Figure 7. 2 Comparison of (a) upstream PCM temperature, and (b) downstream PCM temperature as a function of flow time during the PCM melting test with inlet air velocity and temperature of 0.8 m/s and 308 K or 35 °C and initial temperature of 289 K or 16 °C

Figures 7.1a and 7.1b illustrate a comparison of the moving average value of the temperature difference between the inlet and outlet air temperatures for system cooling and the outlet air temperature as a function of time for the melting test, with inlet air velocity and temperature of 0.8

m/s and 308 K (or 35 °C), respectively, and an initial temperature of 289 K (or 16 °C). The findings indicate that the melting patterns of the PCM in the tube arrays are virtually identical for both tube materials. The use of PVC has a minimal effect on module performance because its thermal resistance to conduction is significantly lower compared to the resistance to convection. This is due to its lower thermal conductivity compared to carbon steel tubes (see Table 7.1). Consequently, the cooling effect persists slightly longer for PVC tubes compared to carbon steel tubes, due to its low thermal conductivity and high heat transfer resistance (see Figure 7.1a). This confirms that the use of PVC tubes in the array meets the predefined performance criteria of 4 °C for a 4-hour duration. Additionally, the results of the outlet air temperature from Figure 7.1b demonstrate that the numerical prediction using PVC tubes exhibits better agreement with the measured results than the numerical prediction using carbon steel tubes. This suggests that PVC material offers higher resistance to heat transfer compared to carbon steel.

Figure 7.2 displays a comparison of PCM temperatures at the upstream and downstream ends of the tube array. The numerical model predicts a shorter melting time compared to the experimental results for both tube materials, albeit slightly longer for the PVC tubes compared to the carbon steel tubes due to higher heat resistance, as mentioned earlier. The possible reasons behind the discrepancy between the numerical prediction and measured values of PCM temperatures have already been discussed in Chapter 4 and are not repeated in this section to avoid redundancy. Since the melting front is propagating through the tube array in the direction of the flow, the PCM in the upstream tube melts approximately 2 hours earlier compared to the downstream tube.

During the transition from solid to liquid PCM, both the PCM temperature (shown in Figure 7.2) and the outlet air temperature (shown in Figure 7.1b) stay fairly steady. Once all the PCMs in the tube have melted completely, both the PCM temperature and the outlet air temperature rise quickly until they reach the same temperature as the incoming air.

Table 7. 2 Comparison of hydraulic and thermal performance and module weight

ΔP (Pa)			h_{avg} (W/m^2-K)		Weight (kg)	
Carbon Steel Experiment	Carbon Steel Numerical	PVC Numerical	Carbon Steel Numerical	PVC Numerical	Carbon Steel Numerical	PVC Numerical
70 ± 3	56.34	56.34	51.27	31.72	322.4	59.5

Table 7.2 summarizes the hydraulic and thermal performance of the tube array for two different tube materials. It indicates that there is no difference in the pressure drop between the different tube materials, as the same prototype-scale module was used for comparison. However, the heat transfer coefficient is lower for PVC tubes compared to carbon steel, suggesting higher heat resistance and a slower melting process, or longer cooling effect when using PVC as tube materials. The thermal conductivity of PVC (0.15 W/m.K) is significantly smaller than that of carbon steel (45 W/m.K). This results in lower wall heat-flux for PVC (173 W/m^2) compared to carbon steel (214 W/m^2). Therefore, the average heat transfer coefficient (h_{avg}) is smaller for PVC than that of carbon steel, as presented in Table 7.2.

Additionally, the weight of the prototype-scale module with 208 tubes in the array was calculated for both tube materials [128]. The weight of the module is significantly lighter, approximately 43%, for PVC compared to carbon steel, including 323 kg of PCM inside the tubes (see Table 7.2). This would result in significantly lower construction costs when using PVC tubes instead of carbon steel.

CHAPTER 8: CONCLUSIONS AND FUTURE WORK

8.1. Overview

This chapter outlines the contributions of this research to the existing literature and suggests directions for future research.

8.2. Research contributions

The key contributions of this research work are as follows:

8.2.1. Successful design of the prototype-scale LTES system

- Dry cooling technology of coal power plant was improved using a latent heat cold thermal energy storage (LTES) system, where commercial-grade $CaCl_2$ hexahydrate (CC6) was selected as the phase change material (PCM) based on geographical locations.
- Numerical analysis was conducted to determine the optimum design through parametric analysis. A 13-row tube array consisting of 208 circular tubes, each with an outer diameter of 1.75″, was selected. The tubes were filled to 90% of their volume to accommodate volume expansion of the PCM during phase transition.
- The experimental results obtained from tests conducted at the prototype-scale test facility at Lehigh University in May and June of 2023 meet or exceed project performance specifications regarding the magnitude (4 ºC) and duration (four hours) of the cooling effect for the selected design, with an inlet air velocity of 0.8 m/s and an inlet air temperature of 35 ºC.
- The temperatures measured during the tests demonstrated excellent repeatability, with a maximum difference in ΔT_{air} (= $T_{in} - T_{out}$) across repeated tests within a 1 °C range.

- The pressure drop across the tube array, measured at the inlet and outlet, ranges from 50 to 70 Pa, varying with the superficial inlet air velocity (0.5 or 0.8 m/s), and complies with the requirement of a maximum pressure drop of 100 Pa or less.
- The LTES system effectively cools incoming ambient air during the night, over a period of about six hours, as the PCM freezes and releases heat into the air.
- The numerical results for the temperature at the outlet of the tube array show very good agreement with the measurements, with the maximum difference in the 1 to 2 º C range.
- The differences between the numerical predictions and the measured temperatures of the PCM are likely due to the model's assumption of a constant phase change temperature, which can be affected by impurities in the commercial PCM. Using the specific heat capacity method rather than the enthalpy-porosity technique for modeling the melting and solidification processes of PCM might yield more accurate predictions [43].
- The thermal storage capacity of the prototype-scale tube array ranges from 15 to 18 kWh for the selected operating conditions. The corresponding energy storage density falls between 22 and 27 kWh/m^3 with a maximum energy efficiency of around 96%, assuming no heat loss from the system.
- The final design will feature 2,746 prototype-scale PCM modules attached to two sides of a triangular steel support structure, akin to the "Cooling Delta" found in a mechanical draft cooling tower (Heller Tower) [129].
- The proposed design, which includes ACC precooling and PCM cooling, results in a net annual power generation of 20.8 GWh. This will generate additional net present value (NPV) of $34.2M over the 30-year lifespan of the plant.

- The proposed concept can be applied broadly, including in simple and combined Brayton cycles, as well as in industrial, commercial, residential, and concentrated solar power (CSP) settings.

8.2.2. Analysis of circular and elliptical tube geometries for pressure drop reduction

- Numerical analysis was performed to compare the hydraulic and thermal performance of circular and elliptical tube array geometries, each containing almost the same amount of PCM and having the same heat transfer area as the circular geometry. The spacing between tubes and the ratio of pitch to hydraulic diameter were maintained consistently for both geometries.
- The thermal performance predicted numerically for both the circular and elliptical tubes was nearly identical during the melting and freezing phases.
- However, due to the superior aerodynamics of the elliptical tubes, the pressure drop across the horizontal elliptical tube array is reduced by 80% compared to the circular configuration.
- This reduction in pressure drop suggests that less pumping power is needed to maintain the desired flow rate through the tube array, thereby offering economic advantages with the horizontal elliptical tube array.

8.2.3. Analysis of metallic and non-metallic tube material for weight reduction

- Numerical analysis of PCM melting process was performed to compare the hydraulic and thermal performance of a prototype-scale tube array using two different tube materials: carbon steel (metallic) and PVC (non-metallic).
- There is no difference in the hydraulic performance between the two materials, as the same prototype-scale module was used for the comparison.

- However, due to the lower thermal conductivity of PVC (0.15 W/m.K) compared to carbon steel (45 W/m.K), the melting process is slower for PVC. This suggests a higher heat resistance, which would allow for a longer cooling effect when using PVC as the tube material.
- Additionally, the weight of the prototype-scale module is significantly reduced by approximately 43% when using PVC instead of carbon steel, not including the PCM inside the tubes. This significant reduction in weight can lead to substantially lower construction costs with PVC tubes.

8.3. Recommendations for future research

It typically takes over nine days (approximately 216 hours) to forecast the hydraulic and thermal performance of a prototype-scale LTES system using the commercial software Fluent [81] on Orion HPC clusters. Implementing artificial intelligence (AI) techniques or machine learning (ML) algorithms such as Random Forest Classifier and feed-forward back-propagation artificial neural networks (ANN) could significantly reduce the computational time compared to using Fluent [81]. The multidimensional nature of this future study should account for variations in inlet velocity (V_{in}), inlet temperature (T_{in}), tube diameter (D), lateral tube spacing (S_L), transverse tube spacing (S_T), and the number of tube rows (N_L) in the tube array of LTES system. During the training process, it is crucial to establish correlations between heat storage, pressure drop, Reynolds numbers, and inlet temperatures, while comparing various ML algorithms to identify the most effective predictive model. This innovative approach holds promise for streamlining predictions in general thermal energy storage optimization and could also assist in predicting energy production patterns based on historical data and real-time operating conditions, providing valuable insights for grid operators and energy planners.

REFERENCES

1. EIA, *International energy outlook*, in *U.S. Energy Information Administration*. 2017.
2. *Climate-change, United States Environmental Protection Agency*. 2023.
3. De Trizio, L. and L. Manna, *Forging colloidal nanostructures via cation exchange reactions.* Chemical reviews, 2016. **116**(18): p. 10852-10887.
4. Gerkman, M.A. and G.G. Han, *Toward controlled thermal energy storage and release in organic phase change materials.* Joule, 2020. **4**(8): p. 1621-1625.
5. Kalapala, L. and J.K. Devanuri, *Energy and exergy analyses of latent heat storage unit positioned at different orientations–An experimental study.* Energy, 2020. **194**: p. 116924.
6. Dhaidan, N.S. and J. Khodadadi, *Melting and convection of phase change materials in different shape containers: A review.* Renewable and Sustainable Energy Reviews, 2015. **43**: p. 449-477.
7. EPA, *Federal Water Pollution Control Act, 2002, 33 U.S.C. 1251 et seq. Federal Register.*
8. EPRI, *Water Use for Electricity Generation and Other Sectors: Recent Changes (1985-2005) and Future Projections (2005-2030)*. 2011: Palo Alto, CA.
9. DOE, N., *Estimating Freshwater Needs to Meet Future Thermoelectric Generation Requirements, DOE/NETL-400/2010/1339, Department of Energy, National Energy Technology Laboratory*. 2010.
10. *Multi-bay Air Cooled Condenser (ACC)*. Available from: https://www.babcock.com/home/about/resources/success-stories/spig-cooling-tower-projects.
11. *EBSILON^{R} Professional, The Planning Tool for the Power Plant Process, STEAG Energy Services GmbH, System Technologies* Available from: www.ebsilon.com, www.steag-systemtechnologies.com.
12. Tay, N., M. Belusko, and F. Bruno, *Experimental investigation of tubes in a phase change thermal energy storage system.* Applied energy, 2012. **90**(1): p. 288-297.
13. Agyenim, F., et al., *A review of materials, heat transfer and phase change problem formulation for latent heat thermal energy storage systems (LHTESS).* Renewable and sustainable energy reviews, 2010. **14**(2): p. 615-628.

14. Agrawal, A., A. Kumar, and D. Rakshit, *A novel analytical approach to study the charging characteristics of a shell and tube thermal energy storage system.* Energy Storage, 2022. **4**(1): p. e285.

15. Guo, C. and W. Zhang, *Numerical simulation and parametric study on new type of high temperature latent heat thermal energy storage system.* Energy Conversion and Management, 2008. **49**(5): p. 919-927.

16. Wang, W.-W., et al., *Numerical study of the heat charging and discharging characteristics of a shell-and-tube phase change heat storage unit.* Applied Thermal Engineering, 2013. **58**(1-2): p. 542-553.

17. Tao, Y. and V. Carey, *Effects of PCM thermophysical properties on thermal storage performance of a shell-and-tube latent heat storage unit.* Applied Energy, 2016. **179**: p. 203-210.

18. Wang, P., et al., *Numerical investigation of PCM melting process in sleeve tube with internal fins.* Energy Conversion and Management, 2016. **110**: p. 428-435.

19. Freeman, J., et al., *A small-scale solar organic Rankine cycle combined heat and power system with integrated thermal energy storage.* Applied thermal engineering, 2017. **127**: p. 1543-1554.

20. Canbazoğlu, S., et al., *Enhancement of solar thermal energy storage performance using sodium thiosulfate pentahydrate of a conventional solar water-heating system.* Energy and buildings, 2005. **37**(3): p. 235-242.

21. Zalba, B., et al., *Review on thermal energy storage with phase change: materials, heat transfer analysis and applications.* Applied thermal engineering, 2003. **23**(3): p. 251-283.

22. Koca, A., et al., *Energy and exergy analysis of a latent heat storage system with phase change material for a solar collector.* Renewable Energy, 2008. **33**(4): p. 567-574.

23. Ghalambaz, M. and J. Zhang, *Conjugate solid-liquid phase change heat transfer in heatsink filled with phase change material-metal foam.* International Journal of Heat and Mass Transfer, 2020. **146**: p. 118832.

24. Chen, G., et al., *Experimental and numerical investigation of the latent heat thermal storage unit with PCM packing at the inner side of a tube.* International Journal of Heat and Mass Transfer, 2020. **152**: p. 119480.

25. Khedher, N.B., et al., *Geometry modification of a vertical shell-and-tube latent heat thermal energy storage system using a framed structure with different undulated shapes for the phase change material container during the melting process.* Journal of Energy Storage, 2023. **72**: p. 108365.
26. Chatterjee, S., D. Bhanja, and S. Nath, *Numerical investigation of heat transfer and melting process of phase change material in trapezoidal cavities with different shapes and different heated tube positions.* Journal of Energy Storage, 2023. **72**: p. 108285.
27. Horvat, A., M. Leskovar, and B. Mavko, *Comparison of heat transfer conditions in tube bundle cross-flow for different tube shapes.* International Journal of Heat and Mass Transfer, 2006. **49**(5-6): p. 1027-1038.
28. Mangrulkar, C.K., et al., *Thermal performance escalation of cross flow heat exchanger using in-line elliptical tubes.* Experimental Heat Transfer, 2020. **33**(7): p. 587-612.
29. Mohanan, A.K., B.V. Prasad, and S. Vengadesan, *Flow and heat transfer characteristics of a cross-flow heat exchanger with elliptical tubes.* Heat Transfer Engineering, 2021. **42**(21): p. 1846-1860.
30. Mosa, M.A.M., *Study of circular and elliptical tube arrays as cross flow heat exchangers.* 2009.
31. Jang, J.-Y. and J.-Y. Yang, *Experimental and 3-D numerical analysis of the thermal-hydraulic characteristics of elliptic finned-tube heat exchangers.* Heat Transfer Engineering, 1998. **19**(4): p. 55-67.
32. Swain, A. and M.K. Das, *Convective heat transfer and pressure drop over elliptical and flattened tube.* Heat Transfer—Asian Research, 2016. **45**(5): p. 462-481.
33. Jodaei, A. and K. Zamzamian, *A Study about performance evaluation criteria of tube banks with various shapes and arrangements using numerical simulation.* Journal of Pressure Vessel Technology, 2017. **139**(5): p. 051303.
34. Mohanty, R.L., A. Swain, and M.K. Das, *Thermal performance of mixed tube bundle composed of circular and elliptical tubes.* Thermal Science and Engineering Progress, 2018. **5**: p. 492-505.
35. Saffarian, M.R., F. Fazelpour, and M. Sham, *Numerical study of shell and tube heat exchanger with different cross-section tubes and combined tubes.* International Journal of Energy and Environmental Engineering, 2019. **10**: p. 33-46.

36. Ding, C., et al., *Evaluation and comparison of thermal performance of latent heat storage units with shell-and-tube, rectangular, and cylindrical configurations.* Applied Thermal Engineering, 2023. **218**: p. 119364.
37. Fabrykiewicz, M., K. Tesch, and J.T. Cieśliński, *Numerical Modeling of Charging and Discharging of Shell-and-Tube Pcm Thermal Energy Storage Unit.* Available at SSRN 4669013.
38. Rana, S., M. Zunaid, and R. Kumar, *CFD analysis for heat transfer comparison in circular, rectangular and elliptical tube heat exchangers filled with PCM.* Materials Today: Proceedings, 2022. **56**: p. 637-644.
39. Holman, J.P., *Experimental Methods for Engineers EIGHTH EDITION.* 2021.
40. Khuda, M.A., et al., *Numerical analysis of a developing turbulent flow and conjugate heat transfer for molten salt and liquid sodium in a solar receiver.* Applied Thermal Engineering, 2022. **217**: p. 119156.
41. Pan, C., et al., *Experimental, numerical and analytic study of unconstrained melting in a vertical cylinder with a focus on mushy region effects.* International Journal of Heat and Mass Transfer, 2018. **124**: p. 1015-1024.
42. Poirier, D. and M. Salcudean, *On numerical methods used in mathematical modeling of phase change in liquid metals.* 1988.
43. Iten, M., S. Liu, and A. Shukla, *Experimental validation of an air-PCM storage unit comparing the effective heat capacity and enthalpy methods through CFD simulations.* Energy, 2018. **155**: p. 495-503.
44. Li, D., et al., *Lattice Boltzmann models for axisymmetric solid–liquid phase change.* International Journal of Heat and Mass Transfer, 2017. **112**: p. 795-804.
45. Qu, Z., *Heat transfer enhancement technique of pcms and its lattice Boltzmann modeling*, in *Thermal Energy Battery with Nano-enhanced PCM*. 2018, IntechOpen.
46. Gimenez, O., et al., *WinBUGS for population ecologists: Bayesian modeling using Markov Chain Monte Carlo methods.* Modeling demographic processes in marked populations, 2009: p. 883-915.
47. Goodarzi, M., et al., *Applying Bayesian Markov chain Monte Carlo (MCMC) modeling to predict the melting behavior of phase change materials.* Journal of Energy Storage, 2022. **45**: p. 103570.

48. Assis, E., et al., *Numerical and experimental study of melting in a spherical shell.* International Journal of Heat and Mass Transfer, 2007. **50**(9-10): p. 1790-1804.

49. Assis, E., G. Ziskind, and R. Letan, *Numerical and experimental study of solidification in a spherical shell.* 2009.

50. Nemati, H. and M. Habibi, *Analytical and numerical analysis of phase change material solidification in partially filled capsules considering breathing vent.* Journal of Energy Storage, 2021. **40**: p. 102725.

51. Regin, A., S. Solanki, and J. Saini. *Experimental and numerical analysis of melting of PCM inside a spherical capsule*. in *9th AIAA/ASME Joint Thermophysics and Heat Transfer Conference*. 2006.

52. Bilir, L. and Z. Ilken, *Total solidification time of a liquid phase change material enclosed in cylindrical/spherical containers.* Applied thermal engineering, 2005. **25**(10): p. 1488-1502.

53. Benbrika, M., et al., *Effect of orientation of elliptic tube on the total melting time of latent thermal energy storage systems.* Journal of Thermal Engineering, 2021. **7**(6): p. 1479-1488.

54. Bazai, H., et al., *Numerical study of circular-elliptical double-pipe thermal energy storage systems.* Journal of Energy Storage, 2020. **30**: p. 101440.

55. Eisapour, A.H., et al., *Optimum design of a double elliptical latent heat energy storage system during the melting process.* Journal of Energy Storage, 2021. **44**: p. 103384.

56. Faghani, M., M. Hosseini, and R. Bahrampoury, *Numerical simulation of melting between two elliptical cylinders.* Alexandria Engineering Journal, 2018. **57**(2): p. 577-586.

57. Alnakeeb, M.A., et al., *The influence of elliptic aspect ratio and inclination angle on the melting characteristic of phase change material in concentric cylindrical enclosure.* Journal of Energy Storage, 2023. **62**: p. 106832.

58. Sebti, S., et al., *A numerical investigation of solidification in horizontal concentric annuli filled with nano-enhanced phase change material (NEPCM).* World Applied Sciences Journal, 2011. **13**(1): p. 09-15.

59. Das, N., et al., *Enhanced melting behavior of carbon based phase change nanocomposites in horizontally oriented latent heat thermal energy storage system.* Applied Thermal Engineering, 2017. **125**: p. 880-890.

60. Trp, A., K. Lenic, and B. Frankovic, *Analysis of the influence of operating conditions and geometric parameters on heat transfer in water-paraffin shell-and-tube latent thermal energy storage unit.* Applied Thermal Engineering, 2006. **26**(16): p. 1830-1839.
61. Bechiri, M. and K. Mansouri, *Study of heat and fluid flow during melting of PCM inside vertical cylindrical tube.* International Journal of Thermal Sciences, 2019. **135**: p. 235-246.
62. Das, N., et al., *Effect of carbon nano inclusion dimensionality on the melting of phase change nanocomposites in vertical shell-tube thermal energy storage unit.* International journal of heat and mass transfer, 2017. **113**: p. 423-431.
63. Jones, B.J., et al., *Experimental and numerical study of melting in a cylinder.* International Journal of Heat and Mass Transfer, 2006. **49**(15-16): p. 2724-2738.
64. Shmueli, H., G. Ziskind, and R. Letan, *Melting in a vertical cylindrical tube: Numerical investigation and comparison with experiments.* International Journal of Heat and Mass Transfer, 2010. **53**(19-20): p. 4082-4091.
65. Sultan, M., H.M. Mostafa, and E.A. Elngiry, *Effect of Inlet and Geometrical Parameters on the Melting of PCM Capsules of Elliptical Cross Section.* ERJ. Engineering Research Journal, 2021. **44**(1): p. 11-20.
66. Arıcı, M., et al., *Melting of nanoparticle-enhanced paraffin wax in a rectangular enclosure with partially active walls.* International Journal of Heat and Mass Transfer, 2017. **104**: p. 7-17.
67. Silva, P.D., L. Goncalves, and L. Pires, *Transient behaviour of a latent-heat thermal-energy store: numerical and experimental studies.* Applied energy, 2002. **73**(1): p. 83-98.
68. Iachachene, F., et al., *Melting of phase change materials in a trapezoidal cavity: Orientation and nanoparticles effects.* Journal of Molecular Liquids, 2019. **292**: p. 110592.
69. Sharma, R., et al., *Numerical study for enhancement of solidification of phase change materials using trapezoidal cavity.* Powder technology, 2014. **268**: p. 38-47.
70. Hosseinzadeh, K., et al., *Effect of fin and hybrid nano-particles on solid process in hexagonal triplex latent heat thermal energy storage system.* Journal of Molecular Liquids, 2020. **300**: p. 112347.
71. Sheikholeslami, M., et al., *Heat transfer simulation during charging of nanoparticle enhanced PCM within a channel.* Physica A: Statistical Mechanics and its Applications, 2019. **525**: p. 557-565.

72. Li, Z., et al., *Time-dependent heat transfer simulation for NEPCM solidification inside a channel.* Journal of Thermal Analysis and Calorimetry, 2019. **138**: p. 721-726.
73. Dhaidan, N.S., *Thermal performance of constrained melting of PCM inside an elliptical capsule of two orientations.* Iranian Journal of Science and Technology, Transactions of Mechanical Engineering, 2021. **45**: p. 515-521.
74. Ebadi, S., et al., *Melting of nano-PCM inside a cylindrical thermal energy storage system: Numerical study with experimental verification.* Energy Conversion and Management, 2018. **166**: p. 241-259.
75. Niyas, H. and P. Muthukumar, *A novel heat transfer enhancement technique for performance improvements in encapsulated latent heat storage system.* Solar Energy, 2018. **164**: p. 276-286.
76. Jourabian, M., et al., *Melting of NEPCM within a cylindrical tube: numerical study using the lattice Boltzmann method.* Numerical Heat Transfer, Part A: Applications, 2012. **61**(12): p. 929-948.
77. Jourabian, M., M. Farhadi, and A.A. Rabienataj Darzi, *Heat transfer enhancement of PCM melting in 2D horizontal elliptical tube using metallic porous matrix.* Theoretical and Computational Fluid Dynamics, 2016. **30**: p. 579-603.
78. Ismail, K.A. and J. Henrıquez, *Numerical and experimental study of spherical capsules packed bed latent heat storage system.* Applied Thermal Engineering, 2002. **22**(15): p. 1705-1716.
79. Ismail, K.A., et al., *Experimentally validated two dimensional numerical model for the solidification of PCM along a horizontal long tube.* International Journal of Thermal Sciences, 2014. **75**: p. 184-193.
80. Nandi, S. and Y. Sanyasiraju, *A second order accurate fixed-grid method for multi-dimensional Stefan problem with moving phase change materials.* Applied Mathematics and Computation, 2022. **416**: p. 126719.
81. ANSYS, *ANSYS Fluent - CFD Software | ANSYS*. 2022.
82. Zukauskas, A., *Advances in heat transfer.* Adv. Heat Transf, 1972. **8**: p. 93-160.
83. Bergman, T.L., et al., *Introduction to heat transfer*. 2011: John Wiley & Sons.
84. Churchill, S.W. and H. Ozoe, *Correlations for laminar forced convection with uniform heating in flow over a plate and in developing and fully developed flow in a tube.* 1973.

85. Hilpert, R., *Heat transfer from cylinders.* Forsch. Geb. Ingenieurwes, 1933. **4**(5): p. 215.

86. Erek, A. and I. Dincer, *A new approach to energy and exergy analyses of latent heat storage unit.* Heat Transfer Engineering, 2009. **30**(6): p. 506-515.

87. Socaciu, L.G., *Thermal energy storage with phase change material.* Leonardo Electronic Journal of Practices and Technologies, 2012. **20**: p. 75-98.

88. Suresh, C. and R.P. Saini, *Thermal performance of sensible and latent heat thermal energy storage systems.* International Journal of Energy Research, 2020. **44**(6): p. 4743-4758.

89. Wang, W., et al., *Experimental study on the direct/indirect contact energy storage container in mobilized thermal energy system (M-TES).* Applied energy, 2014. **119**: p. 181-189.

90. Zhang, P., F. Ma, and X. Xiao, *Thermal energy storage and retrieval characteristics of a molten-salt latent heat thermal energy storage system.* Applied Energy, 2016. **173**: p. 255-271.

91. Abedin, A.H. and M.A. Rosen, *Closed and open thermochemical energy storage: Energy- and exergy-based comparisons.* Energy, 2012. **41**(1): p. 83-92.

92. Balasubramanian, G., et al., *Modeling of thermochemical energy storage by salt hydrates.* International Journal of Heat and Mass Transfer, 2010. **53**(25-26): p. 5700-5706.

93. Li, G., *Energy and exergy performance assessments for latent heat thermal energy storage systems.* Renewable and sustainable energy reviews, 2015. **51**: p. 926-954.

94. Guelpa, E., A. Sciacovelli, and V. Verda, *Entropy generation analysis for the design improvement of a latent heat storage system.* Energy, 2013. **53**: p. 128-138.

95. Kaygusuz, A.S., Kamil, *Energy and exergy calculations of latent heat energy storage systems.* Energy sources, 2000. **22**(2): p. 117-126.

96. Rezaei, M., et al., *Performance and cost analysis of phase change materials with different melting temperatures in heating systems.* Energy, 2013. **53**: p. 173-178.

97. Islam, S., N. Jahan, and M.T. Ali, *STUDY OF THE NATURE OF VARIATION OF VELOCITY AROUND THE BODIES OF DIFFERENT GEOMETRIC SHAPES.* Journal of Mechanical and Industrial Engineering Research, 2018. **7**(1): p. 11-17.

98. Soni, V., et al., *Real-time experimental study and numerical simulation of phase change material during the discharge stage: Thermo-fluidic behavior, solidification morphology, and energy content.* Energy Storage, 2019. **1**(1): p. e51.

99. Rahdar, M.H., A. Emamzadeh, and A. Ataei, *A comparative study on PCM and ice thermal energy storage tank for air-conditioning systems in office buildings.* Applied Thermal Engineering, 2016. **96**: p. 391-399.

100. Dincer, I., *On thermal energy storage systems and applications in buildings.* Energy and buildings, 2002. **34**(4): p. 377-388.

101. Gong, Z.-X. and A.S. Mujumdar, *Thermodynamic optimization of the thermal process in energy storage using multiple phase change materials.* Applied Thermal Engineering, 1997. **17**(11): p. 1067-1083.

102. Neeper, D., *Thermal dynamics of wallboard with latent heat storage.* Solar energy, 2000. **68**(5): p. 393-403.

103. Mahfuz, M., et al., *Performance investigation of thermal energy storage system with Phase Change Material (PCM) for solar water heating application.* International Communications in Heat and Mass Transfer, 2014. **57**: p. 132-139.

104. Öztürk, H.H., *Experimental evaluation of energy and exergy efficiency of a seasonal latent heat storage system for greenhouse heating.* Energy conversion and management, 2005. **46**(9-10): p. 1523-1542.

105. Pagkalos, C., et al., *Evaluation of water and paraffin PCM as storage media for use in thermal energy storage applications: A numerical approach.* International Journal of Thermofluids, 2020. **1**: p. 100006.

106. McMaster-CARR. *Polished Multipurpose 304 Stainless Steel Round Tube*. 2023; Available from: https://www.mcmaster.com/1750T23/.

107. Zhao, C., et al., *Phase change behaviour study of PCM tanks partially filled with graphite foam.* Applied Thermal Engineering, 2021. **196**: p. 117313.

108. Zukauskas, A. and R. Ulinskas, *Heat transfer in tube banks in crossflow.* 1988.

109. FLUENT, A., *Documentation, Theory Guide. 2015.*

110. Dincer, I. and M.A. Rosen, *Thermal energy storage: systems and applications*. 2021: John Wiley & Sons.

111. Agency, I.E., *Technology roadmap: solar heating and cooling*. 2012: International Energy Agency.

112. Liu, G., et al., *Effects of different sizes and dispatch strategies of thermal energy storage on solar energy usage ability of solar thermal power plant.* Applied Thermal Engineering, 2019. **156**: p. 14-22.

113. Mosleh, H.J. and R. Ahmadi, *Linear parabolic trough solar power plant assisted with latent thermal energy storage system: A dynamic simulation.* Applied Thermal Engineering, 2019. **161**: p. 114204.

114. Uddin, M., A.S. Virk, and C. Park, *Natural Convection in the Melting of Phase Change Materials in a Cylindrical Thermal Energy Storage System: Effects of Flow Arrangements of Heat Transfer Fluid and Associated Thermal Boundary Conditions.* Journal of Thermal Science and Engineering Applications, 2023. **15**(11).

115. Khuda, M.A., et al., *Energy and exergy analysis of a laboratory-scale latent heat thermal energy storage (LTES) using salt-hydrate in a staggered tube arrangement.* Journal of Energy Storage, 2024. **87**: p. 111320.

116. Yan, L., et al., *Experimental investigation of the thermal performance of pervious concrete integrated with phase change material for dry cooling applications.* Applied Thermal Engineering, 2023: p. 121749.

117. Yan, L., et al., *Optimizing supercooling and phase stability by additives in calcium chloride hexahydrate for cyclical latent heat storage.* International Communications in Heat and Mass Transfer, 2023. **149**: p. 107119.

118. Longeon, M., et al., *Experimental and numerical study of annular PCM storage in the presence of natural convection.* Applied energy, 2013. **112**: p. 175-184.

119. Khuda, M.A., et al., *Design, analysis, and testing of a prototype-scale latent heat thermal energy storage (LTES) system.* Journal of Energy Storage, 2024.

120. Shokouhmand, H. and B. Kamkari, *Experimental investigation on melting heat transfer characteristics of lauric acid in a rectangular thermal storage unit.* Experimental Thermal and Fluid Science, 2013. **50**: p. 201-212.

121. Dhaidan, N.S., *Melting phase change of n-eicosane inside triangular cavity of two orientations.* Journal of Renewable and Sustainable Energy, 2017. **9**(5).

122. Saitoh, T. and K. Hirose, *High Rayleigh number solutions to problems of latent heat thermal energy storage in a horizontal cylinder capsule.* 1982.

123. Prasad, A. and S. Sengupta, *Numerical investigation of melting inside a horizontal cylinder including the effects of natural convection.* Journal of Heat Transfer (Transactions of the ASME (American Society of Mechanical Engineers), Series C);(United States), 1987. **109**(3).

124. Dhaidan, N.S. and A.F. Khalaf, *Experimental evaluation of the melting behaviours of paraffin within a hemicylindrical storage cell.* International Communications in Heat and Mass Transfer, 2020. **111**: p. 104476.

125. Darzi, A.A.R., M. Jourabian, and M. Farhadi, *Melting and solidification of PCM enhanced by radial conductive fins and nanoparticles in cylindrical annulus.* Energy conversion and management, 2016. **118**: p. 253-263.

126. *Thermal Properties of Metals, Conductivity, Thermal Expansion, Specific Heat*. Available from: https://www.engineersedge.com/properties_of_metals.htm.

127. Mahfuja, A.K., et al., *STUDY OF FLOW CHARACTERISTICS OVER AND BEHIND NACA0012 AIRFOIL.* International Journal of Advanced Engineering and Science, 2018. **7**(1): p. 17-23.

128. *Pipe Weight Calculator*. Available from: https://www.omnicalculator.com/construction/pipe-weight.

129. Balogh, A., *HELLER System: The Economical Substitute for Wet Cooling - to avoid casting a shadow upon the sky, EPRI Workshop on Advanced Thermal Electric Power Cooling Technologies July 8-9, 2008, Charlotte (NC).*